NUMERICAL MODELING OF HILLSLOPE THERMAL HYDROLOGY TO

UNDERSTAND SPATIAL AND TEMPORAL TRENDS IN SOIL ICE FORMATION AND

IMPLICATIONS FOR HYDROLOGIC PARTITIONING

by

MICHAEL JOSEPH RUSH

B.S., University of Minnesota, 2010

M.S., University of Colorado, 2018

A thesis submitted to the

Faculty of the Graduate School of the

University of Colorado in partial fulfillment

of the requirement for the degree of

Doctor of Philosophy

Department of Civil, Environmental, and Architectural Engineering

2020

Committee Members:

Harihar Rajaram

Robert Anderson

Suzanne Anderson

Michael Gooseff

Eve-Lyn Hinckley

Roseanna Neupauer

Rush, Michael Joseph (Ph.D., Civil, Environmental, and Architectural Engineering)

Numerical Modeling of Hillslope Thermal Hydrology to Understand Spatial and Temporal

Trends in Soil Ice Formation and Implications for Hydrologic Partitioning

Thesis directed by Professor Harihar Rajaram

The intensity, duration, and spatial distribution of frozen soil influences hydrologic flow paths, soil biogeochemistry, and slope geomorphology. In mountain environments, steep topography produces strong gradients in solar insolation, vegetation, and snowpack dynamics that lead to large differences in soil temperature over short distances, suggesting a need for high-resolution, process-based models that quantify the influence of topography. Surface energy balance calculations and a physical snowpack model based on the Utah Energy Balance have been coupled with PFLOTRAN-ICE, a subsurface thermo-hydrologic model that simulates water and energy transport in the subsurface, including freeze-thaw processes. A thermo-hydrologic modeling study is presented against the backdrop of field observations from Gordon Gulch and Niwot Ridge, seasonally snow-covered catchments in the headwaters of the Boulder Creek watershed. Despite a persistent snowpack on the north-facing slope at Gordon Gulch, seasonally frozen ground is more prevalent and persistent there because of low solar insolation and a thin snowpack. The south-facing slope experiences significantly higher incoming solar radiation that prevents the persistence of frozen ground. Representation of the snowpack and surface energy balance significantly improves soil temperature estimates compared to model forcing based on air temperature alone. At Niwot Ridge, deep (>1m depth) frozen soil underlying bare ground impeded groundwater recharge, and shallow frozen ground (<1m depth) beneath seasonal snow limited infiltration. Modeled alpine and subalpine snowcover exerted a positive effect on soil temperatures but did not prevent or eliminate frozen ground completely. Shallow freezing beneath snow-covered ground exerted a much stronger effect on infiltration than shallow freezing beneath bare ground because the soil beneath the snow remained frozen

while the snowpack was melting, whereas solar insolation thawed bare patches by the time

they received excess snowmelt "run-on". In projections of seasonally frozen ground,

simulations forecast two additional months of unfrozen soils by the end of the 21st century

compared to the 1952-1970 time period. A permafrost analysis provides support for the

occurrence of permafrost above 3800m and suggests that the deep soil thaw that has taken

place over the last several decades is small compared to deep soil thaw that should be

expected throughout the current century.

CONTENTS

CHAPTERS

TABLES

Table

FIGURES

viii

CHAPTER I

INTRODUCTION

1. Background and Motivation

Many high-latitude and high-elevation regions experience the seasonal formation of frozen ground. Frozen ground can be divided into permafrost and seasonally frozen soils. Permafrost is perennially frozen ground that remains at or below 0°C for at least two years [Harris et al., 1988] and occupies about 25% of exposed land in the northern hemisphere [Zhang et al., 2003]. Seasonally frozen ground (SFG) freezes and thaws annually [Harris et al., 1988], generally occurs at lower latitudes and altitudes than permafrost, and covers approximately 50% of the exposed land in the northern hemisphere [Zhang et al., 2003]. Permafrost is further divided into continuous, discontinuous, sporadic, and isolated zones based on its spatial extent [Zhang, 2003]. Throughout this thesis, freezing "intensity" refers to the number of degrees below 0°C, "frequency" refers to the number of intra-annual freezing and thawing events, and "duration" refers to the length of time that the ground is frozen.

The spatial distribution of frozen soil exerts a strong control on subsurface water flow and transport processes by reducing soil permeability, impeding infiltration, and inducing surface runoff [Walvoord & Kurylyk, 2016]. Accordingly, degradation of frozen ground may alter streamflow seasonality, groundwater flow paths, and subsurface storage in mountain watersheds that account for over 30% of global discharge [Meybeck, 2001]. Such differences in subsurface flow paths and soil moisture also suggest heterogeneities in local nutrient cycling and connected biogeochemical processes. In addition to hydrology, soil temperature strongly controls soil microbial activity and diversity in alpine regions, which in turn influence local vegetation dynamics and global biogeochemical cycles, especially the carbon cycle [Donhauser and Frey, 2018]. Seasonal freezing and thawing also influences hillslope

geomorphology through the process of frost creep. From a civil engineering perspective, information about the intensity, frequency, and duration of soil freezing is important for construction and maintenance of infrastructure, as well as for water resources planning and management.

Climate change has produced increasing permafrost temperatures throughout the northern hemisphere [e.g. Romanovsky et al., 2009; Harris et al., 2009; Osterkamp, 2005] and modeling studies predict continued warming and permafrost degradation throughout the 21st century [e.g. Pastick et al., 2015; Jones et al., 2014; Slater and Lawrence, 2013; Koven et al., 2013; Lawrence et al., 2012]. At Niwot Ridge, CO, seasonally frozen ground was recently observed [Leopold et al., 2014] at sites where permafrost had been observed in the 1970's [Ives and Fahey, 1971]. Both the current and projected areal extent of permafrost are highly uncertain (e.g. 6-29% permafrost loss for each 1°C of high latitude warming) due to differences in land surface models used to simulate frozen ground [Koven et al., 2013; Slater and Lawrence, 2013]. In addition, projections are sensitive to the emissions pathways included in the analysis; for example, under RCP2.6, present-day permafrost is expected to largely persist ($10^6 \, km^2$ reduction from 2020 to 2100), whereas under RCP8.5, extensive permafrost degradation is expected ($10^7 \, km^2$ from 2020 to 2100) [Slater and Lawrence, 2013].

Similarly, previous studies have found reductions in the extent and duration of seasonally frozen ground (SFG) due to a warming climate. Reductions in seasonal freezing depth have been observed in high-latitude Europe [e.g. Frauenfeld and Zhang, 2011] and the Tibetan plateau [e.g. Zhao et al., 2004]. Simulations project continued reductions in seasonal freezing depth on the Tibetan Plateau [Cuo et al., 2015; Guo and Wang, 2013] and SFG extent throughout the northern hemisphere (reductions in SFG extent of 4% for RCP2.6 to 15% for RCP8.5) [Lawerence et al., 2012]. On the Tibetan Plateau, soils froze 10 days later and thawed 14 days earlier across the 1988-2007 period, or 16.8 days per decade [Li et al.,

2012]. Projections at the Hubbard Brook Experimental Forest suggest a trend of 0.09-0.6 fewer days of seasonal frost each year throughout the 21st century [Campbell et al., 2010].

Infiltration in frozen soils remains an active area of investigation. Many studies have shown that frozen soils reduce infiltration [e.g. Dunne and Black, 1971; Kane and Stein, 1983; Thunholm et al., 1989; Stähli et al., 1996, Laudon et al., 2004; Bayard et al., 2005], while others have found no connection between frozen soils and runoff generation [Shanley and Chalmers, 1999; Nyberg et al., 2001; Lindström et al., 2002; Fuss et al., 2016]. Hydraulic conductivity decreases by orders of magnitude during the transition from unfrozen to frozen ground [Burt and Williams, 1976; McCauley et al., 2002], although partially frozen ground may still transmit liquid water flow [e.g. Boike et al., 1998; Scherler et al., 2010]. In permafrost regions, studies show that the frost table exerts a strong control on subsurface flow paths [e.g. Yamazaki et al., 2006; Wright et al., 2009, Koch et al., 2014].

Many studies have projected the effects of warming permafrost on subsurface hydrology. Degradation of permafrost may lead to changes in soil moisture, streamflow seasonality, and connectivity and partitioning between surface and subsurface waters [Walvoord and Kurylyk, 2016]. Thawing permafrost is likely to open previously frozen vertical and lateral flow paths [Walvoord and Kurylyk, 2016] and may contribute to increasing river discharges [Evans et al., 2018; Connon, 2014; Caine, 2010]. However, mountain catchments in the western United States are already exhibiting earlier snowmelt and peak stream flows [McCabe and Clark, 2005] due to a warming climate [e.g. Mote, 2006; Clow, 2010; Pribulick et al., 2016], independent of frozen ground influences. Recent studies have simulated the effects of climate change on seasonally frozen soil and implications for surface and subsurface hydrology. Simulations show a reduction in seasonally frozen ground extent [Mastin and Josberger, 2014; Cuo et al., 2015; Qin et al., 2016] and increases in groundwater recharge [Mastin and Josberger, 2014; Evans and Ge, 2017]. Changes in subsurface flow paths have been observed in seasonally frozen regions [Fuss et al., 2016],

3

and modeling suggests that degradation of seasonally frozen ground will increase groundwater discharge to streams [Evans et al., 2018].

Subsurface flow paths exert a strong control on nutrient cycling in frozen ground environments [Koch et al., 2014]. Reductions in the depth and duration of the snowpack can lead to increased soil freezing [Hardy et al., 2001], root mortality [Tierney et al., 2001], and limited heterotrophic activity in the subsurface, inducing nitrogen export [Brooks and Williams, 1999]. Watershed and hillslope studies show increased nitrate export following freezing events [Mitchell et al., 1996; Groffman et al., 1999; Fitzhugh et al., 2001; Groffman et al., 2001; Judd et al., 2007; Groffman et al., 2011], while long-term watershed records demonstrate inconsistent effects of soil freezing on nitrogen export [Kaste et al., 2008; Fitzhugh et al., 2003].

In a warming climate, all biogeochemical cycles will accelerate due to increased photosynthesis and respiration, but the net effect of such changes remains unclear [Donhauser and Frey, 2018]. For example, arctic permafrost regions may exhibit higher contributions to atmospheric carbon because soil depths expected to thaw are high in organic matter, whereas in alpine regions, permafrost soils are low in organic matter [Donhauser and Frey, 2018]. In addition, enhanced microbial activity will lead to increased mineralization of organic matter, while enhanced vegetation activity will incorporate much of this organic matter [Donhauser and Frey, 2018].

Thawing cryospheric features may lead to increased solute, heavy metal, and nutrient concentrations in headwater streams. Increasing solute and heavy metal concentrations in surface waters throughout the Swiss Alps have been linked to climate change [Thies et al., 2007; Thies et al., 2013]. In the Colorado Front Range, increased nitrogen export has been linked to melting permafrost in alpine catchments [Barnes et al., 2014]. Warmer air

temperatures have induced nitrogen export from alpine catchments in the Swiss Alps [Rogora, 2007] and the Colorado Rockies [Baron, 2009].

Ice formation in soils has traditionally received a great deal of attention due to the process of frost heave, which can damage infrastructure in regions with seasonal freezing and thawing. Frost heave is not caused by expansion of water during phase change, but by transport of liquid water toward the freezing fringe that forms "segregated" ice lenses, a process known as cryosuction [Taber, 1929]. Laboratory experiments [Harris et al., 2009] and numerical modeling [Anderson et al., 2012] demonstrate that patterns of frost damage processes differ on seasonally frozen and perennially frozen slopes. The migration of water toward the freezing front contributes to the process of frost "cracking", in which the growth of fracture networks alters hydrogeologic properties like porosity and permeability and contributes to the generation of mobile regolith. Frost cracking is strongly dependent on the availability of liquid water and the distance across which the water must travel to the freezing front [Anderson et al., 2012]. As the intensity of frost cracking depends on the daily temperature cycle [Anderson et al., 2012], the insulating effects of snow cover are expected to reduce frost cracking intensity.

Thawing permafrost may result in slope destabilization [Gruber and Haeberli, 2007] and accelerated solifluction processes [Harris et al., 2009]. Solifluction is a general term referring to slow migration of soils downslope in cold regions [Andersson, 1906], and includes the processes of frost creep and gelifluction. Frost creep occurs when a soil heaves normally to its surface during a freezing cycle, and then settles downslope due to gravity, while gelifluction occurs when oversaturated surface soils migrate downslope during a thawing cycle [Matsuoka, 2001]. These processes are dependent primarily on the frequency and depth of soil freezing, which tends to increase with increasing frost duration [Matsuoka, 2001], and constitute the primary mechanisms of downslope soil movement in the Colorado Front Range [Benedict, 1970]. The depth of frost penetration has been shown

to determine the shape of low-relief interfluves and regolith thickness in the Laramide ranges of the western United States [Anderson, 2002].

The first step in projecting the evolution of hydrologic, geomorphic, and biogeochemical environments influenced by seasonally frozen ground and permafrost is to develop a quantitative understanding of the factors controlling occurrence of frozen ground and its response to contemporary climate change. Although many such studies are underway in high latitude environments, high elevation regions present a unique set of challenges for accurately simulating soil temperatures. In mountain environments, steep topography produces strong gradients in solar insolation, vegetation, and snowpack dynamics that lead to large differences in soil temperature over short distances that are not adequately represented in a model driven by air temperature forcing alone (e.g. 15°C over a horizontal distance of 1km [Riseborough et al., 2008]). In such regions, the influence of slope, aspect, and elevation on the surface energy balance must be taken into account [Riseborough et al., 2008].

The presence of a seasonal snowpack exerts a strong control on ground temperatures due to the high albedo and low thermal conductivity of snow [Zhang, 2005]. A thin snowpack reflects incident radiation, while allowing for some heat conduction between the soil and the atmosphere; in this case, ground temperatures tend to track air temperatures. As the thickness of the snowpack increases, the snowpack's insulating effects prevent heat transfer between the air and soil [e.g. Iwata et al., 2008]. In addition, the timing of the seasonal snowpack produces variations in ground temperature: an early onset tends to insulate warm ground, while a late onset tends to insulate cooler ground; early melt exposes the ground to the air, while late melt preserves the cool state of the ground late into the spring [e.g. Zhang, 1997]. Climate change has already reduced snow cover in the northern hemisphere, and projections suggest that the extent of snow cover will continue to decrease [IPCC, 2013]. Lower elevation regions near the 0°C isotherm exhibit the greatest

reductions in snow cover, and fewer changes have been observed in higher elevation snow cover [Stewart, 2009].

The effects of a seasonal snowpack on frozen ground formation are well understood in continuous permafrost regions, where deep snowpacks tend to increase ground temperatures by insulating the ground from cold air temperatures [Zhang, 2005]. In contrast, the effects of snow cover on the formation of seasonally frozen ground are not well understood. Much of the literature extends knowledge from permafrost regions to seasonally frozen ground, suggesting that seasonal snow cover reduces the frequency of ground freezing events [Zhang, 2005]. However, recent evidence suggests that compared to a deep snowpack, a thin or absent snowpack can produce higher frequency and intensity of seasonal freezing, while reducing frost duration [Hardy et al., 2001; Bayard et al., 2005; Sarady and Sahlin, 2016; Fuss et al., 2016]. At the Hubbard Brook Experimental Forest, observations suggest that less snow cover will produce increased soil freezing [Hardy et al., 2001], while simulations predict no change in frost depth, a small increase in freezing events, and a significant reduction in the number of days with soil frost [Campbell et al., 2010]. Quantifying the effects of thin or ephemeral snow cover on ground temperatures remains an active area of investigation.

While arctic permafrost is well understood, the occurrence of frozen ground along elevation gradients in temperate regions has received less attention. In arctic regions, increases in latitude correspond directly to both decreases in temperature and solar radiation. However, in alpine regions, higher elevation sites are exposed to low air temperatures while receiving high solar radiation, complicating efforts to analyze frozen ground along elevation gradients. In lower elevation regions, soil frost may occur more frequently at lower elevations where higher temperatures limit snow accumulation [e.g. Fuss et al., 2016], whereas in higher elevation regions, soil frost may be found more frequently at higher elevations where high wind speeds limit snow accumulation [e.g. Ives and Fahey, 1971].

Soil frost occurs more frequently on the lower end of alpine talus slopes in the Swiss Alps [Lambiel and Pieracci, 2008; Scapozza, 2011]. Since the greatest reductions in snow cover tend to occur at lower elevation regions near the freezing point [Stewart, 2009], the greatest increases in frozen ground formation may occur at lower elevations.

Aspect controls on snow accumulation, soil moisture, soil temperature, and hillslope hydrology have been identified by many studies [Comola et al., 2015; Langston et al., 2015; Hinckley et al., 2014b; Gabarrón-Galeote et al., 2014; Gutiérrez-Jurado et al., 2013]. Classical optics holds that electromagnetic radiation incident upon an inclined plane is maximized perpendicularly to that plane, described by an "angle of incidence," defined as 0° when the incident ray is perpendicular to the plane. It follows that compared to a flat plane, hillslopes inclined toward the equator experience lower angles of incidence and higher shortwave solar insolation, whereas slopes inclined toward the poles experience higher angles of incidence and lower shortwave solar insolation. Such differences in solar radiation can favor the development of vegetation regimes [Walker et al., 1993] that further influence net radiative fluxes into the soil. The ability of a snowpack to persist also depends on aspect [e.g. Hinckley et al., 2014b; Jepsen et al., 2012; Litaor et al., 2008]. Such differences contribute to aspect-related differences in hillslope hydrology [Hinckley et al., 2014b; Langston et al., 2015], resulting in differences in nitrogen contributed to streams from north- and south-facing slopes [Hinckley et al., 2014a].

2. Models for Simulating Frozen Ground

In permafrost terrain, many large-scale models have been used to simulate frozen ground [Koven et al., 2013; Slater and Lawrence, 2013; Lawrence et al., 2011], and its hydrologic consequences [Andresen et al., 2020; Cuo et al., 2015]. Such models are typically run on large grids (e.g. kilometers to degrees latitude) and suffer from a lack of high-resolution snowpack and soil datasets to constrain and verify model outputs. Relatively fewer models are available for simulating seasonally frozen ground in mountainous terrain, where

complex topography creates a high degree of heterogeneity in the surface energy balance and snowpack water and energy balance. However, recent computational and numerical modeling advances provide the tools necessary for coupling land surface processes with thermo-hydrologic processes in the shallow subsurface to simulate the formation of frozen ground and its hydrologic consequences in seasonally snow-covered, high-elevation catchments.

Various modeling approaches have been developed for simulating ground temperatures. The heat diffusion equation can be used to study thermal conduction in soils [Carslaw and Jaeger, 1959], which can be coupled to surface temperatures or heat fluxes as a boundary condition to estimate ground temperatures [e.g. Cautenet et al., 1985]. Simple analytical solutions have been proposed to estimate the depth of freezing incorporating phase change of water such as the Stefan (1891) and Kurdyavtsev (1977) equations [Walvoord and Kurylyk, 2016], but do not account for differences in soil water content with depth or advective heat fluxes. Accordingly, such analytical methods are not fully appropriate for hydrologic applications, and a coupled thermo-hydrologic model is required.

The development of coupled thermo-hydrologic models throughout the 20th century was driven by the need to understand frost heave processes. One of the first models proposed to describe frost heave was the capillary model. The capillary model of ice formation [Smith, 1985] extends information from the soil characteristic curve, which relates capillary pressure to soil water content, to describe the relationship between soil temperature and unfrozen water content in freezing soils. The capillary model is limited in its ability to predict frost heave in soils with a large pore size distribution, and to explain banding patterns of ice lens formation [Peppin and Style, 2013]. In addition, the method assumes local thermodynamic equilibrium between the solid and liquid phases of water, which can be violated during rapid temperature changes and snowmelt infiltration [Walvoord and Kurylyk, 2016] and overestimate ice formation [Peppin and Style, 2013].

The first class of coupled thermo-hydrologic models (known as frozen-fringe models) [Harlan 1973] used a set of conservation equations in water and energy analogous to the Richards equation that can be solved using numerical methods [e.g. Luthin et al., 1975; Guymon et al., 1980; Jame and Norum, 1980]. These models originally used empirical approaches to relate temperature to unfrozen water content and hydraulic conductivity [e.g. Harlan, 1973; Jame and Norum, 1980] that were later replaced with physical relationships describing the partitioning between solid and liquid water [e.g. Guymon and Luthin, 1974]. Soil permeability can then be obtained from liquid water content. Such models have been improved over the years to match experimental data by simulating vapor diffusion in the unsaturated zone [Painter and Karra, 2014]. Although such approaches do not simulate banding patterns of ice formation, they are considered the standard for thermo-hydrologic applications in the unsaturated zone.

The limitations of the early coupled thermo-hydrologic models in describing the banding patterns of ice lenses led to the development of methods such as secondary frost heave, rigid ice, and pre-melting models [Davis, 2000; Peppin and Style, 2013]. In general, these models consider the flow of liquid water through thin films on the surface of soil particles. While such models improve on previous models in simulating frost heave, they are not essential for simulating seasonally frozen ground and its hydrologic consequences.

Some large-scale distributed hydrological and land surface models such as NCAR's Community Land Model [Oleson et al., 2010] include a one-dimensional representation of frozen ground and the snowpack in permafrost terrain. Andresen et al. [2020] provide an in-depth comparison of such models. The models included in their comparison (CLM 4.5, CoLM, JULES, ORCHIDEE-IPSL, LPJGUESS, SIBCASA, TEM-604, and UWVIC) contain multi-layer snowpack representations (with the exception of UWVIC, which contains a bulk snowpack model), and simulate the influence of the snowpack on soil temperatures. Soil ice content is calculated physically incorporating the effects of soil water content on phase

change and is used to adjust the infiltration capacity. Runoff from hydrologic models including frozen ground is typically compared against stream discharge data. However, the large-scale distributed models do not simulate the advection of heat with infiltration, lateral fluxes of heat and water, or vapor diffusion in the shallow subsurface. While many contain sub-grid scale parameterized representations of complex topography, in-situ data scarcity and the low resolution of model grids, remotely sensed data, and gridded reanalysis products limit the extent to which such models can accurately simulate local climate [Riseborough et al., 2008].

Whereas one-dimensional models are often sufficient for simulating basin-scale runoff processes in relatively low relief landscapes, hillslope scale problems require a multi-dimensional thermo-hydrologic model due to the lateral flow of water and heat [Walvoord and Kurylyk, 2016; Kumar, 2016]. Recently, numerous two- and three-dimensional coupled thermal hydrologic simulators have emerged, including SUTRA-ICE [McKenzie et al., 2007], GEOtop 2.0 [Endrizzi et al., 2014], PFLOTRAN-ICE [Karra et al., 2014], and Arctic Terrestrial Simulator (ATS) [Painter et al., 2016; Atchley et al., 2015], among others. Applications of these models have generally been restricted to permafrost regions, where the models predict increasing storage in the shallow subsurface and connectivity between aquifers above and below permafrost [Walvoord and Kurylyk, 2016].

Of these models, ATS and GEOtop incorporate the insulating effects of the snowpack, which is a leading source of uncertainty in estimating ground temperatures [Staub et al., 2015; Zhang, 2005]. SUTRA-ICE simulates soil ice formation only within the saturated zone, although unreleased developments include freezing in the vadose zone [Evans et al., 2018]. GEOTop simulates the influence of complex terrain on the surface energy balance and features a multi-layer snowpack model that is numerically coupled to the soil heat and water equations. However, in order to reduce computational time, GEOTop solves the soil heat and water equations in a time-lagged manner rather than in a fully coupled manner.

PFLOTRAN-ICE solves the soil heat and water equations in a fully coupled manner, incorporating the process of vapor diffusion in the unsaturated zone. However, PFLOTRAN-ICE does not feature surface energy or surface runoff and overland flow. ATS also solves the soil heat and water equations in a fully coupled manner, and features surface energy and hydrological models, and a bulk snowpack model [Atchley et al., 2015]. However, the ATS snowpack model is unable to sustain a thermal gradient between the bulk snowpack temperature and the snow surface temperature, and thus does not fully represent the influence of the diurnal temperature cycle on the snowpack energy balance. In addition, ATS simulates shallow overland flow using a coupled boundary condition [Kollet and Maxwell, 2006]. For problems involving ice formation in the unsaturated zone (e.g. seasonal soil freezing), ATS and PFLOTRAN-ICE maintain the highest degree of fidelity to underlying physical processes by incorporating vapor diffusion but require very high computational times.

As the development of ATS is recent and ongoing and features a limited snowpack model, PFLOTRAN-ICE was selected as the simulator of choice, at the time when this thesis research was initiated. PFLOTRAN-ICE [Karra et al., 2014] is based on a three-phase formulation of coupled water and heat flow developed for the MarsFlo code [Painter, 2011]. The code has successfully been used to study coupled flow of heat and water in a discontinuous permafrost environment with seasonal variability and climate change [Frampton, 2011]. An improved constitutive relationship between solid, liquid, and vapor phases was introduced to match experimental results from very unsaturated soils [Painter and Karra, 2014]. PFLOTRAN-ICE has successfully been used to simulate the polygonal tundra landscape near Barrow, Alaska, USA [Kumar et al., 2016].

3. Thesis Goals and Objectives

Frozen ground in low latitude, high elevation environments presents a unique set of conditions beyond the current capabilities developed for arctic permafrost regions.

Specifically, local topography creates a large degree of heterogeneity in soil temperatures across the landscape through strong gradients in solar radiation, snow accumulation, and vegetation patterns. Thus, there is a strong need for soil freezing models that simulate the complex interaction of the surface energy balance in complex mountainous terrain, the seasonal snowpack, and soil moisture and temperature. Moreover, the presence of shallow soil ice influences the snowpack energy balance and snowmelt infiltration capacity, while the snowpack strongly controls the ground thermal regime. Accordingly, simulating frozen ground and its consequences requires that the surface energy balance, snowpack water and energy balance, and subsurface thermo-hydrology are fully coupled. Projections of soil temperature and evolution of frozen ground regimes in mountain environments in response to warming also require such fully coupled models.

The focus of the thesis is to develop such coupled models against the backdrop of long-term datasets from the Boulder Creek Critical Zone Observatory (BcCZO) and the Niwot Ridge Long-Term Ecological Research program (LTER). The Boulder Creek Watershed is a complex landscape whose rugged terrain creates an extensive mosaic of microclimates. The Colorado Front Range mountains were formed during the Tertiary Laramide Orogeny when hard, crystalline rocks were forced up against soft, marine sediments of the Plains [Anderson et al., 2012]. Pleistocene glaciation carved wide U-shaped valleys in the headwaters, and streams cut narrow V-shaped canyons into the Rocky Mountain Surface [Anderson et al., 2012]. As the Continental Divide consists of a generally north-south oriented massif [Benedict, 1992], such valleys and streams trend mostly east-west, creating north- and south-facing aspects with dramatic differences in vegetation and solar insolation. In addition to aspect, the watershed features strong gradients in elevation, temperature, and snow accumulation that provide a rich setting for developing, verifying, and validating a soil temperature model for mountain environments.

In this thesis, a comprehensive framework for modeling soil temperatures, seasonally frozen ground, and permafrost in heterogeneous montane, sub-alpine, and alpine landscapes is presented (Chapter II and Appendix A). First, surface energy balance and snowpack models are developed and verified against radiation and snow depth datasets. The original snowpack model is modified to better represent the influence of snow depth on ground temperature and heat fluxes. Next, model outputs are used to force a soil surface temperature model, which is fully coupled to subsurface thermo-hydrologic flow code PFLOTRAN-ICE. An infiltration capacity formulation is devised that allows snow models to generate surface flow when the buildup of moisture and ice in the shallow subsurface prevents additional snowmelt infiltration. The coupled model is applied to two field sites within the Boulder Creek watershed, Gordon Gulch (Chapter III) in the montane climate zone and Niwot Ridge (Chapter IV) in the sub-alpine and alpine climate zones, and implications for hydrology are explored.

At Gordon Gulch, meteorological, radiation, soil temperature, and snow depth data from 2013-2016 are used to verify and validate surface energy, snowpack energy balance, and soil temperature models for complex terrain, and to determine the influence of hillslope aspect on the occurrence of frozen ground. The site features steep north- and south-facing slopes that provide an ideal setting for developing such models. This study was inspired by previous work at the site demonstrating differences in subsurface flow between the north- and south-facing slopes [Langston et al., 2015; Hinckley et al., 2014b]; soil temperatures suggested that frozen ground may play a role in these differences. In developing the soil temperature model, the influence of solar radiation and snowpack thickness on winter ground temperatures is analyzed.

At Niwot Ridge, the coupled model developed at Gordon Gulch is applied to subalpine and alpine sites to determine the influence of frozen ground on subsurface flow beneath bare and snow-covered ground patches along the elevation gradient, as well as to project decadal

14

changes in the ground thermal regime. Soil temperatures from 2000-2014 are used to validate the model and to determine how the cold content of snow at various elevations influences ground temperatures. Soil temperatures from water year 2008 are combined with thermo-hydrologic analysis to determine how frozen soil beneath bare and snow-covered ground patches influences subsurface flow, and how these processes change with elevation. Long-term climate datasets for 1952-1970 and 2000-2013 and projections for the end of the 21st century are compiled to analyze how changes in Front Range air temperature, snowfall, and snowpack cold content may influence seasonally frozen ground and permafrost occurrence. Implications of changes in frozen ground dynamics for geomorphology and biogeochemistry are discussed.

CHAPTER II

MODEL DEVELOPMENT

1. Introduction to Modeling Framework

The purpose of this chapter is to develop a model for accurately simulating frozen ground and its hydrologic consequences in mountain environments by combining the surface energy balance (section 2), the snowpack water and energy balance (section 3), and coupled thermo-hydrologic flow in the subsurface (section 4). Subsurface model layering and thermal and hydrologic parameter estimation is described in section 5. Thermal and hydrologic boundary conditions for the subsurface model are described generally in section 6. The surface and subsurface models are thermally and hydrologically coupled using a soil surface model (section 7). Figure 1 describes the conceptual framework of the model. The model takes hourly forcings of meteorological data including air temperature (T_{air}), relative humidity (RH), and windspeed (WS), precipitation as rainfall (P_r) and snowfall (P_r), and site-specific inputs of slope angle, aspect, and elevation (not shown in Figure 1). The surface energy balance is calculated using these inputs on an hourly timestep.Net shortwave (Q_{sn}) and longwave (Q_{ln}) radiation terms, and sensible (Q_h), latent (Q_e), and evapotranspirative (Q_e) energy heat fluxes are calculated internally as a function of geographical and meteorological information. The snow model computes evaporation (E) and outputs snow depth (not shown in Figure 1), bulk snowpack temperature (T_{snow}), and snowmelt water flux (M_r). The subsurface model outputs soil temperatures (T_{soil}), subsurface water and ice saturation, and subsurface liquid water flux (v_l) at 10-20cm resolution. Energy and water state variables are U and W for the snow model, and temperature T and liquid pressure (p_l) for the subsurface model. During periods without snowcover, the snow model is not relevant, and the surface energy and hydrologic forcings are applied directly to the ground surface.
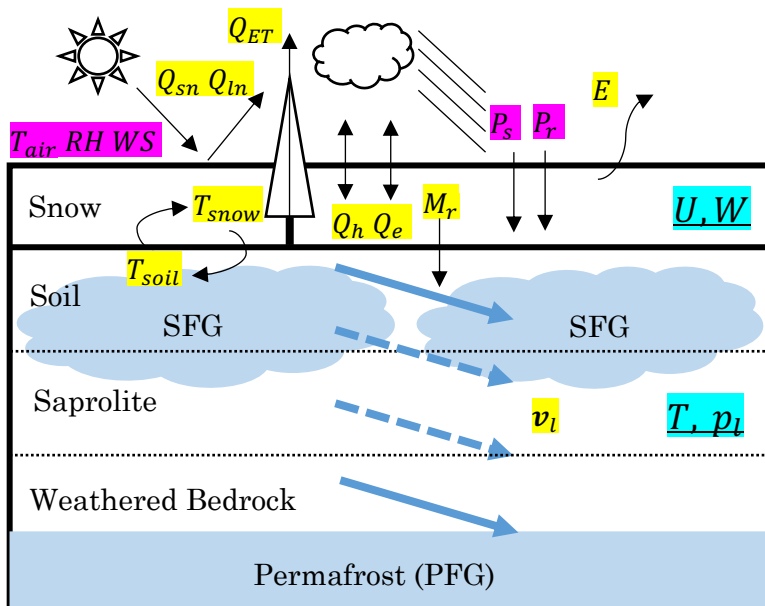
Figure 1. Conceptual framework of coupled model. Internally calculated quantities are highlighted in yellow, model inputs are highlighted in magenta, and state variables are highlighted in cyan. Variables depicted in this figure are introduced briefly in section 1 and described in greater detail throughout this chapter. The model is capable of simulating seasonally frozen ground (SFG) and permafrost (perennially frozen ground, PFG).

2. Surface Energy Balance Model

A surface energy balance model is used to estimate the energy available for snowpack accumulation and ablation and provide a heat flux boundary condition for the soil surface when a snowcover is not present. The model calculates net shortwave and longwave radiation, including the influence of hillslope aspect, slope, and canopy shading. Atmospheric transmissivities are parameterized based on the optical air mass, and canopy and cloud cover are estimated based on radiation data. Horizon shading is not evident in radiation datasets and was therefore not included in the surface energy model.

2.1 Model Description:

Incoming solar radiation on a sloping surface was estimated following Dingman (2015). The incident radiation flux on an inclined plane in the absence of atmospheric scattering k_{et} ("extraterrestrial") is calculated as:

$$k_{et} = I_{sc} E_0 \left[cos\left(\Lambda_{eq}\right) cos(\delta) cos\left(\omega t + \Omega_{eq}\right) + sin\left(\Lambda_{eq}\right) sin(\delta) \right] \tag{1}$$

The terms within brackets in (1) are the cosine of the solar zenith angle θ. I_{sc} is the solar constant, E_0 is the orbital eccentricity, Λ_{eq} is equivalent latitude, δ is the solar declination (latitude at which the sun is directly overhead), ω is the angular velocity of Earth's rotation, t is hours before (-) or after (+) noon, and Ω_{eq} is equivalent longitude. Equivalent latitude Λ_{eq} and equivalent longitude Ω_{eq} are calculated according to Lee [1962]:

$$\Omega_{eq} = \Omega + tan^{-1} \left[\frac{sin(\beta) sin(\alpha)}{cos(\beta) cos(\Lambda) - sin(\beta) sin(\Lambda) cos(\alpha)} \right] \tag{2}$$

$$\Lambda_{eq} = sin^{-1} \left[sin(\beta) cos(\alpha) cos(\Lambda) + cos(\beta) sin(\Lambda) \right] \tag{3}$$

α is the slope aspect, β is the angle of inclination, Λ is latitude, and Ω is longitude. Orbital eccentricity E_0 and solar declination δ are functions of Earth's position in its orbit, given by the day angle Γ, where J is the day of the Julian year:

$$\Gamma = \frac{2\pi(J - 1)}{365} \tag{4}$$

Orbital eccentricity E_0 and solar declination δ can then be expressed as:

$$E_0 = 1.000110 + 0.034221\,cos(\Gamma) + 0.001280\,sin(\Gamma) + 0.000719\,cos(2\Gamma) \tag{5}$$

$$+ 0.000077 sin\,(2\Gamma)$$

$$\delta = 0.006918 - 0.399912\,cos(\Gamma) + 0.070257\,sin(\Gamma) - 0.006758\,cos(2\Gamma) \tag{6}$$

$$+ 0.000907\,sin(2\Gamma) - 0.002697\,cos(3\Gamma) + 0.00148 sin\,(3\Gamma)$$

Figure 2 depicts angles α, β, δ, and θ. Incident radiation is attenuated by absorption and reflection of the atmosphere:

$$k_{dir} = k_{et}\tau_{wa}\tau_{da}\tau_{ws}\tau_{rs}\tau_{ds}\tau \tag{7}$$

τ are transmissivities are parameterized according to Suckling and Hay [1976] based on the precipitable water content W and optical air mass M:

- Absorption by water vapor:

$$\tau_{wa} = 1 - 0.077(MW)^{0.3} \tag{8}$$

- Absorption by dust and solid aerosols:

$$\tau_{da} = 0.965^M \tag{9}$$

- Scattering by water vapor:

$$\tau_{ws} = 1 - 0.0225MW \tag{10}$$

- Scattering by air molecules:

$$\tau_{rs} = 0.972 - 0.08262M + 0.00933M^2 + 0.00095M^3 + 0.0000437M^4 \tag{11}$$

- Scattering by dust and solid aerosols:

$$\tau_{wa} = 0.965^M \tag{12}$$

Precipitable water content W (cm) is estimated from air temperature T_A (K) and relative humidity RH (%):

$$W = 0.00493(\frac{RH}{T_A})e^{(26.23 - \frac{5416}{T_A})} \tag{13}$$

Optical air mass is estimated from Yin [1997]:

$$M = e^{\frac{-z}{z_{scale}}} \frac{1.021}{0.008307 + sin(\Lambda)\,sin(\delta) + cos(\Lambda)\,cos(\delta)\,cos(\omega t)} - 0.01259 \tag{14}$$

where z is the elevation (m) and z_{scale} is the scale height of the atmosphere (8000m). As z increases compared to z_{scale}, the optical air mass M decreases. Taking the Boulder Creek watershed as an example, the exponential term $e^{\frac{-z}{z_{scale}}}$ is 0.83 at the elevation of the Eastern Plains (1480m) and 0.60 at the elevation of the Continental Divide (4120m). As optical air mass M decreases, incoming "extraterrestrial" shortwave radiation k_{et} is attenuated less by water vapor, air molecules, dust, and solid aerosols, resulting in higher incoming shortwave radiation at the ground surface k_{dir}.

Approximately one half of the radiation scattered by the atmosphere is incident upon Earth's surface as diffuse radiation:

$$k_{dif} = 0.5k_{et}\tau_{wa}\tau_{da}(1 - \tau_{ws}\tau_{rs}\tau_{ds}) \tag{15}$$

Earth materials reflect radiation to varying degrees. Albedo a describes the fraction of incident radiation that is reflected. Snow reflects most incoming radiation (0.5-0.8) whereas bare soil reflects a small fraction of radiation (0.1-0.3). Of the reflected radiation, approximately one half is scattered back to the surface by the atmosphere:

$$k_{bs} = a(k_{dir} + k_{dif})[0.5\tau_{wa}\tau_{da}(1 - \tau_{ws}\tau_{rs}\tau_{ds})] \tag{16}$$

Combining direct, diffuse, and backscattered fluxes gives total shortwave clear-sky radiation:

$$k_{cs} = k_{dir} + k_{dif} + k_{bs} \tag{17}$$

Incoming shortwave radiation k_{cs} is adjusted for reflectance a of the land surface, cloud cover τ_C, and canopy interception τ_F, giving net shortwave radiation Q_{sn}:

$$Q_{sn} = k_{cs}(1 - a)\tau_C\tau_F \tag{18}$$

τ_C is estimated from Croley [1989] and τ_F is estimated for lodgepole pine from Dunne and Leopold [1978]. Longwave energy exchange is modeled by treating Earth and its atmosphere as blackbodies and applying the Stefan-Boltzmann law.

Incoming and outgoing longwave radiation are given by:

$$L_{in} = \varepsilon_{atmosphere}\sigma T_{at}^4 \tag{19}$$

$$L_{out} = \varepsilon_{surface}\sigma T_{surface}^4 + (1 - \varepsilon_{surface})\varepsilon_{atmosphere}\sigma T_{at}^4 \tag{20}$$

σ is the Stefan-Boltzmann constant, T is absolute temperature, $\varepsilon_{atmosphere}$ is atmospheric emissivity, and $\varepsilon_{surface}$ is emissivity of the snow or soil surface. Combining the longwave terms gives net longwave radiation Q_{ln}:

$$Q_{ln} = L_{in} - L_{out} \tag{21}$$

Sensible heat transfer Q_h is calculated according to a temperature gradient between the air T_a and soil or snow surface $T_{surface}$:

$$Q_h = K_h \rho_a c_p (T_a - T_{surface}) \tag{22}$$

c_p is air specific heat capacity, ρ_a is air density, K_h is heat conductance. Similarly, latent heat flux is calculated according to a vapor pressure gradient:

$$Q_e = K_e \frac{h_v 0.622}{R_d T_a}[e_a - e_s(T_{surface})] \tag{23}$$

h_v is the latent heat of sublimation, R_d is the dry gas constant, e_s is the vapor pressure calculated by assuming saturation at the soil or snow surface, and K_e is vapor conductance. Energy associated with evapotranspiration Q_{ET} is modeled according to Priestley and Taylor [1972]:

$$Q_{ET} = \alpha \frac{s}{s + \gamma}(R_n - G) \tag{24}$$

γ is the psychrometric constant, R_n is net radiation, G is the ground heat flux, s is the slope of the saturation vapor pressure curve, and α is the Priestley-Taylor coefficient.

The subscript ET is used to distinguish Q_{ET} from "extraterrestrial" radiation k_{et} (1).

G is the ground heat flux:

$$G = \kappa \nabla T_{surface}$$

(25)

The ground heat flux is the amount of energy flowing into or out of the soil and influences the energy available for evapotranspiration (24), as well as the snowpack energy balance (see section 3.1). G is defined as positive into the soil and is estimated from the subsurface model (section 7.1.1).
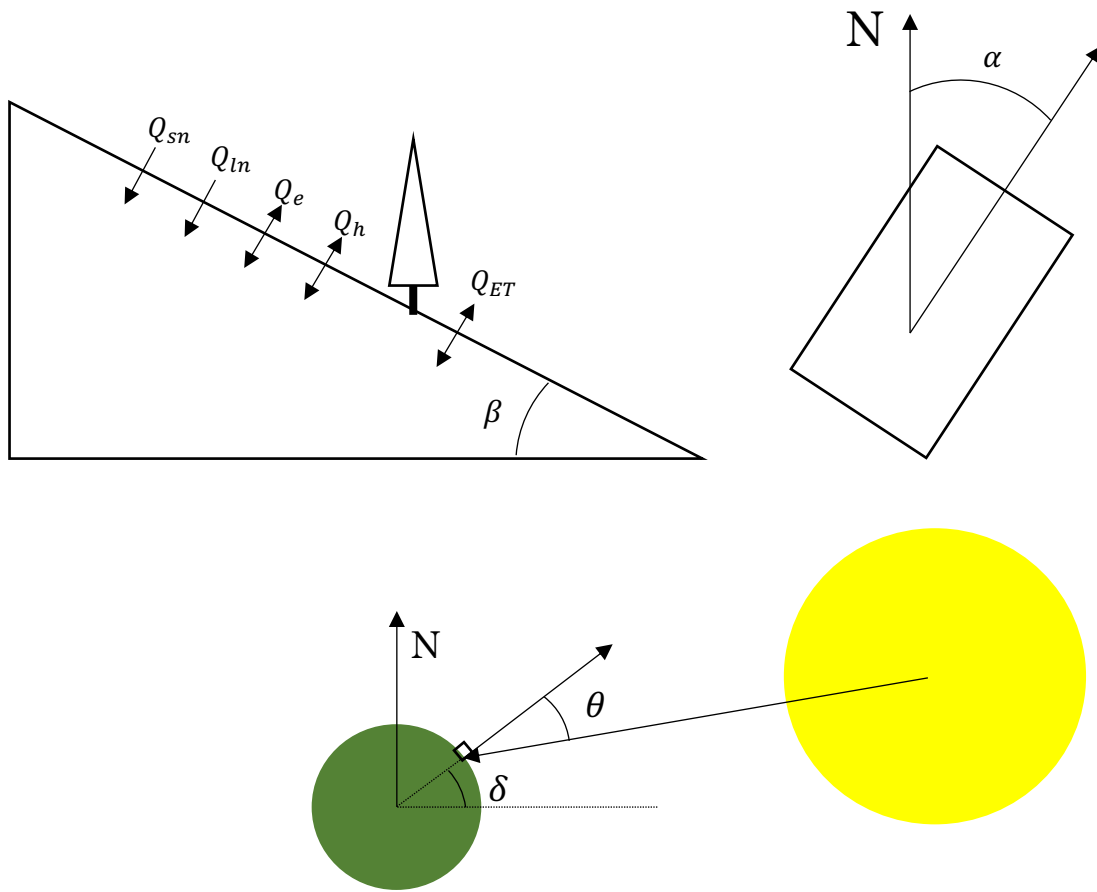
Figure 2. Schematic of surface energy balance fluxes and slope angle β (top left), aspect angle α (top right), zenith angle θ and solar declination angle δ (bottom). Q_{sn} and Q_{ln} are net shortwave and longwave radiation, Q_h and Q_e are sensible and latent heat, and Q_{ET} is evapotranspirative heat transfer. Slope angle (top left) is depicted from the side; aspect angle (top right) is depicted from above. Radius of the Earth (green) and solar declination angle are exaggerated; the sun (yellow) currently does not exceed a declination angle of 23.5°N (Tropic of Capricorn).

2.2 Model Verification

2.2.1 Comparison to NREL Data

Shortwave radiation calculations are compared against data from the National Renewable Energy Laboratory's (NREL) Solar Radiation Research Lab (Figure 3). Global shortwave radiation refers to the sum of direct (k_{dir}), diffuse (k_{dif}), and backscattered (k_{bs}) radiation terms. Diffuse shortwave radiation is simply k_{dif}. Two days during 2016 were selected for minimum cloud cover by visual inspection: winter – January 1, 2016 and summer –June 15, 2016 (Figure 3). Latitude, longitude, and elevation of the NREL Solar Radiation Lab are 39.7424°N, 105.1785°W, and 1828.8m, respectively. The model reproduces global radiation very accurately, and diffuse radiation relatively well. Differences between the model and the data are related to calculation of the optical air mass M, which must be estimated numerically. As global radiation constitutes a much greater share of incoming shortwave radiation (500-1000 W m^{-2}) than diffuse radiation (60-80 W m^{-2}), errors in the estimation of diffuse radiation do not significantly affect estimations of shortwave radiation. Discrepancies in diffuse radiation estimates during summer (Figure 3, top right) are related to differences in local meteorological conditions (e.g. relative humidity) between the Gordon Gulch and NREL sites.

(b) Summer: June 15, 2016
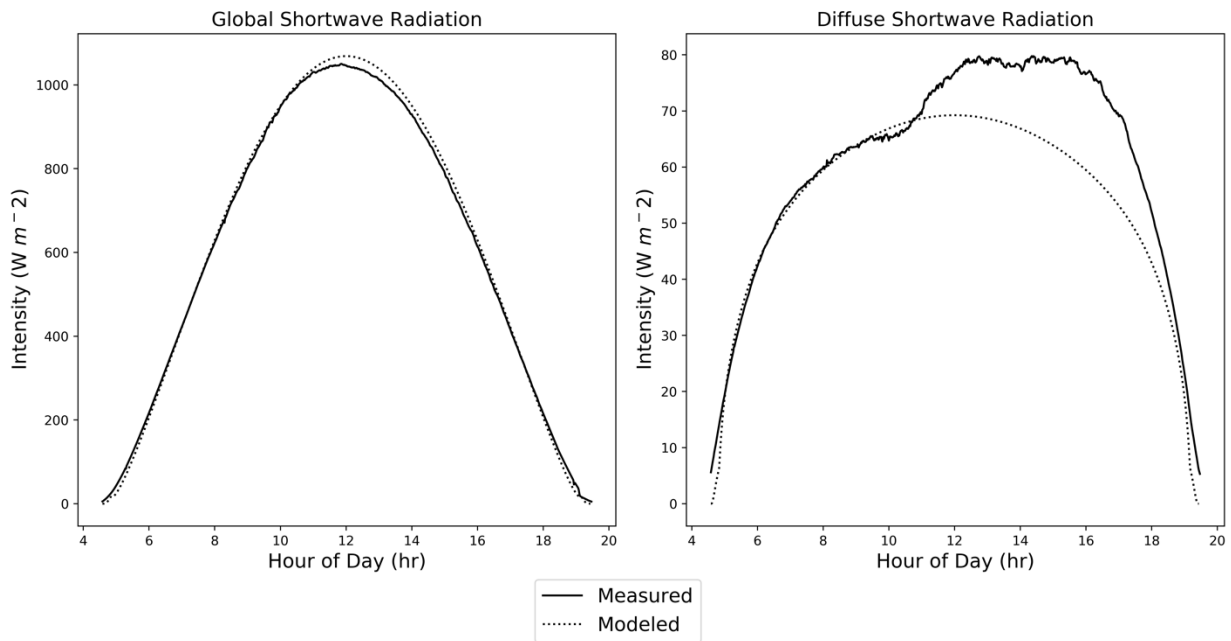
(a) Winter: January 1, 2016
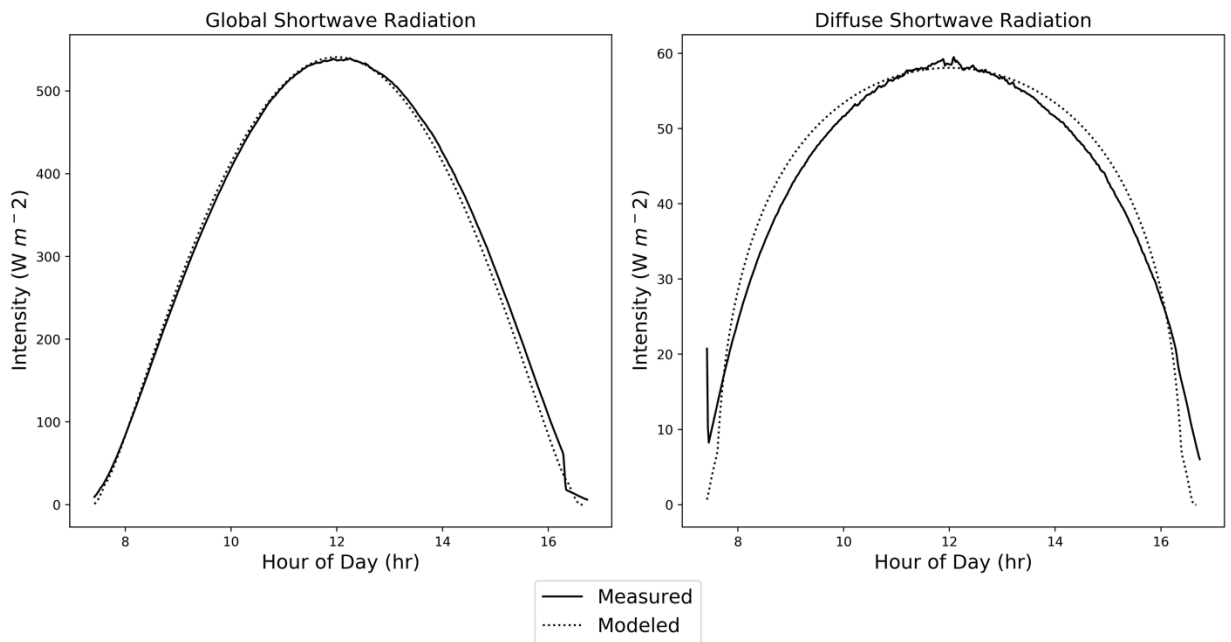
Figure 3. Global shortwave radiation (left) and diffuse shortwave radiation (right) on winter (a) and summer (b) days with minimal cloud cover. Differences between the model and the data are related to calculation of the optical air mass M, which must be estimated numerically.

2.2.2   Comparison to Data from Gordon Gulch, CO

The surface energy balance model is compared to radiation data from Gordon Gulch, CO, a seasonally snow-covered montane sub-catchment of the Boulder Creek watershed in the Colorado Rockies monitored by the Boulder Creek Critical Zone Observatory (BcCZO). The field site is described in more detail in Chapter III and summarized briefly here for the purposes of solar radiation model verification. The site is located at a latitude of 40.01°N and mean elevation of 2650m. A map of the site including tree cover is presented in Figure 4. The south-facing slope is sparsely vegetated with ponderosa pine (*Pinus ponderosa*) and low-lying grasses, forbs, and shrubs; the north-facing slope is densely forested with lodgepole pines (*Pinus contorta*) and some Douglas fir (*Pseudotsuga menziesii*). The meteorological station on the south-facing slope is unobscured by forest canopy aside from a single ponderosa pine downslope from the station, whereas the meteorological station on the north-facing slope is located in a small clearing surrounded by dense coniferous forest. Average slopes (β) were estimated as 21° and 15° for the south- and north-facing slopes, and average aspects (α) were estimated as 177° and 10° for the south- and north-facing slopes, respectively (aspect is measured clockwise from 0°N). A full list of site-specific parameters necessary to drive the solar radiation model is presented in Table 1.

In this section, incoming shortwave radiation data from the meteorological stations on the north- and south-facing slopes are compared to modeled incoming shortwave radiation. As the radiation instrumentation is a flat surface (not inclined parallel to the hillslope), flat-surface calculations are compared to the incoming shortwave radiation data. Although net all-wave radiation measurements were collected from both slopes, a comparison between data and calculations of net longwave radiation involve modeling outgoing longwave radiation (including the soil and snowpack) and thus do not serve as an appropriate modeling target for the solar radiation model. The application of the full surface energy balance model to the soil temperature and thermo-hydrologic modeling in Chapters III and

IV indirectly provides validation of the representation of longwave radiation and other energy flux terms.
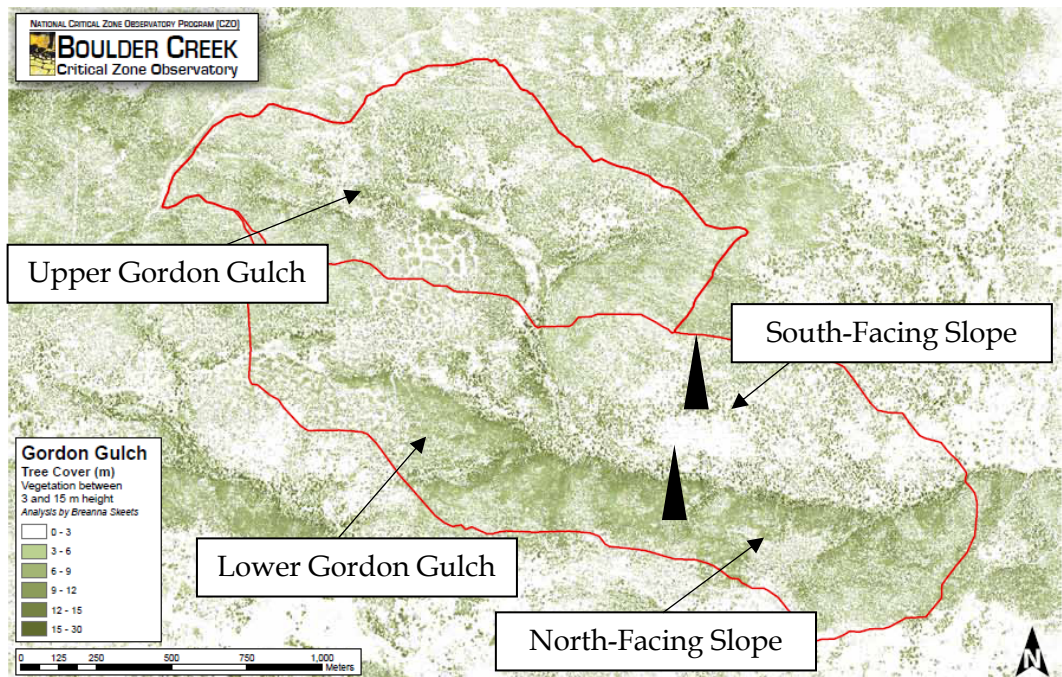
Figure 4. Tree cover at Gordon Gulch (courtesy of Brianne Sheets, Eric Parrish – BCCZO). Meteorological stations ( ) are located on the north- and south-facing slopes of Lower Gordon Gulch (locations approximate).

	South-Facing Slope	North-Facing Slope
Aspect (α)	177°	10°
Slope (β)	21°	15°
Elevation	2565m	2629m
Canopy Shading Fraction	0.0	0.02-0.50
Latitude	40.01°N	
Longitude	105.5°W	

Table 1. Site-specific parameters used in incoming shortwave radiation estimates.

The south-facing slope serves as an ideal location to verify shortwave radiation calculations due to minimal canopy shading. The model is first applied to calculate the incoming shortwave radiation on a flat surface at the location of the south-facing slope, excluding cloud cover (Figure 5a). This serves to analyze the overall seasonal match between the model and shortwave radiation data, because the shortwave radiation measurements are made on an instrument with a flat orientation, rather than one inclined parallel to the slope. Next, the effects of slope and aspect are included in the calculation of incoming shortwave radiation, while cloud cover remains excluded (Figure 5b). As expected, the calculation including the effects of slope and aspect produces higher estimates of incoming shortwave radiation compared to the measurements and calculation without slope and aspect influence. A similar verification cannot be performed on the north-facing slope due to a strong canopy shading effect (see below), as well as frequent snow cover on the instrumentation.

On the north-facing slope, a strong canopy shading effect can be seen from calculations excluding slope and aspect. The canopy shading effect is much stronger during October-February than during March-September. During the winter when solar zenith angles are very low, incoming shortwave radiation travels laterally through the forest canopy and insolation is attenuated by many trees. In contrast, during the summer when solar zenith angles are high, incoming shortwave radiation travels vertically through the forest canopy and insolation is only attenuated by a small number of trees. Two canopy interception schemes (for the time periods October-January and February-September) are used to account for the seasonal dependence of canopy interception and are presented in Figure 6. Next, the effects of slope, aspect, and canopy shading are combined in the calculation of incoming shortwave radiation, while cloud cover remains excluded (Figure 7b) (for comparison, flat-surface calculations including canopy cover from Figure 6b are reproduced in Figure 7a). As expected, measurements of incoming shortwave radiation exceed

calculations including the effects of slope and aspect, because the radiation instrumentation is not inclined parallel to the slope.

Cloud cover fraction is modeled as a random number between 0.0 and an upper bound (0.74), which is selected to minimize percent error between measured and modeled incoming shortwave radiation on the south-facing slope. The same cloud cover scheme is applied to the north-facing slope. Modeled flat-surface incoming shortwave radiation fluxes including cloud cover are presented in Figure 8. Percent error in estimations of flat-surface incoming shortwave radiation fluxes on the south-facing slope are presented in Table 2.

Overall, the flat-surface estimates (Figures 5a and 6b) achieve a very good match to seasonal trends in incoming shortwave radiation on the south- and north-facing slopes. As the geometric adjustments for hillslope inclination are exact (given slope and aspect), the model provides a unique insight into the large differences in energy available across the two hillslopes. These shortwave radiation calculations suggest that compared to a flat slope at the latitude and elevation of Gordon Gulch, incoming shortwave radiation on the south-facing slope is augmented annually by 22% due to the slope's equatorward inclination, whereas incoming shortwave radiation on the north-facing slope is attenuated annually by 23% due to the slope's poleward inclination and 22% by canopy shading. Thus, the south-facing slope receives over twice as much incoming shortwave radiation as the north-facing slope on an annual basis.
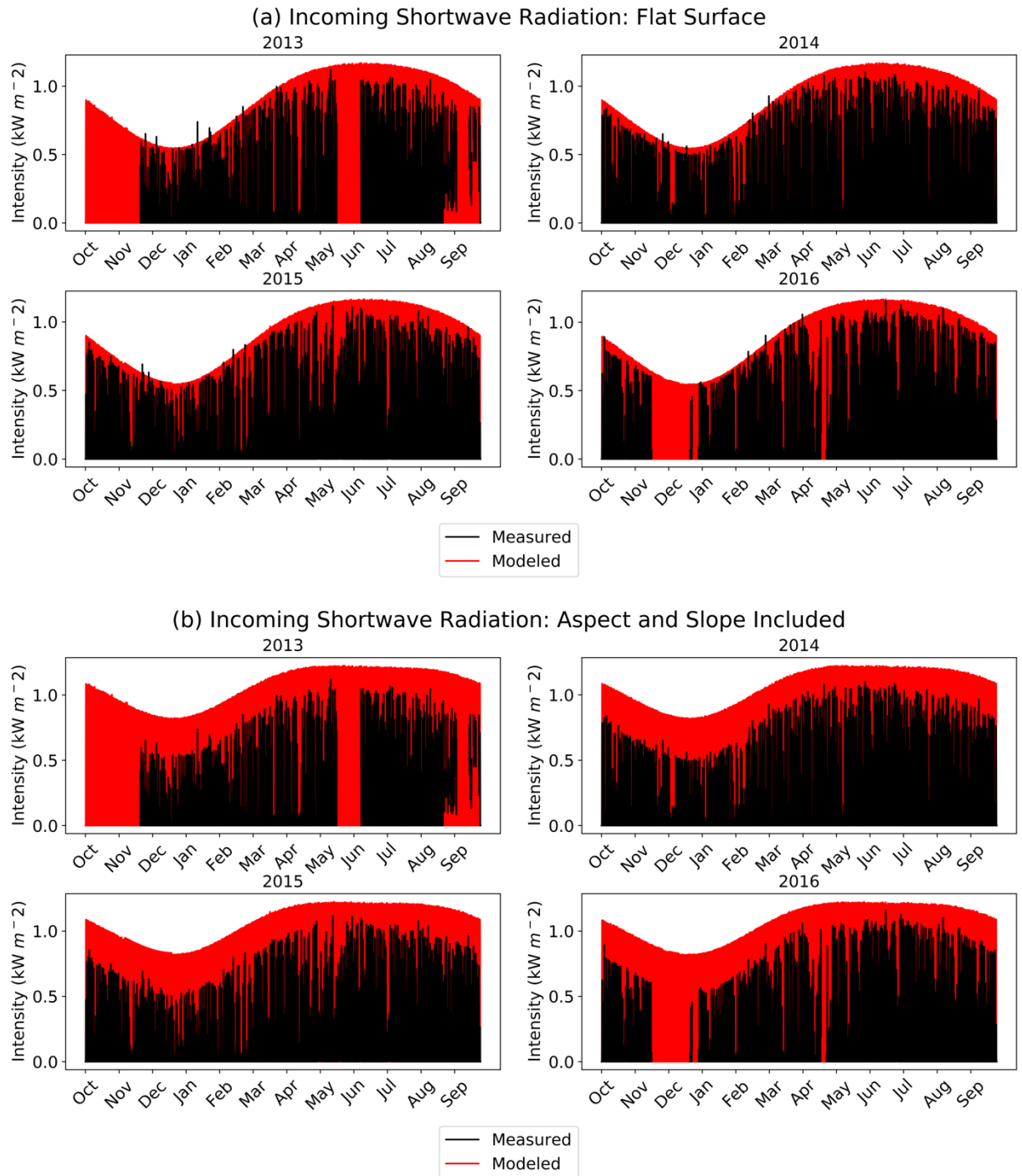
Figure 5. Incoming shortwave radiation (kW m^{-2}) on the south-facing slope (a) excluding and (b) including the effects of slope and aspect. Radiation measurements are made on an instrument with a flat orientation, rather than parallel to the slope. Hence, the calculations excluding the influence of slope and aspect are expected to match the measured values closely, while the calculations with slope and aspect influence included should exceed the measured incoming shortwave radiation.
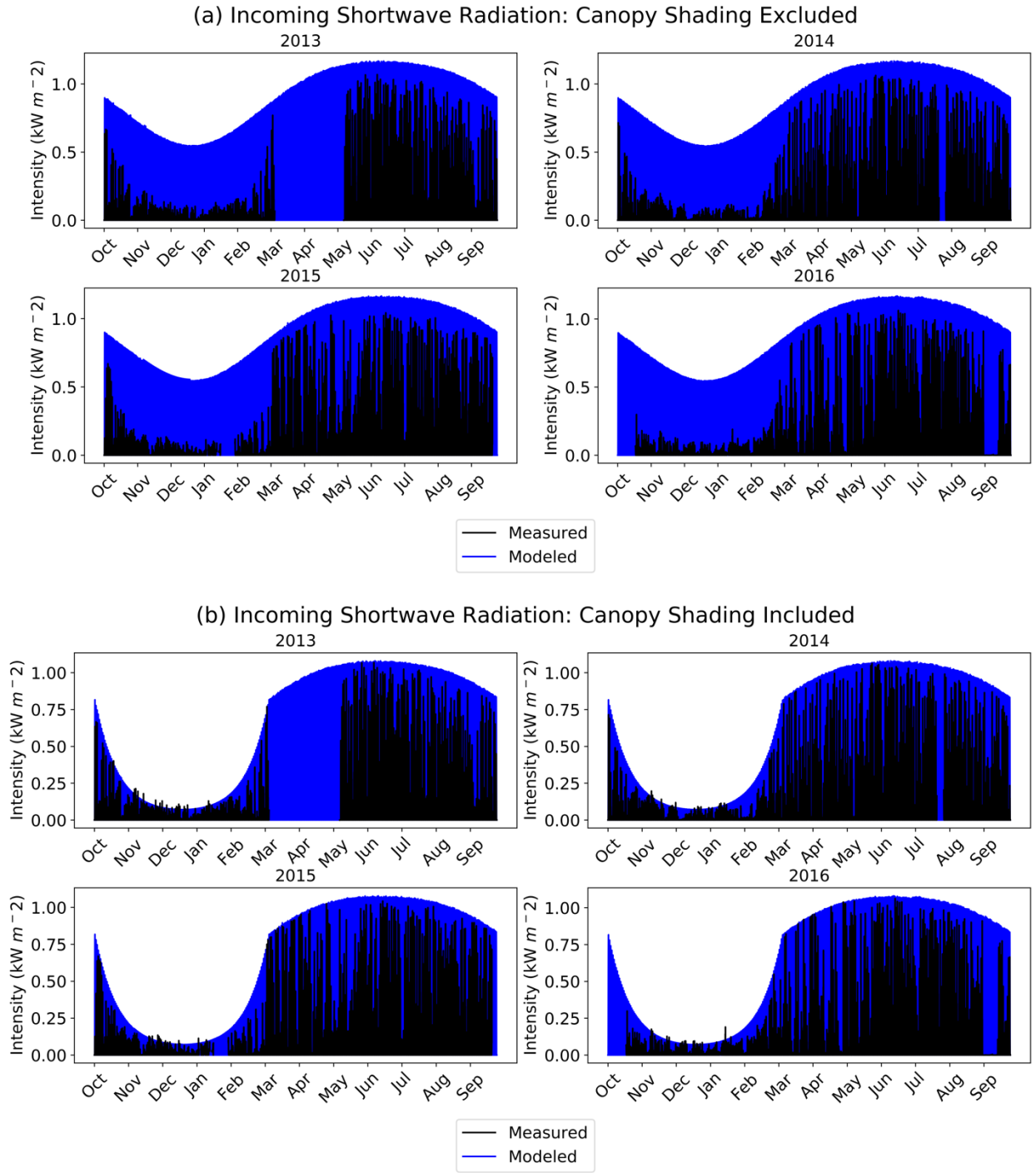
Figure 6. Incoming shortwave radiation (kW m⁻²) on the north-facing slope (a) without accounting for canopy shading and (b) including a seasonally dependent canopy shading scheme. Both sets of radiation calculations are for a flat surface.
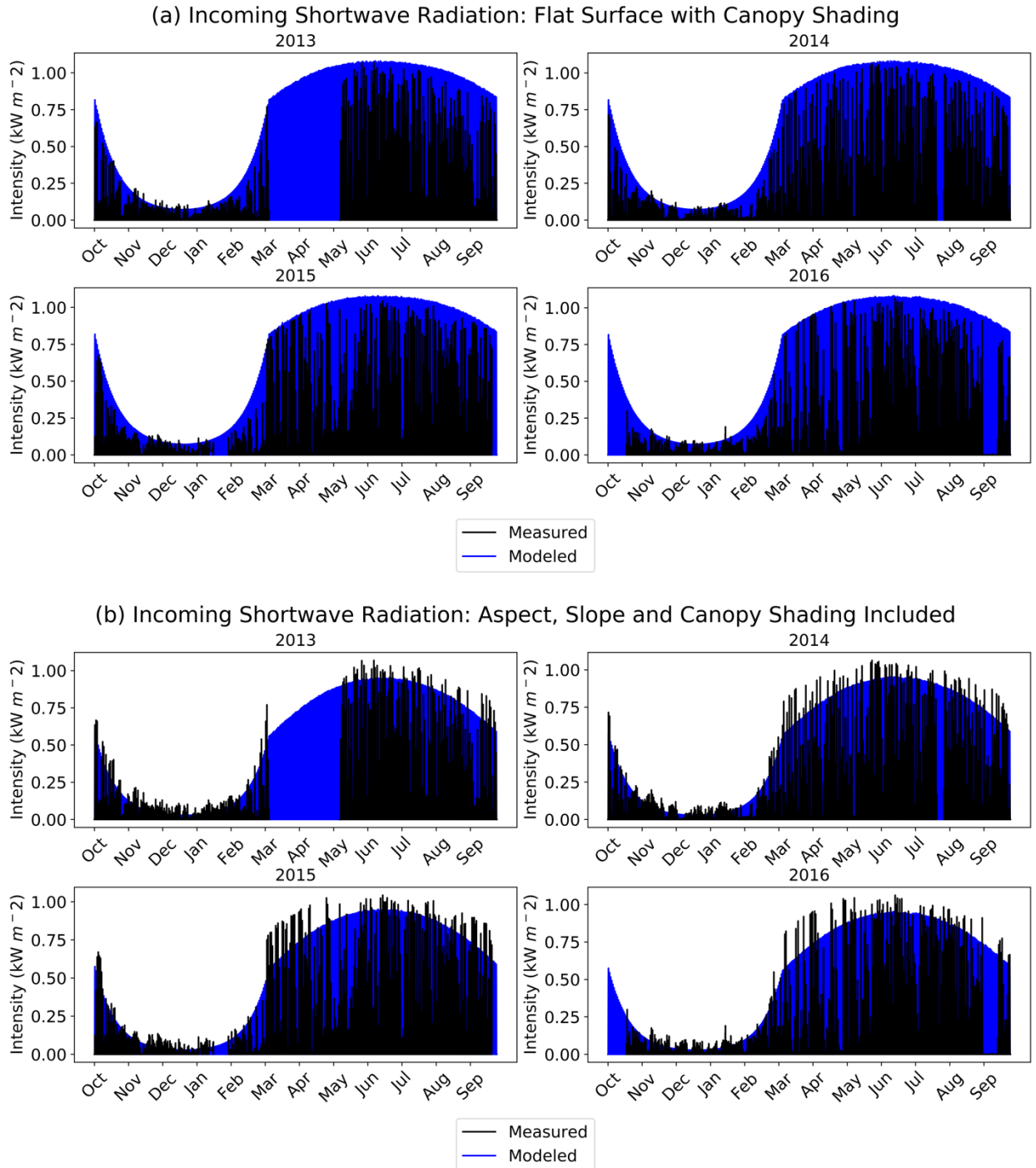
Figure 7. Incoming shortwave radiation (kW m^{-2}) on the north-facing slope (a) flat-surface accounting for canopy shading and (b) including slope, aspect, and canopy shading. Figure 7a is identical to Figure 6b and is included here for comparison. Radiation measurements are made on an instrument with a flat orientation, rather than parallel to the slope. Hence, measured values are expected to match the calculations excluding slope and aspect closely, while the measured incoming shortwave radiation should exceed calculations with slope and aspect influence included.
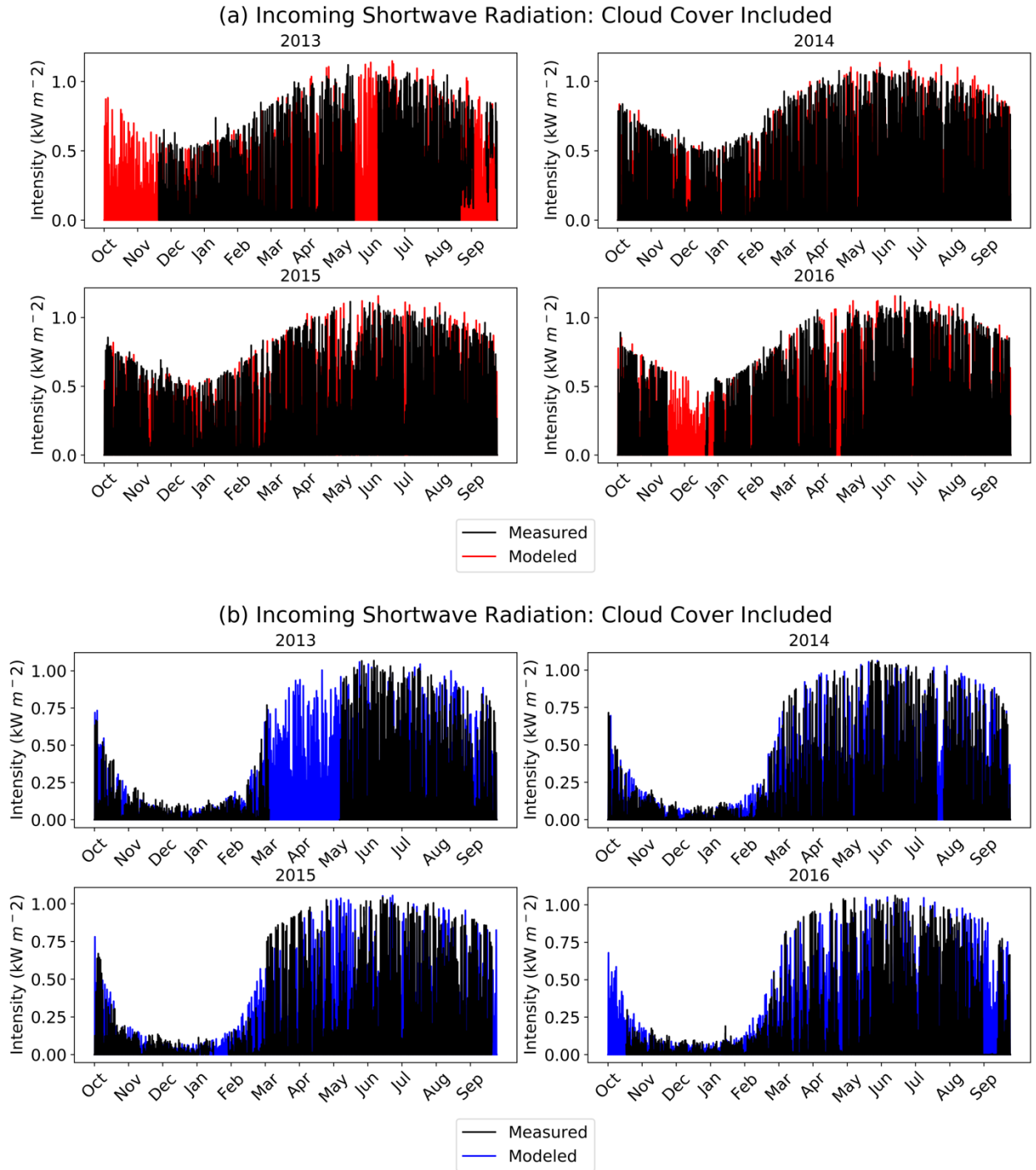
Figure 8. Incoming shortwave radiation (kW m^{-2}) on the (a) south-facing slope and (b) north-facing slope accounting for cloud cover on both slopes and canopy shading on the north-facing slope. Both sets of radiation calculations are for a flat surface.

Period	WY2013	WY2014	WY2015	WY2016	Overall
Flat-Surface Incoming Shortwave Radiation Percent Error (%)	1.8%	-0.64%	-0.88%	-1.9%	-0.08%

Table 2. Percent error between modeled and measured flat-surface incoming shortwave radiation fluxes on the south-facing slope.

3. Snowpack Model

3.1 Model Description

The snowpack is modeled closely following the Utah Energy Balance model [Tarboton & Luce, 1996], with a modification (section 3.2) that allows the snowpack model to better reflect the influence of snow depth on snowpack cold content and consequent winter ground temperature estimates. Water equivalence W [m m^{-2}] and energy content U [J m^{-2}] are determined in each time step by solving the following set of two coupled, non-linear ordinary differential equations:

$$\frac{dU}{dt} = Q_{sn} + Q_{ln} - Q_g + Q_h + Q_e + Q_p - Q_m \tag{26}$$

$$\frac{dW}{dt} = P_r + P_s - M_r - E \tag{27}$$

Q_{sn} is net shortwave radiation (18), Q_{ln} is net longwave radiation (21), Q_g is the ground heat flux (25) (defined as positive into the soil), Q_h is sensible heat flux (22), and Q_e is latent heat flux (23). Q_p is heat advected with precipitation:

$$Q_p = P_s c_s \rho_w \, min(T_A, 0) + P_r [h_f \rho_w + c_w \rho_w \, max(T_A, 0)] \tag{28}$$

P_s is snowfall rate, c_s is snow specific heat capacity, ρ_w is the density of water, T_A is air temperature, P_r is rainfall rate, and c_w is the specific heat capacity of water.

Q_m is heat advected out of the snowpack with meltwater:

$$Q_m = \rho_w h_f M_r \tag{29}$$

M_r is melt rate:

$$M_r = K_{sat} S^{*3} \tag{30}$$

K_{sat} is saturated hydraulic conductivity of snow and S* is the volumetric saturation S*:

$$S^* = \frac{\frac{L_f}{1 - L_f} - L_c}{\frac{\rho_w}{\rho_s} - \frac{\rho_w}{\rho_i} - L_c} \tag{31}$$

L_c is the fractional volume of water retained by capillary forces, ρ_i is the density of ice, and L_f is the liquid mass fraction of the snowpack:

$$L_f = \frac{U}{\rho_w h_f W} \tag{32}$$

The depth of water transferred with latent heat is given by:

$$E = -\frac{Q_e}{\rho_w h_v} \tag{33}$$

Net available energy at the surface is balanced by conduction into or out of the snow, parameterized as a heat exchange between the bulk snowpack (at temperature T_{snow}) and the snow surface (at temperature T_{ss}):

$$Q_{sn} + Q_{li} + Q_p - Q_{le}(T_{ss}) + Q_h(T_{ss}) + Q_e(T_{ss}) = K_s \rho_s c_s(T_{ss} - T_{snow}) \tag{34}$$

ρ_s is snow density (kg m³), c_s is the specific heat of snow, and K_s is a snow surface heat conductance (m hr⁻¹) related to the thermal diffusivity of the snow α_s and the depth over which the gradient acts Z_e:

$$K_s = \frac{\alpha_s}{Z_e} \tag{35}$$

The non-linear equation (34) is solved in each time step for T_{ss}. If the solution is greater than 0°C, the surface energy cannot be completely conducted into the snow: the surface temperature is then set to 0°C, and the remaining energy is available for melting the snowpack. Finally, the average temperature of the snowpack T_{snow} is determined from the energy content U of the snowpack relative to 0 °C:

$$if\ U < 0 \qquad\qquad T_{snow} = \frac{U}{W\rho_w C_s + \rho_g D_e C_g} \tag{36}$$

$$if\ 0 < U < W\rho_w h_f \qquad T_{snow} = 0°C \tag{37}$$

3.2 Snow Model Modification

During snowpack model development, it was determined that the cold content of the snowpack (which is important for accurately simulating winter soil temperatures) was

almost entirely controlled by snow events, compared to heat loss at the snowpack surface. Recent observations and modeling of snowpack cold content in the Rocky Mountains [Jennings et al., 2018] indicate that precipitation exerts the primary control on cold content development (73-84%), while heat lost at the snowpack surface is responsible for a much smaller fraction (16-27%). Thus, a snowpack temperature model should be more dependent on precipitation events than heat fluxes but should still reflect the influence of heat fluxes at the snowpack surface.

In the original model, the snow surface heat conductance K_s is held constant. A sensitivity analysis was performed in which the value of the heat conductance parameter K_s (35) was scaled by a factor of 10 for snowpacks of varying depths, simulated by multiplying and dividing snowfall by a factor of 2 (Appendix A). Due to the low thermal conductivity of snow, heat fluxes at the snowpack surface should influence snowpack cold content (and the ground temperature beneath) more strongly for a thin snowpack (dividing by two) than for a thick snowpack (multiplying by two). In each K_s case (original, multiplying by 10, dividing by 10), shallow soil temperatures were insensitive to changes in snow depth, indicating that the K_s parameter could not simply be adjusted to account for the influence of snowpack cold content on ground temperatures, suggesting that a modified parameterization is required.

In the original model, the effective depth Z_e, over which the thermal gradient between the snowpack surface temperature T_{ss} and bulk snowpack temperature T_{snow} acts, is held constant at the depth of thermal penetration of diurnal temperature variations at the snowpack surface. While the depth of thermal penetration of heat exchanges at the snowpack surface is expected to remain constant, the effective depth Z_e between T_{snow} and T_{ss} should increase as the depth of the snow increases. The fixed Z_e of the original model was replaced with a quantity that scales with snow depth: Z_e was assumed to be equal to half of the snow depth and α_s was assigned such that the range of K_s is similar to the parameter used in the original model.

4. Subsurface Flow Model

Three-phase flow and transport in the subsurface is modeled using balance equations for mass and energy of water in PFLOTRAN-ICE [Karra et al., 2014]. The balance equations for the liquid, gas, and ice phases of water are given by [Painter, 2011]:

$$\frac{\partial}{\partial t}\left[\phi\left(s_l\eta_l\chi_w^l + s_g\eta_g\chi_w^g + s_i\eta_i\chi_w^i\right)\right] + \boldsymbol{\nabla}\cdot\left[\chi_w^l\eta_l\boldsymbol{v}_l + \chi_w^g\eta_g\boldsymbol{v}_g\right] - \boldsymbol{\nabla}\cdot\left[\phi s_g\tau_g\eta_g D_g\boldsymbol{\nabla}\chi_w^g\right] = Q_w \quad (38)$$

$$\frac{\partial}{\partial t}\left[\phi\left(s_l\eta_l U_l + s_g\eta_g U_g + s_i\eta_i U_i\right) + (1-\phi)\rho_r c_r T\right] + \boldsymbol{\nabla}\cdot\left[\boldsymbol{v}_l\eta_l H_l + \boldsymbol{v}_g\eta_g H_g\right] - \boldsymbol{\nabla}\cdot\left[\kappa\boldsymbol{\nabla}T\right] = Q_e \quad (39)$$

Boldface font is used to denote vector quantities. Subscripts l, g, and i refer to liquid, ice, and gas phases of water; ϕ is porosity; s_ζ ($\zeta = i, l, g$) is the saturation of the αth phase; η_ζ ($\zeta = i, l, g$) is the molar density of the ζth phase; χ_w^ζ ($\zeta = i, l, g$) is the mole fraction of H_2O in the ζth phase; τ_g is the tortuosity of the gas phase; D_g is the diffusion coefficient in the gas phase; T is the temperature (assuming all the phases and the soil are in thermal equilibrium); c_r is the specific heat of the soil; ρ_r is the density of the soil; U_ζ ($\zeta = i, l, g$) is the molar internal energy of the ζth phase; H_ζ ($\zeta = i, l, g$) is the molar enthalpy of the ζth phase; Q_e is the heat source; $\boldsymbol{\nabla}()$ is the gradient operator; and $\boldsymbol{\nabla}\cdot()$ is the divergence operator. The Darcy velocities of the gas and liquid phases are:

$$\boldsymbol{v}_g = -\frac{k_{rg}k}{\mu_g}\boldsymbol{\nabla}[p_g + \rho_g gz] \quad (40)$$

$$\boldsymbol{v}_l = -\frac{k_{rl}k}{\mu_l}\boldsymbol{\nabla}[p_l + \rho_l gz] \quad (41)$$

k is the intrinsic permeability; $k_{r\zeta}$ ($\zeta = l, g$) is the relative permeability of the ζth phase; ρ_g and ρ_l are the mass densities of the gas and liquid phases; Q_w is the mass source of H_2O; μ_ζ ($\zeta = l, g$) is the viscosity of the ζth phase; p_ζ ($\zeta = l, g$) is the partial pressure of the ζth phase; g is acceleration due to gravity and z is the vertical distance from a reference datum. Compressibility of the pore space is accounted for through a relationship with liquid pressure:

$$\phi = \phi_0 e^{c(p_l - p_{ref})} \quad (42)$$

ϕ_0 is the porosity of the undeformed soil, p_{ref} is a reference liquid pressure (1 atm), c is a compressibility coefficient (10^{-7} Pa^{-1}). Constraints on the phase saturations of water are given by:

$$s_l + s_g + s_i = 1 \tag{43}$$

Neglecting the amount of air in liquid and ice phases:

$$\chi_a^l = 0, \chi_a^i = 0 \rightarrow \chi_w^l = 0, \chi_w^i = 0 \tag{44}$$

χ_a^ξ ($\xi = l, i$) is the mole fraction of air in the ξth phase. Assuming that p_g is hydrostatic:

$$p_g = p_g|_{z=0} - \rho_g g z \tag{45}$$

$$p_g|_{z=0} = 1 atm \tag{46}$$

The balance equations reduce to:

$$\frac{\partial}{\partial t}\left[\phi\left(s_l \eta_l + s_g \eta_g \chi_w^g + s_i \eta_i\right)\right] + \boldsymbol{\nabla} \cdot [\eta_l \boldsymbol{v}_l] - \boldsymbol{\nabla} \cdot \left[\phi s_g \tau_g \eta_g D_g \boldsymbol{\nabla} \chi_w^g\right] = Q_w \tag{47}$$

$$\frac{\partial}{\partial t}\left[\phi\left(s_l \eta_l U_l + s_g \eta_g U_g + s_i \eta_i U_i\right) + (1 - \phi)\rho_r c_r T\right] + \boldsymbol{\nabla} \cdot \left[\boldsymbol{v}_l \eta_l H_l + \boldsymbol{v}_g \eta_g H_g\right] - \boldsymbol{\nabla} \cdot [\kappa \boldsymbol{\nabla} T] = Q_e \tag{48}$$

$$\boldsymbol{v}_l = -\frac{k_{rl} k}{\mu_l} \boldsymbol{\nabla}[p_l + \rho_l g z] \tag{49}$$

$$\boldsymbol{v}_g = 0 \tag{50}$$

The vapor pressure is calculated from Kelvin's equation [Edlefsen and Anderson, 1943]. Molar gas density η_g is calculated from the ideal gas law. Partitioning of the ice, liquid, and vapor phases at a known temperature and pressure is obtained by solving:

$$s_l = (1 - s_i)S_*(P_{cgl}) \tag{51}$$

$$s_l = S_*\left[-\beta \rho_i h_{iw}^0 H\left(\frac{T_0 - T}{T_0}\right) + S_*^{-1}(s_l + s_i)\right] \tag{52}$$

S_* is the retention curve for unfrozen liquid and gas phases, T_0 is the freezing point of water (273.15 K), h_{iw}^0 is the heat of fusion of ice at 273.15 K, and ρ_i is the mass density of ice. These equations treat ice as a solid and partition vapor and liquid phases using the unfrozen retention curve [Painter and Karra, 2014]. S_* is Van-Genuchten's model:

$$S_* = \begin{cases} [1 + (\alpha_{VG} P_c)^\gamma]^{-\lambda}, & P_c > 0 \\ 1, & P_c > 0 \end{cases} \tag{53}$$

α_{VG} and λ are Van-Genuchten parameters. The subscript VG is used to distinguish Van-Genuchten's α_{VG} from α, which refers to hillslope aspect (section 2.1). γ is related to λ by:

$$\gamma = \frac{1}{1 - \lambda} \tag{54}$$

The relative permeability of liquid water is given by the Mualem model [Mualem, 1976]. Volumetric water content θ_l is calculated from liquid saturation s_l and residual water content θ_r according to:

$$\theta_l = s_l(\phi - \theta_r) + \theta_r \tag{55}$$

Volumetric ice content θ_i is calculated from ice saturation s_i:

$$\theta_i = \phi s_i \tag{56}$$

The thermal conductivity of frozen soil is calculated according to [Painter, 2011]:

$$\kappa = Ke_f \kappa_{wet,f} + Ke_u \kappa_{wet,u} + (1 - Ke_f - Ke_u)\kappa_{dry} \tag{57}$$

Ke_f and Ke_u are Kersten numbers that describe the dependence of bulk thermal conductivity on the thermal conductivity of ice- ($\kappa_{wet,f}$), liquid- ($\kappa_{wet,u}$), and air-saturated (κ_{dry}) soil (see section 5). The subscripts f and u refer to frozen and unfrozen, respectively.

5. Subsurface Model Layers and Parameters:

While the dimensions of the domain vary between studies presented in Chapters III and IV, the model is always run at an hourly timestep and a spatial discretization of 10cm-20cm. The domain consists of three layers, with hydrologic properties presented Table 3. The model was divided into "soil" and "weathered bedrock" layers to represent the thermal and hydrologic differences between soil and weathered bedrock. A third "saprolite" layer was added to smooth the transition between "weathered bedrock" and "soil" layers; this model layer is simply assigned the mean of the "soil" and "weathered bedrock" parameters.

Hydrologic parameters (Table 3) were selected based on a combination of existing studies at Gordon Gulch [Langston et al., 2015; Hinckley et al., 2014b] as well as representative parameters from Charbeneau [2000]. Whereas (57) (section 4) is used to estimate the bulk thermal conductivity of soil containing a mixture of liquid, ice, and air, (58) is used to estimate the bulk thermal conductivity of ice-, liquid-, and air-saturated soil (Table 4) based on parameters for clastic materials from Woo [2012]. Bulk thermal conductivities are derived from constituent materials:

$$\kappa = \prod_{j=1}^{J} \kappa(j)^{f(j)} \tag{58}$$

where $\kappa(j)$ and $f(j)$ are the thermal conductivity and volumetric fraction of the jth soil type. Similarly, the volumetric ground heat capacity C is derived from constituent materials based on a weighted sum:

$$C = \sum_{j=1}^{J} C(j)f(j) \tag{59}$$

where $C(j)$ and $f(j)$ are the volumetric heat capacity and volumetric fraction of the jth soil type. The soil density was obtained from measurements performed by Hinckley et al., [2014b]; soil specific heat (c_r) was computed from the volumetric heat capacity of clastic material [Woo, 2012] and the soil density. Empirical Kersten coefficients that describe the dependence of bulk thermal conductivity on phase saturations (57) are from Karra et al., [2014].

Material	Depth	k [Pa s]	ϕ	α_{VG} [Pa^{-1}]	λ	θ_r
Soil	0-1m	9e-12	0.38	8.15e-5	0.09	0.0*
Saprolite	1-2m	4.5e-12	0.29	7.6e-5	0.4	0.0*
Weathered Bedrock	2m-maximum domain depth (varies)	2.4e-14	0.2			

Table 3. Hydrologic properties used in model simulations. k is intrinsic permeability, ϕ is soil porosity, α_{VG} and λ are Van-Genuchten parameters (see equations 53-54), and θ_r is residual water content. *Hinckley et al., [2014b] measured negligible (<0.01) residual water content in soil samples from Gordon Gulch.

Material	κ_{dry}	$\kappa_{wet,u}$	$\kappa_{wet,f}$
Soil	0.21	1.2	2.5
Weathered Bedrock	1.1	2.1	2.8

Table 4. Thermal conductivities (W m^{-1} K^{-1}) used in model simulations. κ_{dry}, $\kappa_{wet,u}$, and $\kappa_{wet,f}$ refer to air-, liquid-, and ice-saturated bulk thermal conductivity.

6. Boundary Conditions for Subsurface Model

Although boundary conditions vary for the studies presented in Chapters III and IV, they are described in general terms in this section. Boundaries are defined in reference to z and x displayed in Figure 9, as well as the domain $depth$ (z_d) and $width$ (x_w), which vary between studies.

6.1 Thermal Boundary Conditions

The thermal boundary condition applied to the soil surface ($z = 0$) is a specified temperature condition:

$$T_{z=0} = T_{surface} \tag{60}$$

$T_{surface}$ is obtained from a one-dimensional soil heat conduction model, which is introduced in section 7.1 The thermal boundary condition applied to the deep subsurface ($z = z_d$) is a geothermal heat flux condition [Ehlers, 2004]:

$$\frac{\partial T_{z=z_d}}{\partial z} = 0.04 \; W \; m^{-2} \tag{61}$$

The remaining boundaries ($x = 0; x = x_w$) are assigned zero heat flux conditions:

$$\frac{\partial T_{x=0}}{\partial z} = 0 \tag{62}$$

$$\frac{\partial T_{x=x_w}}{\partial z} = 0 \tag{63}$$

6.2 Hydrologic Boundary Conditions

The hydrologic influence of the hillslope inclination β is represented by a geometric adjustment to gravitational acceleration g in the z and x dimensions:

$$g_z = gcos(\beta) \tag{64}$$

$$g_x = gsin(\beta) \tag{65}$$

Throughout this chapter, the variable q_k is used to denote the kth component of the Darcy flux $\boldsymbol{v}_l$ (49) (section 4) with $k = z, x$:

$$q_k \equiv \boldsymbol{v}_l|_k \tag{66}$$

The hydrologic boundary condition applied to the soil surface ($z = 0$) is a specified flux condition $q_{z,infiltration}$, which is adjusted for infiltration capacity (section 7.2):

$$q_{z=0} = q_{z,infiltration} \tag{67}$$

To allow water to exit the domain through the deep subsurface boundary ($z = z_d$), a hydrostatic condition is applied, with atmospheric pressure specified at $x = x_w, z = z_d$:

$$p_{l,z=z_d} = p_l|_{x=x_w,z=z_d} + \rho_l g_x(x - x_w) \tag{68}$$

$$p_l|_{x=x_w,z=z_d} = 1atm \tag{69}$$

To allow water to exit the domain through the "downstream" boundary ($x = x_w$), an additional hydrostatic condition is applied, with atmospheric pressure specified at location $x = x_w, z = z_d$ (69):

$$p_{l,x=x_w} = p_l|_{x=x_w,z=z_d} + \rho_l g_z(z - z_d) \tag{70}$$

In most cases, a zero-flux hydrologic boundary condition is applied at the "upstream" boundary ($x = 0$):

$$q_{x=0} = 0 \tag{71}$$

For cases in which a water table is established across the full extent of the hillslope based on data (e.g. Chapter IV, section 3.2), a hydrostatic condition is applied to the "upstream" boundary ($x = 0$) analogous to (70), with atmospheric pressure specified at $x = 0, z = z_d$:

$$p_{l,x=0} = p_l|_{x=0,z=z_d} + \rho_l g_z(z - z_d) \tag{72}$$

$$p_l|_{x=x_w,z=z_d} = 1atm \tag{73}$$
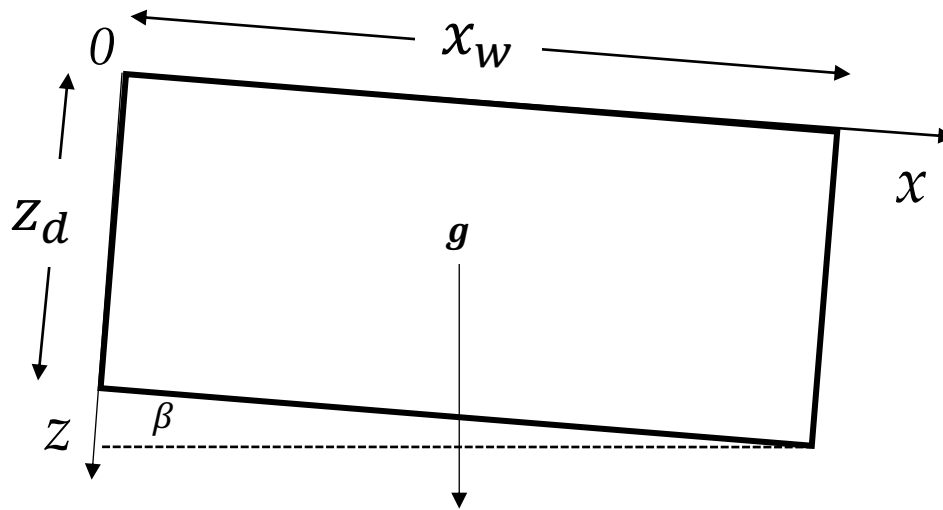
Figure 9. Inclined domain used for subsurface simulations. β is the hillslope angle, $\boldsymbol{g}$ is the gravitational acceleration vector, origin is denoted as 0, z and x are the vertical and horizontal dimensions in reference to the model domain, z_d and x_w are the depth and width of the domain.

7. Coupling of Surface and Subsurface Models

7.1 Thermal Coupling

7.1.1 Ground Heat Flux

The ground heat flux G (25) is used in the surface energy model to estimate the amount of energy available for evapotranspiration (24) (section 2.1), as well as in the snowpack energy balance model (section 3.1). G is defined as positive into the soil and is estimated from the subsurface model using surface nodes denoted with the superscript J (depths 0-dz) and $J-1$ (depths dz-$2dz$):

$$G = \frac{\kappa^J + \kappa^{J-1}}{2} \frac{T^J - T^{J-1}}{dz} \tag{74}$$

7.1.2 One-Dimensional Soil Heat Conduction Model

Due to computational difficulties in prescribing energy flux boundary conditions in PFLOTRAN-ICE, a one-dimensional heat conduction model evaluates the surface energy balance to generate a prescribed soil surface temperature boundary condition for PFLOTRAN-ICE. The model runs in tandem with PFLOTRAN-ICE at an hourly timestep, 1cm resolution, and 10m depth, and serves to remove the surface energy balance computations from PFLOTRAN-ICE, freeing resources for the computationally intensive subsurface freezing process modeling. In each time step, the surface energy balance is computed within the 1D model; for outgoing longwave radiation, the PFLOTRAN-ICE soil temperature at 0-10cm depth from the previous time step is used as the surface temperature. Soil properties within the 1D model are adjusted using the PFLOTRAN-ICE liquid, solid, and gas phase water saturations from the previous time step (see below). The 1D model is forced with a temperature boundary condition if a snowpack is present or an energy flux boundary condition if a snowpack is not present. In order to maintain a temperature gradient in the top 10cm of the domain at higher resolution (1cm) than the low resolution (10cm) PFLOTRAN-ICE simulations, soil temperatures in the 1D model are allowed to vary independently from PFLOTRAN-ICE. Such a configuration allows for a

higher resolution computation of the surface energy balance than can be performed in the lower resolution subsurface simulations. While the overall depth of the 1D model is large enough (10m) to minimize the effects of the deep subsurface boundary condition, only the surface region is directly used in model computations: the temperatures in the top 10cm of the domain are averaged to produce a temperature boundary condition $T_{surface}$ for PFLOTRAN-ICE.

A Crank-Nicholson scheme with a time step of 1hr and vertical resolution of 1cm is used to simulate the propagation of heat through the subsurface to a depth of 10m below the soil surface according to Fourier's law:

$$\frac{\partial u}{\partial t} = \frac{\kappa}{C}\frac{\partial^2 u}{\partial z^2} \tag{75}$$

u is temperature, t is time (s), κ is thermal conductivity, C is soil volumetric heat capacity, and z is depth. The boundary condition in the deep subsurface is zero-flux, which does not significantly affect soil temperatures in the top 10cm of the 10m domain:

$$\frac{\partial T_{z=10m}}{\partial z} = 0 \tag{76}$$

The boundary condition at the soil surface depends on the presence of snowcover. When a snowpack is present, the soil surface is forced with a prescribed temperature condition:

$$T_{z=0m} = T_{snow} \tag{77}$$

When a snowpack is not present, the ground surface in the model is forced with a prescribed flux condition, including net shortwave and longwave radiation Q_{sn} (18) and Q_{ln} (21), sensible and latent heat transfer Q_h (22) and Q_e (23):

$$-\kappa\frac{dT_{z=0m}}{dz} = Q_{sn} + Q_{ln} + Q_h + Q_e \tag{78}$$

Since the 1D model is used to evaluate heat fluxes at the soil surface, bulk soil is assigned the mean of thermal parameters for organic and clastic materials from Woo [2012] using equations (57), (58), and (59) and thermal parameters are updated at the beginning of each

hourly time step based on the simulated presence of pore water in the PFLOTRAN-ICE

simulations. A large number of models are available for computing bulk thermal

conductivity as a function of liquid and ice saturation, which differ on the order of ~1 W m^{-1}

K^{-1} [Zhang and Wang, 2017]; accordingly, thermal parameter selection likely introduces a

comparable amount of uncertainty compared to the choice of mixing model. In any case, the

1D model simply produces surface temperatures for the PFLOTRAN-ICE simulations that

simulate three-phase flow of energy and water. The detailed representation of phase-

fraction dependent properties is handled within the PFLOTRAN-ICE computations. A

schematic of the coupling is presented in Figure 9.

```
                    ┌─────────────────────────┐
                    │  Determine Presence of  │
                    │ Snowcover as Existing   │
                    │  Snow or Snowfall       │
                    └─────────────────────────┘
         Snow                              No Snow
┌─────────────────────────┐      ┌─────────────────────────┐
│  Compute snowpack energy│      │  Compute surface energy │
│         balance         │      │  balance for bare soil  │
└─────────────────────────┘      └─────────────────────────┘
┌─────────────────────────┐
│  Compute bulk snowpack  │
│ temperature and snowmelt│
│          rate           │
└─────────────────────────┘
┌─────────────────────────┐      ┌─────────────────────────┐
│   Compute soil surface  │      │   Compute soil surface  │
│  temperature within 1D  │      │  temperature within 1D  │
│   conduction model from │      │   conduction model from │
│   snowpack temperature  │      │  surface energy balance │
└─────────────────────────┘      └─────────────────────────┘
┌─────────────────────────┐      ┌─────────────────────────┐
│ Compute snowmelt recharge│     │ Compute rainfall recharge│
│  rate based on infiltration│   │ rate based on infiltration│
│        capacity         │      │        capacity         │
└─────────────────────────┘      └─────────────────────────┘
              ┌─────────────────────────────────┐
              │  Apply soil surface temperature │
              │  and recharge rate to subsurface│
              │  flow model PFLOTRAN-ICE        │
              └─────────────────────────────────┘
              ┌─────────────────────────────────┐
              │  Run subsurface model for one   │
              │  timestep, compute water        │
              │  saturations, water fluxes, and │
              │  subsurface temperatures        │
              └─────────────────────────────────┘
              ┌─────────────────────────────────┐
              │  Compute subsurface properties  │
              │  for the next timestep:         │
              └─────────────────────────────────┘
              ┌─────────────────────────────────┐
              │        Ground Heat Flux         │
              └─────────────────────────────────┘
              ┌─────────────────────────────────┐
              │  Infiltration Capacity, Thermal │
              │  Conductivity, and Heat         │
              │  Capacity                       │
              └─────────────────────────────────┘
```
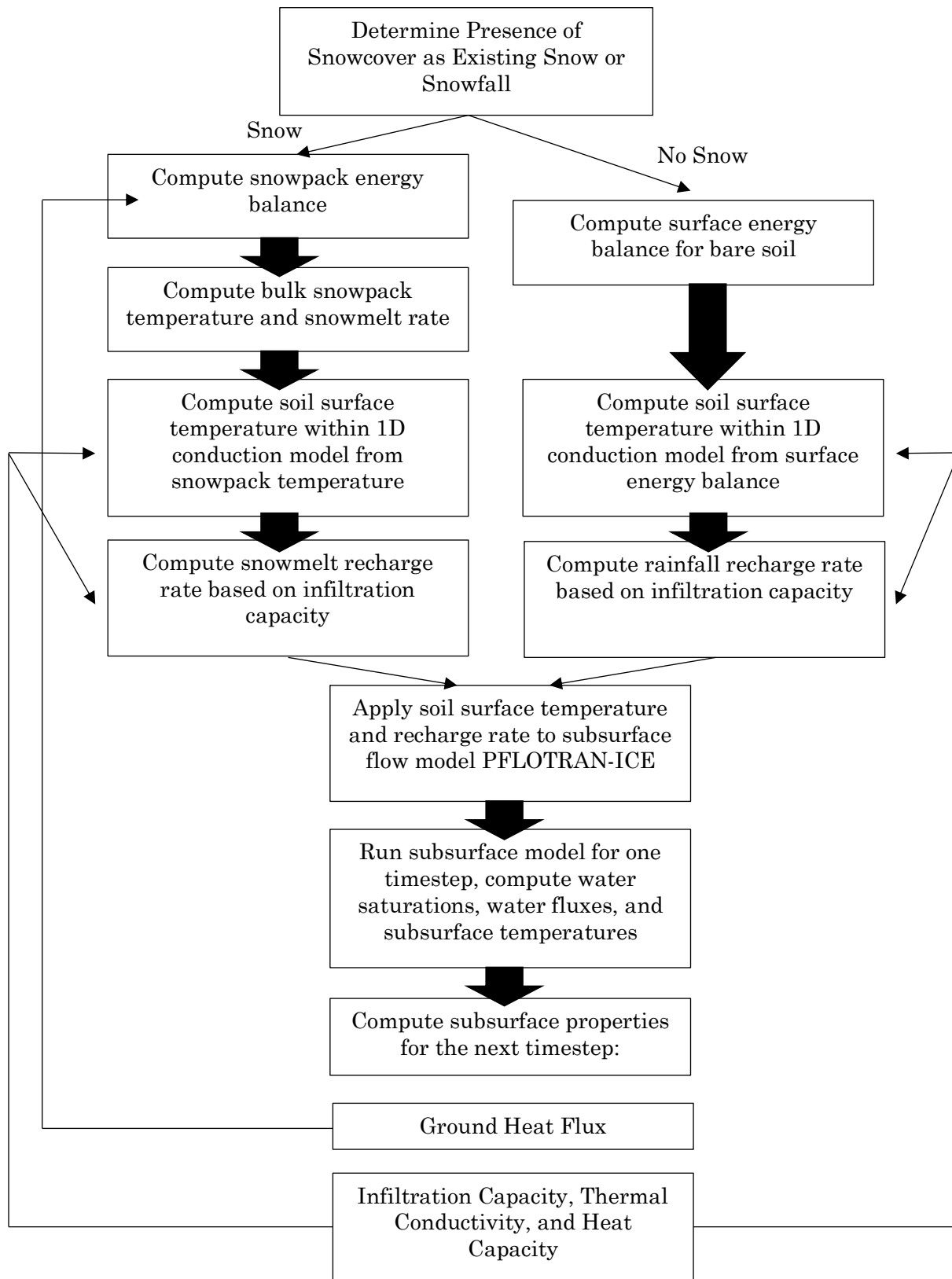
Figure 10. Thermo-hydrologic coupling when snow is present (left) and absent (right).

7.2 Hydrologic Coupling

During the process of coupling surface models to subsurface models, it was determined that the coupling scheme required an infiltration capacity formulation to modify the quantity of recharge applied to the subsurface model. When more recharge is applied to the subsurface model than can be accommodated by shallow soils, the subsurface model does not converge on a solution. Accordingly, a simple rule is used to determine whether the shallow subsurface has the capacity for additional infiltration from snowmelt or rainfall flux $q_{z,in}$. As in section 6, the variable q_k is used to denote the kth component of the Darcy flux $\boldsymbol{v}_l$ (49) (section 4) with $k = z, x$ (66). Information from the previous timestep is used to estimate the infiltration capacity for the current timestep. The empty pore space L_{empty} (units of length or volume per unit area) in a surface cell denoted J with depth Δz, porosity ϕ, liquid saturation $s_l{}^J$, and ice saturation $s_i{}^J$ is given by:

$$L_{empty} = \phi \Delta z (1 - s_l{}^J - s_i{}^J) \tag{79}$$

The quantity of water $q_{z,outflow}$ (units of length per time) expected to flow out of the cell during the time step is estimated as the Darcy flux:

$$q_{z,outflow} = -\frac{k_{rl}^J k^J}{\mu_l^J} \left[\frac{p_l^J - p_l^{J-1}}{\Delta z} + \rho_l^J g \cos\theta \right] \tag{80}$$

The infiltration capacity $L_{capacity}$ is estimated as the sum of L_{empty} and $q_{z,outflow}$ multiplied by the length of the timestep:

$$L_{capacity} = L_{empty} + q_{z,outflow} dt \tag{81}$$

If there is snowfall or snow accumulation during the time step, snowmelt is directed toward the subsurface:

$$q_{z,in} = M_r \tag{82}$$

If there is no snowfall or snow accumulation during the time step, rainfall is directed toward the subsurface:

$$q_{z,in} = P_r \tag{83}$$

If the quantity of meltwater or rainfall $q_{z,in}$ is greater than the infiltration capacity $L_{capacity}$, hourly infiltration rate $q_{infiltration}$ is set as the infiltration capacity and the difference is retained as runoff:

$$if\ q_{z,in} > L_{capacity}: \qquad q_{z,infiltration} = L_{capacity} \qquad q_{z,runoff} = q_{z,in} - L_{capacity} \tag{84}$$

$$else: \qquad q_{z,infiltration} = q_{in} \qquad q_{z,runoff} = 0$$

The hourly infiltration rate $q_{z,infiltration}$ is applied as a hydrologic flux boundary condition for the PFLOTRAN-ICE simulations (section 6.2). The quantity $q_{z,runoff}$ is not analyzed throughout the studies presented in Chapters III and IV.

CHAPTER III

MODELING ASPECT CONTROLLED FORMATION OF SEASONALLY FROZEN

GROUND ON MONTANE HILLSLOPES: A CASE STUDY FROM GORDON GULCH, CO

1.   Introduction

Frozen soils are typically classified as permafrost and seasonally frozen ground (SFG).

Permafrost soils remain at or below 0˚C for at least two years, while SFG freezes and thaws

annually [Harris et al., 1988]. Permafrost typically occurs at high latitudes and altitudes,

occupying about 25% of land in the northern hemisphere, while SFG prevails at lower

latitudes and altitudes, affecting approximately 50% of land in the northern hemisphere

[Zhang et al., 2003].

Hydrology and infiltration are influenced by SFG [Hayashi, 2013]. Hydraulic conductivity

decreases by orders of magnitude during the transition from unfrozen to frozen ground

[McCauley et al., 2002; Burt and Williams, 1976], although partially frozen ground may

still transmit liquid water [e.g. Scherler et al., 2010; Boike et al., 1998]. Many studies have

shown that frozen soils reduce infiltration [e.g. Bayard et al., 2005; Laudon et al., 2004;

Stähli et al., 1996; Thunholm et al., 1989; Kane and Stein, 1983; Dunne and Black, 1971],

while others have found no connection between frozen soils and runoff generation [Fuss et

al., 2016; Lindström et al., 2002; Nyberg et al., 2001; Shanley and Chalmers, 1999].

In addition to altering hydrologic flow paths, seasonal soil freezing patterns influence soil

biogeochemistry, plant phenology, and slope geomorphology [Hayashi, 2013]. Soil freezing

may lead to microbial and root mortality, which can change the chemical composition of

connected aquatic ecosystems. For example, plot-scale studies have observed nitrogen

export following freezing events [Groffman et al., 1999; Fitzhugh et al., 2001; Groffman et

al., 2001b; Groffman et al., 2011]. Frozen ground also contributes to downslope soil

migration through the process of frost creep, which depends on the depth of soil freezing (which also tends to increase with increasing frost duration) [Matsuoka, 2001], and constitutes a primary mechanism of downslope soil movement on the Colorado Front Range [Benedict, 1970].

In light of anticipated changes in the intensity, frequency, and duration of seasonal freezing in a warming climate, there is a need for process-based models of SFG occurrence as a step towards quantifying watershed-scale changes in hydrology, biogeochemistry, and geomorphology. In mountain watersheds, models of frozen ground should consider the influence of steep topography, which produces strong gradients in solar insolation, vegetation, and snowpack dynamics that lead to large differences in soil temperature over short distances [Riseborough et al., 2008]. Throughout this study, freezing "intensity" refers to the number of degrees below 0°C, "frequency" refers to the number of intra-annual freezing and thawing events, and "duration" refers to the length of time that the ground is frozen.

It is well-established that a seasonal snowpack strongly influences the occurrence of frozen ground [Zhang, 2005]. As the thickness of the snowpack increases, its insulating effects limit heat transfer between the soil and the atmosphere [e.g. Iwata et al., 2008]. Various "rules of thumb" suggest that snow depths greater than 30-50cm [Hill et al., 2019], 80-100cm [Imhof et al., 2000], or 30-40cm [Brooks et al., 1995; Brooks et al., 1998; Cline, 1995 qtd. in Brooks and Williams, 1999] act to decouple the ground from the atmosphere. Numerical modeling of idealized snow scenarios by Barlett et al., [2004] suggested that a snowpack that accumulates to a maximum thickness of 1.0 m completely insulates the ground from air temperature changes with seasonal periods, and 1.7 m of snow is required to decouple the ground from air temperature changes with an annual period. However, Zhang [2005] points out that when the snowpack accumulates above 40cm, it melts later in

the spring, insulating the ground from above-0°C air temperatures and preventing ground warming. That is, in addition to snow depth, the effect of snowpack insulation on ground temperatures depends on the seasonal onset and duration of the snowpack: an early snowpack insulates warm ground, while a late onset insulates cold ground; early melt exposes the ground to the warm spring air temperatures, while late melt preserves the cold state of the ground late in to the spring [Zhang, 2005; Bartlett et al., 2004; Ishikawa, 2003; Haeberli and Patzelt, 1982]. Such differences in snow onset timing can have profound effects on the deep subsurface thermal regime over centennial timescales [Bartlett et al., 2004]. Thus, the overall effect of snow on ground temperatures depends on both the thermal history of the ground and the surface air temperature, and snow cover during periods with above-0°C air temperatures counteracts the ground warming effects of snow cover during periods with sub-0°C air temperatures [Bartlett et al., 2004].

In high-latitude regions where snow cover is typically present when air temperatures are low, a deep snowpack serves primarily to increase ground temperatures [Zhang, 2005], while SFG regions experience a wide range of variability in the depth and persistence of snow cover, as well as ambient air temperatures during periods of snow cover. In regions that experience SFG, field evidence demonstrates that, compared to a deep snowpack, a thin or absent snowpack permits thermal coupling between the ground and atmosphere, increasing the frequency and intensity of frozen ground compared to a deep snowpack, while reducing the duration [Fuss et al., 2016; Sarady and Sahlin, 2016; Bayard et al., 2005; Hardy et al., 2001]. Thus, a warmer climate in which snow develops later in the season could expose the soil to increased freezing [Hardy et al., 2001], and "colder soils in a warmer world" [Groffman et al., 2001a].

In mountainous regions with steep terrain and heterogenous topography, the ability of a snowpack to persist depends on many geographical factors including elevation, slope,

aspect, canopy and ridge shading, vegetation, and wind redistribution [Hinckley et al., 2014b; Jepsen et al., 2012; Litaor et al., 2008; Bayard et al., 2005; Erickson et al., 2005; Walker et al., 1993; Ives and Fahey, 1971]. Some of these factors also influence the surface energy balance and ground heat fluxes that regulate SFG occurrence in snow-free regions. Thus, the occurrence and persistence of SFG is expected to be very patchy. In addition, the combination of these topographic variables confounds efforts to project snow and soil thermal regimes within geographical zones. For example, alpine sites tend to receive more solar radiation than montane sites, but alpine sites are subjected to colder air. A montane south-facing slope may receive more solar radiation than a sub-alpine north-facing slope despite its lower elevation. A wind-scoured north-facing slope might retain less snow than a nearby south-facing slope despite experiencing lower solar radiation. Models of SFG occurrence in mountainous regions should employ an energy-based approach to adequately resolve the complexity of these topographic factors.

In this study, we report observations and thermo-hydrologic modeling of seasonally frozen ground occurrence at a seasonally snow-covered montane sub-watershed (Gordon Gulch) within the Boulder Creek watershed, which is one of the intensively studied sites monitored by the Boulder Creek Critical Zone Observatory (BcCZO). The field site features two instrumented hillslopes with opposing aspects: the snowpack on the north-facing slope persists throughout much of the winter season, while the snowpack on the south-facing slope is highly ephemeral. Despite the persistent snowpack on the north-facing slope, seasonally frozen ground is more prevalent and persistent there, likely due to two reasons: lower incoming radiation due to the slope's poleward inclination and forest canopy shading, and a relatively thin snowpack. The south-facing slope experiences significantly higher incoming radiation that likely prevents the persistence of frozen ground.

Differences in soil moisture, subsurface flow paths, and soil development have been reported at Gordon Gulch in several studies [Langston et al., 2015; Hinckley et al., 2014b; Anderson et al., 2013]. Soil moisture data and hillslope-scale unsaturated flow modeling performed using a temperature-index snow model showed that the north-facing slope sustains high soil moisture because the snowpack melts continuously and delivers steady recharge to the subsurface, whereas the south-facing slope maintains low soil moisture because the snowpack melts in rapid events that deliver brief pulses of water to the subsurface [Langston et al., 2015]. Plot-scale tracer experiments showed that the north-facing slope is characterized by steady connected flow through the soil matrix, whereas the south-facing slope soils experience brief periods of rapid vertical transport [Hinckley et al., 2014b].

We employ thermo-hydrologic modeling to evaluate the factors controlling the occurrence of seasonally frozen ground at Gordon Gulch and its hydrologic consequences using PFLOTRAN-ICE, a thermo-hydrologic subsurface flow and transport model [Karra et al., 2014] coupled to a lumped snowpack model similar to the Utah Energy Balance model [Tarboton and Luce, 1996]. A surface energy balance model incorporating solar radiation and snowpack processes is used to reproduce soil temperature data from water years 2013-2016. Representation of the snowpack significantly improves soil temperature estimates on the north-facing slope, particularly the duration of soil freezing in the spring, which is underestimated by 1-2 months without including the snowpack.

2.   Modeling Approach

In mountain environments, steep topography produces strong gradients in solar insolation, vegetation, and snowpack dynamics that lead to large differences in soil temperature over short distances that are not adequately represented in a model driven by air temperature forcing alone. The overall modeling framework combines surface energy balance and

snowpack models with a subsurface thermo-hydrologic model that simulates water and energy transport in the subsurface, including freeze-thaw processes, with an hourly timestep (Figure 1). The surface energy balance calculations account for the differences in aspect between the north- and south-facing slopes, and the influence of the coniferous canopy in shading incoming solar radiation. The snowpack model is a lumped model similar to the Utah Energy Balance [Tarboton and Luce, 1996]. The subsurface thermo-hydrologic modeling was performed using PFLOTRAN-ICE, whose capabilities for handling a three-phase ice-water-air system are outlined in Karra et al. [2014] and Painter and Karra [2014]. In previous work, PFLOTRAN-ICE has been used in the arctic to simulate polygonal tundra landscapes [Kumar et al., 2016] and the discontinuous permafrost zone under seasonal variability and climate change [Frampton, 2011]. Due to computational difficulties in prescribing energy flux boundary conditions in PFLOTRAN-ICE, we introduce an auxiliary one-dimensional temperature model. The purpose of the one-dimensional conduction model is to efficiently evaluate the surface energy balance outside of PFLOTRAN-ICE, freeing resources for the computationally intensive subsurface freezing process modeling. In the following sub-sections, we further describe each of these model components.

2.1 Surface Energy Balance Model:

Incoming shortwave and net radiation are estimated closely following Dingman [2015]. The solar radiation computations account for aspect (north- or south-facing), canopy shading, and ridge shading. The detailed equations involved in these computations are presented in Chapter II. Shortwave radiation calculations performed during the study years (water years 2013-2016) suggest that compared to a flat slope at the latitude and elevation of Gordon Gulch, incoming shortwave radiation on the south-facing slope is augmented annually by 22% due to the slope's equatorward inclination; incoming shortwave radiation

on the north-facing slope is attenuated annually by 23% due to the slope's poleward inclination and by an additional 22% due to canopy shading.

2.2 Snowpack Model:

The snowpack model closely follows the structure of the Utah Energy Balance model [Tarboton and Luce, 1996]. Snow water equivalent and energy content are determined in each time step by solving the following set of two coupled, non-linear ordinary differential equations:

$$\frac{dU}{dt} = Q_{sn} + Q_{ln} - Q_g + Q_h + Q_e + Q_p - Q_m \qquad (26)$$

$$\frac{dW}{dt} = P_r + P_s - M_r + E \qquad (27)$$

where U and W are energy and water content, respectively. In (26), Q_{sn} is net shortwave radiation, Q_{ln} is net longwave radiation, Q_g is the ground heat flux, Q_h is sensible heat flux, Q_e is latent heat flux, Q_p is heat advected with precipitation, and Q_m is heat advected with meltwater. In (27), P_r is rainfall rate, P_s is snowfall rate, M_r is snowmelt water, E is evaporation, condensation, and sublimation. The model equations are discussed in detail in Chapter II.

The low thermal conductivity of a snowpack is able to sustain strong thermal gradients between the bulk snowpack and the snowpack surface. Although the snowpack model is based on a single-layer formulation, the average snowpack temperature T_{snow} and the snow surface temperature T_{ss} are tracked separately to represent such gradients. Net available energy at the surface is balanced by conduction into or out of the snow, parameterized as a heat exchange between the bulk snowpack (at temperature T_{snow}) and the snow surface (at temperature T_{ss}):

$$Q_{sn} + Q_{li} + Q_p - Q_{le}(T_{ss}) + Q_h(T_{ss}) + Q_e(T_{ss}) = K_s \rho_s c_s (T_{ss} - T_{snow}) \qquad (34)$$

Q_{li} is incoming longwave radiation (which does not depend on T_{ss}) and Q_{le} is outgoing

longwave radiation (which does depend on T_{ss}). ρ_s is snow density (kg m³), c_s is the specific

heat of snow, and K_s is a snow surface conductance (m hr⁻¹). The non-linear equation (35) is

solved in each time step for T_{ss}. If the solution is greater than 0˚C, the surface energy

cannot be completely conducted into the snow: the surface temperature is then set to 0˚C,

and the remaining energy is available for melting the snowpack. Finally, the average

temperature of the snowpack T_{snow} is determined from the energy content U of the

snowpack relative to 0 ºC:

$$if\ U < 0 \qquad\qquad T_{snow} = \frac{U}{W\rho_w C_s + \rho_g D_e C_g} \qquad\qquad (36)$$

$$if\ 0 < U < W\rho_w h_f \qquad T_{snow} = 0°C \qquad\qquad (37)$$

2.3 Subsurface Simulations with PFLOTRAN-ICE

Three-phase flow of water in the subsurface is modeled using balance equations for mass

and energy in PFLOTRAN-ICE [Karra et al., 2014]. The model is summarized in Chapter II

and described in detail in Karra et al. [2014] and Painter and Karra [2014].

2.3.1   Domain and Soil Properties

A two-dimensional domain with dimensions 10m by 5m and vertical discretization of 10cm

is run at an hourly timestep. The domain is inclined at the hillslope angle. The domain

consists of three layers: the model was initially divided into "soil" and "weathered bedrock"

layers to represent the thermal and hydrologic differences between soil and weathered

bedrock; subsequently a third "saprolite" layer was added to smooth the transition between

"weathered bedrock" and "soil" layers; this model layer is assigned the mean of the "soil"

and "weathered bedrock" parameters. A saprolite horizon at Gordon Gulch has been

identified during field campaigns and reported in multiple studies [Langston et al., 2015;

Hinckley et al., 2014; Anderson et al., 2011]. Hydrologic parameters (Table 3) were selected

based on a combination of existing studies at Gordon Gulch [Langston et al., 2015; Hinckley et al., 2014b] as well as representative parameters from Charbeneau [2000]. Bulk thermal conductivities (Table 4) are derived from constituent materials according to Woo [2012].

2.3.2   Soil Temperature Model

Due to computational difficulties in prescribing energy flux boundary conditions in PFLOTRAN-ICE, a one-dimensional heat conduction model evaluates the surface energy balance to generate a prescribed soil temperature boundary condition for PFLOTRAN-ICE. The model runs in tandem with PFLOTRAN-ICE at an hourly timestep and 1cm resolution and serves to remove the surface energy balance computations from PFLOTRAN-ICE, freeing resources for the computationally intensive subsurface freezing process modeling. In each time step, the surface energy balance is computed within the 1D model; for outgoing longwave radiation, the PFLOTRAN-ICE soil temperature at 0-10cm depth from the previous time step is used as the surface temperature. Soil properties within the 1D model are adjusted using the PFLOTRAN-ICE liquid, solid, and gas phase water saturations from the previous time step (see below). The 1D model is forced with a temperature boundary condition if a snowpack is present or an energy flux boundary condition if a snowpack is not present. In order to maintain a temperature gradient in the top 10cm of the domain at higher resolution (1cm) than the low resolution (10cm) PFLOTRAN-ICE simulations, soil temperatures in the 1D model are allowed to vary independently from PFLOTRAN-ICE. Such a configuration allows for a higher resolution computation of the surface energy balance than can be performed in the lower resolution subsurface simulations. While the overall depth of the 1D model is large enough (10m) to minimize the effects of the deep subsurface boundary condition, only the surface region is directly used in model computations: the temperatures in the top 10cm of the domain are averaged to produce a temperature boundary condition $T_{surface}$ for PFLOTRAN-ICE. The model is described in detail in Chapter II.

2.3.3   Boundary Conditions

The thermal boundary condition on the soil surface (z=5 in Figure 11) in the PFLOTRAN-ICE subsurface model is specified as the average temperature from the top 10 centimeters of the one-dimensional heat conduction model (section 2.3.2); the remaining boundaries (z=0, x=0, x=10 in Figure 11) are assigned zero-conductive-flux conditions. The hydrologic boundary condition on the soil surface (z=5 in Figure 11) is a prescribed infiltration flux condition determined from the amount of rainfall or snowmelt produced during that timestep, adjusted for the occurrence of surface flow. Although the thermal influence of evapotranspiration is included within the soil surface boundary condition, its hydrologic influence is not incorporated into the model. The downstream boundary (x=10) is assigned a "hydrostatic" condition to allow flow out of the system with atmospheric pressure prescribed at (x=10, z=0), while the remaining boundaries are assigned zero-flux conditions. PFLOTRAN-ICE does not contain capabilities for coupling surface runoff and subsurface flow. Thus, there is a need for a surface flow formulation when the buildup of moisture/ice in the shallow subsurface prevents additional infiltration, and the simulation is unable to proceed. A simple rule is used to determine whether the shallow subsurface has the capacity for additional infiltration from snowmelt or rainfall flux. The infiltration capacity is computed as the available pore space of a surface cell with given liquid and ice saturations, along with the quantity of liquid water expected to leave the cell via Darcy flow. If the amount of infiltration is greater than the capacity, the excess is labeled surface flow. Surface runoff generation has not been widely observed in Gordon Gulch. Correspondingly, the occurrences of modeled surface flow are restricted to infrequent occasions of rapid snowmelt and large summer rain events.

2.3.4   Initial Conditions:

The initial conditions were selected to minimize the effects of interannual "memory". Simulations consist of a 10-year spin-up routine, followed by a 1-year model run. The spin-

up routine is initiated with unsaturated conditions at the measured soil temperature corresponding to the first day of the water year for each slope, and then run continuously for 10 years at an average recharge rate to obtain a steady-state condition. The recharge rate is computed from the mean annual precipitation during water years 2013-2016. Model runs then begin on the first day of the water year (October 1) when typically snow has not accumulated, and soils are unfrozen.
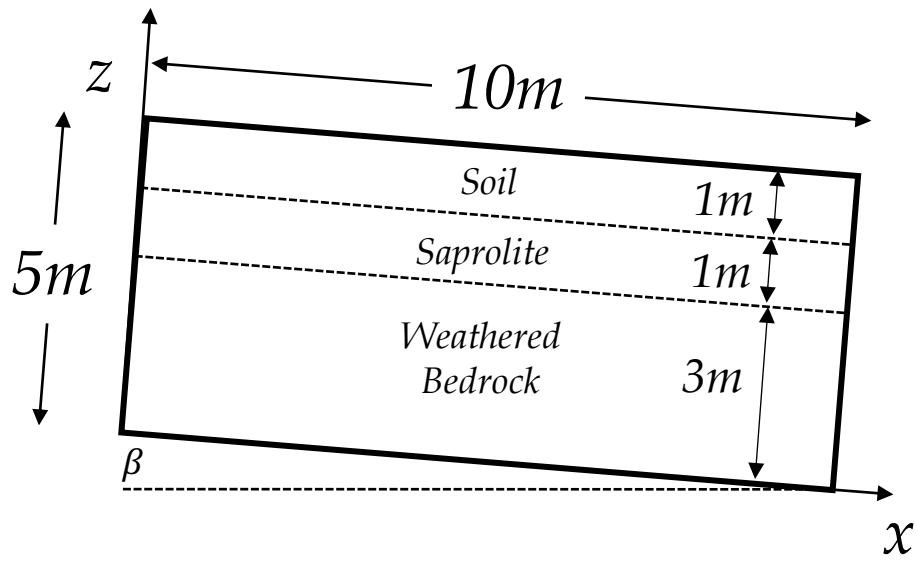
Figure 11. Dimensions and layering of model domain. The domain is inclined at the hillslope angle β. Atmospheric pressure is prescribed at x=10m, z=0.

3.   Field Data

3.1 Field Site Description

Gordon Gulch is a seasonally snow-covered montane sub-catchment of the Boulder Creek watershed in the Colorado Rockies monitored by the Boulder Creek Critical Zone Observatory (BcCZO). The site is located at a latitude of 40.01°N and mean elevation of 2650m. Mean annual air temperature (MAAT) is 5.1°C. Mean annual precipitation is 519mm, with a maximum in May. The underlying bedrock is biotite gneiss, and the site was not influenced by Pleistocene glaciation. A map of the site including tree cover is presented in Figure 4 (Chapter II). The south-facing slope is sparsely vegetated with ponderosa pine (*Pinus ponderosa*) and low-lying grasses, forbs, and shrubs; the north-facing slope is densely forested with lodgepole pines (*Pinus contorta*) and some Douglas fir (*Pseudotsuga menziesii*). The meteorological station on the south-facing slope is unobscured by forest canopy aside from a single ponderosa pine downslope from the station, whereas the meteorological station on the north-facing slope is located in a small clearing surrounded by dense coniferous forest.

Average slopes (β) were estimated as 21° and 15° for the south- and north-facing slopes, and average aspects (α) were estimated as 177° and 10° for the south- and north-facing slopes, respectively (aspect is measured clockwise from 0°N). These estimates were obtained from a digital elevation map (DEM) of the site, including Lower and Upper Gordon Gulch. First, the hillslopes of interest were isolated from the DEM by selecting grid points south and east of a reference point (indicated in Figure 12) near the boundary between Upper and Lower Gordon Gulch (40.017046°N, -105.473226°W; Easting=459616, Northing=4429756). Within this subset, slopes and aspects from grid points with aspects falling within a set of bounds were averaged (Table 5). The choice of aspect bounds ($\pm 90°$, $\pm 45°$, and $\pm 10°$) has a strong effect on the north-facing slope's aspect, (23.8°-1.1°), and very little effect on the north-facing slope's slope and the south-facing slope's aspect and slope.

Differences in radiative forcings resulting from the poleward and equatorial inclinations of the north- and south-facing slopes can be put in context of changes in latitude Lee [1962]. Classical optics holds that electromagnetic radiation incident upon an inclined plane is maximized perpendicularly to that plane, described by an "angle of incidence," defined as 0° when the incident ray is perpendicular to the plane. It follows that compared to a flat plane, hillslopes inclined toward the equator experience lower angles of incidence and higher solar insolation, whereas slopes inclined toward the poles experience higher angles of incidence and lower solar insolation. At Gordon Gulch, then, the south-facing slope (21°) receives shortwave radiation fluxes that are comparable to Manzanillo (19°N) or Mexico City, Mexico, an increase of 22% annually. The north-facing slope (15°) receives shortwave radiation fluxes that are comparable to Lac La Ronge (55°N) in central Saskatchewan, a reduction of 23% annually. In a similar way, deviations from perfectly north-facing (0°) and perfectly south-facing (180°) can be translated to equivalent shifts in longitude. An east-facing surface (e.g. the Boulder Flatirons) receives shortwave fluxes comparable to a flat surface to the east, while a west-facing surface receives shortwave fluxes comparable to a flat surface to the west. However, these shifts primarily change the timing or *phase* of shortwave fluxes, rather than the net daily magnitude of shortwave fluxes.

Gordon Gulch is highly representative of the Boulder Creek Watershed. A 1m-resolution Digital Elevation Model [Parrish and Anderson, 2020] was used to compute the elevation and aspect distributions for the Boulder Creek Watershed (Figures 13 and 14). 30% of elevations in the watershed fall within the elevation range of Gordon Gulch (2446m-2737m). The majority of the watershed is made up north- and south-facing slopes: 30% are south-facing and 25% are north-facing.
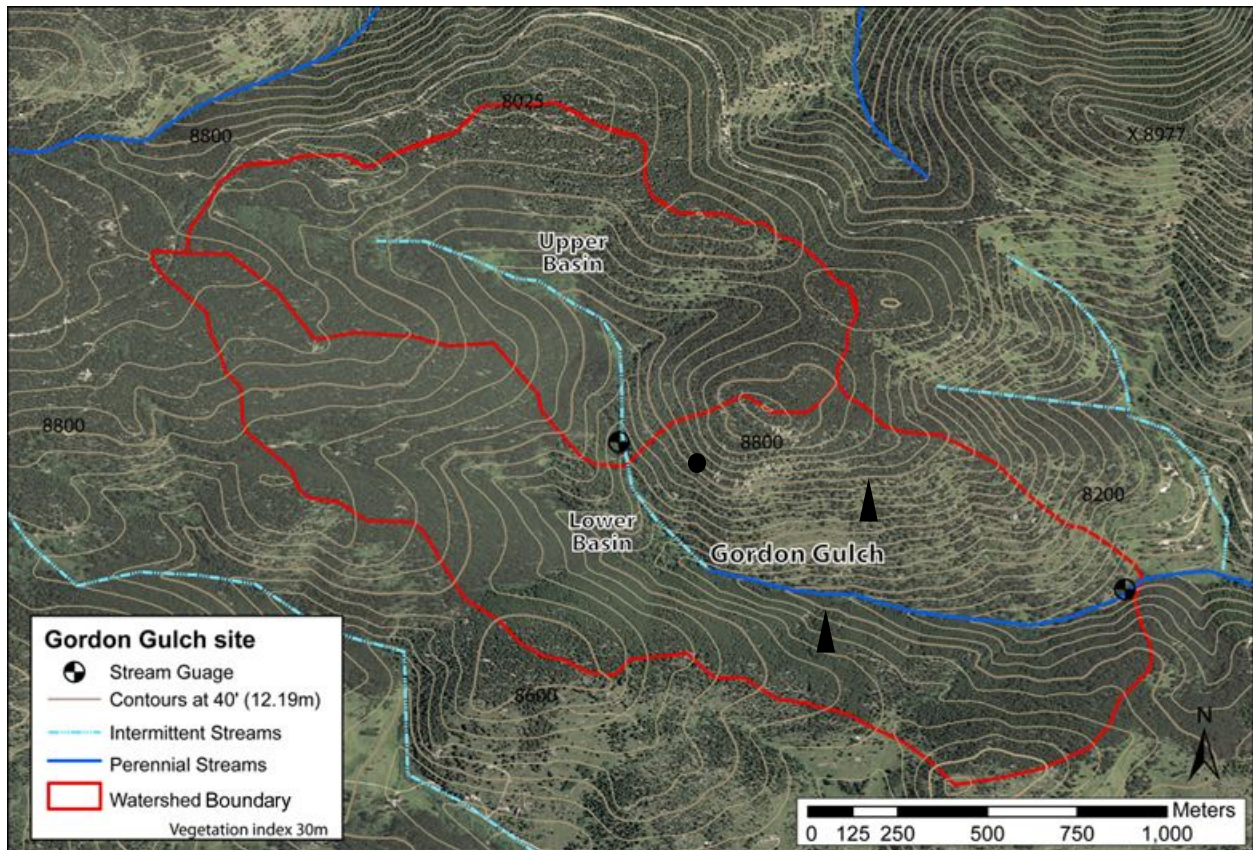
Figure 12. Map of Gordon Gulch including contours at 40 feet (12.19m). Reference point used in slope/aspect estimations indicated as ● . Meteorological stations marked as ▲ (locations approximate).
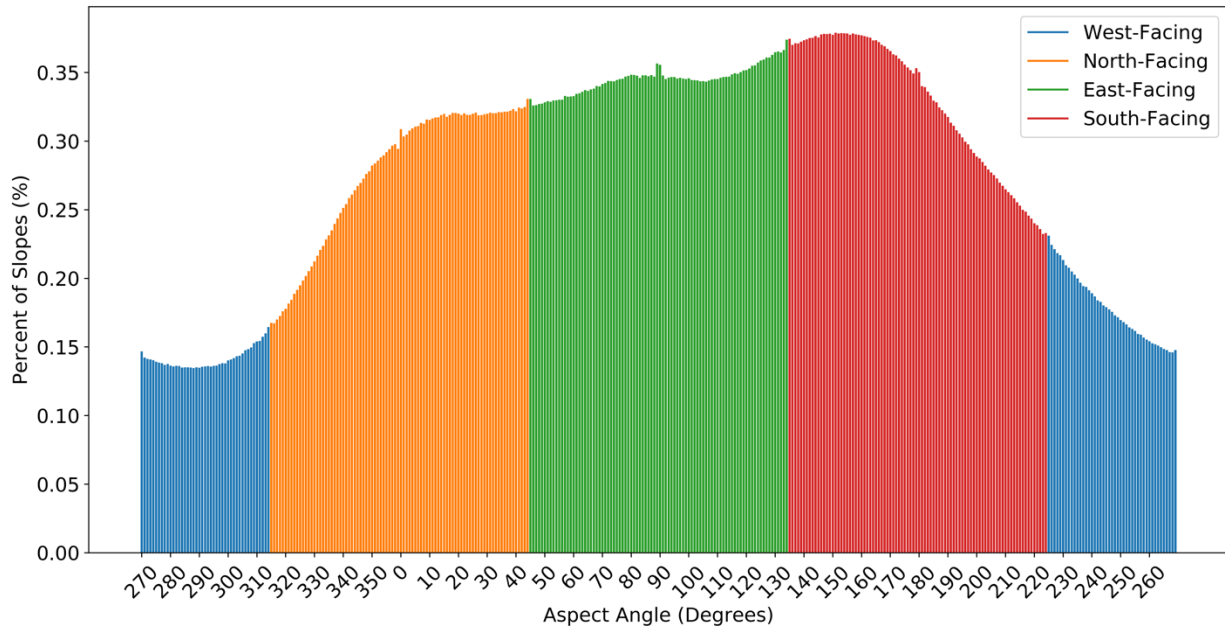
Figure 13. Aspect distribution of the Boulder Creek Watershed. 30% and 25% of slopes are south- and north-facing, respectively. The watershed generally faces east due to the north-south orientation of the Front Range mountains.
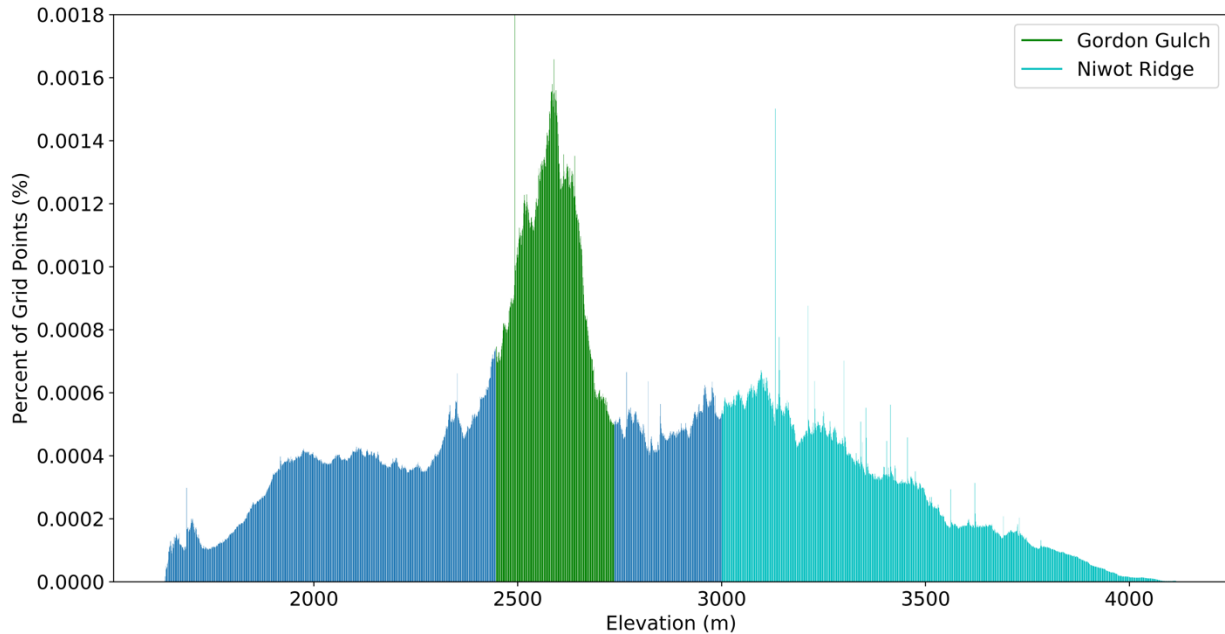

Figure 14. Elevation distribution of the Boulder Creek Watershed. Elevation ranges of the Gordon Gulch site (2446m-2737m) and the well-known Niwot Ridge site (>3000m; see Chapter IV) are identified.

		Aspect Bounds:			
		±90°	±45°	±10°	Average
South-Facing	Aspect (α)	177.9	174.0	178.7	176.9
	Slope (β)	20.7	20.6	21.8	21.0
	Elevation (m)	2566	2563	2567	2565
North-Facing	Aspect (α)	23.8	5.84	1.1	10.3
	Slope (β)	15.2	15.3	14.9	15.2
	Elevation (m)	2624	2629	2634	2629

Table 5. Estimation of slope and aspect for the north- and south-facing slopes at Gordon Gulch. For aspect bounds ±90°, south-facing (180°) grid points are considered those with aspects between 90° and 270°. For aspect bounds ±45°, south-facing (180°) grid points are considered those with aspects between 135° and 225° etc.

3.2 Soil Temperature Data

Soil temperature data are presented from sensors at 22cm beneath the soil surface on the north- and south-facing slopes at the same location as the meteorological stations [Anderson and Ragar, 2018a; Anderson and Ragar, 2018b]. Additional soil temperature measurements from soil pits at Gordon Gulch were not selected for this study because shallow (~20cm) soil temperatures were not available for both slopes, and due to the disturbed condition of the soil there. Soil temperature measurements for water years 2013-2016 are shown in Figure 15. The north-facing soil temperatures indicate persistent seasonal frost in most water years that occurs during the months of January and February, followed by a period of near-0°C soil temperatures during the months of March and April. In contrast, south-facing slope soils experience infrequent ground freezing (e.g. January 2013, January 2016), and do not experience long periods of near-0°C temperatures aside from January-February 2014.
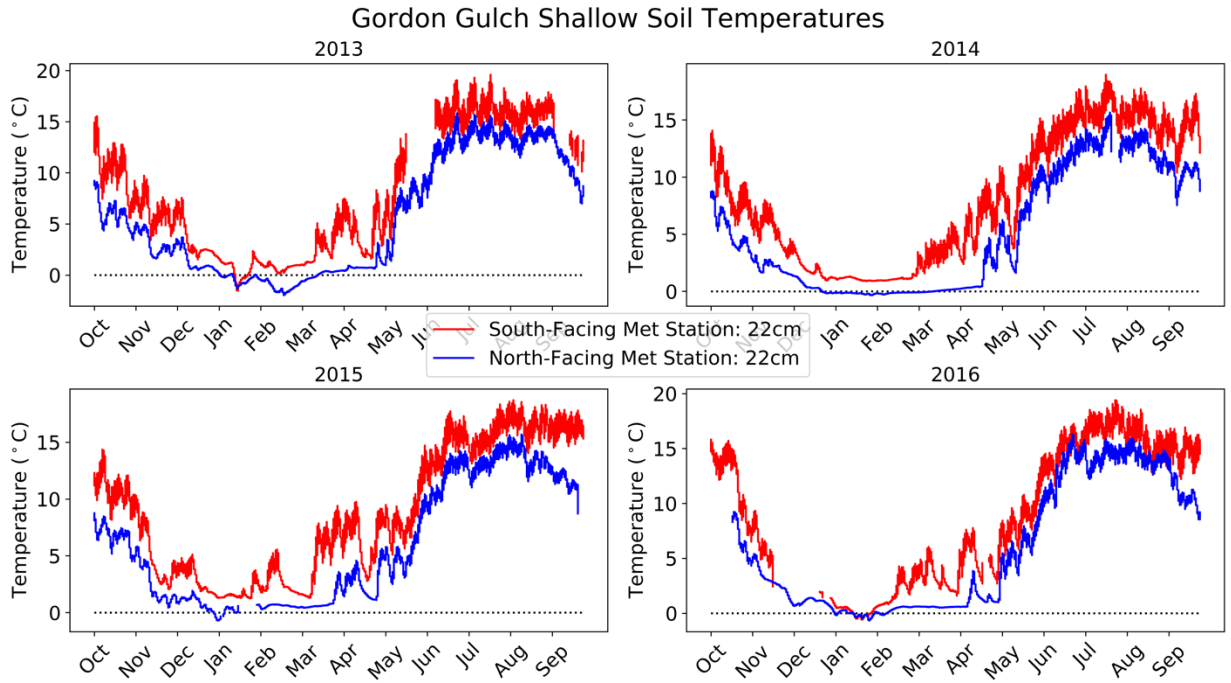
Figure 15. Measured shallow soil temperatures on the north- and south-facing slopes at Gordon Gulch. The north-facing soil temperatures at 22cm demonstrate freezing of the shallow soil during most water years; south-facing soil temperatures demonstrate infrequent ground freezing.

3.3 Meteorological Data

Meteorological data including air temperature, wind speed, incoming shortwave radiation, and net radiation are averaged hourly [Anderson and Ragar, 2018a; Anderson and Ragar, 2018b]. Rainfall data is summed hourly. When there is no meteorological data available for a model time step, an average of the remaining three years is substituted. As relative humidity data was not available for Gordon Gulch, data from the Betasso Preserve, a nearby foothills field site, was used as a proxy [Anderson et al., 2019].

3.4 Snow Depth and Snowfall Data:

Snow depth data is available at 10-minute intervals for multiple sites on each slope and are not collocated with the soil temperature measurements used in this study [Anderson and Ragar, 2018c]. Snow depth is taken as the maximum depth within the hour across all sites on each slope, and snow depth measurements are shown in Figure 16. The snowpack on the north-facing slope persists throughout the winter season, while the snowpack on the south-facing slope is ephemeral. The snowpack on the north-facing slope typically persists until early May, suggesting that the main reason for near-0°C soil temperatures throughout March and April on the north-facing slope (Figure 15, section 3.2) is the duration of the snowpack, not a "zero-curtain" effect, which traditionally refers to the time required for phase changes in soil water during soil freezing and thawing. On the south-facing slope, higher snow accumulation during water year 2014 (maximum depth 25-30cm) produces the period of near-0°C soil temperatures throughout January and February (Figure 15, section 3.2).
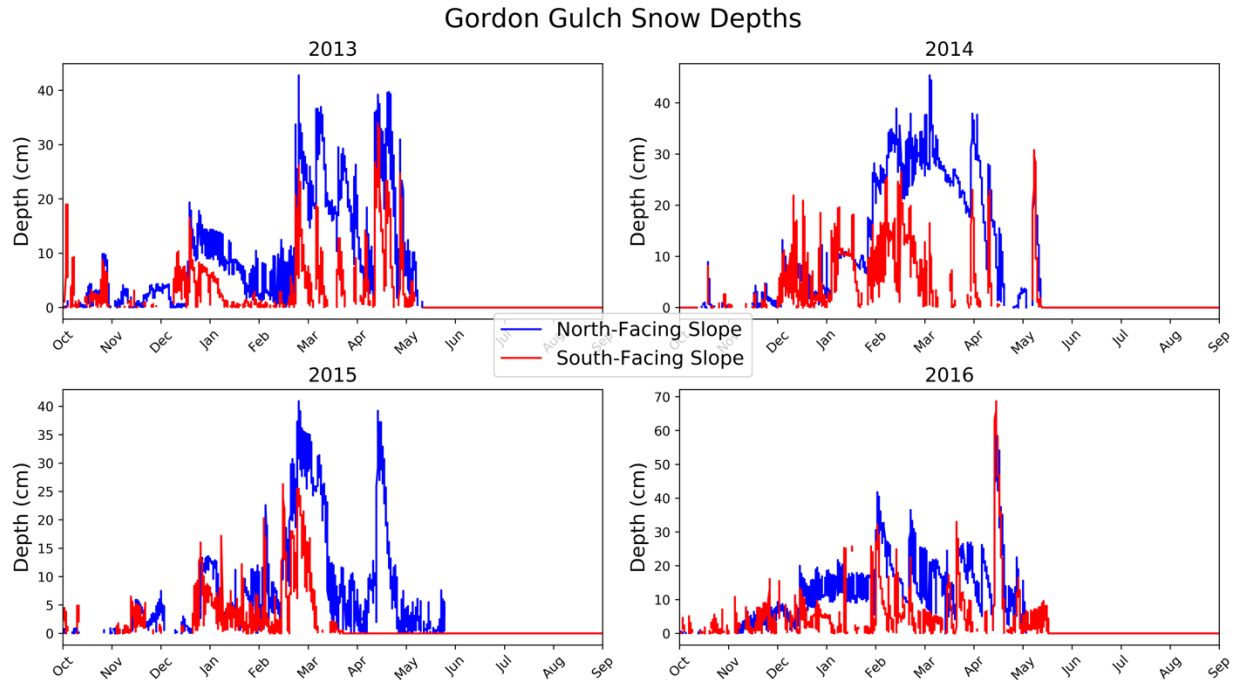
Figure 16. Hourly snow depths on the north- and south-facing slopes at Gordon Gulch. Snow depth data are available from multiple sites on each slope; for this study, snow depth is taken as the maximum depth across the sites on each slope. The snowpack on the north-facing slope persists throughout the winter season, while the snowpack on the south-facing slope is more ephemeral. A snow event observed during April 2015 on the north-facing slope was not recorded in the south-facing slope data. For this time period, the snow model on the south-facing slope was forced with snowfall data from the north-facing slope.

Although snow depth data is available at 10-minute intervals for multiple sites on each slope, no direct measurements of snowfall are available. Snowfall rate is estimated as positive changes in snow depth computed at 10-minute intervals. The 10-minute snowfall rates across the sites on each slope are integrated into an hourly snowfall rate. Snow accumulation occurring during April-May 2015 on the north-facing slope (Figure 16) is not recorded in the south-facing slope data; for this time period, snowfall estimated from north-facing slope data is used to drive the south-facing slope snow model. Snow density measurements conducted weekly during the 2008-2015 snow seasons show densities as high as 477 kg m^{-3} and as low as 3 kg m^{-3} [Anderson and Rock, 2017]. As few physically-based methods for computing fresh snow density as a function of air temperature and relative humidity are available, an iterative calibration was performed on the snowfall data in order to efficiently address the complexities involved with estimating snow density, produce a reasonable match with the snow depth and duration indicated by the data, and estimate the thermal state of the snowpack. Incoming snowfall is initially assumed to occur at the averaged measured snow density of 263 kg m^{-3}, and a snow model run is performed. The error in the modeled snow depth is used to adjust the snow density for the next iteration, until a snowfall dataset is obtained that produces a snow depth estimate that matches observations with a Nash-Sutcliffe (NS) coefficient of >0.6, for up to 2000 iterations. The Nash-Sutcliffe (NS) model efficiency coefficient is used throughout this study to characterize the accuracy of model outputs. While this statistic has traditionally been reserved for streamflow models, it is used here to characterize soil temperatures and snow depths. A NS score of 1 corresponds to a perfect match between simulations and observations, whereas a coefficient of 0 indicates that the model is no more efficient than the mean of the observations.

4.   Results

Simulations of snow depth, soil temperature, and subsurface water flow were performed for four water years (2013-2016) on the north- and south-facing slopes at Gordon Gulch. First, simulated snow depths are compared to the maximum observed snow depth across all measurement sites on each slope. Next, the one-dimensional soil heat conduction model (detailed in Chapter II, section 7.1; described briefly in Chapter III, section 2.3.2) is used to determine the factors controlling the surface energy balance at Gordon Gulch. Next, the fully coupled thermo-hydrologic model is validated by simulating shallow soil temperatures including and excluding the influence of the snowpack. Results are compared to soil temperature observations at 22cm depth. Two sets of sensitivity simulations are performed to analyze how energy balance factors (i.e. solar radiation and snowpack energy balance) control the occurrence of frozen ground. Snow depth and solar radiation were manipulated to isolate the influence of these two factors on the soil thermal regime. The magnitude and direction of wintertime subsurface water fluxes simulated by the thermo-hydrologic model are compared. Finally, a third set of sensitivity simulations is performed to determine the extent to which frozen ground alters subsurface hydrologic fluxes. Hydrologic fluxes from simulations forced with measured soil temperatures are compared to fluxes from "control" simulations, in which the soil is prevented from freezing by setting any temperatures below 0°C to 0°C. Throughout this section, the Nash-Sutcliffe (NS) model efficiency coefficient is used to characterize the accuracy of model outputs. While this statistic has traditionally been reserved for streamflow models, it is used here to characterize soil temperatures and snow depths. A NS score of 1 corresponds to a perfect match between simulations and observations, whereas a coefficient of 0 indicates that the model is no more efficient than the mean of the observations.

4.1 Snow Depth

Snow model results are presented in Figures 17 and 18. Snow model outputs are compared to daily-averaged snow depth data. The model produces a good match with observed snow depth and duration. In particular, the model sufficiently resolves the differences in snow accumulation on the north- and south-facing slopes. Aside from periods of very thin snow cover (e.g. Nov-Dec 2013, May 2015), the duration of seasonal snow is reproduced well on the north-facing slope. Modeled snow depths on the north-facing slope display a bias towards high depths between snowfall events when the snowpack is accumulating during the winter (e.g. January 2013, February 2016). This is likely a consequence of ignoring wind redistribution and snow compaction, which are not included in the snow depth calculation. To a much lesser extent, the model occasionally simulates more rapid snowmelt than is observed in the data during the spring (e.g. March-April 2016). This is likely a consequence of underestimating the magnitude of snowfall because of near-simultaneous melt that confounds the computation of snowfall from changes in snow depth. That is, an observed change in snow depth is influenced by both snow inputs and melt outputs from below. The south-facing slope features a thin snowpack that melts rapidly, and the model suffers from the same "spring" bias as the north-facing slope. For example, water year 2016 was characterized by many small snow events that are challenging to model due to the near-simultaneous occurrence of melt.
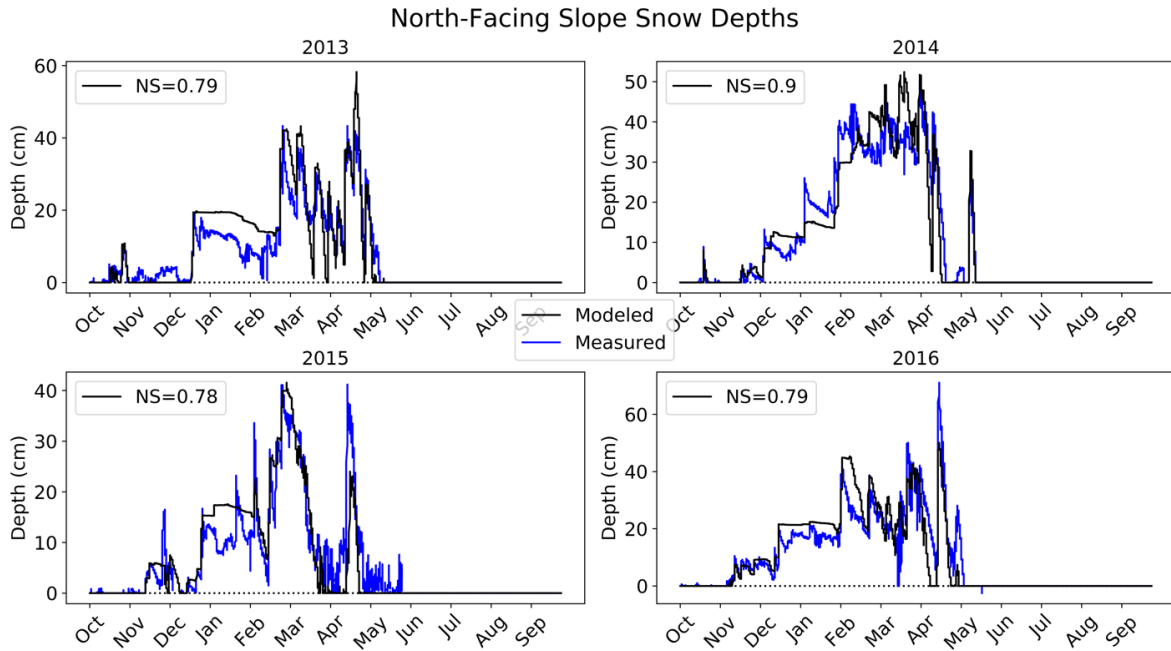
Figure 17. Daily-averaged measured (blue) and modeled (black) snow depths on the north-facing slope. Simulations produce a reasonable match to observed snow depths; during all years the model achieves a Nash-Sutcliffe coefficient greater than 0.78.
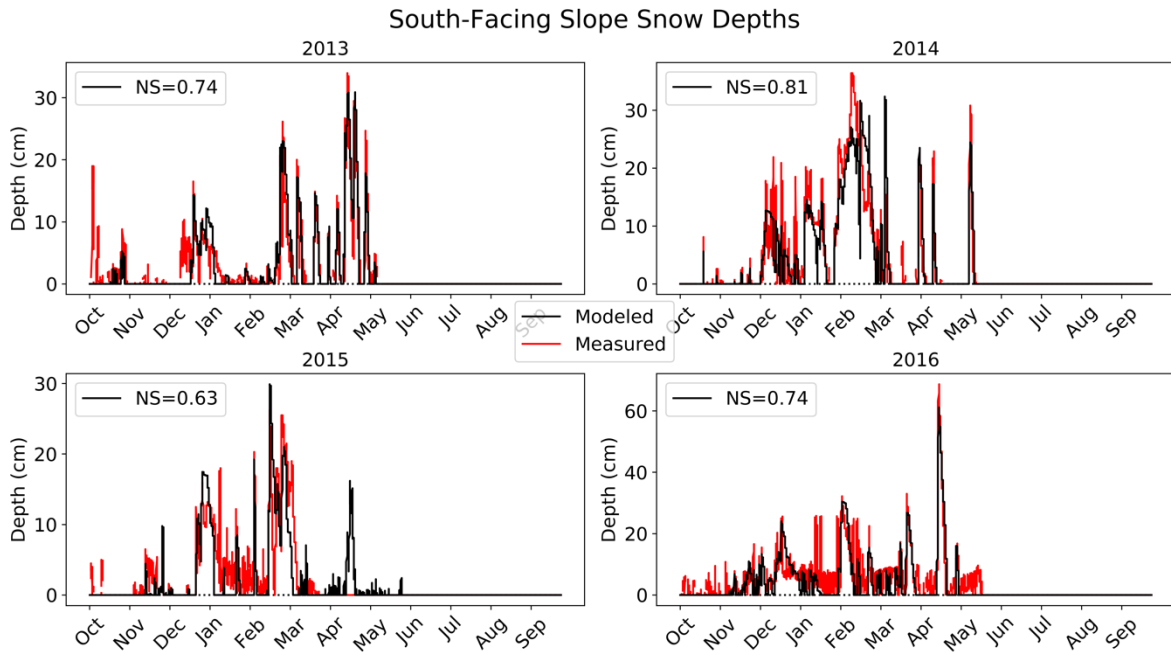

Figure 18. Measured (red) and modeled (black) snow depths on the south-facing slope. Simulations produce a reasonable match to observed snow depths; during all years the model achieves a Nash-Sutcliffe coefficient greater than 0.63. A snow event observed during April 2015 on the north-facing slope was not recorded in the south-facing slope data; thus, the model was forced with snowfall data from the north-facing slope during that period. April and May 2015 were excluded from the Nash-Sutcliffe coefficient calculation.

4.2 One-Dimensional Soil Temperature Modeling

In this section, soil temperatures simulated by the one-dimensional soil heat conduction model (detailed in Chapter II, section 7.1; described briefly in Chapter III, section 2.3.2) are compared to measured soil temperatures in order to determine the factors controlling the energy balance at Gordon Gulch. The subsurface thermo-hydrologic model PFLOTRAN-ICE was not used for the results in this section. The goal of the simulations presented in this section is to validate the surface energy balance model and to provide an analysis of the influence of environmental factors (especially aspect) at Gordon Gulch. By evaluating the sensitivity of a purely conductive soil temperature model to surface boundary conditions, surface energy balance forcing, and snowpack influence, these simulations serve as a "screening" exercise to establish the important factors to consider in the full thermo-hydrologic modeling presented in Section 4.3. Four sets of boundary conditions are compared (Table 6).

Set	Figure	Conceptual Description	Soil Surface Boundary Condition	
			No Snow Present	Snow Present
1	19	Standard Approach	Specified Temperature $T_{z=0m} = T_{air}$	
2	20	Addition of Snowpack	Specified Temperature $T_{z=0m} = T_{air}$	$T_{z=0m} = T_{snow}$
3	21	Full Surface Energy Balance During Snow-Free Periods	Specified Flux $-\kappa \dfrac{dT_{z=0m}}{dz} = Q_{sn} + Q_{ln} + Q_h + Q_e$	Specified Temperature $T_{z=0m} = T_{snow}$
4	22	Addition of Evapotranspiration Heat Term on North-Facing Slope	Specified Flux $-\kappa \dfrac{dT_{z=0m}}{dz} = Q_{sn} + Q_{ln} + Q_h + Q_e + Q_{ET}$	Specified Temperature $T_{z=0m} = T_{snow}$

Table 6. Boundary conditions used in one-dimensional soil heat conduction modeling.

The model forced at the soil surface with measured air temperatures (Figure 19) significantly overestimates the occurrence of soil freezing and, to a much smaller extent, overestimates summer soil temperatures on the north-facing slope (Figure 19a). When the influence of the snowpack is included in the specified surface temperature condition (Figure 20), winter soil temperature estimates significantly improve on both slopes. However, during snow-free periods (snow data shown in Figure 16), the specified air temperature condition significantly overestimates soil freezing on the south-facing slope (e.g. January 2013, January 2014, November 2015, January 2016) and to a lesser extent on the north-facing slope (e.g. November 2015).

When the full surface energy balance is incorporated into the model using a specified-flux condition during snow-free periods (Figure 21), winter soil temperature estimates improve on both slopes (Figure 21). However, the model using a specified-flux condition during snow-free periods was found to overestimate summer temperatures significantly on the north-facing slope (Figure 21a), leading to a large decrease in NS scores between Figures 20b and 21b. The model slightly overestimates summer temperatures on the south-facing slope (Figure 21b), leading to a small decrease in NS scores between Figure 20b and 21b, despite a better match to winter temperatures. To account for the missing heat sink on the north-facing slope, energy associated with evapotranspiration Q_{ET} (25) was added to the surface energy balance in on the north-facing slope. The south-facing slope is significantly less forested than the north-facing slope (Figure 4) and does not exhibit evidence of significant evapotranspirative heat loss. Although this term is required to account for the surface energy balance on the north-facing slope, uncertainties in the estimation of Q_{ET} lead to slight decreases in NS scores from Figure 20a to Figure 22a during water years 2013, 2014, and 2016, with a slight increase in 2015, which suffered most from the cold bias during snow-free periods described above (November 2015, Figure 21a). Since the goal of soil temperature modeling efforts is accurate simulation of soil freezing, the combined

boundary condition incorporating the snowpack and the full surface energy balance during

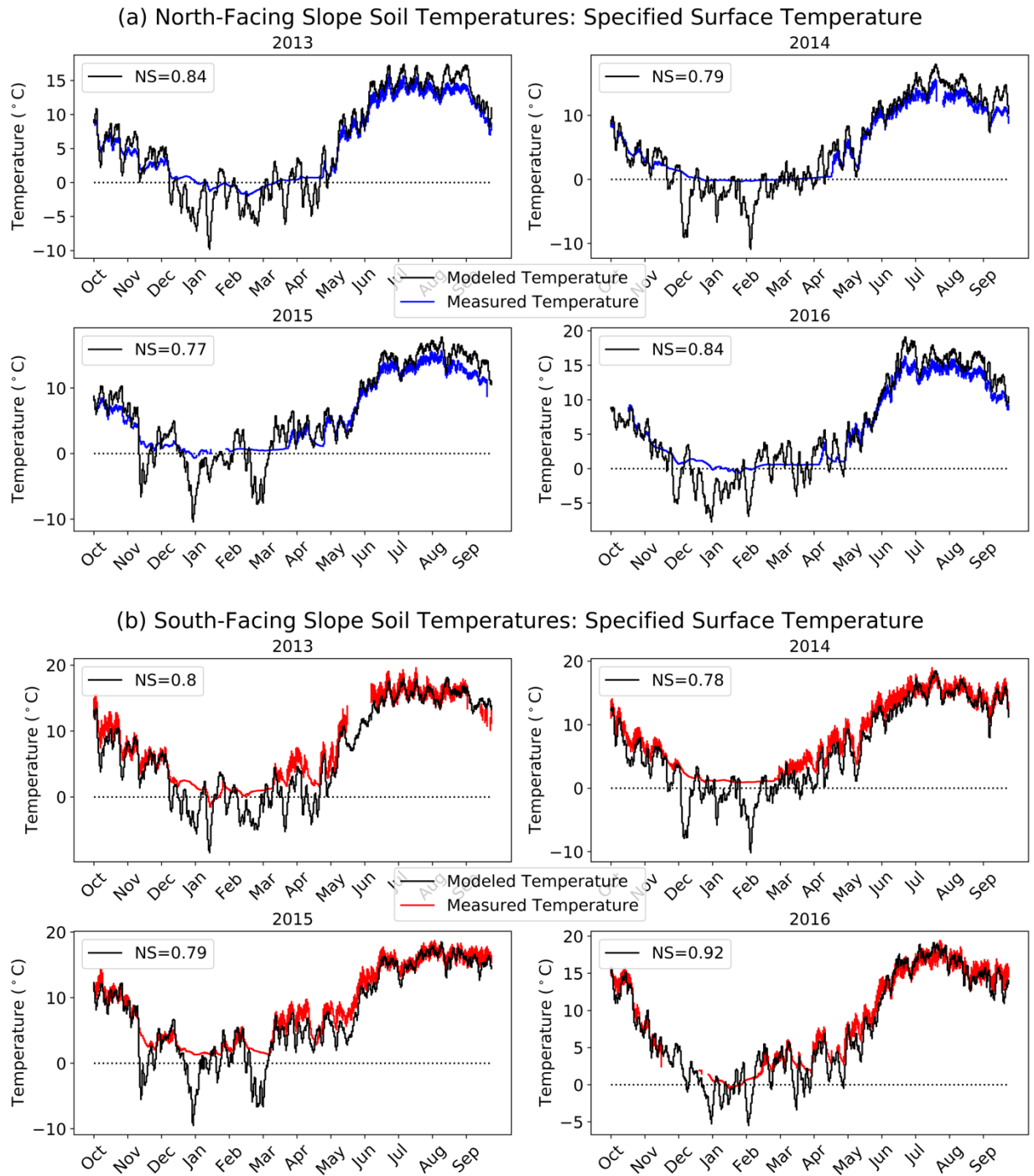snow-free periods was selected for the simulations presented in the remainder of this

thesis.

Figure 19. Soil temperature estimates (black) compared to data from the north-facing slope (blue – a) and south-facing slope (red – b) at 22cm depth. Soil surface temperature is specified as the measured air temperature. Winter soil temperature are significantly underestimated using the specified surface temperature boundary condition.
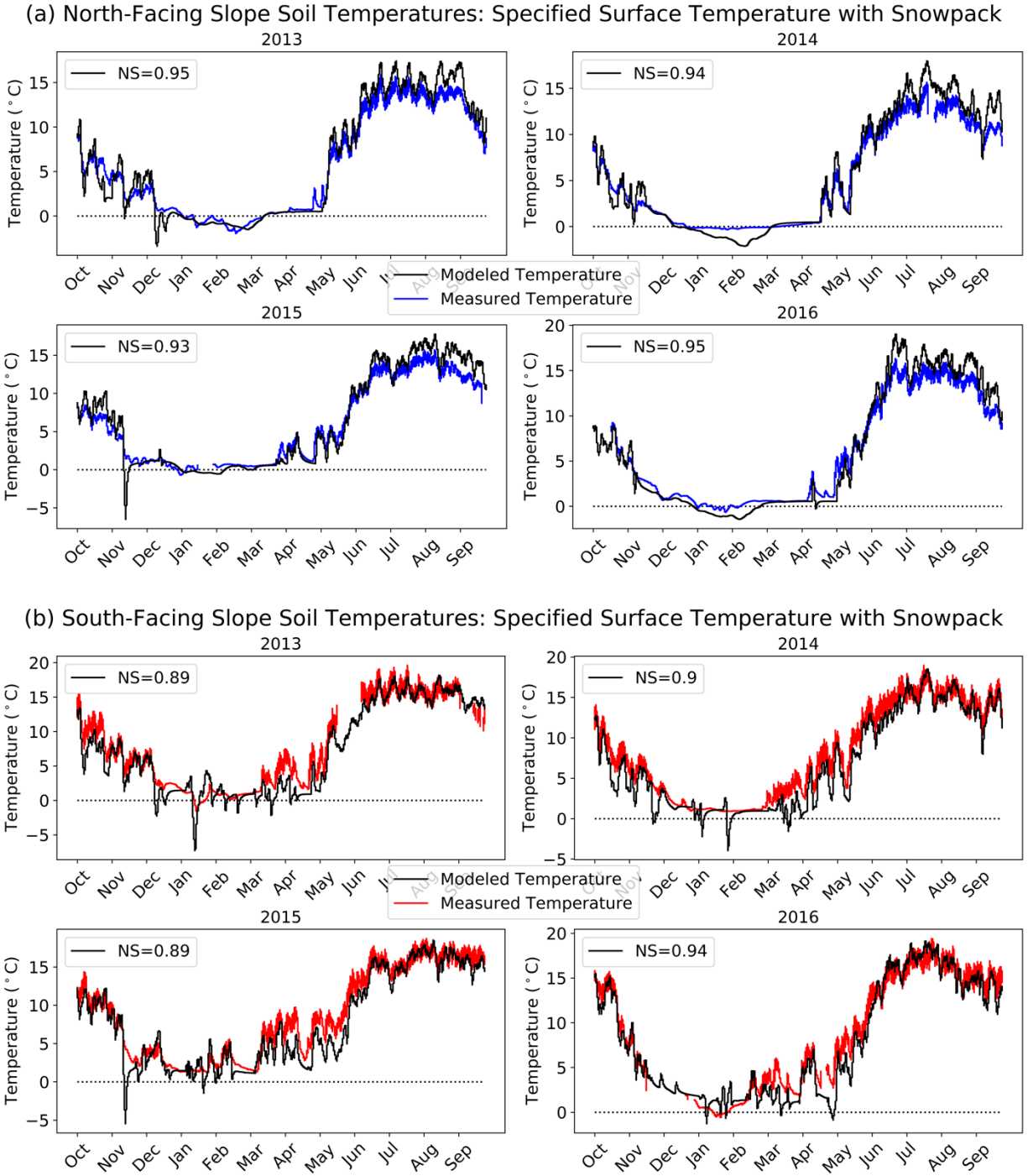
Figure 20. Soil temperature estimates (black) compared to data from the north-facing slope (blue – a) and south-facing slope (red – b) at 22cm depth. Soil surface temperature is specified as the modeled snowpack temperature when snow is present and measured air temperature when snow is not present. Winter soil temperature estimates are significantly improved by incorporating the snowpack, but temperatures are underestimated during snow-free periods.
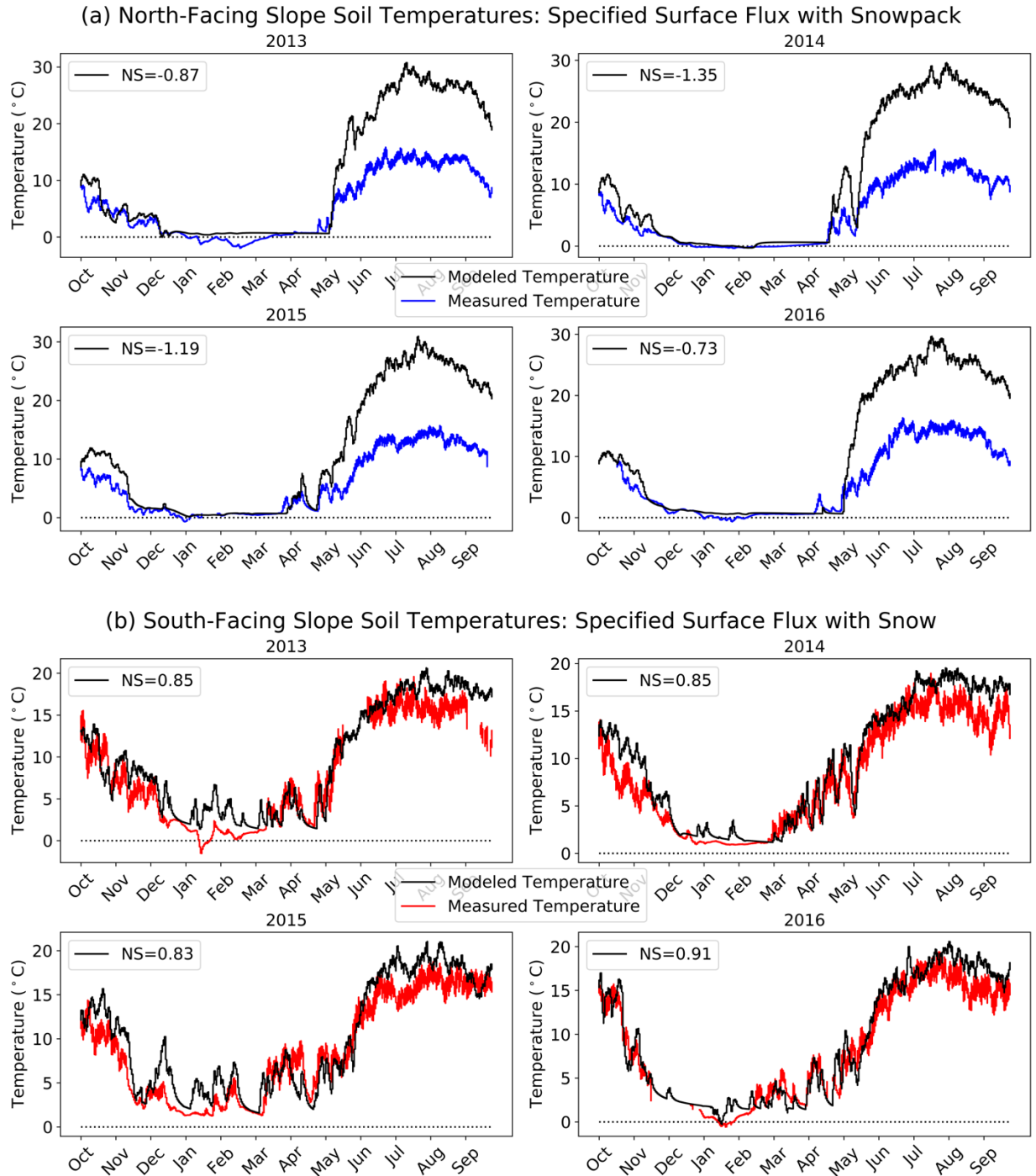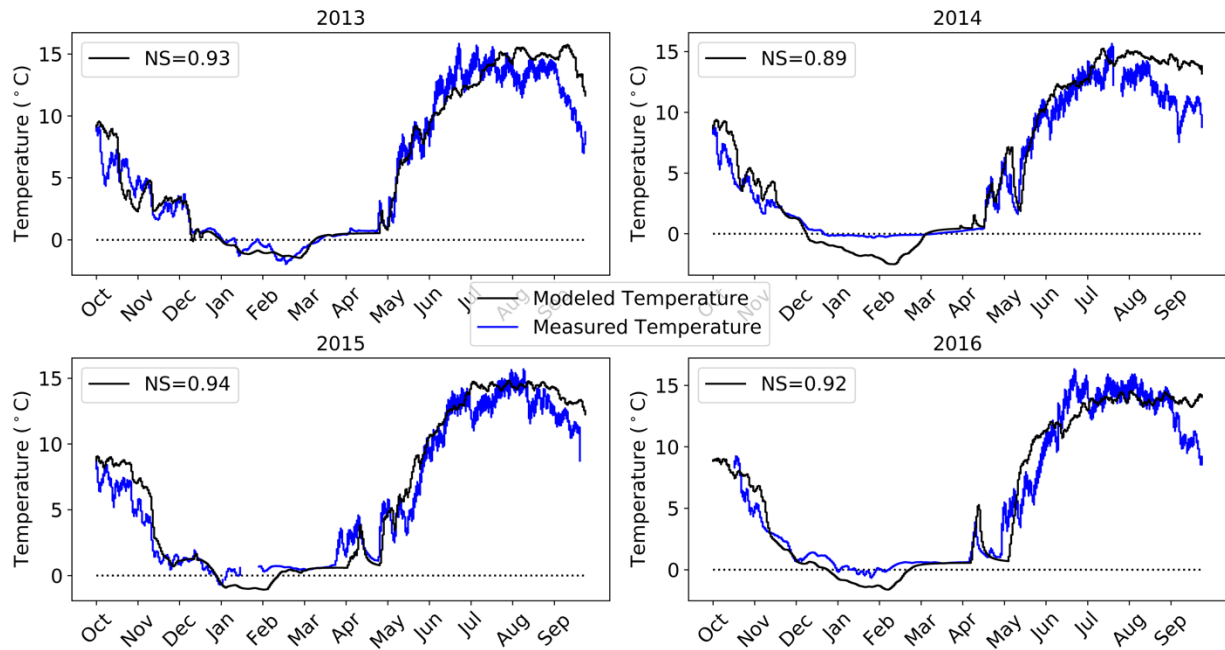
Figure 21. Soil temperature estimates (black) compared to data from the north-facing slope (blue – a) and south-facing slope (red – b) at 22cm depth. Soil surface boundary condition is specified as the snowpack temperature when snow is present and specified surface heat flux (modeled) when snow is not present. Winter soil temperature estimates are improved by incorporating the snowpack and bare soil surface energy balance on both slopes, but summer temperatures are dramatically overestimated on the north-facing slope, and slightly overestimated on the south-facing slope.
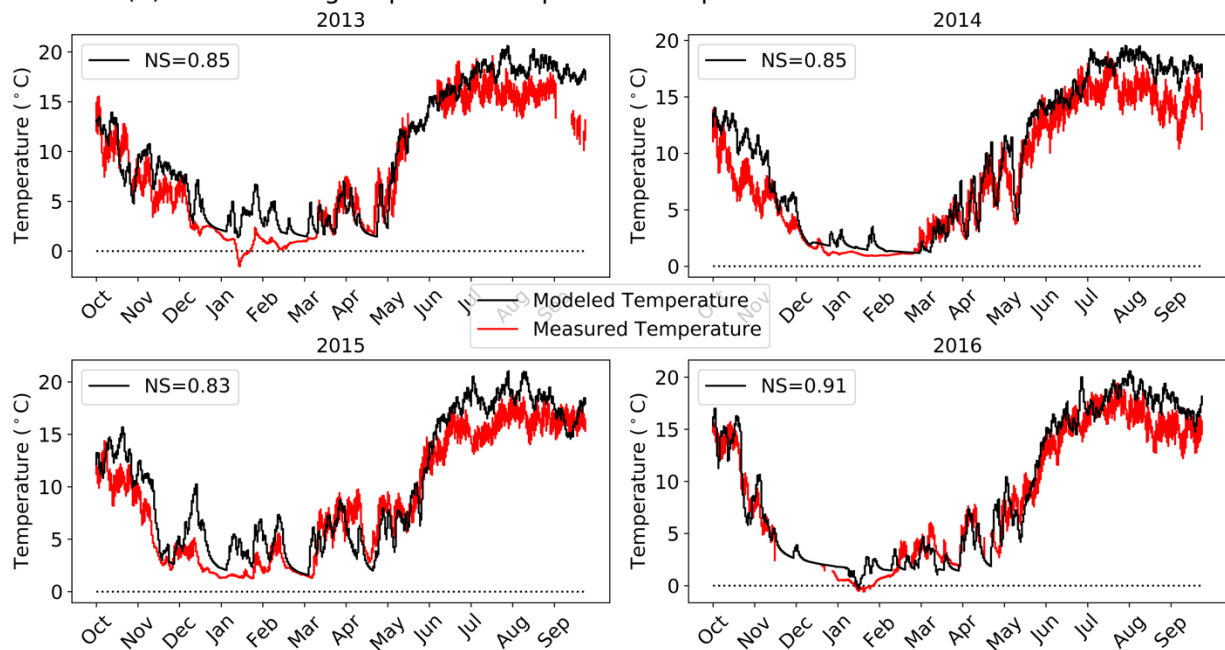
Figure 22. Soil temperature estimates (black) compared to data from the north-facing slope (blue – a) and south-facing slope (red – b) at 22cm depth. Soil surface boundary condition is specified as the snowpack temperature when snow is present and specified surface heat flux (modeled) when snow is not present. The model incorporating the snowpack, surface energy balance, and evapotranspirative heat loss on the north-facing slope achieves the best match to winter temperatures, and a reasonable match to summer temperatures.

4.3 Soil Temperatures from Coupled Thermo-Hydrologic Model:

Next, soil temperatures from the coupled thermo-hydrologic model are presented in Figures 23 and 24, and meteorological station soil temperature data are used to compute NS scores to compare model performance between the two slopes. In comparison to soil temperatures from the one-dimensional model presented in section 4.2, the soil thermal diffusivity is higher in the coupled thermo-hydrologic model due to the presence of water and ice. A comparison of simulations including and excluding the snowpack demonstrates that incorporating the thermal effects of the snowpack significantly improves estimates of soil temperatures during every water year on the north-facing slope (NS score increases by 0.30-0.58). Simulations that account for the snowpack improve predictions of soil temperatures and major seasonal trends on the north-facing slope. In particular, duration of soil freezing in March and April is reproduced very well by simulations that include snow. In the no-snow simulations, soils have thawed by early March, and temperatures rise throughout March and April. In the snow simulations, soils remain near freezing throughout March and April, in agreement with observations. Although soil freezing duration may not exert a strong control on hydrology and subsurface flow paths in the mid-elevation montane zone, the seasonal onset of above-zero soil temperatures in the shallow subsurface influences soil microbial activity and vegetation growth.

To a small extent, modeled "zero-curtain" temperatures on the north-facing slope track systematically below observed "zero-curtain" temperatures. Here, the term "zero-curtain" is used loosely, because the persistence of near-0°C soil frost in this case is due to the presence of the snowpack more than the latent-heat barrier. Since the *duration* of soil frost is simulated accurately by the model, but not the *temperature,* we suggest that this discrepancy is probably unrelated to thermal diffusivity. Rather, the soil characteristic curve, which is used by the subsurface model to calculate both the soil water content as a function of capillary pressure as well as soil water content as a function of temperature

[Painter and Karra, 2014], likely overestimates freezing point depression compared to the actual soil.

During water years 2014 and 2016, the model underestimates winter (January-March) temperatures, which in the data track relatively close to 0°C, whereas in water year 2013, soil temperatures during the same period are reproduced relatively well. As snow depth is simulated relatively accurately during these time periods, it is unlikely that snow model errors contributed to this result. The snowpack remains relatively thin (approximately 15-20cm) in January 2013, 2014, and 2016, indicated by both modeled and measured snow depths, so it is surprising that the data indicate less intense soil freezing in January 2014 and 2016 than in January 2013. The "no-snow" simulations in Figure 23 indicate that the surface energy balance is relatively consistent during these time periods and that there is no shortage of cold content from the atmosphere, suggesting differences in snowpack composition (e.g. density, layering), which are not allowed to vary within the model. Thus, future efforts to simulate the influence of the seasonal snowpack on ground temperatures may benefit from a more rigorous representation of snow deposition and layering, snow density evolution, and consequent heterogeneity in thermal properties such as heat capacity and thermal conductivity.

On the south-facing slope, a comparison of simulations including and excluding the snowpack demonstrates that incorporating the thermal effects of the snowpack improves estimates of soil temperatures during all water years. During all water years on the south-facing slope, simulations including snow produce a significantly better match to observed temperatures than snow-free simulations (NS score increases by 0.15-0.43). Generally, since the south-facing slope experiences ephemeral snow cover, it is expected that the soil thermal regime is not as strongly controlled by snowpack dynamics as the north-facing slope, which experiences significant snow accumulation. The model slightly overestimates summer soil temperatures, as the soil temperature measurements are taken from a flat

terrace on the steep south-facing slope, whereas the goal of the modeling was to simulate

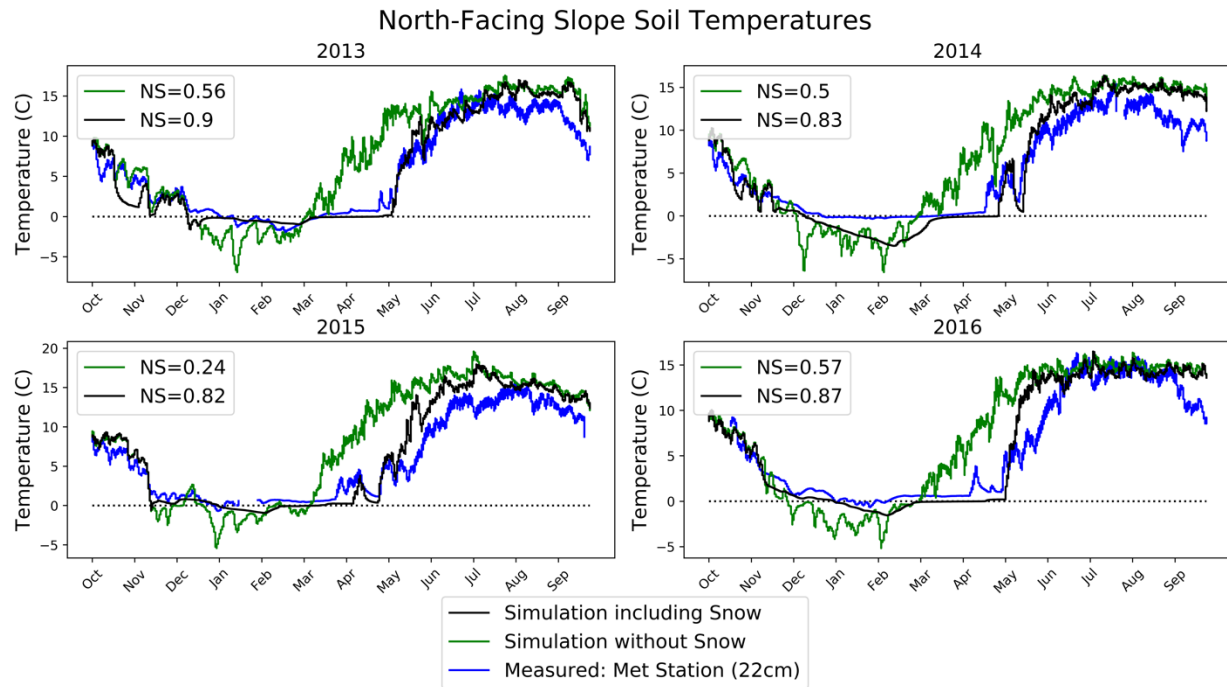the soil temperature behavior of the hillslope as a whole.

Figure 23. Modeled (22cm) and measured (22cm) soil temperatures on the north-facing slope. Simulations including snow (black) demonstrate a better match (NS score increases by 0.30-0.58) to observed temperatures (blue) than simulations excluding snow (green), with especially accurate estimates of the duration of soil frost in the spring, while simulations excluding snow produce much colder temperatures (more freezing) in winter and overestimate ground warming in late spring/early summer.
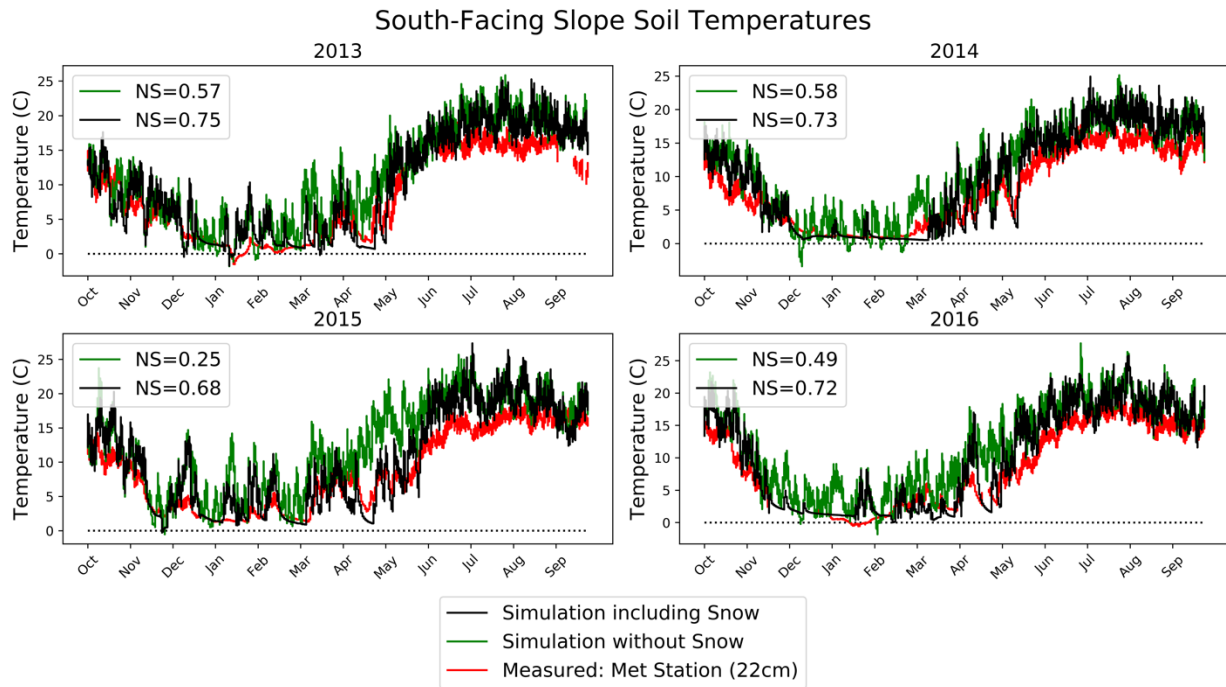
Figure 24. Modeled (at 22cm) and measured (at 22cm) shallow soil temperatures on the south-facing slope. Both simulations including (black) and excluding snow (green) match observed temperatures (red) well with high Nash-Sutcliffe efficiencies. The model excluding snow produces a significantly better match to observed temperatures during all water years (NS score increases by 0.15-0.43). The model slightly overestimates summer soil temperatures, as the soil temperature measurements are taken from a flat terrace on the steep south-facing slope, whereas the goal of the modeling was to simulate the soil temperature behavior of the hillslope as a whole.

4.4 Energy balance factors controlling the incidence of frozen ground:

Sensitivity simulations are performed to analyze how aspect differences in solar radiation and the snowpack energy balance influence the incidence of frozen ground.

4.4.1   Snowpack:

It is generally accepted that in high-latitude regions where snow cover is typically present when air temperatures are low, a thick snowpack insulates the ground and prevents the formation of frozen ground [Zhang, 2005]. In regions that experience SFG, field evidence demonstrates that, compared to a deep snowpack, a thin or absent snowpack permits thermal coupling between the ground and atmosphere, increasing the frequency and intensity of frozen ground compared to a deep snowpack, while reducing the duration [Fuss et al., 2016; Sarady and Sahlin, 2016; Bayard et al., 2005; Hardy et al., 2001]. Various "rules of thumb" suggest that snow depths greater than 30-50cm [e.g. Hill et al., 2019] act to decouple the ground from the atmosphere (see section 1). Since the maximum snow accumulation on the north-facing slope of Gordon Gulch is typically around 40cm and winter temperatures often rise above 0°C, this site serves as a prime example of this phenomenon for the case of snow depth influence in low-latitude regions. Simulations were performed with different snowfall rates to evaluate the influence of snow depth. The snowfall rate of the original base case simulation (Figure 17) was multiplied by factors of 0, ½, and 2; the resulting soil temperatures are presented in Figure 25a.

The 0-snow case results in the highest intensity, but lowest duration of soil freezing, in agreement with the field observations discussed above. Dividing snowfall by two produces lower soil temperatures than in the 1X and 2X snow cases, while multiplying by two prevents frozen ground almost entirely (exceptions include December 2013; January-February 2014; February 2016). These results suggest that the typical snowpack at Gordon

Gulch is thin enough to allow soil freezing, but that twice the amount of snowfall would prevent frozen ground from occurring.

Another consequence of changing the snow depth is to shift the timing of soil thaw in the spring. Manipulating snowfall results in significant shifts in the duration of the snowpack: increasing snowfall by a factor of two extends the duration of soil freezing by approximately three months compared to the simulation in which snowfall is reduced by a factor of two. Snow that accumulates to greater depths simply requires more time to melt completely. Such differences may shift the duration of subnivial (beneath-the-snow) soil microbial activity and the onset of plant growth in the spring, as well as associated biogeochemical processes.

Air temperatures are superimposed on soil temperature results in Figure 25b in order to provide context for the influence of snow depth on thermal coupling between the ground and atmosphere. From December - February, snow primarily occurs during periods of sub-0°C air temperatures; during this period, the thin snowpacks of the 0.5X and 1X cases permit heat loss from the soil and soil freezing, whereas the thick snowpack of the 2X case prevents heat loss from the soil and soil freezing (except for brief time periods noted above). From March-May, air temperatures are primarily above 0°C, and the thin snowpacks of the 0.5X and 1X cases allow underlying soils to thaw in April, whereas the thick snowpack of the 2X case prevents the ground from thawing until late May. Thus, the thick snowpack of the 2X case acts to warm the ground during December-February and cool the ground during March-May, compared to the thin (0.5X and 1X) and absent (0X) snowpack cases. That is, the influence of thick snowcover on ground temperatures strongly depends on the air temperatures from which the ground is being insulated, as other authors have noted [Zhang, 2005; Bartlett et al., 2004].
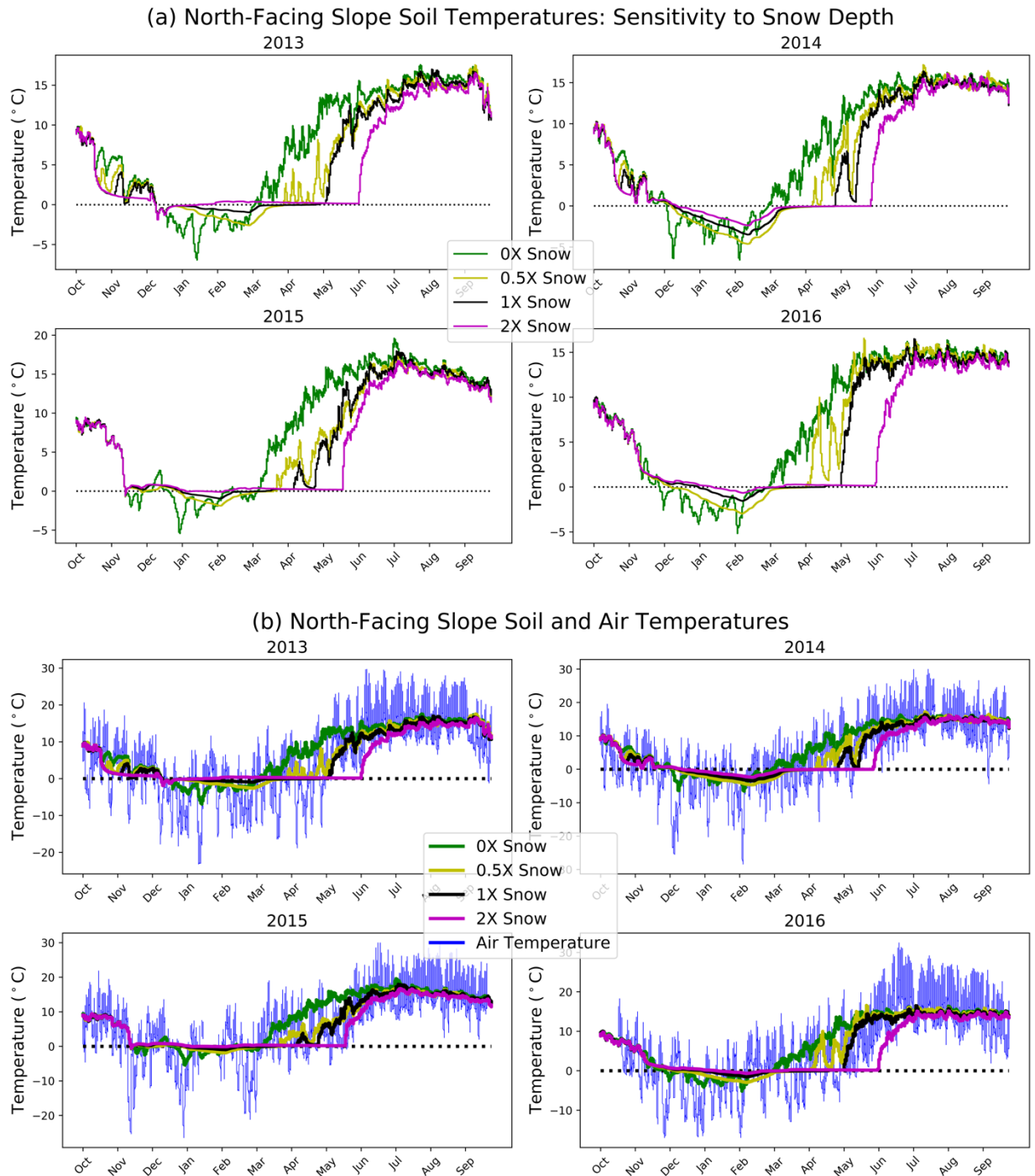
Figure 25. Sensitivity of modeled soil temperatures (22cm) to snow depth based on simulations in which snowfall on the north-facing slope was multiplied by a scaling factor. Soil temperature results are presented in (a), and measured air temperatures are superimposed on soil temperature results in (b). Increasing the snowpack depth extends the duration of soil frost in the spring, while decreasing the snowpack depth increases the incidence of sub-freezing temperatures during the winter.

4.4.2 Solar Radiation:

In the previous section, we determined that when the snowpack is removed from the north-facing slope, the model predicts a higher intensity, but shorter duration of frozen ground. However, the south-facing slope does not allow for persistent frozen ground occurrence despite an ephemeral snowpack and exposure of bare soil to the atmosphere. We hypothesize that this is due to the higher solar insolation (compared to the north-facing slope), which prevents frozen ground formation despite exposure of bare soil to the atmosphere. In order to examine this further, a simulation is performed on the south-facing slope forced by the solar insolation received by the north-facing slope (including the effects of its poleward orientation, canopy shading, and horizon shading). In the perturbed simulation, lower solar radiation allows the snowpack to accumulate more than in the original simulation. Soils freeze persistently during December-February in water years 2013-2015 and briefly during water year 2016 because of low solar radiation during snow-free periods. Summer temperatures are relatively similar between the simulations because canopy shading on the north-facing slope, which consists of evergreen forest, is stronger during the winter than during the summer, leaving only horizon shading and aspect differences. In the winter when solar angles are low, incoming radiation is intercepted by many more trees than during the summer when solar angles are high and incoming radiation is intercepted only by the canopy directly above the ground. The results demonstrate that the higher insolation received on the south-facing slope compared to the north-facing slope explains why it does not experience prolonged seasonally frozen ground during snow-free periods.
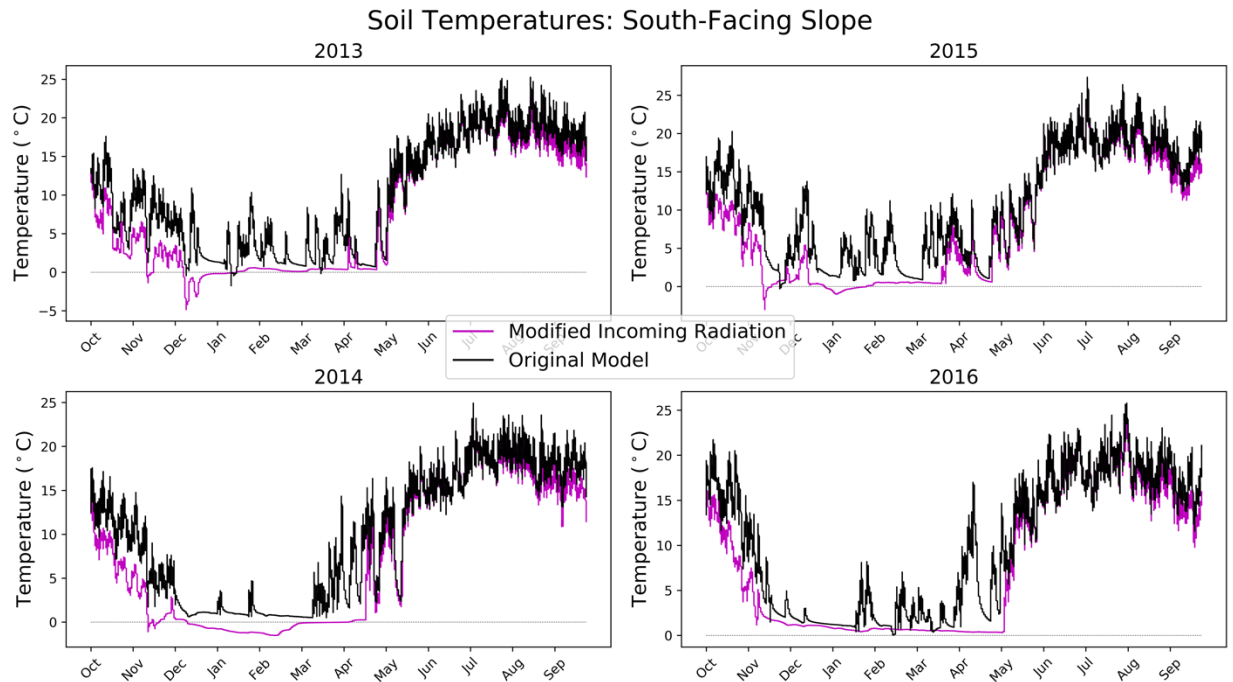
Figure 26. Sensitivity of modeled soil temperatures (at 22cm) to incoming solar radiation on the south-facing slope based on a simulation in which the south-facing slope was forced with the insolation received by the north-facing slope. Reducing the incoming radiation on the south-facing slope induces soil freezing, indicating that the fundamental reason the south-facing slope does not typically experience persistent frozen ground is due to higher solar insolation.

4.5 Hydrologic Consequences of Frozen Ground Occurrence:

Modeled soil moisture and subsurface fluxes simulated using both measured and modeled soil temperatures are used to understand differences in subsurface flow and water content between the north- and south-facing slopes and determine the extent to which frozen soils influence hydrologic processes. Subsurface soil moisture and fluxes simulated using modeled soil temperatures during the winter season are presented in Figure 27. These results include a variety of hydrologic factors that influence subsurface water content: shallow soil freezing, snowmelt timing and magnitude, and overland flow generation. Thus, Figure 27 provides an integrated view of the hillslopes and their hydrologic differences. Generally, the south-facing slope is characterized by higher deep (at depths > 1m) subsurface water content than the north-facing slope. Vertical infiltration through the shallow soil (at depths < 1 m) followed by lateral flow through the deep subsurface (at depths > 1 m) is evident on the south-facing slope, whereas the combined effects of soil freezing and snowmelt timing limit wintertime vertical infiltration through the shallow soil (at depths < 1 m), reducing the contribution from the shallow infiltration to deep subsurface flux, which is primarily lateral. Shallow soil freezing creates pressure gradients that drive flow toward the soil surface on the north-facing slope during water years with significant freezing (water years 2013 and 2014). The effects of evapotranspiration on subsurface water content and fluxes are not simulated in the model.
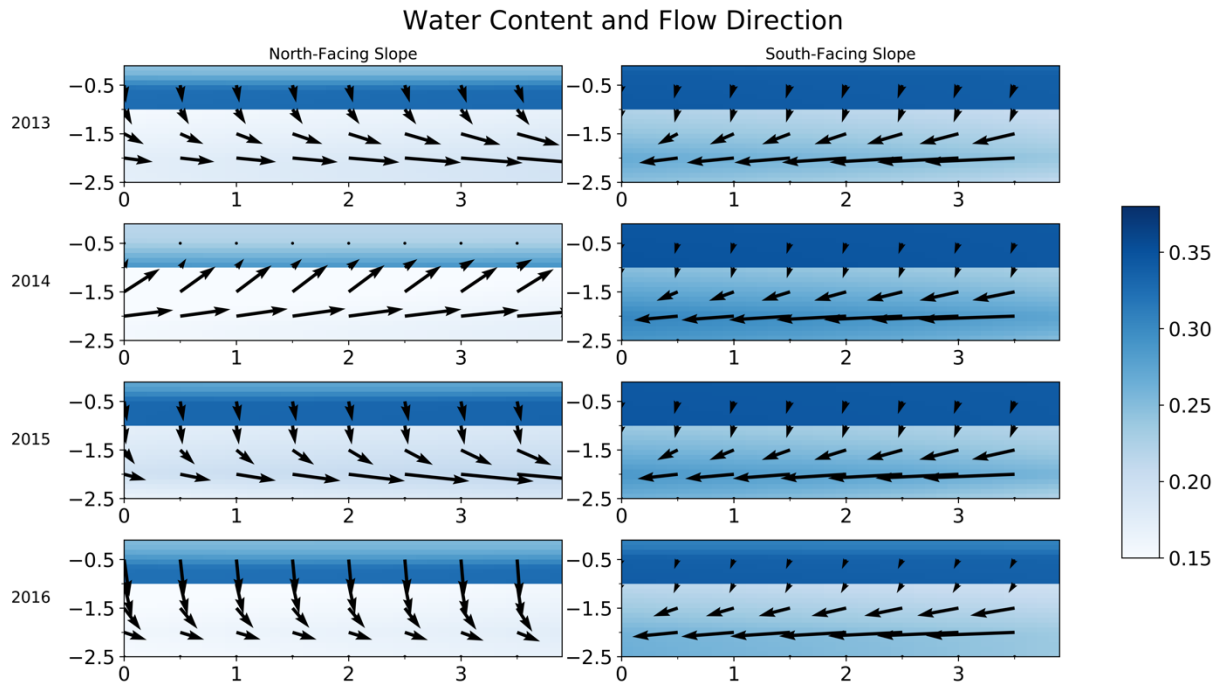
Figure 27. Modeled soil moisture content (blue color scale) and subsurface liquid water flux (arrows) at depths $0 - 2.5$ m below the ground surface averaged across the winter season. Note that soil moisture content is defined based on liquid water content. Horizontal axes are selected to mimic the orientation of the hillslopes in relation to the stream channel: water flows downslope toward the center of the figure (left-to-right on the north-facing slope; right-to-left on the south-facing slope). The slope of the hillslopes is not represented in this figure. The stark difference in soil moisture evident between depths of $0 - 1$ m and $1 - 2.5$ m is related to model layers: the moisture retention function used in the "soil" layer ($0 - 1$ m) corresponds to a higher moisture content than that used in the deeper layers ($1 - 2.5$ m). The low (liquid) moisture content in the shallow soil on the north-facing slope is produced by the displacement of liquid water by ice. Upward fluxes (e.g. north-facing slope water year 2014) are due to cryosuction, which draws water to the freezing front.

In this section, the influence of frozen ground on hydrology at Gordon Gulch is analyzed using the model and three sets of soil temperature observations from the north-facing slope, for a total of four analyses: (1) modeled soil temperatures, (2) 22cm depth meteorological station data introduced in section 3.2 [Anderson and Ragar, 2018a], (3) 20cm soil temperatures from soil pits in lower Gordon Gulch [Anderson et al., 2020], and (4) 16cm soil temperatures from measurements in upper Gordon Gulch [Anderson and Ragar, 2020]. For the simulations using data, the soil temperature data at 16cm-22cm depth are imposed as a soil surface boundary condition for the subsurface model. Simulations including the formation of frozen ground were compared to simulations in which the soil is prevented from freezing by setting any sub-zero temperatures to 0°C. This approach serves to quantitatively evaluate the influence of frozen ground in the absence of other hydrologic factors such as snowmelt magnitude and timing, as well as overland flow generation. The cumulative flux into the hillslope at 50cm depth for simulations including and excluding ice is presented in Figure 28.

This analysis reveals significant interannual and spatial variability in the influence of frozen ground on infiltration, which has been noted in previous studies [Fuss et al., 2016; Bayard et al., 2015]. At all three measurement locations (Figure 28 b-d) and the model (Figure 28 a), the incidence of frozen ground reduces infiltration significantly during water year 2013, which featured more intense soil freezing than any other water year. During all other water years in (b) and (d), frozen ground does not affect infiltration significantly. At the soil pit site (c), some influence of frozen ground is simulated in water years 2014-2016, a reflection of the disturbed nature of the soil pit. The model simulates frozen ground influence in water years 2014 and 2016 due to an underestimation of shallow soil temperatures, which has been discussed in section 4.3.

In water year 2013, frozen ground reduced infiltration most strongly at the soil pit site, followed by the model, followed by the Upper Gordon Gulch site, followed by the

meteorological station site. These differences are simply related to the intensity of soil freezing, which varies due to microclimatic conditions such as snow depth and canopy shading. While the soil temperature measurement depths varied slightly across sites (16cm-22cm), the fact that the strongest influence was seen from the 20cm data suggests that such small differences in measurement depth do not affect results.

(a) Flux into the Hillslope: 22cm Modeled Soil Temperatures
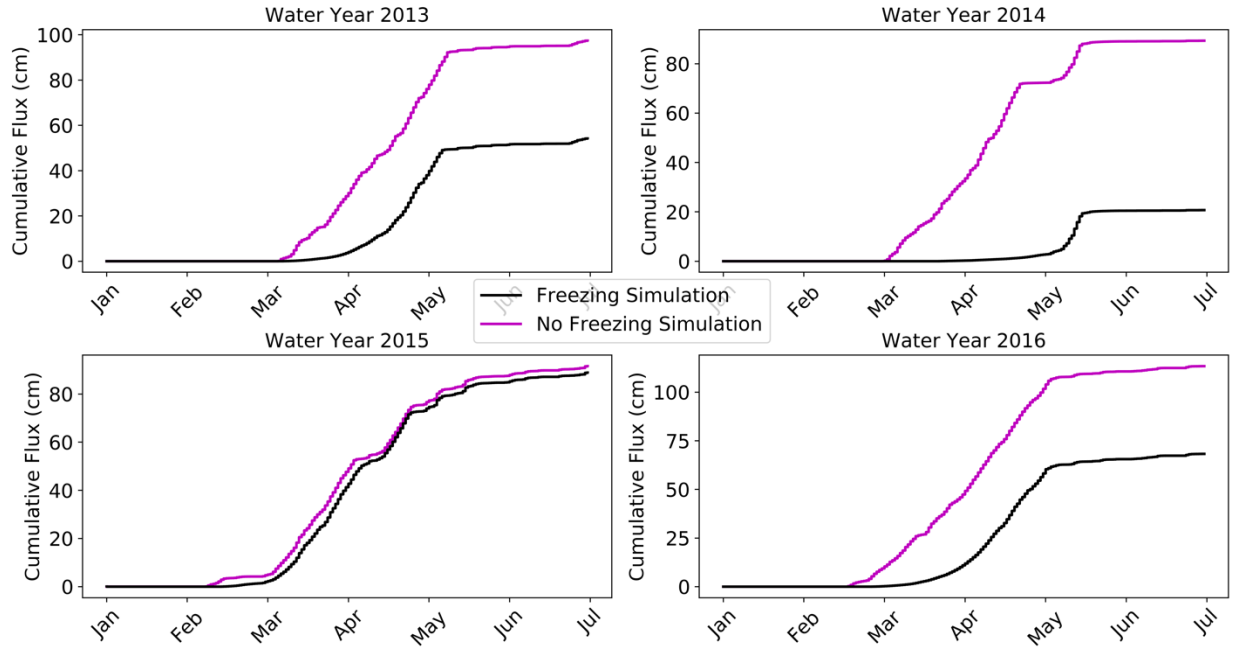
(b) Flux into the Hillslope: 22cm Soil Temperatures from Meteorological Station
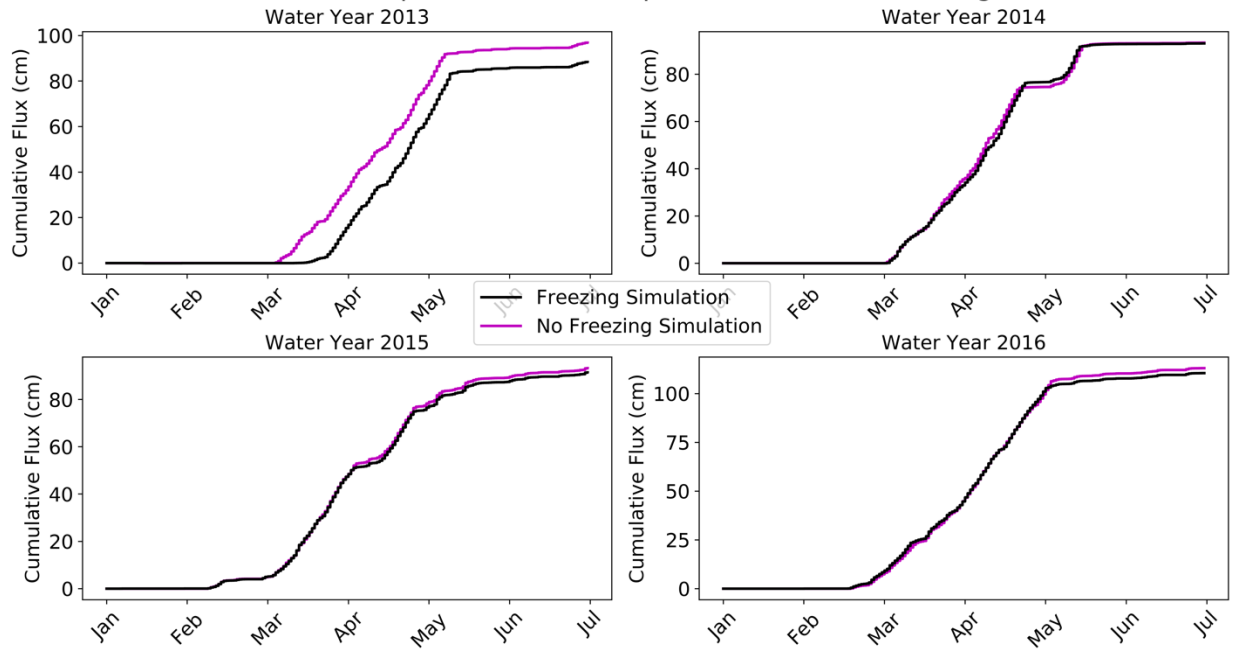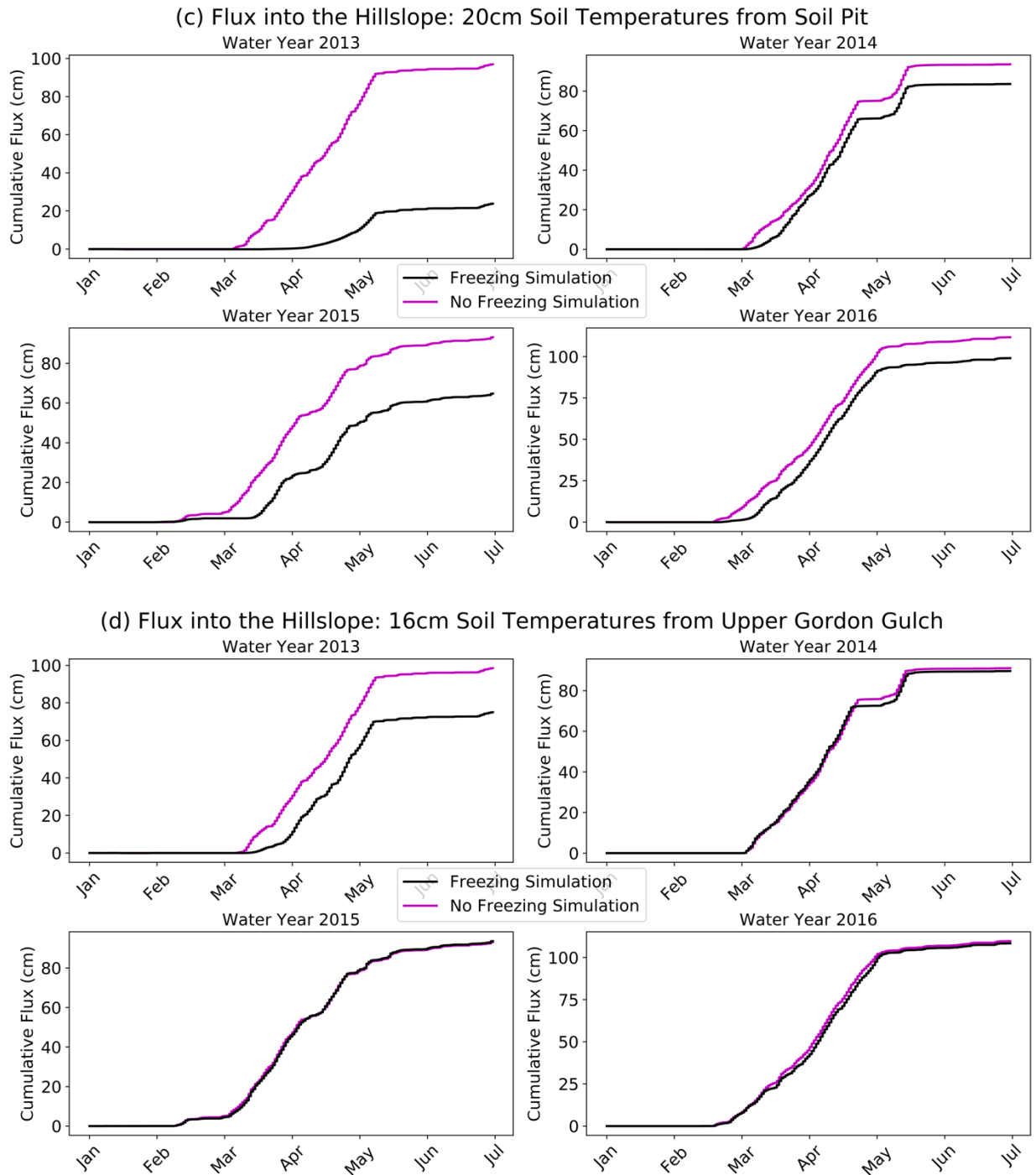
Figure 28. Cumulative vertical flux (infiltration) on the north-facing slope at a depth of 50cm below the soil surface produced by simulations including frozen ground (black) and excluding frozen ground (magenta) using modeled soil temperatures (a) and three sets of measured soil temperatures (b-d). During water year 2013, which featured more intense soil freezing than any other year (see Figure 15), the presence of frozen ground significantly reduces the magnitude of infiltration. During water years 2014 and 2015, frozen ground reduces infiltration, but not significantly.

5. Conclusions

We have presented a thermo-hydrologic modeling study of the factors controlling frozen ground in mountainous regions based on observations from Gordon Gulch, CO. We coupled a surface energy balance and physical snowpack model to PFLOTRAN-ICE, reproducing soil temperature observations very accurately (NS scores 0.68-0.90). Intense and persistent soil freezing, which occurs primarily on the north-facing slope, reduced infiltration during one out of four water years, and to a different extent throughout the catchment.

Compared to simulations without the snowpack, representation of the snowpack significantly improves estimates of soil temperatures on the north-facing slope. Here, incorporation of the snowpack serves to accurately reproduce the duration of soil freezing in the spring; snow-free simulations underestimate the duration of frozen ground by 1-2 months. Compared to simulations without the snowpack, representation of the snowpack does not significantly improve soil temperature estimates on the south-facing slope. Accordingly, the snowpack should be represented in SFG models for sites that experience persistent snow accumulation and can be safely excluded from sites that experience only ephemeral snow accumulation, where a boundary condition based on the bare soil surface energy balance is typically sufficient. Despite experiencing long snow-free periods during the winter, the south-facing slope does not experience intense or prolonged frozen ground due to its higher solar insolation compared to the north-facing slope. Thus, a modeling framework based on air temperature alone is not sufficient to simulate soil temperatures; the full surface energy balance is required.

On the north-facing slope, numerical snow depth experiments showed that manipulating snowfall by a factor of two produces changes in the intensity of soil freezing during the winter (December-February): reducing snowfall led to higher intensity of soil freezing, while increasing snowfall prevented soil freezing. That such an effect can be simulated

using a single-layer snowpack model reinforces the utility of the snowpack modification presented in Chapter II, section 3.2. By allowing the relative contributions of snow surface heat exchanges to the overall snowpack energy balance to vary with snow depth, we are better able to model the influence of the snowpack on ground temperatures. Such a key modeling capability is particularly important in regions with significant snow accumulation, such as the subalpine and alpine zones of the Colorado Front Range (see Chapter IV). As high solar insolation limits snow accumulation on montane south-facing slopes and foothills sites in the Colorado Front Range, the influence of snow depth on ground temperatures is less important there, but can still be simulated accurately with our parameterization, highlighting its universality. This capability can also be applied to simulate the influence of the snowpack on ground temperatures in high-latitude regions, where low solar insolation and air temperatures permit deep snow accumulation.

While we have focused strongly on modeling the influence of snow depth on ground temperatures, which was lacking in existing models, it is important to note that the snowpack energy balance depends strongly on the temperature at which snow is deposited. As Jennings et al. [2018] point out, for Rocky Mountain snowpacks, precipitation exerts the primary control on cold content development (73-84%), while heat lost at the snowpack surface is responsible for a much smaller fraction (16-27%). In the Colorado Front Range, both snowfall and snow accumulation are expected to change throughout the 21st century due to the combined effects of projected precipitation and air temperature changes [Liu et al., 2017]. Higher air temperatures will affect both mechanisms of cold content development: snowfall events are expected to occur at higher temperatures, bringing less cold content to the snowpack, while heat exchanges at the snowpack surface may accelerate, as gradients between the snowpack surface temperature and ambient air temperature increase. Thus, for projections of ground temperatures under a changing climate in seasonally snow-covered regions, an approach that accurately represents the

relative contributions of energy exchanges to the overall snowpack energy balance, such as the one we have outlined, is necessary.

It is also well-known that the effect of snowpack insulation on ground temperatures depends on the thermal state of the ground at snowpack onset: an early snowpack insulates warm ground, while a late onset insulates cold ground [Zhang, 2005; Bartlett et al., 2004]. Although no attempts were made in this study to manipulate the onset timing of the snowpack and simulate resulting differences in ground temperatures as we did with snow depth, thermal history effects on ground temperatures were explicitly represented in our modeling approach. Although we were able to successfully incorporate all snowpack energy exchanges into a computationally-efficient single-layer model, it is likely that ground temperature estimates could be refined further with a multi-layer snowpack model that tracks the thermal history and evolution of successive snow layers deposited throughout the season, with particular consideration for the thermal state of the lowest snow layers. The low thermal conductivity of snow produces stark thermal gradients within a snowpack that are not fully represented in a lumped model. In particular, snow layers close to the soil surface are warmer compared to the snowpack as a whole. These layers, deposited earliest in the season, are directly affected by the ground heat flux, are insulated from the air by snow layers above, and are only minimally cooled by subsequent colder snow events due to snow's low thermal conductivity. In addition, the lower density of base snow layers as well as the formation of depth hoar further restricts heat flow at the base of the snowpack [Zhang et al., 1996]. In permafrost studies, the basal temperature of snow cover (BTS) at the end of the snow season is widely used as an indicator of the ground thermal regime [e.g. Janke, 2005]; permafrost is assumed to occur where BTS is below -3°C [Haeberli, 1973 in Zhang, 2005]. While ground contributions to the snowpack energy balance are small, they are more important within the context of ground surface temperature modeling efforts.

In our analysis of the influence of frozen ground on subsurface hydrology, we found that frozen ground significantly influenced the ability of snowmelt water to infiltrate during one out of four water years, and to a different extent throughout the catchment. During that year (water year 2013), the coupled thermo-hydrologic model including the seasonal snowpack produced estimates of the influence of soil freezing on cumulative infiltration similar to those estimated from three datasets. During two other water years (2014 and 2016), the thermo-hydrologic model simulated greater influence of soil freezing in infiltration than the datasets, due to a slight underestimation of soil temperature in the model during those years. As the model simulated snow depth accurately, accounted for the thermal history of the ground, and included the contribution of precipitation cold content to the snowpack energy balance, we suggest that future efforts to simulate ground temperatures beneath a seasonal snowpack should seek to account for the evolution of snow density and layering (e.g. depth hoar [Zhang et al., 1996]), and consequent changes in snowpack thermal properties.

CHAPTER IV

INCORPORATING THE SEASONAL SNOWPACK INTO THERMO-HYDROLOGIC
MODELING OF FROZEN GROUND AT NIWOT RIDGE

1.   Introduction

The occurrence of frozen ground throughout the subalpine and alpine zones of the Colorado
Front Range has received a great deal of attention, from the perspectives of civil
engineering and hydrology as well as fundamental ecosystem and geological sciences. The
spatial distribution of frozen soil influences the ability of snowmelt water to infiltrate,
cycling of carbon and nitrogen during and after the snowcover season, and long-term
changes in soil production, downslope soil migration, and subsurface properties. With long-
term climate and ground temperature observations established in the 1950's and
maintained by the NSF Long-Term Ecological Research program, Niwot Ridge, a seasonally
snow-covered alpine catchment in the headwaters of the Boulder Creek watershed, serves
as an ideal location for analyzing the occurrence of frozen ground and its hydrologic effects
under a changing climate. Frozen soils are classified as permafrost (perennially frozen)
soils and seasonally frozen ground (SFG). Permafrost consists of ground that remains at or
below 0˚C for at least two years, while SFG thaws annually [Harris et al., 1988]. Conditions
are favorable for permafrost development at high latitudes and altitudes, approximately
25% of land in the northern hemisphere, whereas SFG occurs across a wide range of
latitudes and altitudes, approximately 50% of land in the northern hemisphere [Zhang et
al., 2003].

The seasonal snowpack exerts a strong control on the occurrence of frozen ground [Zhang,
2005]. A thorough discussion of the insulating effects of the snowpack is provided in
Chapters I and III, and is summarized briefly in this section, with site-specific details
provided in section 2. Generally, snowpacks exceeding a depth threshold (30-50cm [Hill et

al., 2019], 30-40cm [Brooks et al., 1995; Brooks et al., 1999; Cline (1995) in Brooks et al., 1999]), or 80-100cm [Imhof et al., 2000]) act to decouple the soil from the atmosphere. However, the seasonal influence of deep snowpacks on ground temperatures depends on the thermal history of the ground, as well as air temperatures and solar radiation from which the ground is insulated. For example, if the snow accumulates after the ground has already frozen, deep snowcover will act to preserve the frozen state of the ground (subject to the influence of the geothermal heat flux). In high latitude regions where snowcover is typically present when air temperatures are low, deep snowpacks tend to increase ground temperatures [Zhang, 2005]. However, deep snowcover that persists late into the spring may act to protect the cold state of the ground from high solar radiation. In SFG regions that experience thin or ephemeral snowcover, thermal coupling between the ground and the atmosphere acts to increase the frequency and intensity of soil freezing, while decreasing the duration [Fuss et al., 2016; Sarady and Sahlin, 2016; Bayard et al., 2005; Hardy et al., 2001]. In a warmer climate with snow accumulation that is reduced and occurs later in the season may induce increased freezing [Hardy et al., 2001], and "colder soils in a warmer world" [Groffman et al., 2001a].

It is well known that frozen ground influences infiltration and subsurface hydrology [Hayashi, 2013; Walvoord and Kurylyk, 2016]. Hydraulic conductivity decreases by orders of magnitude in freezing soils [McCauley et al., 2002; Burt and Williams, 1976], but frozen soils may still transmit liquid water [e.g. Sherler et al., 2010; Boike et al., 1998], since liquid water is able to persist in frozen soils. Frozen soils limit infiltration [e.g. Bayard et al., 2005; Laudon et al., 2004; Stähli et al., 1996; Thunholm et al., 1989; Kane and Stein, 1983; Dunne and Black, 1971], but may not generate runoff in all cases [Fuss et al., 2016; Lindström et al., 2002; Nyberg et al., 2001; Shanley and Chalmers, 1999].

In addition to hydrology, soil freezing strongly affects plant phenology [Hayashi, 2013] and soil microbial activity, which is possible at temperatures as low as -5°C [Brooks et al., 1997;

Schimel et al., 1996; Brooks et al., 1995] to -6.5°C [Coxson & Parkinson, 1987], below which liquid water is increasingly unavailable. In this way, frozen soils may act as a "switch" [Brooks et al. 1997], controlling when microbial respiration can take place in the soil [Brooks et al., 1997], in addition to the more general temperature-dependence of soil microbial activity and biogeochemical pathways [Donhauser and Frey, 2018]. Soil freezing may lead to microbial and root mortality [Hayashi, 2013; Tierney et al., 2001; Groffman et al., 2001a; Brooks et al., 1997], which can change the chemical composition of connected aquatic systems [Fitzhugh et al., 2003; Fitzhugh et al., 2001; Brooks et al., 1998].

In addition to interest from the hydrologic and biogeochemical sciences communities, ice formation in soils has traditionally received a great deal of attention from geotechnical engineering and geomorphology due to the process of frost heave, which can damage infrastructure in regions with seasonal freezing and thawing and accelerate downslope soil migration. Frost heave is not caused by expansion of water during phase change, but by transport of liquid water toward the freezing fringe that forms "segregated" ice lenses, a process known as cryosuction [Taber, 1929]. Laboratory experiments [Harris et al., 2008] and numerical modeling [Anderson et al., 2012] demonstrate that patterns of frost damage processes differ on seasonally frozen and perennially frozen slopes. The migration of water toward the freezing front contributes to the process of frost "cracking", in which the growth of fracture networks alters hydrogeologic properties like porosity and permeability and contributes to the generation of mobile soils. Frost cracking is strongly dependent on the availability of liquid water and the distance across which the water must travel to the freezing front [Anderson et al., 2012]. As the intensity of frost cracking depends on the daily temperature cycle [Anderson et al., 2012], the insulating effects of snow cover are expected to reduce frost cracking intensity. Thus, coupled thermo-hydrologic models including the snowpack can inform such processes by explicitly including the seasonal hydrologic cycle.

Further, thawing permafrost may result in slope destabilization [Gruber and Haeberli, 2007] and accelerated solifluction processes [Harris et al., 2009]. Solifluction is a general term referring to slow migration of soils downslope in cold regions [Andersson, 1906], and includes the related processes of frost creep and gelifluction. Frost creep occurs on an inclined hillslope when a soil heaves normally to its surface during a freezing cycle, and then settles downslope due to gravity, while gelifluction occurs when oversaturated surface soils migrate downslope during a thawing cycle [Matsuoka, 2001]. These processes are dependent primarily on the frequency and depth of soil freezing, which tends to increase with increasing frost duration [Matsuoka, 2001], and constitute the primary mechanisms of downslope soil movement in the Colorado Front Range [Benedict, 1970]. The depth of frost penetration has been shown to determine the shape of low-relief interfluves and soil thickness in the Laramide ranges of the western United States [Anderson, 2002].

As a template for understanding the variety of hydrologic, biogeochemical, and geomorphological changes associated with an evolving ground thermal regime, there is a need for rigorous ground temperature analyses that account for the influence of the seasonal snowpack, the surface energy balance including solar radiation, and subsurface thermo-hydrology. In this study, we seek to determine how the cold content of snow at various elevations influences the ground thermal regime, how frozen ground beneath bare and snow-covered patches influences subsurface flow, and how the influence of frozen ground on infiltration and groundwater recharge changes with elevation. While our primary goal is to explore the influence of the snowpack on soil freezing, consequent subsurface flow paths, and implications for biogeochemistry and geomorphology, the coupled thermo-hydrologic model we have developed provides a novel perspective to ongoing cryosphere research at Niwot Ridge. As the location of a Long-Term Ecological Research site, Niwot Ridge has an extensive history of frozen ground investigations, dating back to the 1960's. We project how end-of-21st-century changes in Front Range air temperature,

snowfall, and cold content will influence the ground thermal regime, both from the perspective of seasonally frozen ground and permafrost, in comparison to the 1952-1970 period.

We employ a coupled thermo-hydrologic model developed at the montane Gordon Gulch site (Chapters II-III) to simulate seasonally and perennially frozen ground at Niwot Ridge sites: alpine D1 (3740 m) and Saddle (3530 m) sites with thin snowcover and subalpine C1 (3020 m) site that features a deep snowpack (maximum depths 80cm-140cm). First, we validate the model using soil temperatures from water years 2000-2013 to determine the influence of the snowpack on ground temperatures along the elevation gradient at Niwot Ridge. Next, using water year 2008 as an example year, we perform a thermo-hydrologic analysis of subsurface flow to determine how soil freezing beneath snow-covered and bare ground patches influences the contribution of snowmelt infiltration to subsurface flow. Finally, we compile climate data from the 1950s-1970s and 2000-2013, as well as end-of-century regional climate change projections to retrospectively and prospectively simulate soil temperatures at Niwot Ridge at various depths. Throughout this study, freezing "intensity" refers to the magnitude of sub-0°C temperatures, "frequency" refers to the number of intra-annual freezing and thawing events, and "duration" refers to the length of time that the ground is frozen. Each of these frozen ground characteristics are expected to influence the ability of snowmelt water to infiltrate, cycling of carbon and nitrogen during and after the snowcover season, and long-term changes in soil production, downslope soil migration, and subsurface properties.

2. Field Site Description, Previous Studies, and Datasets

2.1 Field Site Description

Niwot Ridge is a large interfluve on the Colorado Front Range that extends eastward from the Continental Divide and the site of a Long-Term Ecological Research (LTER) observatory. The Colorado Front Range was thrust upward during the Laramide Orogeny

into a generally north-south trending massif; Pleistocene glaciation created wide U-shaped valleys that trend east-west [Anderson et al., 2012]. The site experiences low air temperatures and high wind speeds, which redistribute snow toward sheltered areas, creating a heterogeneous snowcover environment [Seastadt et al., 2004; Greenland and Losleben, 2001]. Annual precipitation on the order of 1m arrives as winter snow originating from the west, spring snow from the east, and summer rainfall from convective storms [Greenland and Losleben, 2001]. Snow constitutes at least 75% of precipitation in this region [Greenland and Losleben, 2001]. Snowpack accumulation begins during November in the subalpine and during December-January in the alpine zone [Brooks et al., 1996]. By protecting the ground from cold air and high wind speeds and providing meltwater, snow cover is the primary control on plant growth at Niwot Ridge; in particular, early season snow is believed to protect the ground from freezing [Walker et al., 2001]. Late season snow both delays the onset of plant growth, while providing moisture for plant activity [Greenland and Losleben, 2001]. Although some plants initiate growth beneath the snowpack, snowmelt timing strongly controls vegetation development and total primary production [Walker et al., 2001]. Tree line is located at an elevation of approximately 3400m-3600m, above which the alpine tundra is populated in patches by mosses, woody shrubs and low-lying herbaceous plants [Walker et al., 2001]. At elevations greater than ~3800m, talus slopes and bare rock remain mostly uncolonized by vegetation.

2.2 Field Observations and Previous Studies

Recent work has begun to establish a connection between the occurrence of frozen ground at Niwot Ridge and trends in streamflow. Caine [2010] attributed increasing autumn streamflow in the Green Lakes Valley at Green Lake 4 (3550m) to permafrost thaw, while similar flow trends were not observed in nearby catchments considered unlikely to be underlain by permafrost. Hill [2015] proposed a conceptual model in which ground insulated by a thick (>30cm) snow blanket remains thawed year-round, recharges

112

groundwater, and induces a streamflow response earlier than ground covered by a thin (<30cm) snow blanket, which remains seasonally frozen into the snowmelt season, limits groundwater recharge, and induces a streamflow response later into the summer. Evans et al. [2018] showed that frozen ground plays a role in determining the timing of groundwater discharge to streams, while snowmelt timing controls seepage from hillslope faces.

An extensive body of knowledge has been developed at Niwot Ridge regarding nitrogen and carbon dynamics beneath seasonal alpine snowpacks [Fisk et al., 2001; Brooks and Williams, 1999; Brooks et al., 1998; Brooks et al., 1997; Brooks et al., 1996; Brooks et al., 1995] and applies broadly to similar high-elevation environments. Alpine sites along the eastern flank of the Colorado Front Range mountains like Niwot Ridge experience high wind speeds that create a heterogeneous snowcover environment [Seastedt et al., 2004; Greenland and Losleben, 2001] (see section 2.1). Such gradients in snowcover drive significant spatial variability in available soil moisture during the growing season, vegetation growth, and nutrient cycling [Fisk et al., 2001]. Despite the annual occurrence of soil freezing, experimental evidence indicates high "subnivial" (beneath the snowpack) microbial biomass and activity [Fisk et al., 2001; Brooks et al., 1998; Brooks et al., 1996; Brooks et al., 1995], including significant cycling of nitrogen [Brooks et al., 1998] and fluxes of carbon dioxide [Brooks et al., 1997]. Eddy covariance measurements at Niwot Ridge have demonstrated significant winter-time soil respiration that results in a seasonal transition from negative net ecosystem exchange (carbon source) to positive net ecosystem exchange (carbon sink) [Knowles et al., 2015; Blanken et al., 2009]. Due to strong elevational gradients in temperature and windspeed at this site, the alpine zone transitions from carbon uptake to carbon loss earlier in the fall and later in the spring than the subalpine zone. Due to such differences, the subalpine site acted as a net carbon sink in that study, while the alpine site acted as a net carbon source to the atmosphere due to the short high elevation growing season [Knowles et al., 2015; Blanken et al., 2009]. However, small

changes in seasonal snowcover and projected trends in air temperature may shift the relative seasonal contributions of uptake and loss in such environments.

Subnivial microbial activity immobilizes nitrogen and prevents export to surface waters [Brooks, 1998]. Plant growth and microbial activity are tightly coupled through the process of nitrogen mineralization, which transforms organic nitrogen (derived from atmospheric sources and plant litter) to inorganic forms that are available to plants. By influencing the intensity and duration of soil frost, the seasonal onset of snowcover and the depth to which the snowpack accumulates exert a primary control on nitrogen and carbon fluxes in these environments. Significant subnivial microbial CO_2 production is possible, particularly beneath a deep snowpack that accumulates late in the season [Brooks et al., 1997], which permits deep freezing events that provide soil carbon "substrate" for microbial growth and activity [Brooks et al., 1996] once soil temperatures increase above a threshold of -5°C during the snow season [Brooks et al., 1997; Brooks et al., 1995]. However, beneath deep, persistent snowpacks, production of CO_2 and NO_2 gases tends to decrease at the end of the snow season as resources for microbial respiration become scarce [Brooks et al., 1997].

As decadal trends in precipitation and temperature at Niwot Ridge had only begun to emerge during the late 1990's and have been influenced by anthropogenic activity in the past several decades, coupled projections of snowcover and ground temperatures in the current study provide a timely follow-up to the foundational work of the 1990's. A shift toward more / less intense early-season soil freezing events would be associated with more / less carbon substrate and more / less CO_2 production. A shift toward shallower snowpacks may result in less microbial activity, CO_2 production, and nitrogen mineralization. Earlier snowmelt in traditionally moderate duration snowpacks would reduce the subnivial microbial respiration window (which is confined by the availability of carbon substrate [Brooks et al. 1997]), while reductions in the duration of traditionally persistent snowpacks

outside of the microbial respiration window would not be expected to significantly affect biogeochemical processes.

Field observations in the vicinity of Niwot Ridge provide evidence that frozen ground may persist beneath a deep snowpack in high-elevation regions, and that maximum snow depth cannot indicate the presence or absence of frozen ground without considering the thermal history of the soil. Between the snow seasons of 1993 (maximum snow depth 0.85m-1.1m) and 1994 (maximum snow depth 2.4m-2.6m), Brooks et al., [1995] measured higher soil temperatures beneath the deeper snowpack (increase in minimum soil temperature of 9°C-12°C) but during both years, the soil surface remained frozen through early May. In both cases, it is likely that the ground froze intensely in October and November before snow had accumulated above the threshold necessary for soil-atmosphere decoupling (data was available for January-May). Von Witsch's basal temperature of snow (BTS) measurements during spring 1999 in the Colorado Front Range imply that the deep snowpack (>1m) at Green Lakes, Lake Albion, and Blue Lake does not act to thaw ground that had previously frozen [cited in Janke, 2005]. In the BTS method developed by Haeberli (1973) [cited in Zhang, 2005], the basal temperature of the snowpack is measured during the spring, prior to snowmelt. When the snowpack has accumulated significantly (>80cm), the basal temperature of the snowpack is strongly influenced by the ground. In this method, BTS measurements of <-3°C indicate permafrost occurrence whereas measurements above -2°C suggest low likelihood of permafrost [Haeberli, 1973 cited in Zhang, 2005]. A soil temperature field campaign along Trail Ridge Road consistently observed freezing temperatures beneath snow-covered sites [Janke et al., 2012]. While no depth information is available, snow-free sites averaged −9.4°C while snow-covered sites averaged −7.5°C. Some studies have found that coarse surface debris may provide channels for cold air flow and permit soil freezing in areas that are otherwise dominated by thick snowcover [e.g.

Ishikawa, 2003]. Process-based modeling of soil freezing that includes the seasonal snowpack generalizes such information beyond specific sites and microclimates.

Anecdotal reports of permafrost occurrence at 3-4m depth surfaced during the construction of the Silver Lake and Left Hand reservoirs in 1962 and 1965; although this site is below tree line, wind scouring limits snow accumulation and tree growth. Fahey began a ground temperature measurement campaign in 1968 near the current "Saddle" site (3500m), which features a shallow water table and significant wind-scouring that limits snow accumulation [Ives and Fahey, 1971]. The "Fahey site" measurements indicated the occurrence of permafrost beneath a 2-5m active layer [Ives and Fahey, 1971]. Higher elevation ground temperature measurements to the west of the Fahey site near the location of the D1 climate station (3800m) indicated the presence of permafrost beneath a 2m active layer [cited in Janke, 2005]. Greenstein's (1983) analysis of basal temperature of snow (BTS) measurements suggested permafrost at elevations greater than 3500m, in agreement with Ives and Fahey [1971] and Ives (1974) [cited in Janke, 2005]. Freeze-thaw indices implied a continuous permafrost zone above elevations of 3600m on south-facing slopes and 3550m on north-facing slopes, and a discontinuous permafrost zone as low as 3300m on south-facing slopes and 3200m on north-facing slopes, which is more extensive than the permafrost zonation suggested by Ives (1974) [cited in Janke, 2005]. Von Witsch's BTS measurements near Green Lakes, Lake Albion, and Blue Lake also confirmed earlier results, with a larger permafrost zone than previously suggested [cited in Janke 2005]. Janke [2005] mapped the likelihood of permafrost on the Front Range using a probabilistic model based on rock glacier topographic information and validated with mean annual air temperature (MAAT) and bottom temperature of snow (BTS) data and confirmed the permafrost zonation suggested by Ives (1974) and Greenstein's BTS measurements. Janke's predictive model placed the high-probability permafrost zone at higher elevations than Greenstein's freeze-thaw index analysis and Von Witsch's BTS measurements. Janke et al. [2012] evaluated

the accuracy of permafrost index or zonation models by measuring ground temperatures along Trail Ridge Road and found no permafrost in three boreholes. Following the campaign on Trail Ridge Road, Leopold et al. [2014] collected ground temperature measurements and performed one-dimensional heat conduction modeling that questioned both the current and past occurrence of permafrost at the sites where permafrost had been ostensibly observed in the 1970's. Leopold et al. [2014] suggested that sites between 3500m-3800m do not currently permit the occurrence of permafrost, and probably did not in the 1970's. However, Leopold and others' modeling work allowed for the occurrence of permafrost on solifluction lobes, north-facing slopes, and sites above 3800m (i.e., D1).

2.3 Datasets Used in this Study

Climate and 5cm soil temperature data are available at the high alpine D1 [Morse and Losleben, 2019b], alpine tundra Saddle [Morse and Losleben, 2019c], and subalpine C1 sites during 2000-2014 [Morse, 2019]. Model results are also compared to soil temperatures at depth from the Fahey site [Ives and Fahey, 1971; Leopold et al., 2014] and the Ives (1974) sites [in Leopold et al., 2014]. Original data from the Ives and Fahey sites were not available; accordingly, manual reproductions of the data originally presented in Leopold et al. [2014] were graciously provided by Dr. Matthias Leopold. A quality-controlled, infilled meteorological dataset [Jennings et al., 2019] was used to drive the surface energy balance and snowpack models during 2000-2013, and the precipitation record was used in projections of frozen ground. Modeled snow depths at C1 and Saddle were compared to snow depth data from water year 2012 [Lestak et al., 2013]. C1 and Saddle snow depths were taken as the mean of all "control" plots from the upper subalpine and alpine sites. Climate information compiled from water years 2000-2014 for temperature [Morse, 2019; Morse and Losleben, 2019b; Morse and Losleben, 2019c] and precipitation [Jennings et al., 2019] at each site are presented in Table 7.

	Elevation (m)	Mean Annual Daily Mean Temperature (°C)	Mean Annual Daily Maximum Temperature (°C)	Mean Annual Daily Minimum Temperature (°C)	Annual Precipitation (cm)
D1	3729	-2.3	2.1	-6.0	78.4
Saddle	3528	-0.58	4.2	-4.7	86.6
C1	3022	2.6	10.6	-3.9	51.2

Table 7. Elevation (m), temperature (°C), and precipitation (cm) information for high alpine (D1), alpine tundra (Saddle), and subalpine (C1) sites computed from 2000-2014 data.
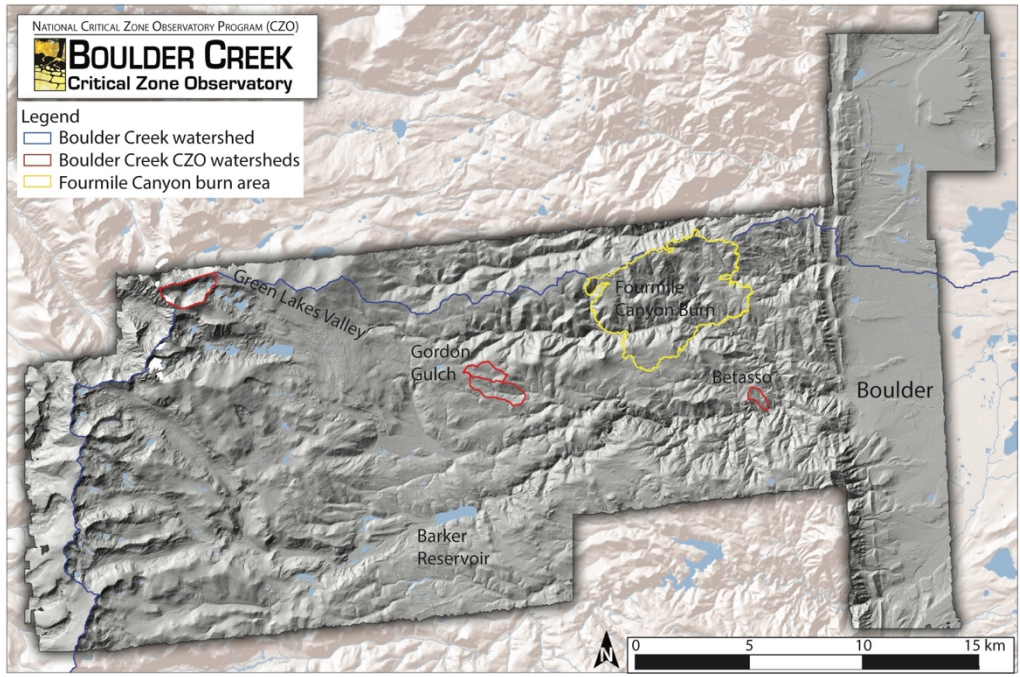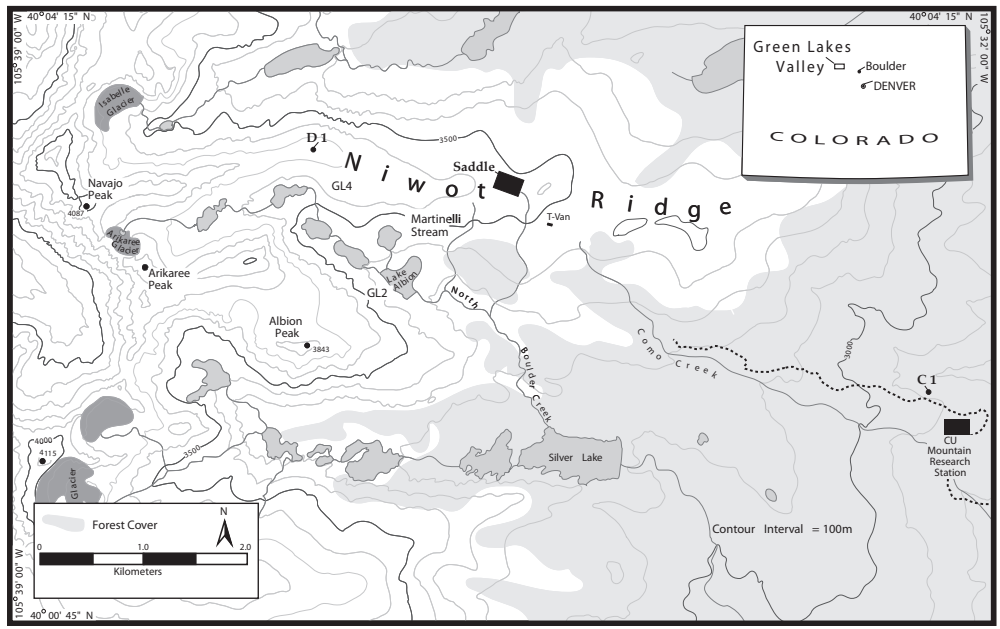
Figure 29. Top: Map of Niwot Ridge and Green Lakes Valley with 1000m elevation contours, including D1, Saddle, and C1 climate stations (courtesy of the Niwot Ridge LTER program). Tree line is located at an elevation of 3400-3600m. Bottom: Map of the Boulder Creek Watershed and BcCZO sites (courtesy of the BcCZO program). Green Lakes Valley, flanked by Niwot Ridge, is the highest elevation BcCZO site. The continental divide is on the left side of both maps.

3.   Modeling Approach

For this study, the coupled model developed in Chapters II-III is used to simulate seasonal and perennial soil freezing at Niwot Ridge and its hydrologic consequences. The model consists of surface energy balance estimates and a physical snowpack model that are used to produce surface temperatures and infiltration rates as boundary conditions for a subsurface thermo-hydrologic model. The surface energy balance estimates include solar radiation as a function of slope, aspect, elevation, and canopy cover. The physical snow model is adapted from the Utah Energy Balance [Tarboton and Luce, 1996]. The subsurface model (PFLOTRAN-ICE) simulates coupled flows of energy and water in three phases (ice, water, vapor) [Karra et al., 2014; Painter and Karra, 2014]. The details of each model are described in Chapter II. Three sets of simulations are performed in this study. One-dimensional model validation using soil temperature data from 2000-2014 is used to determine the influence of the snowpack on ground temperatures at Niwot Ridge. Two-dimensional modeling including snowmelt infiltration is used to simulate the hydrologic consequences of frozen ground during water year 2008. Climatologies corresponding to past (1952-1970), present (2000-2013), and future (2100) are used to force a one-dimensional model to project soil temperatures at various depths through time. A deep (1km) domain is employed using a 1500 year spin-up to simulate the evolution of permafrost, and a smaller (5m-10m) domain is used for simulations of seasonally frozen ground. Details regarding the motivation and conceptual framework for these simulations are provided in the following sections, and domain information, boundary conditions, and initial conditions are provided in Table 8.

Simulation		Water Year(s)	Domain Dimensions	Domain Depth	Discretization	Snow	Recharge
Modeling the Influence of the Snowpack on Seasonally Frozen Ground		2000-2014	1D	5m	10cm	Yes	No
Hydrologic Consequences of Seasonally Frozen Ground		2008	2D	5m-10m	20cm	Yes	Yes
Soil Temperature Projections	SFG	1952-1970; 2000-2013; 2100	2D	5m	10cm	Yes	Yes
	Permafrost	1952-1970; 2000-2013; 2100	1D	1km	10cm-1m	No	No

Table 8. Simulation details for three sets of analyses performed in this study. For soil temperature projections, the precipitation record from water year 2008 was scaled using climatologies computed for periods 1952-1970, 2000-2013, and 2100.

In general, the thermal boundary condition on the soil surface is derived from surface energy balance calculations performed outside of PFLOTRAN-ICE. When a snowpack is present, the soil surface temperature is specified as the average snowpack temperature; for simulations in which the snowpack is excluded, the thermal boundary condition on the soil surface is derived only from bare ground surface energy balance calculations. The model is initialized with unsaturated conditions at the measured soil temperature corresponding to the first day of the water year for each slope followed by a 10-year spin-up routine with a constant recharge rate applied as a hydrologic forcing. The constant recharge rate is computed as the total snowfall and rainfall for the water year, averaged across the water year. Following the spin-up routine, a 1-year model run begins on the first day of the water year (October 1) when snow has typically not accumulated, and soils are unfrozen. The model consists of 3-4 model layers, depending on the depth of the domain: soil (0m-1m), saprolite (1m-2m), weathered bedrock (2m-10m), and rock (10m-1km). Soils at Niwot Ridge are generally thin with an organic surface layer and vary across the landscape: ridge-top soils are generally deeper and older than the young and thin soils of valley bottoms and sides [Seastadt, 2001]. Soil texture has been estimated as 39% sand, 38% silt, and 23% clay with 22-28% organic matter for dry meadows, and 46% sand, 33% silt, and 21% clay with 16-31% organic matter for moist meadows [Seastadt, 2001]. Due to the lack of previous measurements of soil hydrologic and thermal properties, hydrologic parameters were selected based on representative parameters from Charbeneau [2000], as well as subsurface permeability and saprolite porosity from Gordon Gulch [Langston et al., 2015; Hinckley et al., 2014b]; bulk thermal conductivities are derived from constituent materials according to Woo [2012]. See Chapter III for additional details.

3.1 Modeling the Influence of the Snowpack on Seasonally Frozen Ground

The first set of model runs was performed using soil temperature data at 5cm depth during water years 2001-2013 to determine the influence of the snowpack on ground temperatures

at Niwot Ridge. A simplified set of assumptions permitted many years of simulation (2000-2013), at three sites (D1, Saddle, and C1), including and excluding the influence of the snowpack. Simulations including the effects of the seasonal snowpack were compared to simulations excluding the effects of the snowpack to determine the influence of snowcover at each site. A one-dimensional domain with depth 5m and vertical discretization 10cm was run at an hourly timestep. When snow cover is not present, the soil surface temperature is derived from bare ground surface energy balance calculations; when a snowpack is present, the soil surface temperature is specified as the average snowpack temperature. A geothermal heat flux was imposed on the deep soil boundary [Ehlers, 2005]. Zero-flux hydrologic conditions were imposed on both the soil surface and deep soil boundaries. Compared to one-dimensional simulations excluding infiltration that require computational times on the order of hours to days to complete, two-dimensional simulations including infiltration require weeks to complete due to the complexities of three-phase energy and water flow. Thus, for these initial model runs, infiltration was excluded. Atmospheric pressure was specified at a depth of 5m (the base of the domain) based on depth to water table data from the groundwater wells at the Martinelli site [Williams, 2019] in order to mimic expected hydrologic conditions of the more complex simulations described in section 3.2. In this case, the 10-year spin-up routine was run without recharge, producing a hydrostatic water content profile.

3.2 Modeling the Hydrologic Consequences of Seasonally Frozen Ground

Following the conceptual model proposed by Hill et al. [2015], we computed the influence of seasonally frozen ground on infiltration and groundwater recharge beneath adjacent snow-covered and bare, wind-scoured sites during water year 2008. Although alpine sites at Niwot Ridge experience intermittent periods of snowcover and wind scouring, blurring the distinction between bare ground and ground covered by a thin snowpack, dividing the model boundary into two distinct patches allows our results to broadly apply to

heterogeneous alpine and subalpine environments. Water year 2008 was selected because the snow depth record for the year is representative of the time period 1980-2020; specifically, the SNOTEL snow depth record for the year closely tracks the median snow depth for the period 1980-2020. In order to quantitatively evaluate the influence of frozen ground in the absence of other hydrologic factors such as snowmelt magnitude and timing, as well as overland flow generation, simulations including the formation of frozen ground were compared to simulations in which the soil is prevented from freezing by setting any sub-zero temperatures to 0°C, which ensures an ice fraction of zero. All other variables were held constant. A two-dimensional domain with depth 10m (C1 and Saddle) and 5m (D1), width 20m and spatial discretization of 20cm was employed for these simulations, with an hourly timestep.

Snow-covered and bare ground surface boundary conditions were used within the same simulation. The soil surface boundary (z=10m) was divided into two "patches." One patch (5m<x<10m, Figure 30) was forced with the surface energy balance including the influence of snow, while the other patch (10m<x<15m, Figure 30) was forced with the surface energy balance excluding the influence of snow. This combined boundary condition simulates how the heterogeneous snow cover environment of Niwot Ridge influences (1) subsurface freezing, (2) consequent changes in infiltration due to frozen ground, and (3) the hydrologic interaction of soil underlying snow-covered and bare ground. It is important to simulate the transition zone between snow-covered and bare ground, as snowmelt water that cannot infiltrate into the ground beneath the snowpack due to shallow soil moisture and/or ice is expected to flow downslope until reaching unsaturated, unfrozen soil or a surface water body [e.g. Hill et al. 2015]; in addition, the magnitude and direction of subsurface fluxes beneath bare ground are expected to be influenced by subsurface fluxes beneath snow-covered ground. Thus, such ground patches interact hydrologically and should be simulated together. For the snow patch, the soil surface temperature is derived from bare

ground surface energy balance calculations when the snow is absent and specified as the average snowpack temperature when snow is present. For the bare ground patch, the soil surface temperature is derived only from bare ground surface energy balance calculations. A geothermal heat flux condition [Ehlers, 2004] was applied to the bottom boundary (z=0m), and the remaining boundaries (x=0m,x=20m) were assigned zero heat-flux conditions.

5m "wings" at 0m<x<5m and 15m<x<20m were included on the left and right sides of the domain to minimize the effects of the left and right hydrologic zero-flux boundaries on model results. As described above, the snow-covered and bare ground boundary conditions were imposed on the soil surface boundary at 5m<x<10m, and 10m<x<15m, respectively. The hydrologic boundary condition on the soil surface (z=10m) was assigned a prescribed infiltration flux condition determined from the amount of rainfall or snowmelt produced during that timestep, adjusted for the occurrence of surface flow. The majority of infiltration originates from the snowpack: snowmelt simulated by the model is applied to the soil surface of the snow patch (5m<x<10m). When the shallow soil beneath the snow patch becomes saturated with moisture and/or ice, excess infiltration (calculated as overland flow or runoff from the snow patch) is then applied to the bare ground patch as run-on (10m<x<15m). Thus, during the winter and spring the bare ground patch only receives infiltration due to excess snowmelt from the snow patch. Summer rain is applied to both patches. Any infiltration that could not be accommodated by the bare soil patch was considered as "runoff" and was not analyzed in this study. The spin-up routine was run continuously for 10 years with an average recharge rate computed from the precipitation record from water year 2008. The left and right boundaries (x=0m; x=20m) were assigned "hydrostatic" conditions, with atmospheric pressure specified at the base of the domain (z=0m). A water table was specified across the bottom boundary (z=0m) of the domain, which is 10m in depth for Saddle and C1, and 5m in depth for D1 (not shown in Figure 30).

The location of the water table was based on depth-to-water table data [Williams, 2019]. Data from groundwater wells near C1 and Saddle were used for those sites, whereas data from the groundwater wells at the Martinelli site were used as a proxy at D1, which does not have a groundwater well. While the bottom boundary of the domain was held at atmospheric pressure, the groundwater table was allowed to rise with recharge.

No slope angle was used for this set of simulations, in order to make comparisons across sites with different slopes, and separately calculate fluxes beneath the snow-covered and bare ground patches. If a slope angle were included, subsurface fluxes at depth would then reflect the combined influence of multiple boundaries, and deductions about the hydrologic contributions of snow-covered and bare ground would not be possible. For example, flow beneath the snow-covered patch would reflect the combined influence of the upstream "wing" and the snow patch, and flow beneath the bare ground patch would reflect the combined influence of the snow-covered and bare ground patches. However, as the slope angles in the vicinity of D1, Saddle, and C1 are relatively small (3°-6°), the simulated subsurface flow fields are nearly identical for the slope and no-slope cases.
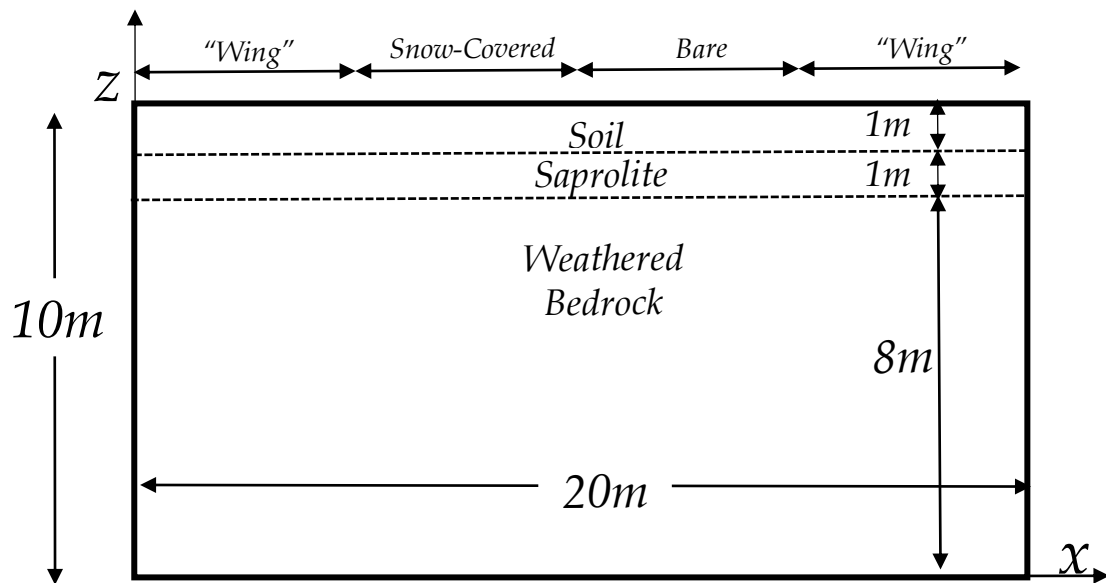
Figure 30. Schematic of model domain for Thermo-Hydrologic Consequences of Frozen Ground analysis. At Saddle and C1, the depth of the domain is 10m, while at D1, the depth of the domain is 5m (not shown). The combination of snow-covered and bare ground on the top boundary of the domain simulates how the heterogeneous snow cover environment of Niwot Ridge influences (1) subsurface freezing and (2) consequent changes in infiltration due to frozen ground. It is important to simulate the transition zone between snow-covered and bare ground, as snowmelt water that cannot infiltrate into the ground beneath the snowpack due to shallow soil moisture and/or ice is expected to flow downslope until reaching unsaturated, unfrozen soil or a surface water body [e.g. Hill et al. 2015]. Thus, such ground patches interact hydrologically and should be simulated together.

3.3 Retrospective and Prospective Soil Temperature Analysis

The long-term environmental observations at Niwot Ridge provide a unique opportunity to analyze the ground thermal regime through time over a range of depths. We simulated the occurrence of permafrost and seasonally frozen ground (SFG) through time at the C1 and D1 sites. Historical air temperature and precipitation data were compiled for 1952-1970 [Morse and Losleben, 2019c], henceforth described as "past". A climatology was computed for this time period by summing precipitation and averaging mean daily temperatures on a monthly basis. Using the same approach, a climatology was similarly computed from 2000-2013 data [Morse, 2019; Morse and Losleben, 2019b], henceforth described as "present". End-of-21st-century projections were obtained from Liu et al. [2017] to create an end-of-21st-century scenario, henceforth described as "future". Liu et al. [2017] used the Weather Research and Forecasting (WRF) model to simulate regional climate on a 4-km grid using a Pseudo Global Warming (PGW) approach. Their study compared model outputs for the time period 2000-2013 forced by ERA-Interim reanalysis data ("control") to model outputs for the same time period forced by ERA-Interim reanalysis data with a 95-year climate perturbation based on the CMIP5 RCP 8.5 scenario (PGW). The future climatology was computed from both sets of model outputs (control and PGW) using the process described below:

1. Gridded control and PGW simulation results were interpolated onto the locations of the D1 and C1 using the four grid points surrounding the sites.

2. For both control and PGW scenarios, precipitation was summed on a monthly basis, and daily mean temperatures were averaged on a monthly basis.

3. Since grid-level model outputs are generally different than in-situ observations, linear regression was used to relate observed 2000-2013 data to the control 2000-2013 scenario for mean daily temperature ($p<10^{-15}$, $R^2=1.0$) and precipitation total (D1: $p=2\times10^{-6}$, $R^2=0.91$; C1: $p=4\times10^{-3}$, $R^2=0.58$).

4. The regression relationship from step 3 was used to back-transform the PGW model outputs to "in-situ" conditions.

5. The in-situ precipitation time series for water year 2008 [Jennings et al., 2018] was selected for analysis because the snow depth record for the year is representative of the time period 2000-2013. The daily precipitation record was scaled on a monthly basis using the climatologies computed for past, present, and future scenarios:

$$P(day, scenario) = P(day, 2008) \times \frac{P(month, scenario)}{P(month, 2008)} \tag{85}$$

Using the same precipitation time series with adjusted magnitudes preserves snowfall and rainfall patterns and allows for direct comparison across the three time periods without the influence of interannual precipitation variability. Scaling factors are presented in Figure 31.

6. A temperature time series was constructed for each time period using a sinusoid based on the mean daily temperature. The amplitude of the function was constrained by monthly-averaged minimum and maximum daily temperatures from the 2000-2013. This analysis then tracks changes in mean temperature, not temperature extremes.

Temperatures and precipitation scaling factors are presented in Figure 31 and 32.
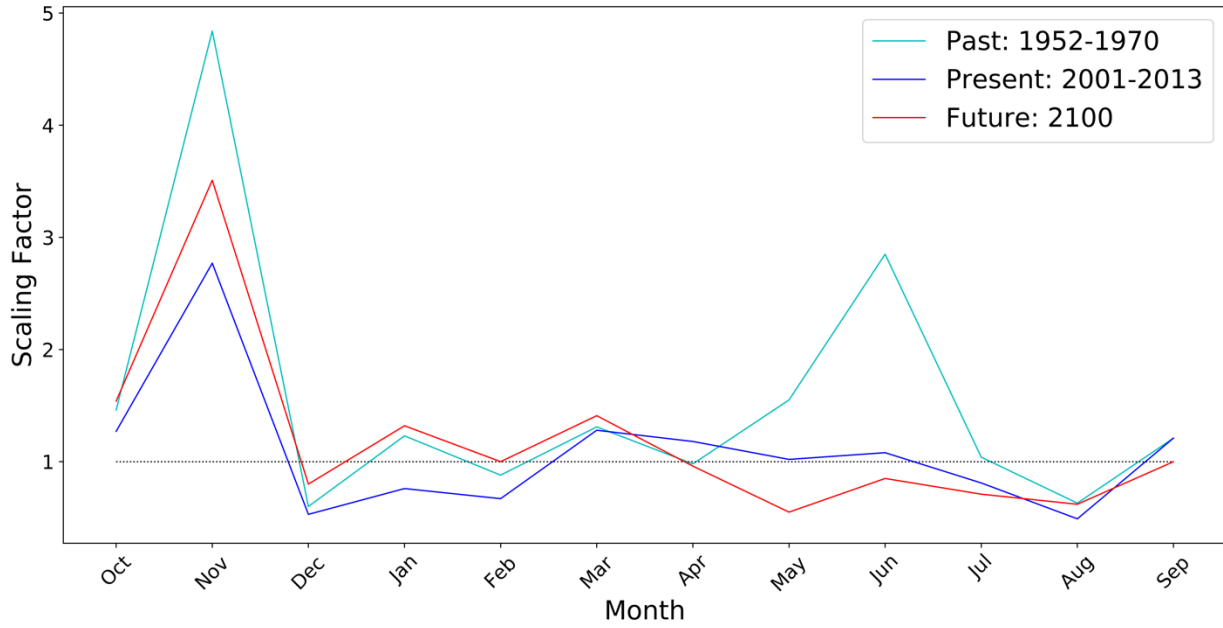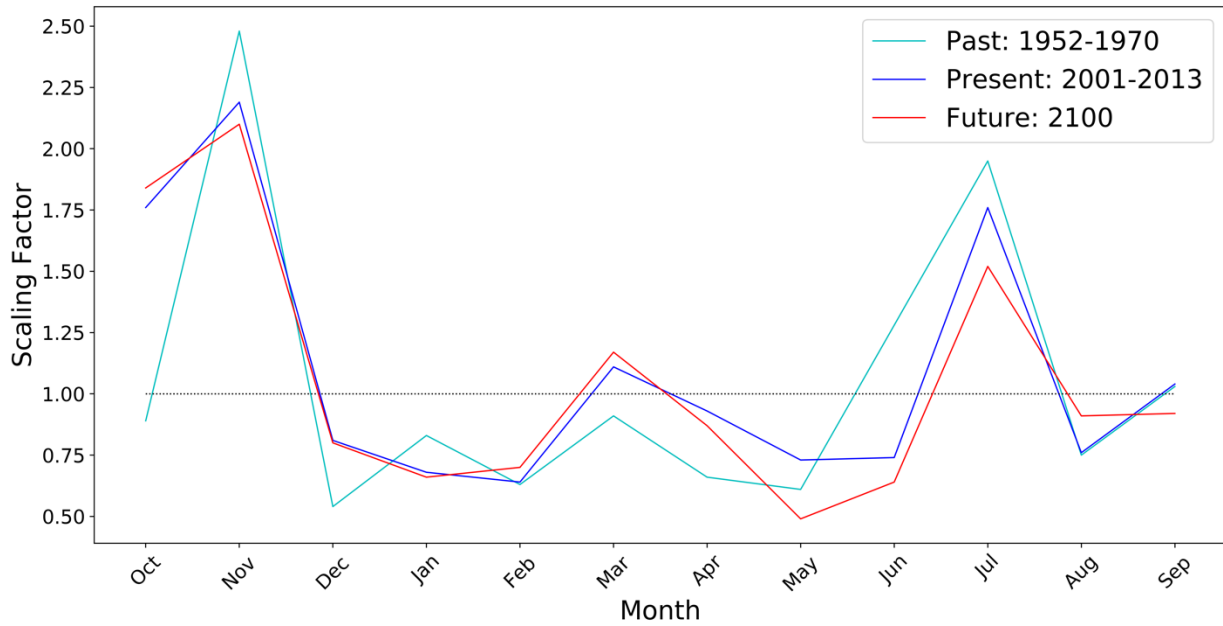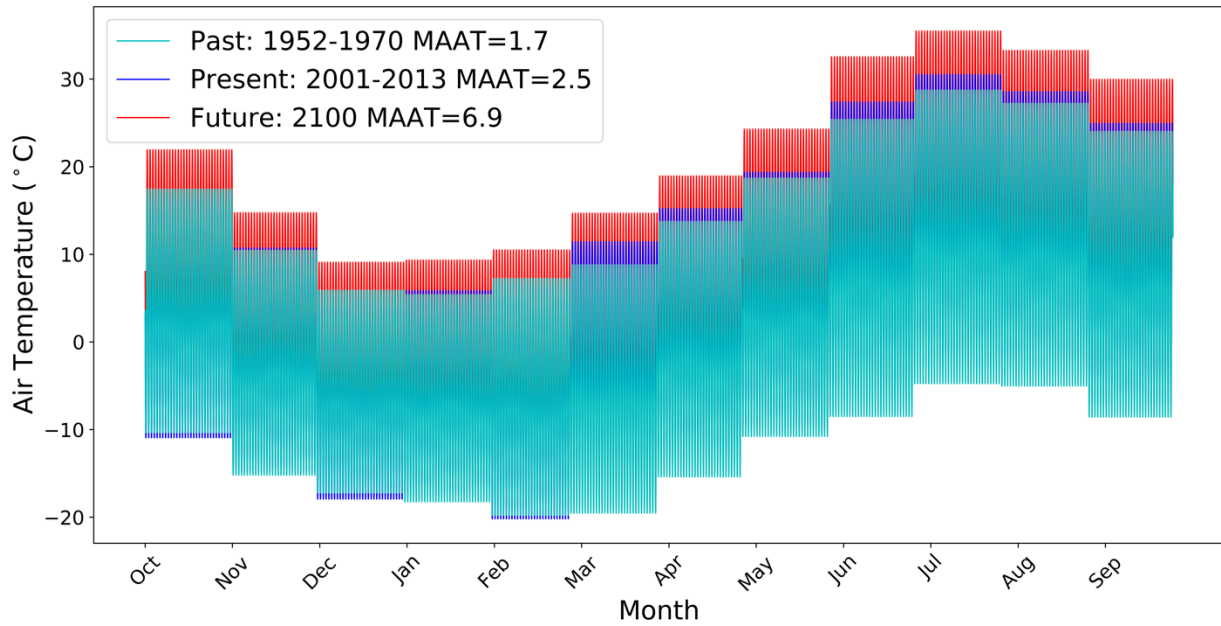
Figure 31. Precipitation scaling factors used in projections of frozen ground for (a) C1 and (b) D1 sites. November scaling factors are large for all time periods, as the precipitation total for November 2008 was relatively small compared to long-term averages.
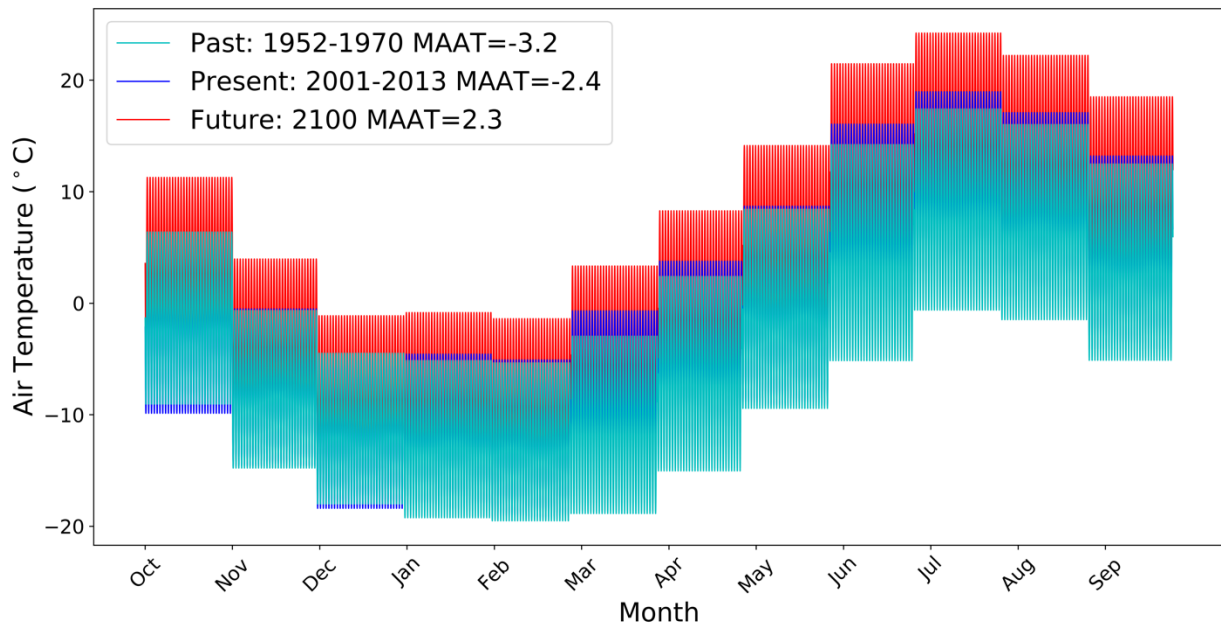
Figure 32. Temperature time series used in projections of frozen ground for (a) C1 and (b) D1 sites. Mean annual air temperature (MAAT) is displayed in the figure legends.

3.3.1   Projections of Seasonally Frozen Ground:

For SFG simulations, a two-dimensional domain with width 5m and depth 5m (D1) and depth 10m (C1) and a spatial discretization of 10 centimeters was run at an hourly timestep. The domain was inclined at the slope angle, estimated using a terrain mapping tool. Four sets of SFG simulations were performed and are summarized in Table 8: C1 and D1 sites, including and excluding snow. The hydrologic boundary condition on the soil surface is a prescribed infiltration flux condition determined from the amount of rainfall or snowmelt produced during that timestep, adjusted for the occurrence of surface flow. A water table was established at the base of the domain (5m depth for D1, and 10m depth for C1) based on depth-to-water table data [Williams, 2019]. Data from groundwater wells near C1 were used for that site, whereas data from the groundwater wells at the Martinelli site were used as a proxy at D1, which does not have a groundwater well. The downstream boundary was assigned a "hydrostatic" condition to allow "interflow" from the system, while the remaining boundaries were assigned zero-flux conditions. The surface flow formulation is described in Chapter II.

3.3.2   Projections of Permafrost:

For permafrost simulations, a one-dimensional domain with depth 1km and a vertical discretization of 10 centimeters at depths 0m-10m and 1m at depths 10m-1km was run at a daily timestep. Such a deep domain is required to accurately simulate the permafrost "base", which occurs at depths on the order of hundreds of meters below the soil surface. The model layer at depths 10m-1km was populated with parameters for bedrock ($\phi = 0.01$; $\kappa = 10^{-15}\ m^2$) [Welch and Allen, 2014]. As these simulations require many years of spin-up to achieve a steady state condition, the thermal boundary condition imposed on the soil surface was simplified significantly: the surface was forced with monthly average air temperatures. The deep soil boundary was assigned a geothermal heat flux condition [Ehlers, 2004]. All boundaries were assigned zero-flux hydrologic conditions and no

recharge was applied to the domain. Atmospheric pressure was specified at a depth of 10m below the soil surface. Simulations were performed using forcings from the high alpine D1 site and the subalpine C1 site, but as no permafrost was simulated in any scenario at C1, results are presented from D1 only. While mapping the full extent of permafrost would require a multi-dimensional domain with a detailed representation of surface topography due to the influence of lateral heat fluxes [Noetzli et al. 2007; Gruber and Haeberli, 2007], one-dimensional simulations provide a useful starting point, particularly for evaluating active layer dynamics.

Because deep soil temperatures respond very slowly to changes in climate, permafrost simulations were designed to proceed in a pseudo-transient fashion. The simulation for the past (1952-1970) scenario was initialized similarly to the SFG simulations above, and the model was forced with past temperatures for 1500 years, the amount of time required for the depth-averaged change in mean annual ground temperature to fall below 1%. Although the soil temperature profiles are nearly equilibrated after 1500 years, the model domain is not considered to have reached a steady state condition, as evidenced by the continued descent of the permafrost base following the spin-up routine (see section 4.4). While no attempt was made to simulate changes in climate over those 1500 years, a spin-up approach in which the climate for a defined period is repeated for many model runs is common in the literature (e.g. 1979-1983 data for 10 model runs in Fiddes et al. [2015]; 1951 data for 400 model runs in Guo et al. [2012]). The solution from the past simulation was restarted and forced with a temperature time series linearly interpolated between the past and present scenarios. We computed the difference between monthly temperatures in the past and present scenarios, and then divided by 46, the number of years between the midpoint of the climatology time period (i.e. 2007 – 1961). With each year of simulation, then, the temperature forcings increasingly resemble the present temperatures, representing the amount of time that has progressed between the past and present

scenarios without incorporating the measured data from the period 1970-2000. Next, the solution from the present simulation was restarted and forced with a temperature time series linearly interpolated between the present and future scenarios. We computed the difference between the present and future temperatures and then divided by 95, the number of years associated with the climate perturbation used in the original projections from Liu et al. [2017]. With each year of simulation, then, the temperature forcings increasingly resemble the future temperatures. Thus, the simulation begins with a quasi-steady state climate corresponding to past (1952-1970) and then proceeds in a pseudo-transient fashion to present (2000-2013) and future (2100), retaining thermal memory within the system.

4.   Results

The results from three classes of simulations described in section 3 are presented in this section. Throughout this section, the Nash-Sutcliffe (NS) model efficiency coefficient is used to characterize the accuracy of model outputs. While this statistic has traditionally been reserved for streamflow models, it is used here to characterize soil temperatures and snow depths. A NS score of 1 corresponds to a perfect match between simulations and observations, and a coefficient of 0 indicates that the model is no more efficient than the mean of the observations.

4.1 Modeled Snow Depths

Simulations including the effects of the seasonal snowpack were compared to simulations excluding the effects of the snowpack to determine the influence of snowcover at each site. Snow model outputs for the C1 and Saddle sites were qualitatively compared to snow depth data at Niwot Ridge from water year 2012 [Lestak et al., 2013] to assess model accuracy. C1 and Saddle snow depths were taken as the median of all "control" plots from the upper subalpine and alpine sites in that study. Although snow density information is generally not available and the snow depth observations are not collocated with the soil temperature

sensors, snow depth data provide an order-of-magnitude estimate of model accuracy. This comparison demonstrated that the model accurately simulated the snowpack at the alpine Saddle site (Figure 33a, middle), but dramatically underestimated snow depth at the subalpine C1 site (not shown in Figure 33a). Simulated snow depths in the subalpine were significantly improved by removing the evaporation and sublimation term from the snow water balance (shown in Figure 33a, right), although it should be noted that the mechanism leading to greater snow depths is related to wind. In the subalpine forests of the Colorado Front Range, wind typically removes snow from one site and deposits it at an adjacent downslope site; these additional snow inputs resulting from windblown snow may not be measured by heated precipitation gages. Thus, we assume that most snow removed from the surface of the snowpack by wind is serially replaced by upslope snow. In the alpine zone, however, snow that is removed from exposed sites is not likely to be replaced.

Modeled snow water equivalent is presented in Figure 33b. Using the snow density parameter in the model (450 kg m^{-3}) to convert from snow water equivalent (SWE) to approximate snow depth, maximum depths are 1.2m, 79cm, and 69cm, at D1, Saddle, and C1, respectively. Taking 50cm as the snow depth threshold required for decoupling between the ground and atmosphere, the transition from "thin" to "thick" snowpack occurs on February 3 at D1, March 1 at Saddle, and March 27 at C1. Modeled snowpack duration is different across sites: although significant accumulation begins in early December at all sites, complete meltout occurs in mid-June at D1, late May at Saddle, and mid-May at C1.
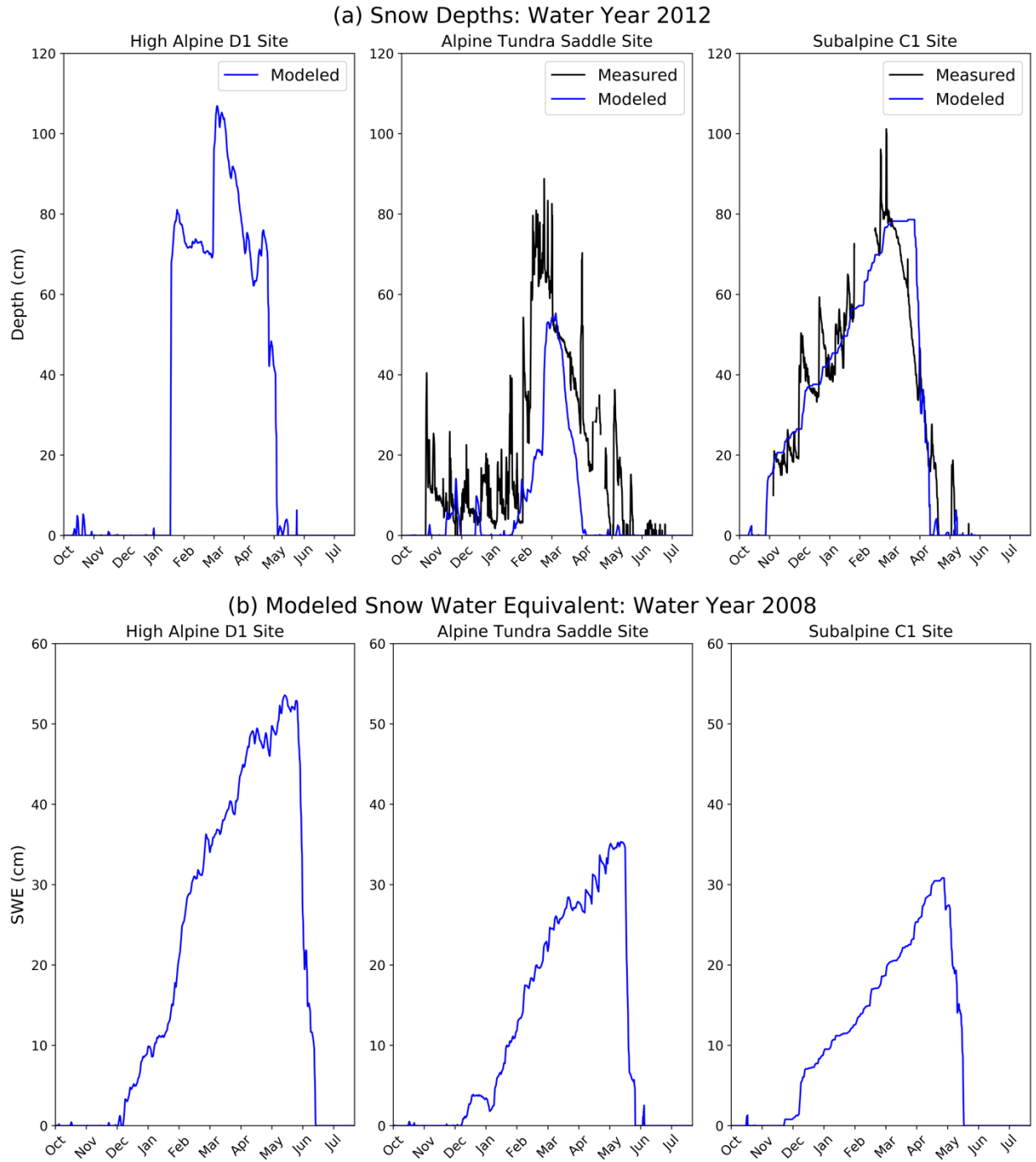
Figure 33. Modeled and measured snow depth for water year 2012 (a) and modeled snow water equivalent for water year 2008 (b) at the D1, Saddle, and C1 sites. Using the snow density parameter in the model (450 kg m⁻³) to convert from snow water equivalent (SWE) to approximate snow depth, maximum depths at D1, Saddle, and C1 in (b) are 1.2m, 79cm, and 69cm, respectively.

4.2 Modeling the Influence of the Snowpack on Seasonally Frozen Ground

Simulations including the effects of the seasonal snowpack were compared to simulations excluding the effects of the snowpack to determine the influence of snowcover on ground temperatures at each site. Additional simulation details can be found in section 3.1. For each site, results are presented for the entire study period (water years 2000-2014 in the (a) figures) and for years that were identified as demonstrating significant snowpack influence at the subalpine C1 site (water years 2006-2009 in the (b) figures). The second set is presented to highlight the influence of the snowpack at each site.

At D1 (Figure 34a), simulations excluding and including snow reproduce soil temperatures with similar accuracy (NS=0.67 and NS=0.68, respectively), indicating that the high alpine snowpack at D1 does not exert a strong insulating effect on ground temperatures. At this site, the snowpack model tends to overestimate soil temperatures and underestimate the occurrence of soil freezing, suggesting that wind scour may limit snow accumulation to a greater extent than is simulated in the snow model. The influence of the modeled snow depths on decoupling soil temperatures from air temperatures is also not evident in the data that indicate persistent diurnal fluctuations during winter. However, during water years 2006-2009 (Figure 34b), the model including snow improves soil temperature estimates slightly (NS improves by 0.11-0.14) but tends to overestimate November-February temperatures and underestimate March-April temperatures.

At the Saddle site (Figure 35a), simulations including snow achieve higher accuracy (NS=0.80) than those excluding snow (NS=0.61), highlighting the snowpack influence at the Saddle. It is important to note that although the snowpack exerts a warming effect on soil temperatures, it does not prevent ground freezing altogether. Unlike at D1, the data indicate an absence of diurnal fluctuations, an effect which is reproduced by the

simulations with snow. During water years 2006-2009 (Figure 35b), the model including snow significantly improves soil temperature estimates (NS improves by 0.18-0.44).

At C1 (Figure 36), simulations excluding snow do not reproduce soil temperatures as accurately (NS=0.24) as simulations including snow (NS=0.74). The data indicate a wintertime "zero-curtain" type behavior in several years, which is accurately captured by the model with snow. Traditionally, the zero-curtain refers to the latent heat barrier which must be overcome during phase changes in soil water, whereas in this context, the term zero-curtain is used loosely, because the persistence of near-0°C soil frost in this case is due to the presence of the snowpack more than the latent heat barrier. During water years 2006-2009 (Figure 36b) When the model is applied to those years with strong snowpack influence (Figure 36b), the model including the snowpack improves NS scores significantly (NS improves by 0.42-0.52).

Based on the comparison across the sites, it is reasonable to conclude that as elevation increases, the influence of the snowpack decreases as a result of low air temperatures that maintain cold snowpacks and wind scouring that keeps snowcover thin and intermittent. Observations suggest that snowpack cold content is maintained later into the winter season in the alpine zone than in the subalpine zone, with peak cold content occurring February 14 in the subalpine and March 19 in the alpine zone [Jennings et al. 2018]. At the subalpine C1 site, the snowpack exerts a much stronger warming effect on ground temperatures due to its lower cold content compared to the alpine snowpack. In the subalpine zone, the influence of the snowpack is very accurately reproduced using the model including snow because the accumulation and ablation pattern simulated in the model is a good representation of snowpack conditions in the subalpine zone, using the snow model modification for wind redistribution discussed in section 4.1. As with the Saddle site, the snowpack exerts a warming effect on soil temperatures, but does not prevent ground freezing altogether. At the higher elevation sites, significant wind scouring produces

irregular accumulation and ablation patterns that are not perfectly reproduced using the physical snowpack model, which is more strongly controlled by surface energy fluxes than redistribution of snow by wind. That the snowpack model tends to underestimate the occurrence of soil freezing at D1 suggests that wind scour limits snow accumulation to a greater extent than is simulated in the model. In our model, the evolution of 5cm soil temperatures is strongly controlled by the the snowpack temperature; thus, an overestimation of snow depth results in an underestimation of snowpack cold content and an overestimation of ground temperatures. Further, soil temperature measurements are taken from climate stations with ~50cm square data logger boxes that inevitably reduce snow accumulation compared to the surrounding area; thus, our results are representative of the landscape integrated as a whole, despite discrepancies at the measurement locations.
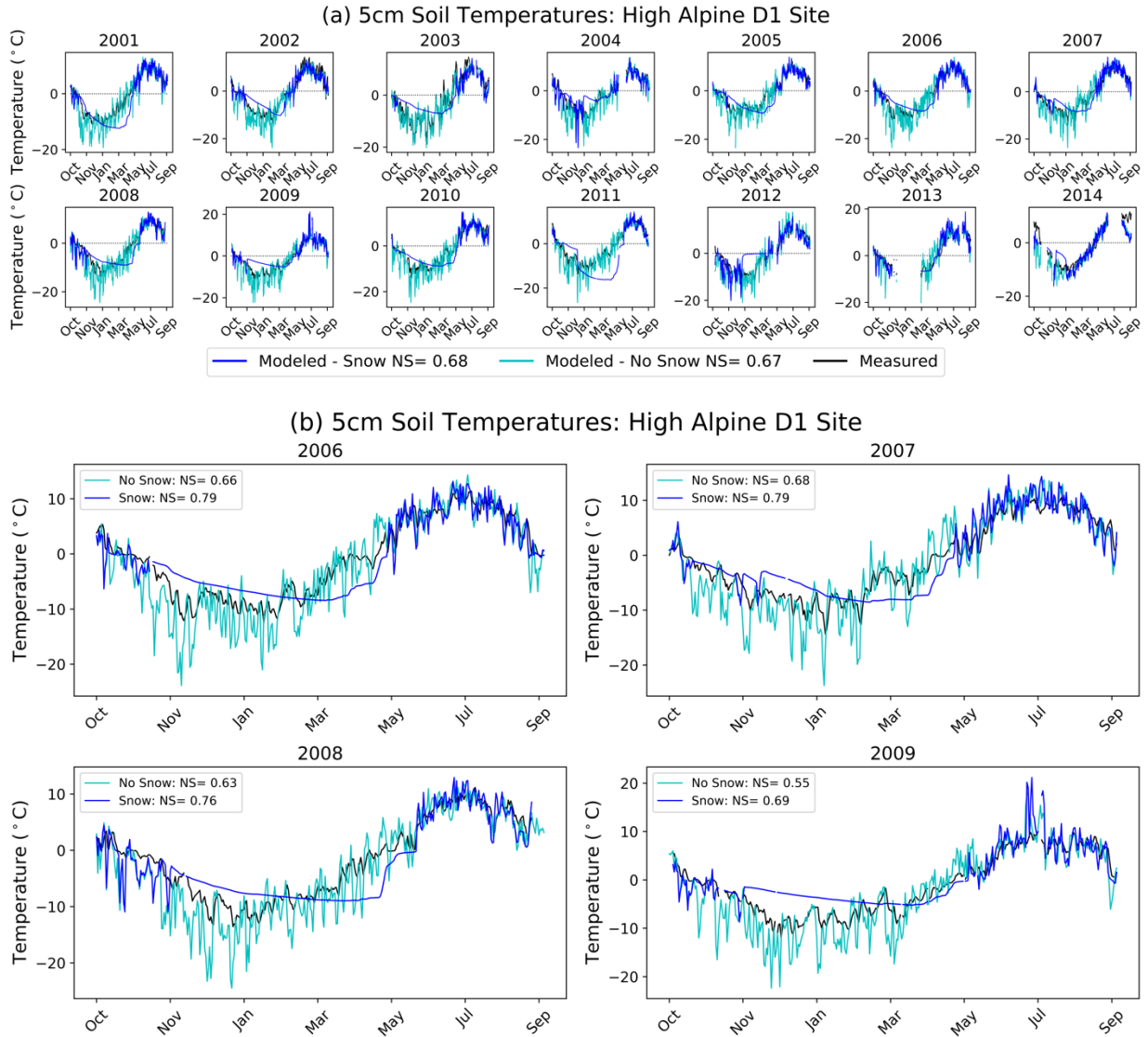
Figure 34. (a) Measured soil temperatures (black) compared to modeled soil temperatures excluding the effects of the snowpack (cyan – NS = 0.67) and including the effects of the snowpack (blue – NS = 0.68) at the high alpine D1 site. (b) Modeled soil temperatures are slightly improved (NS increases of >0.11) by incorporating the snowpack during water years 2006-2009, but the model with snow tends to overestimate November-February temperatures and underestimate March-April temperatures.

Figure 35. (a) Measured soil temperatures (black) compared to modeled soil temperatures excluding the effects of the snowpack (cyan – NS = 0.61) and including the effects of the snowpack (blue – NS = 0.8) at the alpine tundra Saddle site. (b) Modeled soil temperatures are significantly improved (NS increases of >0.18) by incorporating the snowpack during water years 2006-2009.
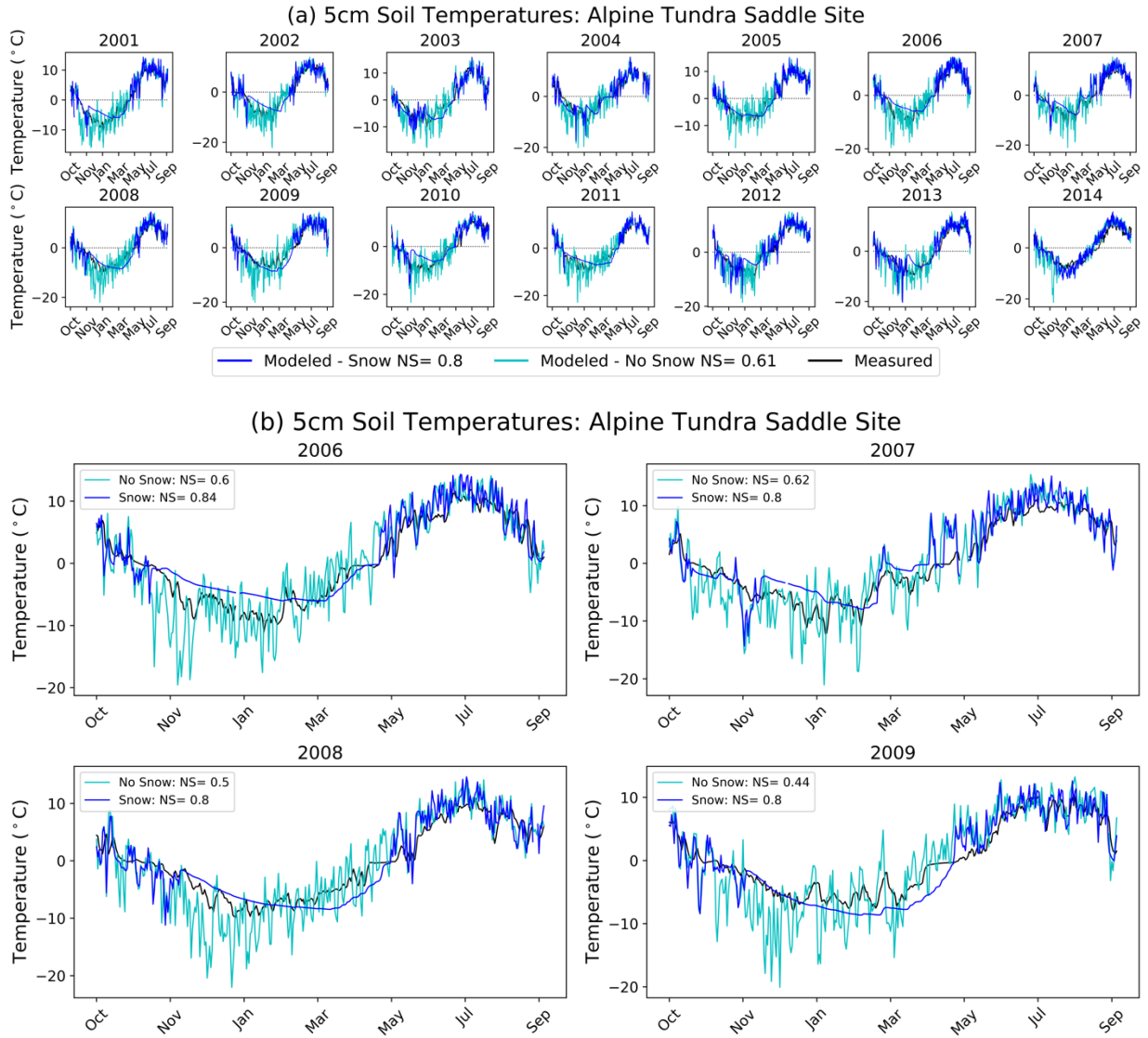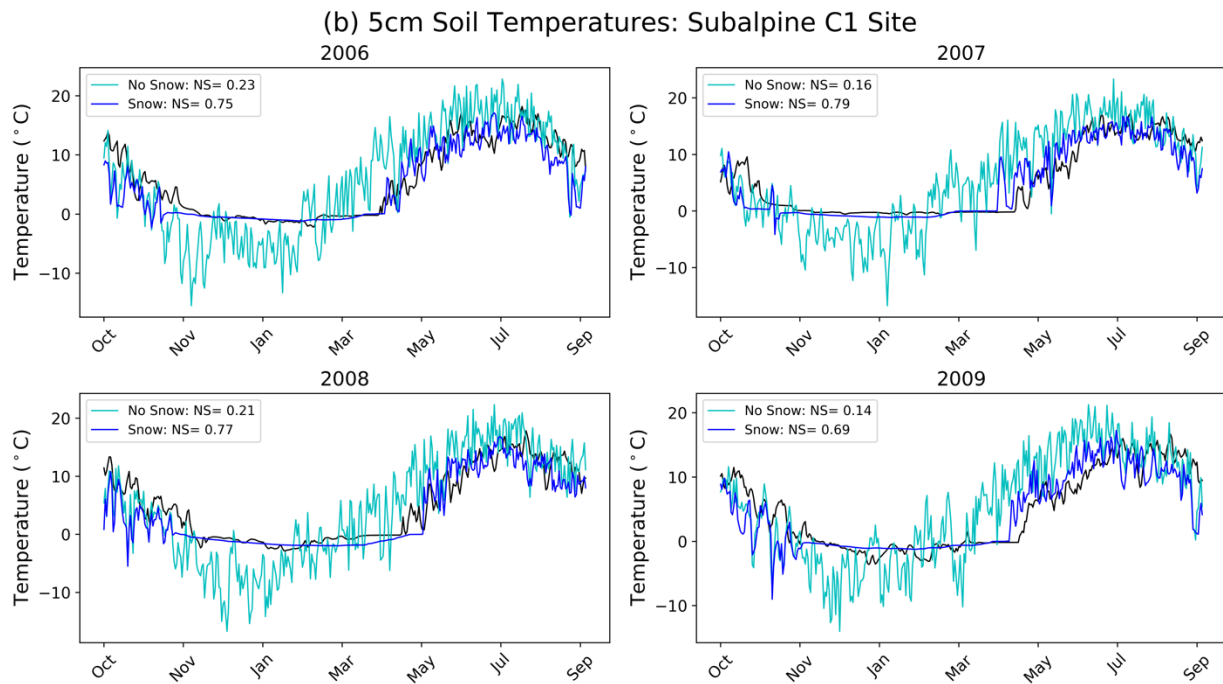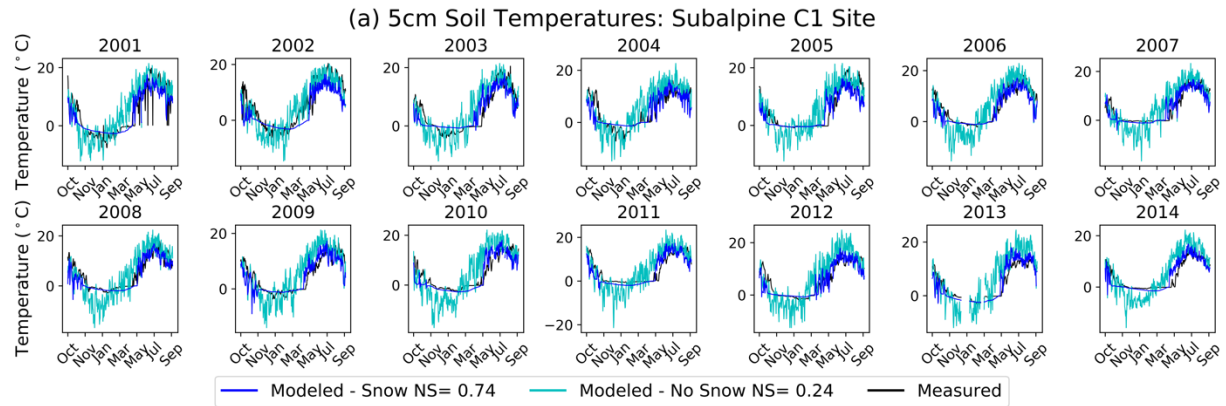
Figure 36. (a) Measured soil temperatures (black) compared to modeled soil temperatures excluding the effects of the snowpack (cyan – NS = 0.24) and including the effects of the snowpack (blue – NS = 0.74) at the subalpine C1 site. (b) Modeled soil temperatures are significantly improved (NS increases of >0.52) by incorporating the snowpack during water years 2006-2009.

Soil temperatures at 2m below the ground surface from 2008 at the Fahey site [Leopold et al., 2014] are compared to model outputs for the Saddle site during the same time period period (Figure 38). Results from the Saddle site (3500m) were chosen for comparison to the Fahey site (3528m) due to similar elevations and proximity (see Figure 37). A variety of model scenarios are compared to determine the influence of the snowpack and soil thermal properties on deep ground temperatures at this site: snow vs. no snow, snowmelt infiltration vs. no infiltration, and clay vs. organic soil thermal properties at depths 0-1m. The simulation using organic soil thermal properties at 0-1m depth, without recharge, and without the influence of snowcover reproduces observed soil temperatures most accurately (NS=0.78), suggesting little influence of snowmelt infiltration and snowpack insulation on deep ground temperatures and the existence of a low-thermal-diffusivity soil layer at that site. Leopold et al. [2014] achieved a good match between modeled and measured soil temperatures January-July by using a low thermal diffusivity (0.85 mm^{2}s^{-1}) but underestimated summer temperatures, suggesting that heat advected with meltwater infiltration acted to thaw the deep soil, followed by a rapid increase in ground temperatures in August after the ice-water phase change had taken place.

Our results suggest a strong role for phase change in driving these deep soil temperatures, but not for heat advected with meltwater infiltration. In our model run, the rapid decrease in soil temperature during January was slowed by phase change at 0°C in February, followed by a period of relatively constant soil temperatures (late February-late April) as the now-ice-filled soils at 2m "passed" cold content down to deeper soil layers, followed by a period of steadily increasing soil temperatures (May-July), driven by both the geothermal heat flux and rising surface temperatures. Following thaw in late July, conduction-driven heat flow rapidly increased soil temperatures. In the model run with meltwater infiltration, the rapid rise in soil temperature was not reproduced well due to higher bulk soil thermal diffusivity with soil water content compared to the lower dry soil thermal diffusivity. Thus,

we suggest that phase change only, and not phase change combined with meltwater infiltration was responsible for the 2m soil temperature patterns observed in 2008.

Our results suggest that soil water generally plays a much stronger role in buffering winter and spring soil temperatures by providing a latent heat barrier than in increasing summer temperatures by advecting heat from the surface to lower layers. Meltwater infiltration did not significantly influence 2m ground temperatures at this site due to either rapid infiltration through the 2m layer to the deeper subsurface or significant shallow lateral flow resulting from layering that limited infiltration into the deeper subsurface. In any case, soil water did not remain in the 2m layer long enough to influence ground temperatures.
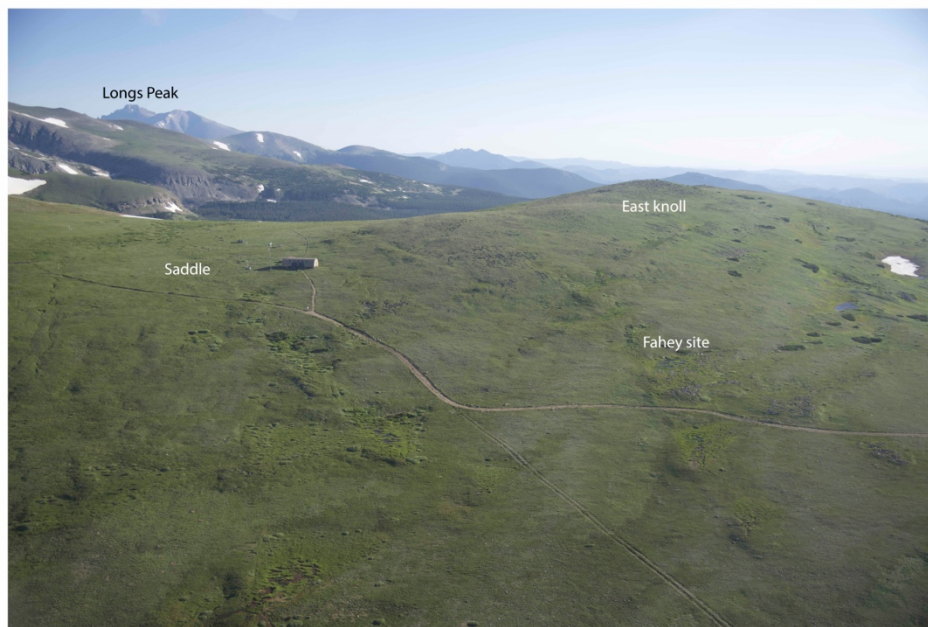
Niwot Ridge aerial view looking north

Figure 37. Satellite map of Niwot Ridge (top) and photograph of Saddle and Fahey sites (bottom) displaying the proximity of the Saddle (3528m) and Fahey (3500m) sites. Images courtesy of Dr. Robert Anderson.

Fahey Site: 2m Ground Temperature 2008
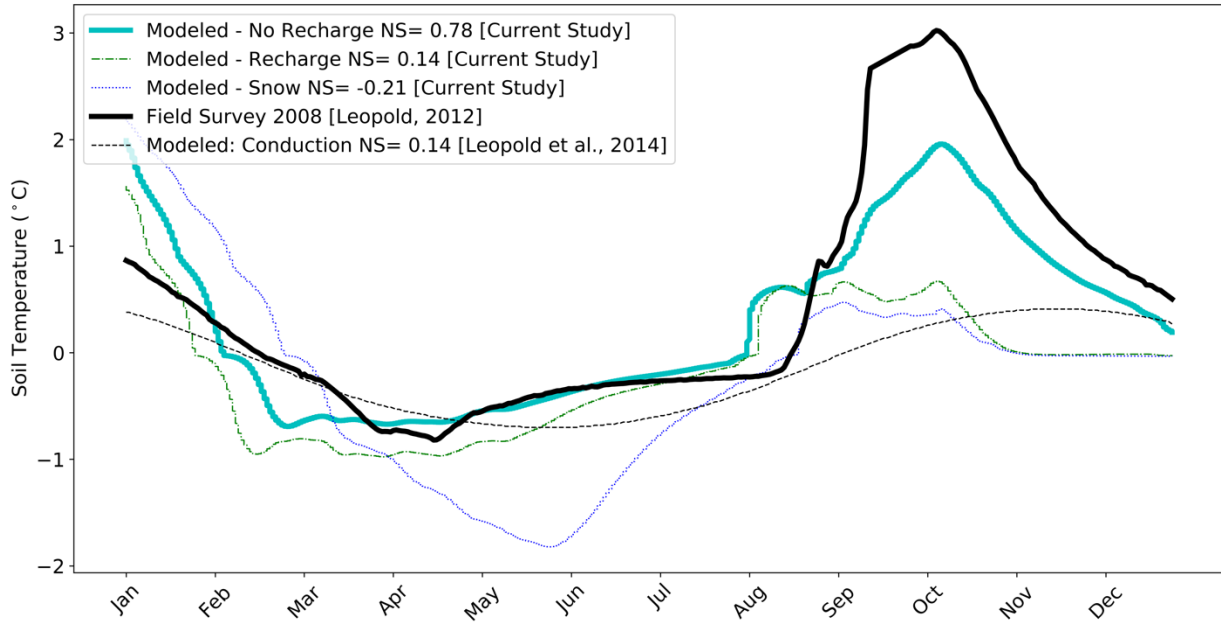
Figure 38. (after Figure 6 from Leopold et al. [2014]) 2008 2m ground temperatures (black – solid) at the Fahey site compared to 2008 simulations excluding snow and recharge (cyan – solid), including snow (blue – dotted), including snow (green – dash-dotted) at the Saddle site. Soil temperatures produced using a conduction model from Leopold et al., [2014] (black – dashed) are also included. The simulation using an organic soil layer, excluding snowpack influence, and excluding meltwater infiltration produces the best match (NS=0.78) to observed temperatures.

4.3 Hydrologic Consequences of Frozen Ground

Following the conceptual model proposed by Hill et al., [2015], we computed the influence of seasonally frozen ground on infiltration and groundwater recharge beneath adjacent snow-covered and bare, wind-scoured sites during water year 2008. Average soil ice content for April 1 – June 30 at each site is presented in Figure 39. The "wings" described in section 3.2 and Figure 30 are excluded from this figure; only the results from 5m-15m are presented. A quantitative evaluation of the influence of frozen ground on subsurface flux is presented in Figure 40. Additional simulation details can be found in section 3.2. At D1 (Figure 39, top), deep (>1m) ice formation occurs beneath snow-covered and bare ground patches, but freezing depth is greater beneath the bare ground patch (1-2m) than beneath the snow-covered patch (1-1.5m). At the Saddle site, deep (>1m) ice formation occurs beneath both snow-covered and bare ground patches, but freezing depth is again greater beneath the bare ground patch (1-2m) than beneath the snow-covered patch (1-1.5m). At C1, only shallow (<1m) ice formation is simulated; freezing is more intense beneath the snow-covered patch because the bare ground patch is exposed to solar radiation and warm air temperatures before the snow-covered patch. Here, our results diverge from the conceptual model in Hill et al., [2015], which considered ground beneath the snowpack to remain completely thawed during snowmelt. Small effects of flow through the "wings" (0-5m and 15-20m) of the domain can be seen at the fringes of the ice lenses displayed in Figure 39, where flow around the lens contributes to higher ice saturation near the edge of the ice lens. For example, at the Saddle site, ice saturation at depth 1-1.2m is slightly higher at 6m and 14m near the "wings", than at 9m and 11m, far from the "wings". However, the fluxes presented in Figures 40 and 41 are calculated at the center of each ground patch (7.4m-7.6m for the snow-covered patch, and 12.4m-12.6m for the bare ground patch) to minimize the effects of the boundaries on results.
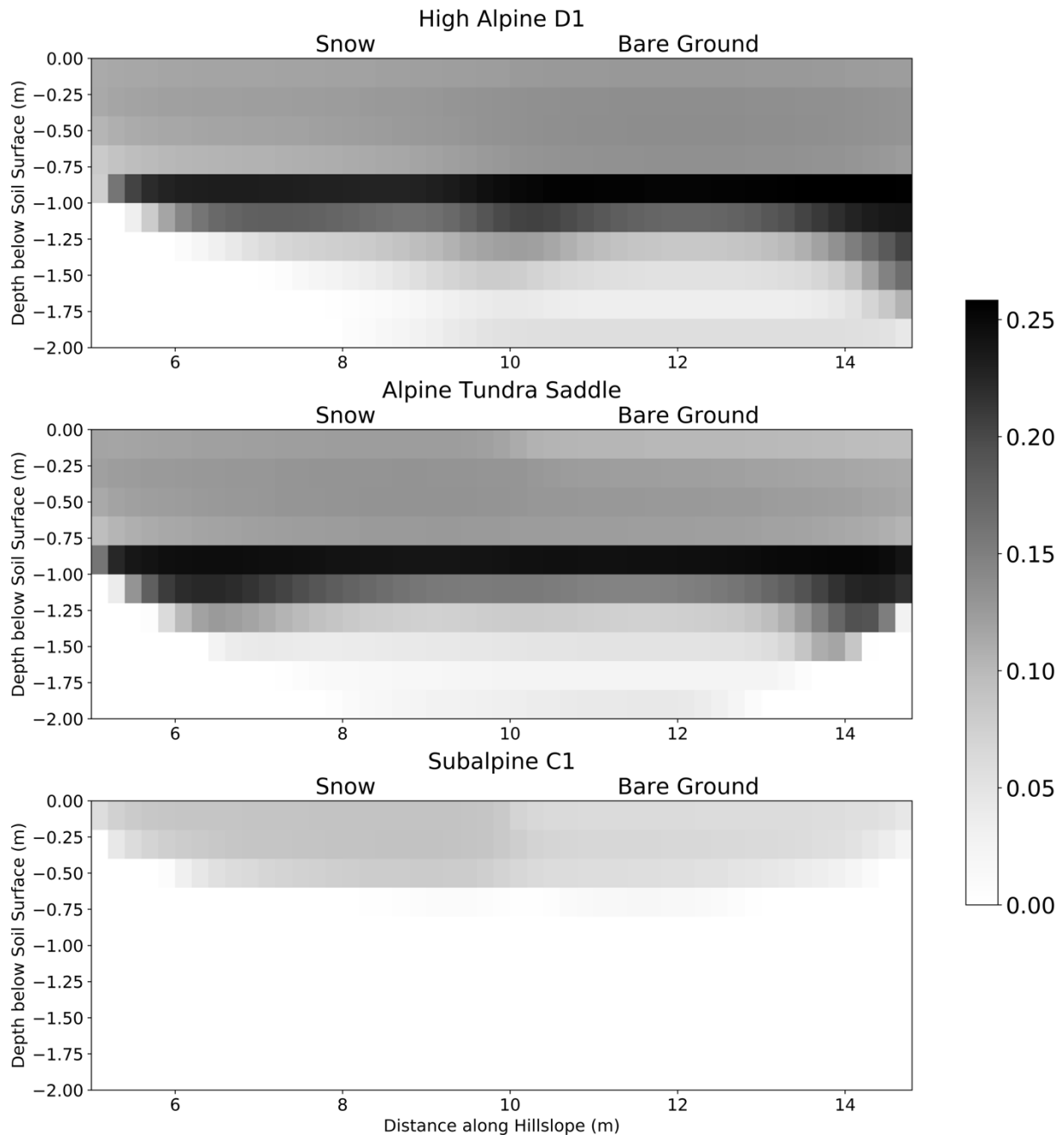
Figure 39. Average subsurface ice content (grayscale) at the high alpine D1 site, alpine tundra Saddle site, and subalpine C1 sites during the thaw period (taken as April 1 – June 30). The "wings" described in section 3.2 and Figure 30 are excluded from this figure; only the results from 5m-15m are presented. At D1 and Saddle, mild freezing occurs in the shallow subsurface and intense freezing occurs at depths >80cm; snow-covered ground experiences less intense freezing due to snowpack insulation. At C1, intense freezing occurs in the shallow subsurface at depths <80cm; bare ground experiences less intense freezing during this time period due to earlier exposure to solar radiation and warm air.

The cumulative reduction in vertical subsurface flux due to the presence of frozen ground is presented in Figure 40. Fluxes were computed at the center of each model patch: 7.4m-7.6m for the snow-covered patch, and 12.4m-12.6m for the bare ground patch. Such an approach serves to isolate the influence of the boundaries imposed on the soil surface at 5m-10m and 10m-15m. Shallow frozen ground (<1m) beneath the snow exerts a strong influence on 1m vertical flux, while deep (>1m) frozen ground beneath bare ground exerts a strong influence on 2m vertical flux.

Freezing in the shallow subsurface (0-1m) beneath snow-covered patches strongly reduces 1m vertical flux (54-73%) because the ground remains partially frozen while the snowpack is melting (Figure 40a). Shallow frozen ground beneath bare ground patches exerts a much smaller effect on 1m fluxes (-14-5%) for two reasons: (1) bare surface soils tend to be thawed by the time they receive excess snowmelt "run-on" from the snow-covered patch (e.g. C1); (2) high intensity winter soil freezing beneath bare ground draws water toward the soil surface (cryosuction), and releases this water during the thawing process. Thus, similar amounts of water flow through 0-1m soils in the simulations with and without freezing. At D1, so much water is drawn to the soil surface that the net annual effect of freezing is to *increase* flux: freezing soils draw water upward from the shallow water table (5m depth) in the winter and release it in the summer, contributing to *higher* flux in the freezing simulation than in the thawed simulation. Overall, these results describe a system in which pore spaces in the soil beneath a snowpack are saturated with liquid and solid water, forcing snowmelt to flow downslope (perhaps within the snowpack or in a thin layer between the ground and the snowpack), and infiltrate into recently-thawed bare ground. Such a conceptual model differs from that presented by Hill et al., [2015]: since frozen soil is able to persist beneath even deep snowpacks in our model, water is prevented from infiltrating into the ground beneath the snowpack. Due to earlier exposure to solar

149

radiation, shallow frozen bare soil thaws earlier than snow-covered ground, allowing more snowmelt infiltration.

At D1 and Saddle, ice formation in the deep subsurface (1-2m) beneath bare ground patches strongly influences 2m fluxes (56% and 23%, respectively) because deep soil ice is able to persist later into the melt season and intercept flow (Figure 40b). At C1, however, no ice formation is simulated in the deep subsurface (>1m depth), but 2m flux is reduced by 44%, suggesting a mechanism through which deep soils beneath the bare ground and snow-covered patches interact hydrologically. When 2m fluxes beneath snow-covered ground decrease, lateral fluxes diverted by the low-permeability saprolite layer into the deep subsurface beneath the bare ground patch also decrease. In the simulation without freezing, greater infiltration into snow-covered ground than bare ground drives deep subsurface flow beneath the bare ground patch due to the low-permeability saprolite layer (>2m depth) that induces lateral flow. In the freezing simulation, the interception of infiltration by frozen soil beneath snow-covered ground reduces deep subsurface fluxes beneath both patches. Thus, by reducing the ability of snowmelt infiltration to enter the deep subsurface (>1m depth), shallow freezing beneath snow-covered ground during the melt season influences the entire system at depths >1m. From the perspective of the deep subsurface, vertical fluxes beneath bare ground and snow-covered patches are reduced to a similar extent.
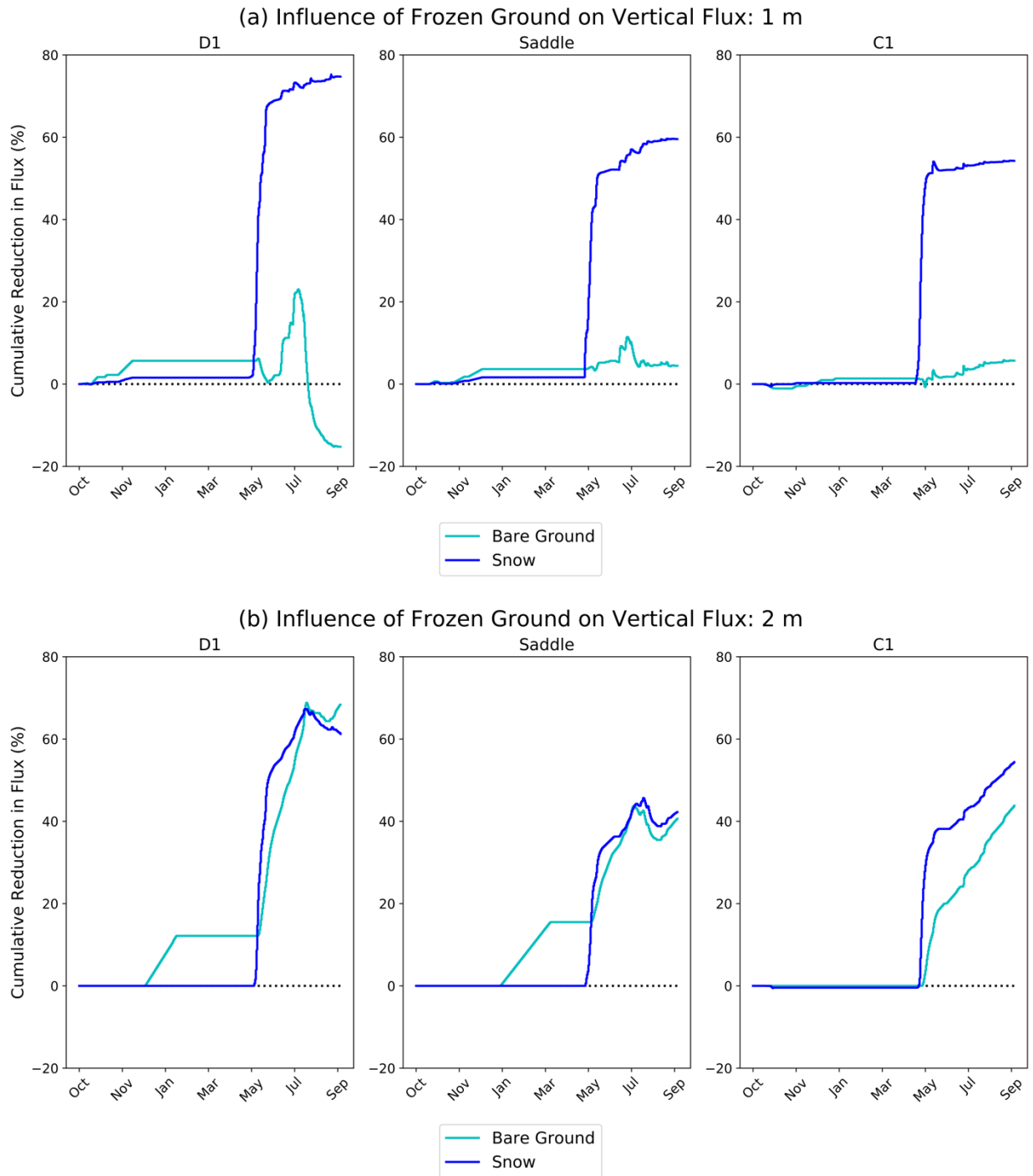
Figure 40. Cumulative reduction (%) in vertical flux at (a) 1m and (b) 2m depth due to the occurrence of frozen ground; a positive value indicates a reduction in flux. Simulations including the formation of frozen ground are compared to simulations in which the soil is prevented from freezing. A "negative reduction" (e.g. top left – 1m D1 snow) is related to cryosuction: freezing soils draw water from the shallow water table in the winter and release it in the summer, contributing to *higher* flux in the freezing simulation.

Figure 41. Ice saturation at 50cm depth beneath bare (cyan) and snow-covered (blue) patches. At C1, the bare ground patch thaws nearly one month before the snow-covered patch due to earlier exposure to solar radiation.

4.4 Retrospective and Prospective Soil Temperature Analysis

Climatologies computed for past (1952-1970), present (2000-2013), and future (Pseudo-Global Warming transformation of 2000-2013) were used to analyze the effects of climate on the occurrence of seasonally froz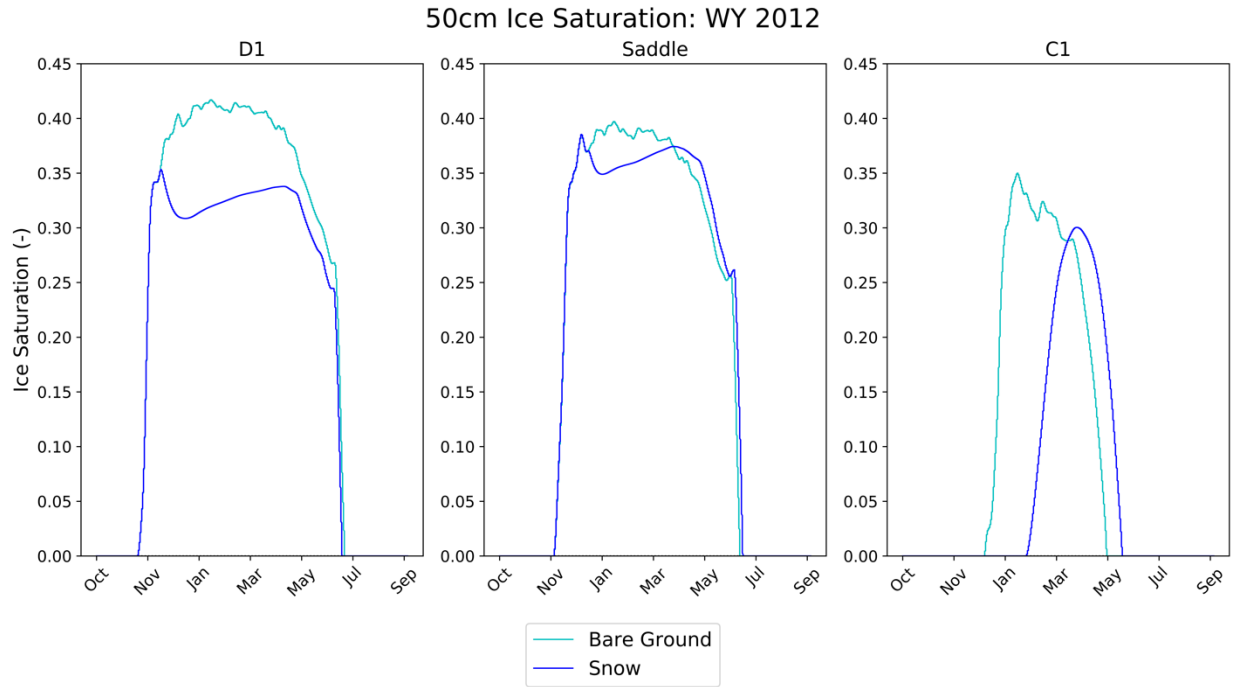en ground and permafrost at Niwot Ridge C1 and D1 sites. Additional simulation details can be found in section 3.3. SFG simulations are presented in Figures 42. In Figure 42a, projections for C1 and D1 were produced by including the snowpack, whereas in Figure 42b, projections were produced using the surface energy balance and air temperature alone. Model validation demonstrated that the ground thermal regime at C1 is strongly controlled by the snowpack, while D1 soil temperatures can be reproduce without the snowpack. Thus, the results from Figure 42a, left (C1 – snow) and Figure 42b, right (D1 – no snow) reflect conditions at measurement sites, while the results in Figure 42a, right (D1 – snow) and Figure 42b, left (C1 – no snow) are included to reflect the full range of ground conditions present across the landscape.

We begin by discussing the simulated snowpack conditions that control ground temperatures in Figure 42a. Compared to the past and present scenarios, snow accumulates less (at C1, maximum SWE is 0.07 in future compared to 0.24 and 0.20 in past and present; at D1, maximum SWE is 0.24 in future compared to 0.29 and 0.36 in past and present), and melts earlier (at C1, during March in future scenario compared to April in past and present; at D1, during April in future scenario compared to May in past and present). At C1, snow accumulates to a greater depth in the past scenario, whereas at D1, snow accumulates to a greater depth in the present scenario than in the past scenario. As the temperature changes from past to present are relatively consistent at C1 and D1 (Figure 32), these differences are related to the precipitation scaling factors used for each site (Figure 31). At C1, past monthly precipitation means are higher than present values, for December-June, whereas at D1, past monthly precipitation means are generally similar to or lower than present values based on WRF model outputs and long-term datasets.

At both sites, compared to past and present, higher November air temperatures in the future scenario produce higher soil temperatures when snow has not yet accumulated: during this time, soils remain thawed at C1, whereas at D1, soils are warmer, but not thawed. At C1, diminished early season snow in the future scenario induces a brief soil freezing event in early December; snow accumulation at D1 during the same time period prevents a similar event from occurring. During the winter (December-March) at C1, frozen soils exhibit higher temperatures beneath the deep snowpack in the past scenario than beneath the moderate-depth snowpack in the present scenario. In the future scenario at C1, soils remain completely thawed beneath a thin snowpack due to high air temperatures and a warmer snowpack, punctuated by brief freezing episodes during periods of thin snow cover. During the winter (December-March) at D1, frozen soils exhibit the highest temperatures in the future scenario and similar temperatures in the past and present scenarios, beneath snowpacks of similar depths. Earlier snowmelt at both sites (March at C1, April at D1) produces episodic soil freezing events in the future scenario unlike the more sustained freezing conditions in the past and present scenarios due to the presence of the snowpack. Later snow accumulation in the fall and earlier snowmelt in the spring result in approximately two total months of additional soil thaw (one month in the fall; one month in the spring) in the future scenarios compared to the past and present scenarios.

In order to provide a first-order estimate of trends in subnivial soil microbial activity, we compute the amount of time, "wet days", during which liquid water in frozen soil beneath the snowpack increases above a moisture threshold, taken as days when water content is greater than $0.22 \ m^3m^{-3}$ and snow is present (Figure 43). While microbial activity presumably continues at temperatures above 0°C and water contents less than $0.22 \ m^3m^{-3}$, our objective here is to specifically quantify changes in microbial activity in frozen soils beneath the snowpack, when vegetation growth and primary production are not taking place. The high alpine D1 site suggests a trend toward increasing frozen soil microbial

154

activity in the shallow subsurface; there, wet days increase from 37 in the past scenario to 63 in the future scenario. At C1, there are 135 total wet days in the future scenario compared to 134 in the past scenario.

At C1, the lack of November soil freezing in the future scenario would be expected to reduce the amount of soil carbon substrate available for the remainder of the snow season, limiting winter CO_2 production. During December-March, however, thawed soils beneath the snowpack would permit a significant increase in microbial growth and activity compared to past and present, leading to higher carbon loss and nitrogen immobilization, especially considering that the snowpack would continue to supply soil moisture during these months. As heterotrophic activity tends to diminish at the end of the snow season [Brooks et al., 1997], the higher incidence of soil freezing in March would be more likely to influence primary production than microbial respiration: early vegetation growth permitted by the earlier-melting snowpack may be interrupted by such intermittent freezing episodes. At D1, higher November soil temperatures are unlikely to reduce the amount of available soil carbon substrate available for the snow season, as the soil still freezes, albeit exhibiting warmer temperatures. Warmer soil temperatures beneath the snowpack in December-March would promote a higher rate of microbial growth and activity, and late-season soil freezing would again be expected to interrupt primary production more than soil respiration. Overall, an additional five months of thawed soil at C1 (punctuated by low-intensity freezing episodes) would dramatically increase soil microbial respiration and loss of carbon to the atmosphere, while also allowing for higher rates of primary production throughout the conifer forest. Warmer winter soils at D1 would also permit higher rates of microbial respiration, without a concurrent increase in primary production since soils remain frozen and no forest is present; an additional month of thawed soil in the spring when subnivial microbial activity has already waned would likely promote an extension of the growing season and higher ecosystem carbon uptake.

Results from soil temperature projections for the case in which the snowpack was excluded are relatively simpler than those with the snowpack included. At both sites, higher air temperatures in the future scenarios produce approximately two additional months of thawed soils: one month in the fall (November at C1; October at D1) and one month in the spring (March at C1; April at D1). In April at D1, soils transition from a persistently frozen state in the past and present scenarios to a high-frequency freeze-thaw cycle in the future scenario; in May at D1, soils transition from a high-frequency freeze-thaw cycle in the past and present scenarios to a persistently thawed state in the future scenario.

Overall reductions in freezing intensity across both sites would be expected to lead to lower rates of frost creep. The frequency of seasonal soil freezing, which also contributes to frost creep, does not change significantly (aside from a slight increase in frost frequency in snow-covered ground at subalpine C1 during March). In addition, such increases in temperatures are likely to accelerate soil biogeochemical processes, especially in cases where sub-freezing temperatures transition from a state in which liquid water is unavailable (<5-6°C) to a state in which some liquid water is present (>5-6°C), e.g. December-February at C1, November at D1, Figure 42b. In such cases, carbon production is likely to accelerate due to higher microbial activity without a concurrent increase in primary productivity, as the ground remains frozen. These changes are also likely to shift the balance of net ecosystem exchange of CO_2. Recent work at Niwot Ridge has demonstrated that the alpine zone serves as a net carbon source to the atmosphere, while the subalpine zone serves as a net carbon sink [Knowles et al., 2015; Blanken et al., 2009]. A two-month shift in the growing season would increase/reduce the amount of time during which both sites serve as carbon sources/sinks, contributing to lower cumulative CO_2 production. The alpine site would become a weaker carbon source, while the subalpine site would become a stronger carbon sink. However, higher winter CO_2 production due to soil temperature transitions from

water-unavailable frozen states to water-available frozen states (e.g. December-February at C1, Figure 42b) should oppose the trend toward higher CO_2 uptake.
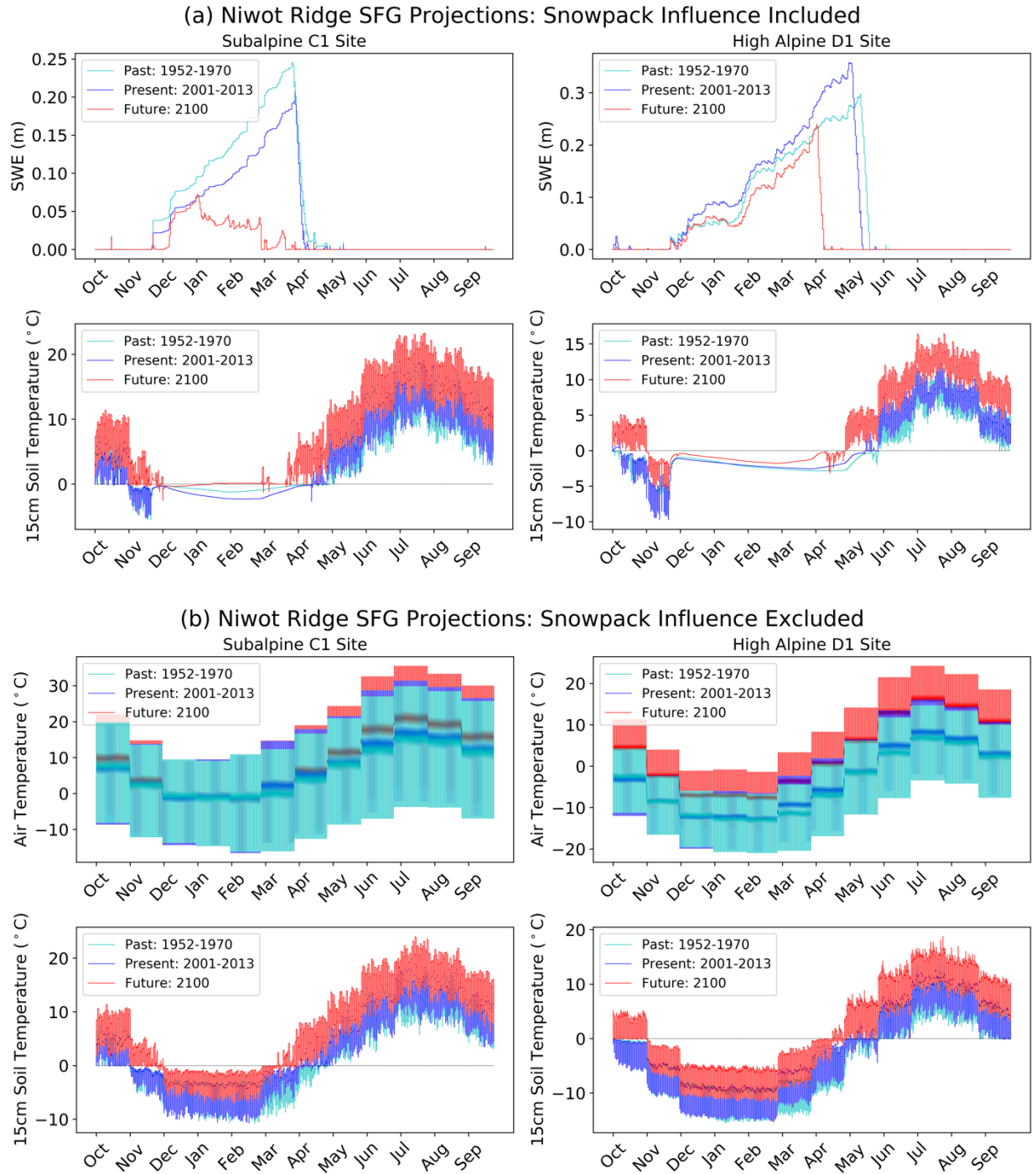
Figure 42. (a) Modeled snow water equivalent (top) and 5cm soil temperatures (bottom) for three climate scenarios at C1 (left) and D1 (right) including the influence of the snowpack on ground temperatures. (b) Air temperature forcings (top) and modeled 5cm soil temperatures (bottom) for three climate scenarios at C1 (left) and D1 (right) excluding the influence of the snowpack on ground temperatures.
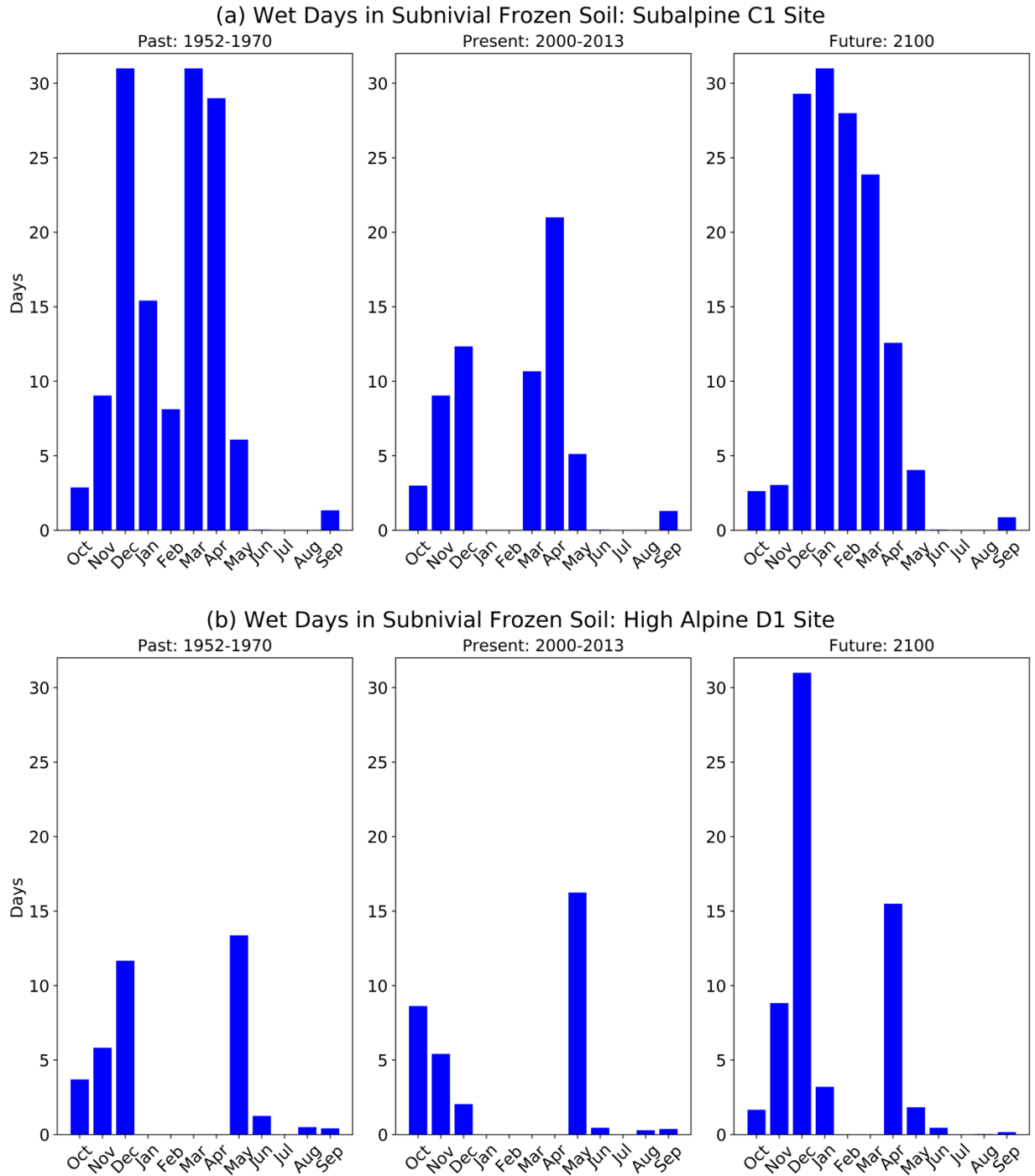
Figure 43. Wet days within subnivial frozen soil (blue) for past, present, and future climate scenarios in surface soils at subalpine C1 site (a) and high alpine D1 site (b). Wet days are defined here as soil water contents (m^3 m^{-3}) greater than 0.22, when snow is present.

Simulated ground temperature profiles beneath the high alpine D1 site are presented for multiple depth ranges in Figure 44 to describe the occurrence of permafrost and identify the active layer thickness and permafrost base. C1 results are not included because they did not suggest permafrost occurrence in any scenario. In the 1952-1970 scenario, permafrost exists at depths ≥1.3m. In the 2000-2013 scenario, permafrost exists at depths ≥1.4m. Finally, in the future scenario (~2100), the active layer depth is 6.4m. The simulated permafrost table at 1.3m depth is relatively shallower than the observations from the 1970's, which suggested an active layer thickness of 2m-5m. This discrepancy suggests that the in-situ thermal diffusivity is higher than the parameter used in the model. Such a difference can be explained by an overestimation of the subsurface porosity: as the porosity decreases, thermal diffusivity increases. A sensitivity analysis in which the porosity was reduced by a factor of 2 (Appendix E) produced active layer thicknesses of 2m, 3m, and 23.9m in the past, present, and future scenarios, respectively. With a higher thermal diffusivity, changes in surface temperature propagate more deeply into the subsurface, resulting in both a thicker active layer in the past and present scenarios, and much greater thaw between the present and future scenarios. Higher rates of thaw are also related to lower water content: the reduction in porosity leads to a reduction in water content and, consequently, a smaller latent heat buffer. An additional sensitivity analysis (Appendix E) in which the water table was specified at the base of the domain, rather than at 10m below the soil surface, demonstrates that the results are largely insensitive to water table depth.

Counterintuitively, the depth of the permafrost base increases slightly in depth between the scenarios (425m in past, 429m in present, and 434m in future). This effect is related to the spin-up routine: although the spin-up routine was performed until subsurface temperatures changed by a small amount with each year of simulation *on average,* the permafrost base continues to descend through the present and future scenarios, revealing a lingering transient effect in the deep subsurface that is unrelated to surface temperature

160

forcing. In both the present and future scenarios, subsurface temperature remains higher at the permafrost base than at depths 100-200m, despite warming at the surface. This temperature gradient drives continued heat flux toward the surface and freezing at the base of the permafrost layer. However, as the goal of the simulations is to quantify changes in active layer thickness and provide a meaningful representation of the response of shallow subsurface temperatures to changes in surface forcing, the deep subsurface behavior is not particularly relevant to the current study, and does not influence the behavior of the active layer. A one-dimensional model comparison is presented in Appendix F to provide context for how conduction and phase change contribute to subsurface temperature profiles.

For each 1°C increase in MAAT the active layer thickness increases 3mm per year from the past to present scenarios and 11mm per year from the present to future scenarios (computed as the change in active layer thickness from Figure 44a divided by the difference in MAAT from Table 7 divided by the number of years between scenarios). Such differences in subsurface response are related to the shift in thermal diffusivity that takes place during the transition from an ice-liquid system to a liquid-vapor water system in thawing soils. As shallow frozen soils thaw, they retain a greater quantity of heat and change temperature more readily. Warmed water in these shallow layers then flows by gravity downward to the still-frozen layers and induces additional soil thaw, producing a non-linear response to changing MAAT.

Since we are unable to perform a similar analysis for a site between D1 and C1 (Saddle site meteorological observations began in the 1970's), our results do not directly address the ongoing questions regarding permafrost occurrence in the 1970's at elevations between 3500m and 3800m. Rather, our results offer temporal context, add depth resolution, and provide support for permafrost occurrence above 3800m. Although this result was not presented in [Leopold et al., 2014], the authors explained in the discussion that one-

dimensional heat conduction simulations performed using 1970's D1 air temperature data allowed for the occurrence of ice lenses that remained frozen through the summer (suggesting permafrost during that time period). Thus, our "past" results agree with that study, whereas our "present" results are more closely in agreement with Janke [2005]. Terrain above 3800m is mostly exposed rock, which may contain water within fracture networks, as well as other cryospheric features like ice fields beneath talus slopes and rock glaciers.

Finally, ground temperatures from the thermo-hydrologic model at 3.8m depth from each scenario are compared to measurements from the Ives (1974) sites [in Leopold et al., 2014] in order to place our results in the context of previous observations. The measurements (Figure 45) were taken at a north-facing site 700m west of the D1 climate station which is characterized by high subsurface thermal diffusivity, as well as large blocks and rock outcrops on the ground surface [Leopold et al. 2014]. Modeled temperatures at 3.8m depth from the present scenario match well with the north slope measurements during January-May, but suggest frozen conditions July-November, whereas the data indicate soil thaw during that period. This discrepancy suggests a difference in soil water content: simulated soil water content is generally high due to the soil water retention curve used in the model, resulting in a large latent heat barrier during the summer. This buffer evident in the simulated subsurface temperatures between August-November is produced by the thawing of soil layers at depths less than 3.8m; heat at the surface cannot propagate to 3.8m due to energy consumed in phase change; the data demonstrate no such buffer, suggesting low water content. Including downslope flow in the model reduces soil water by a small extent, suggesting that such lateral flow would not be sufficient to reduce soil water content to the extent indicated by the data. However, preferential flow through fracture networks, which is not represented in the model, may act to drain soils to the extent indicated by the data. Including the full surface energy balance at the soil surface, rather than an air temperature

boundary condition alone, acts to cool the subsurface on an annual basis due to high wind speeds; thus, it is unlikely that solar radiation plays a role in the discrepancy between the model and observed temperatures. In addition, soil thermal diffusivity is evidently lower in the model than the data suggest, indicating an overestimation of soil porosity in the model.

To test these notions, an analogous model run (Figure 45b) was performed with a heat conduction model, populated with zero water content and half the porosity of the original simulation. Eliminating water content from the model serves to remove latent heat accounting, which is not needed to match the data, while reducing the porosity serves to increase thermal diffusivity. With these changes, the model more accurately reproduces the data. In all scenarios, no permafrost is present at 3.8m, in agreement with the data. This exercise indicates that dry, rocky sites are unlikely to contain permafrost at depths <5m due to (1) the lack of a latent heat buffer and (2) high thermal diffusivity due to a high subsurface mineral fraction. Such sites experience high wind speeds that remove snowcover in the winter and drive high evaporative losses during snow-free periods, reducing soil water content.

From a geomorphology perspective, such changes in deep soil temperature may lead to divergent trends in frost cracking. In order to characterize changes in frost cracking conditions, we compute the amount of time during which subsurface temperatures fall between -3°C and -8°C [Walder and Hallet, 1985] (Figure 46). Conditions are most favorable for frost cracking in the past scenario: seasonally at depths 0-9m and perennially at depths 9-55m. In the present scenario, the maximum depth of frost cracking decreases to 42m, and the depth of seasonal frost cracking descends to 14m. In the future scenario, frost cracking conditions are no longer present, except for during the winter in the shallow subsurface (0-1m), which is composed primarily of mobile soil and not fresh bedrock and is not of interest from the perspective of frost damage and weathering.
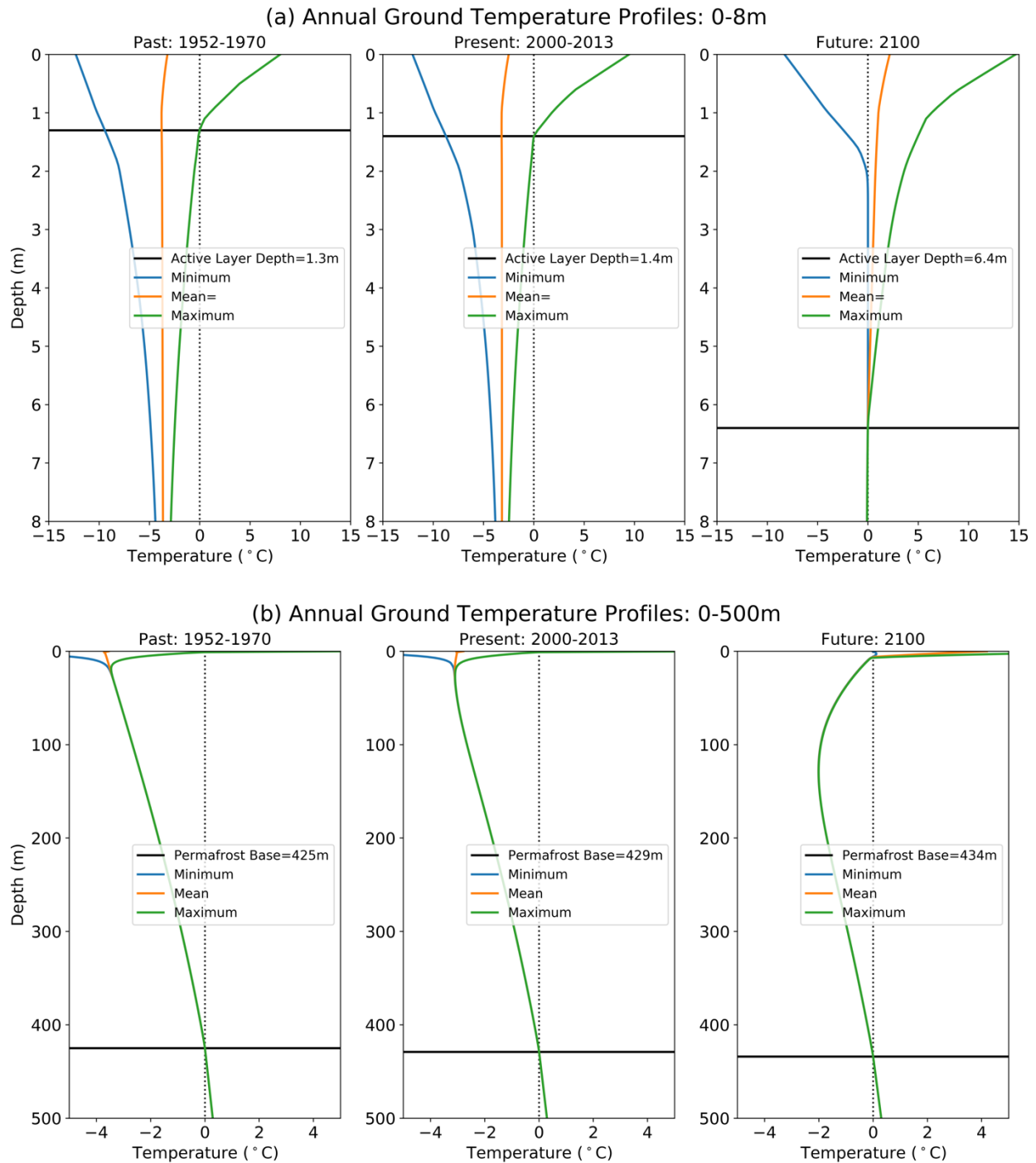
Figure 44. Annual ground temperature profiles (minimum, mean, maximum) at (a) 0m-8m depth and (b) 0m-500m depth beneath high alpine D1 site. Compared to 1952-1970, 2000-2013 simulations suggest little change in active layer depth. However, compared to 2000-2013, end-of-century simulations suggest a transition from permafrost to seasonally frozen ground at depths 2m-6m. The effects of changes in surface forcing propagate to a depth on the order of 100m in the future simulation.

(a) High Alpine Ground Temperature Comparison: Thermo-Hydrologic Model
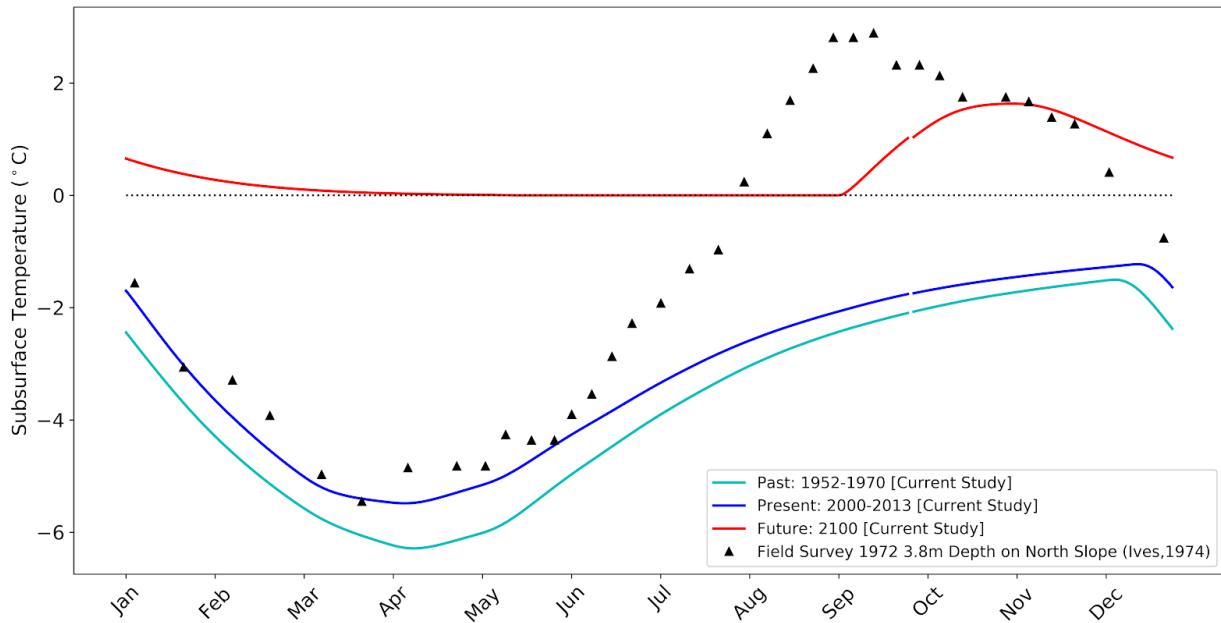
(b) High Alpine Ground Temperature Comparison: Zero Soil Water Content
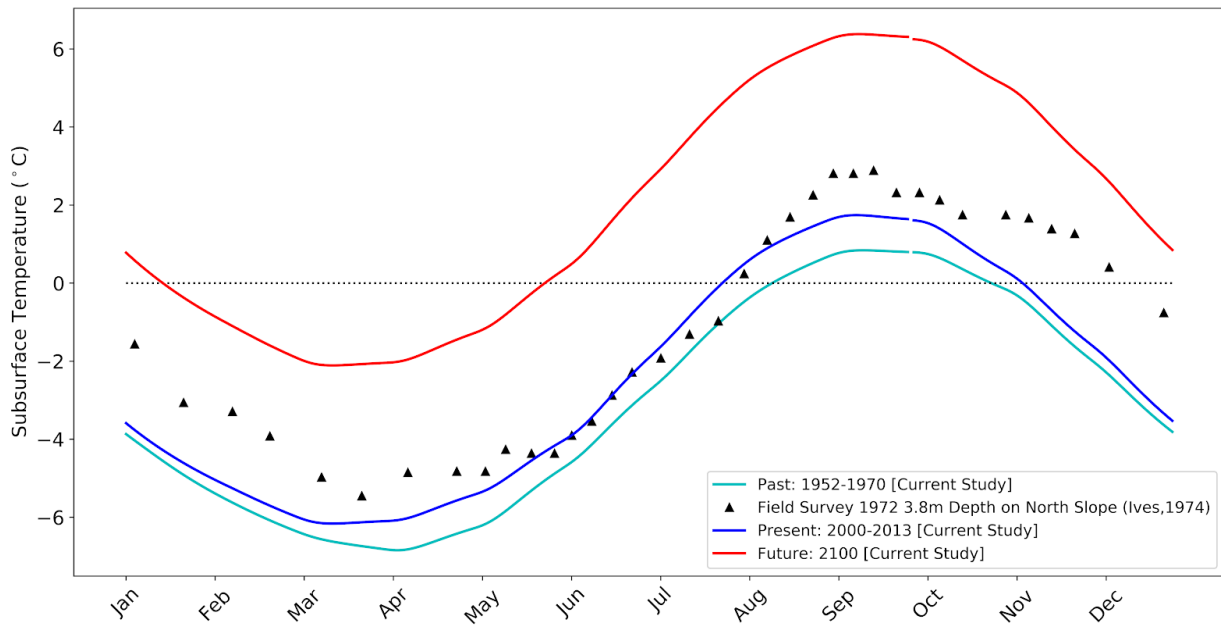
Figure 45. 3.8m ground temperatures from 1972 Ives survey (triangles) [in Leopold et al., 2014] compared to modeled 3.8m ground temperatures using the thermo-hydrologic model (a) and heat conduction model with zero water content (b) from past (cyan), present (blue), and future (red) scenarios.
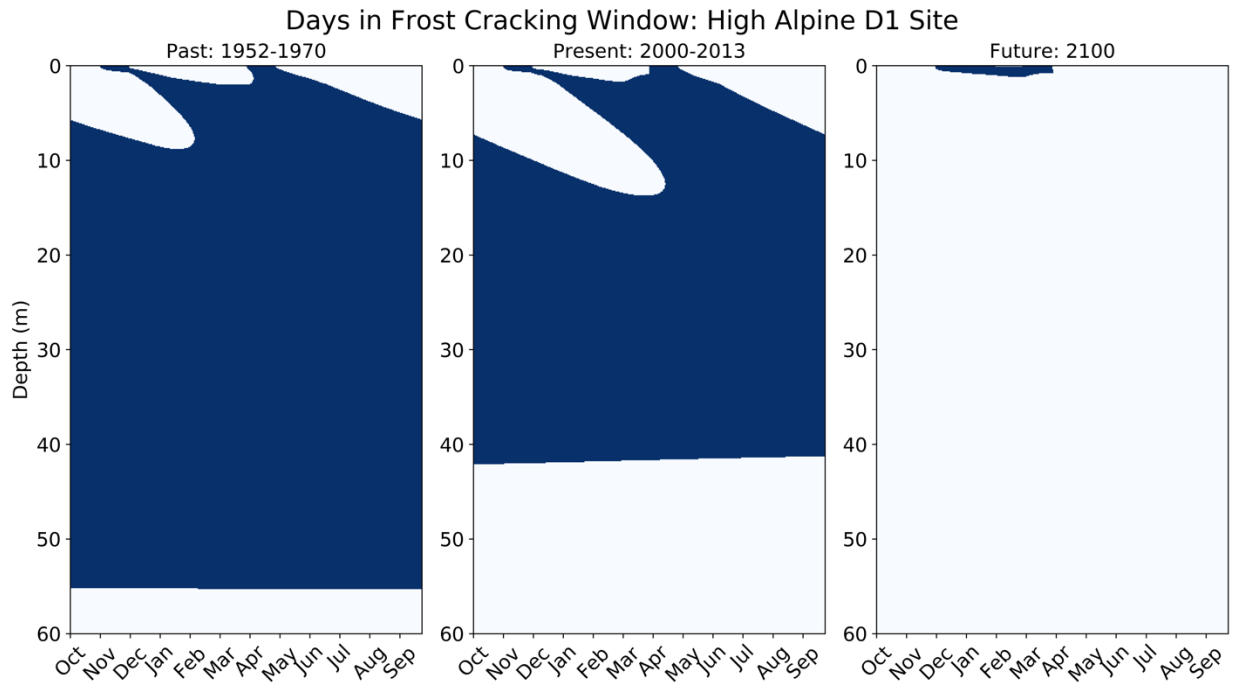
Figure 46. Days within frost cracking window (blue). Conditions are favorable for frost cracking at maximum depth of approximately 55m in the past scenario, 41m in the present scenario, and 1m in the future scenario.

5.   Conclusions

Simulations of SFG indicate that projected changes in the Front Range snowpack and air temperatures will induce complete soil thaw throughout the snow season in the subalpine zone and a ~2-month reduction in frost duration in the alpine zone, while projected changes in air temperature alone will reduce the duration of shallow soil freezing by ~2 months in both zones. Such changes have significant implications for vegetation, microbial dynamics, and biogeochemical cycles. Simulations of deep frozen ground at Niwot Ridge suggest the current and past occurrence of permafrost beneath D1-like sites that is projected to thaw much more significantly throughout the 21st century, in contrast to the past several decades. The active layer thickness increased from 1.3m in the 1952-1970 scenario, to 1.4m in the 2000-2013 scenario, to 6.4m in the end-of-21st century scenario (~2100).

We found that thick alpine and subalpine snowpacks exert a warming effect on soil temperatures, but do not prevent or eliminate frozen ground completely. At C1, the shallow soil beneath the snowpack remained frozen into the snowmelt season, in agreement with the observations of Brooks et al., [1996]. When the snowpack exceeds 50cm and transitions from "thin" to "thick" (February 3 at D1, March 1 at Saddle, and March 27 at C1), no significant change in ice saturation is simulated (Figure 41). At D1 and Saddle, the soil froze intensely prior to exceeding the 50cm depth threshold and the geothermal heat flux was not sufficiently large to thaw soils that had been recently decoupled from the atmosphere. At C1, where the soil froze less intensely, the ground began to thaw following the transition from "thin" to "thick" snowpack. Generally, our modeling suggests that, in addition to snow depth, information about the cold content of high-elevation, continental snowpacks is required to understand the influence of snow on the ground thermal regime in these regions, whereas the influence of warm, isothermal snowpacks of low-elevation and coastal environments can be understood with snow depth alone.

Our results highlight a strong role for frozen ground in determining the ability of snowmelt to infiltrate and recharge groundwater in the subalpine and alpine zones. By comparing simulations with frozen soil to simulations that remain at or above 0°C, we have isolated the effects of frozen ground on overland flow generation from other mechanisms such as infiltration excess overland flow. In contrast to the conceptual model proposed by Hill et al. [2015], we simulate shallow freezing beneath thick snowpacks at all sites that persists into the melt season and limits infiltration. Although we do simulate significant freezing beneath bare ground, early exposure to solar radiation and warm air temperatures thaws the shallow subsurface and allows excess snowmelt run-on to infiltrate. That is, shallow freezing beneath snow-covered ground exerted a much stronger effect on subsurface flow than shallow freezing beneath bare ground (Figure 40a) because the soil beneath the snow remained frozen while the snowpack is melting. In the subalpine zone, frozen soil underlying bare ground patches thaws earlier than soil beneath snow-covered patches, whereas in the alpine zone, frozen soils beneath snow-covered and bare ground thaw at the same time. However, in the alpine zone, we found that deep frozen soil beneath bare ground patches does provide a barrier to 2m vertical flux, in agreement with the Hill et al. [2015] model. We also found that shallow frozen soil beneath snow-covered ground exerts a strong control on the entire system, including deep soils beneath bare ground: by reducing infiltration, this shallow frozen ground reduces 2m fluxes beneath both snow-covered and bare ground patches (e.g. C1, Figure 31b) due to the low-permeability saprolite layer that induces lateral fluxes. Our results support the conclusion of Evans et al., [2018] that frozen ground controls groundwater discharge to streams. While we did not include streamflow in our analysis, the definition of groundwater discharge as flow across the bottom boundary of the domain in Evans et al., [2018] is directly comparable to our analysis of flow across boundaries at depths of 1m and 2m (Figure 40).

Our retrospective and prospective simulations of SFG provide a rigorous template for understanding changes in the role that that alpine ecosystems play in global biogeochemical cycles on seasonal timescales. In all projections, we simulated two additional months of unfrozen soils in the end-of-21st-century scenario than in the 1952-1970 scenario. Although vegetation and soil microbial communities at Niwot Ridge are uniquely adapted to the harsh alpine environment and often thrive during the cold, winter months [e.g. Brooks et al., 1996; Walker et al., 2001] both microbial activity and biogeochemical pathways are strongly controlled by temperature [Donhauser and Frey, 2018], and mechanical transitions occur when water freezes, where ice formation can cause tissue damage [Hayashi, 2013], and liquid water is less available [Brooks et al., 1996]. As soils constitute a larger reservoir of carbon and nitrogen than plants [Hayashi, 2013], a shift toward a longer growing season presents a complicated set of feedbacks: increased soil microbial activity in the spring may lead to higher availability of carbon and nitrogen, but increased primary production may consume many of these nutrients. Projected shifts towards less annual snowfall and accumulation, particularly in the spring [Liu et al., 2017], while extending the growing season, may lead to drier soil conditions overall and restrict growth during the dry late summer and early fall months. Within the context of the "colder soils in a warming world" paradigm [Groffman et al., 2001a], neither less early-season nor late-season snowfall led to significant changes in freezing intensity; such shifts led to a reduction in the duration of frozen soil. Our retrospective and prospective simulations of permafrost provide support for the occurrence of permafrost above 3800m and suggest that the deep soil thawing that has taken place over the last several decades is small compared to deep soil thaw that we should expect throughout the remainder of the current century.

CHAPTER V

CROSS-SITE COMPARISON AND CONCLUSIONS

1. Cross-Site Comparison

In this section, results are compared between the Gordon Gulch and Niwot Ridge sites (see Chapters III and IV). Specifically, reduction in vertical flux due to soil freezing was analyzed with elevation to determine how the influence of frozen ground on hydrology varies with elevation.

The modeling approach is described in Chapter IV, section 3.2 and is summarized here. The influence of seasonally frozen ground on infiltration and groundwater recharge beneath adjacent snow-covered and bare, wind-scoured sites was computed for the subalpine C1, alpine tundra Saddle, and high alpine D1 sites at Niwot Ridge, and the north- and south-facing slopes at Gordon Gulch. Water year 2008 was selected for the Niwot Ridge sites because the snow record is representative of the time period 2000-2013, whereas water year 2013 was selected for the Gordon Gulch sites because the analysis presented in Chapter III, section 4.4 identified that year as reflecting frozen ground influence on subsurface flux most strongly. In order to quantitatively evaluate the influence of frozen ground in the absence of other hydrologic factors such as snowmelt magnitude and timing, as well as overland flow generation, simulations including the formation of frozen ground were compared to simulations in which the soil is prevented from freezing by setting any sub-zero temperatures to 0°C. All other variables were held constant. A two-dimensional domain with depth 10m (C1, Saddle, Gordon Gulch north-facing slope, and Gordon Gulch south-facing slope) and 5m (D1), width 20m, and spatial discretization of 20cm was simulated at an hourly timestep.

For all sites, the soil surface boundary was divided into two "patches." One patch was forced with the surface energy balance including the influence of snow, while the other patch was

forced with the surface energy balance excluding the influence of snow. The hydrologic boundary condition on the soil surface was assigned a prescribed infiltration flux condition determined from the amount of rainfall or snowmelt produced during that timestep, adjusted for the occurrence of surface flow. The majority of infiltration originates from the snowpack: snowmelt simulated by the model is applied to the soil surface of the snow patch. When the shallow soil beneath the snow patch becomes saturated with moisture and/or ice, excess infiltration is then applied to the bare ground patch as run-on. Thus, during the winter the bare ground patch only receives infiltration due to excess snowmelt from the snow patch. Summer rain is applied to both patches. More details regarding the domain and boundary conditions can be found in Chapter IV, section 3.2. No slope angle was used for this analysis in order to compare behavior across sites and to independently identify the contributions of snow-covered and bare ground patches to subsurface flux.

Results of the cross-site comparison are presented in Figure 47. Two trends emerge: with increasing elevation, frozen soil beneath snow-covered ground reduces 1m and 2m vertical fluxes, while frozen soil beneath bare ground reduces 2m vertical fluxes. The reduction in 2m flux beneath snow-covered ground reflects the influence of frozen soil on 1m flux: any water intercepted by frozen soil at 0-1m depth does not travel to depths >1m. Frozen soil beneath bare ground does not influence infiltration at 1m depth because bare ground is exposed earlier to spring solar radiation and warm air and thaws by the time it receives excess snowmelt run-on. As discussed in Chapter IV, reductions in 2m vertical flux beneath bare ground patches are produced by (1) deep frozen soil (1-2m depth) that persists into the melt season at the alpine sites (D1 and Saddle) and (2) decreased lateral flux contributions from the snow-covered patch. When 2m fluxes beneath snow-covered ground decrease, lateral fluxes diverted by the low-permeability saprolite layer into the deep subsurface beneath the bare ground patch also decrease. As in section 5.3, these results contrast with the conceptual model presented by Hill et al., [2015]. In their model, unfrozen soils beneath

snow-covered ground permit infiltration from snowmelt, whereas shallow freezing occurs beneath bare ground and prevents infiltration. In our simulations, the ground is able to freeze beneath the seasonal snowpack and prevents infiltration; bare soil thaws earlier than snow-covered ground due to earlier exposure to solar radiation and warm air, allowing excess snowmelt run-on to infiltrate. That is, the thermal state of the ground during the snowmelt season is the most important factor in determining the ability of snowmelt water to infiltrate.

Simple linear regression is used to characterize the elevation dependence of the influence of frozen soil on 1m and 2m vertical fluxes beneath snow-covered and bare ground patches. Taking $p<0.05$ as a threshold for significance, trends emerge for two subsets: 1m vertical flux beneath snow-covered ground (Figure 47, top left), and 2m vertical flux beneath bare ground (Figure 47, bottom right). For every 100m increase in elevation above an elevation threshold, 1m vertical flux is reduced by 5.4% for snow-covered ground above 2356m ($p=0.02$, $R^2=0.86$), and 2m vertical flux is reduced by 4.8% for bare ground above 2312m ($p=0.03$, $R^2=0.83$). For south-facing slopes, the elevation above which frozen ground significantly influences subsurface fluxes would be expected to occur at a higher elevation (~2600m). Generally, frozen soil influences 1m and 2m fluxes to a moderate extent in the montane zone and more significantly in the subalpine and alpine zones.

The increase in the influence of frozen ground with elevation is related to the snowpack energy balance for the snow-covered case, and the surface energy balance for the bare ground case. As elevation increases, the snowpack becomes increasingly cold and the surface energy balance trends increasingly negative, due to air temperature decreases and wind speed increases. Although solar radiation increases with elevation, its warming effect on the snowpack and surface energy balances is smaller than the cooling effect associated with higher wind speeds and lower air temperatures and limited by snow and ground surface albedo. This may not generally be the case for all mountain environments, however,

as the Colorado Front Range mountains are extraordinarily windy. As expected, the north-facing slope at Gordon Gulch demonstrates stronger influence of frozen ground than the south-facing slope. Its lower energy balance due to poleward inclination and canopy shading creates more favorable conditions for frozen ground development than the adjacent south-facing slope, despite a persistent snowpack.

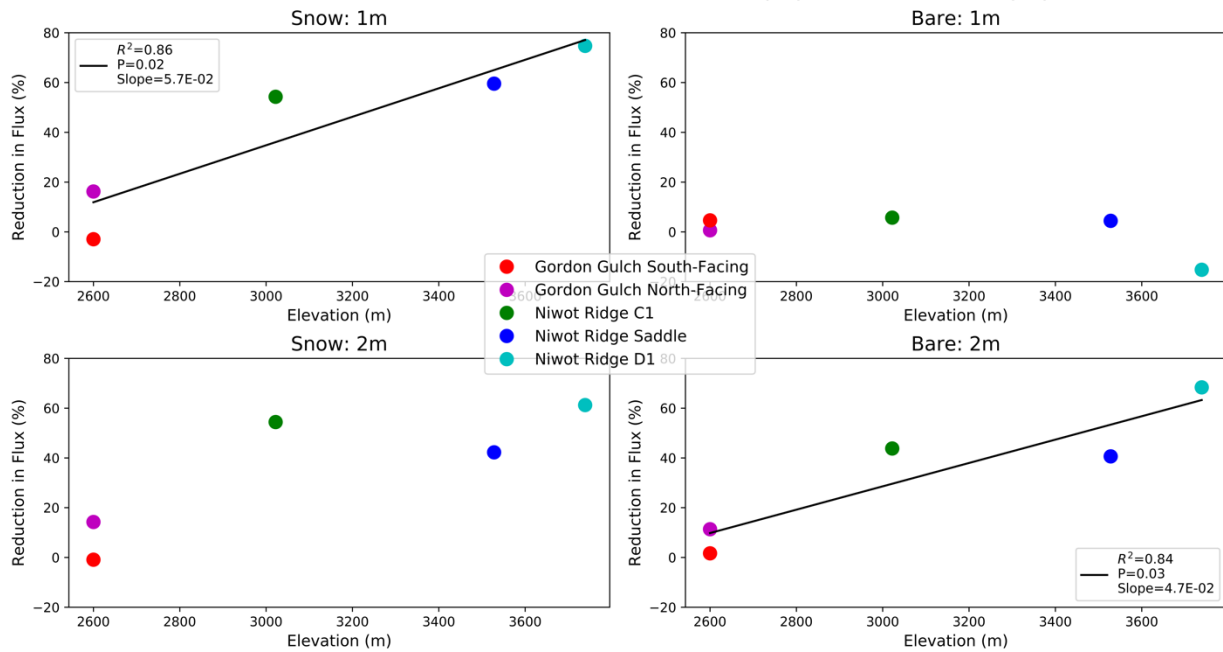Figure 47. Reduction (%) in vertical flux at 1m (top) and 2m (bottom) depth due to the occurrence of frozen ground beneath snow-covered (left) and bare ground (right); a positive value indicates a reduction in flux. Simulations including the formation of frozen ground are compared to simulations in which the soil is prevented from freezing. Linear regressions are presented for relationships with p<0.05.

2. Conclusions

2.1 Research Questions Addressed

This thesis addressed the following research questions:

  a. How does hillslope aspect influence the occurrence of frozen ground?

  b. How does the cold content of snow at various elevations influence the ground thermal regime?

  c. How does frozen soil beneath bare and snow-covered patches influence subsurface flow?

  d. How does the influence of seasonally frozen ground on infiltration and groundwater recharge change with elevation?

  e. How will end-of-21st-century changes in Front Range air temperature, snowfall, and snowpack cold content influence the ground thermal regime?

  f. Compared to the 1952-1970 period, how will end-of-21st-century conditions influence alpine permafrost occurrence?

2.2 Novel Methods Developed

In the process of answering the research questions of section 2.1, a number of novel research methods and models were developed. Surface energy balance, snowpack, and subsurface thermo-hydrologic models (PFLOTRAN-ICE) were coupled to form a sophisticated simulator of frozen ground in mountain environments. A comprehensive framework for modeling soil temperatures, seasonally frozen ground and permafrost in heterogeneous montane and alpine landscapes was detailed. An infiltration capacity formulation was devised that allows snow models to generate surface flow when the buildup of moisture and ice in the shallow subsurface prevents additional snowmelt

infiltration. Finally, lumped snowpack models were modified to better represent the influence of snow depth on ground temperatures and heat fluxes.

2.3 New Results and Insights

How does hillslope aspect influence the occurrence of frozen ground in the montane zone?

At Gordon Gulch, energy balance models showed that the south-facing slope does not experience intense or prolonged frozen ground due to higher solar insolation compared to the north-facing slope, and that the north-facing slope experiences frozen ground because it receives low solar insolation and the snowpack is typically too thin to have an insulating effect. That the soil thermal behavior of slopes lying mere hectometers apart is so divergent and controlled by complex surface energy balance mechanisms highlights the role that high-resolution physical modeling must play in any study of the thermal landscape: large-scale models should be constructed from the "ground up". Moreover, the physical modeler must also learn to intuit the landscape from the perspective of the gardener building a greenhouse on the south-facing side of the canyon, the hiker and the skier seeking shade beneath the forest canopy, the gopher and the pika taking shelter beneath deep snow.

How does the cold content of snow at various elevations influence the ground thermal regime?

The cold alpine snowpack exerts a small warming influence on soil temperatures but does not prevent frozen ground entirely. Subalpine and montane snowpacks exert a strong insulating effect to produce warmer soil temperatures, but also do not prevent frozen ground altogether. The occurrence of frozen ground beneath the snowpack is important, as it limits the amount of meltwater that can infiltrate into the soil. Whereas isothermal snowpacks in low elevation and coastal regions are unlikely to contain sufficient cold content to consume significant ground heat and maintain frozen soils, the cold snowpacks of high-elevation, inland regions have been shown here to serve such a function.

How does frozen soil beneath bare and snow-covered patches influence subsurface flow?

Shallow freezing beneath snow-covered ground exerts a strong influence on infiltration because the soil beneath the snow remains partially frozen while the snowpack is melting. Shallow freezing beneath bare ground exerts little influence on infiltration because solar insolation thaws bare patches by the time they receive excess snowmelt, even though these ground patches freeze more intensely earlier in the winter season. That is, the thermal state of the shallow subsurface during snowmelt is the most important factor in determining the influence of frozen ground on infiltration.

How does the influence of frozen ground on infiltration and groundwater recharge change with elevation?

With increasing elevation, shallow (<1m below ground surface) frozen soil underlying snow-covered ground limits 1m vertical fluxes. In the alpine zone, deep (>1m below ground surface) frozen soil underlying bare ground impedes 2m vertical fluxes. With increasing elevation, the influence of shallow frozen soil underlying snow-covered ground was shown to influence 2m fluxes across the entire system (including beneath bare ground) due to the lateral diversion of fluxes by the low-permeability saprolite layer at depths >2m. At Gordon Gulch, one out of four study years demonstrated significant frozen ground influence on infiltration, with the magnitude of the response varying across measurement sites, highlighting the strong degree of interannual and spatial variability in the influence of soil freezing on subsurface hydrology.

How will end-of-21st-century changes in Front Range air temperature, snowfall, and cold content influence the ground thermal regime?

Compared to 1952-1970, warmer air temperatures alone will reduce the duration of seasonal soil freezing by ~one month in the fall and ~one month in the spring. Compared to 1952-1970, accounting for warmer air temperature and diminished late season snow, the

ground will again freeze ~one month later and thaw ~one month earlier. As no significant increases in freezing intensity or frequency were simulated in warming scenarios, our results do not lend support to the "colder soils in a warmer world" [Groffman et al., 2001a] paradigm for the Colorado Front Range. Rather, we simulated significant reductions in the duration of frozen ground. Despite a reduction in the duration of the snow season, warmer soil temperatures beneath the snowpack would permit higher rates of subnivial microbial respiration, increasing net ecosystem loss. In the subalpine zone, reduced intensity of early-season freezing may limit available carbon substrate for subnivial microbial respiration during the snow season. Generally, such significant reductions in the time when the soil is frozen (2 months) are expected to permit a longer vegetation growing season and higher rates of primary production, increasing net ecosystem uptake in the subalpine and alpine zones. The net annual effect of increased uptake due to a longer growing season and loss due to higher rates of subnivial respiration remains unknown. In the subalpine zone, where subnivial soils remained almost completely thawed in the future climate scenario, decreased intensity of soil freezing beneath the snowpack would permit higher rates of snowmelt infiltration. However, in the alpine zone, where soils remained frozen into the snowmelt season in all climate scenarios, frozen ground will continue to play a role limiting snowmelt infiltration rates.

Compared to the 1952-1970 period, how will end-of-21st-century conditions influence alpine permafrost occurrence?

Permafrost is likely above 3800m with active layer thickness 1.3m (1952-1970), 1.4m (2000-2013) and 6.4m by end of 21st century. The deep soil thaw that has taken place over the last several decades (1970-2020) is very small compared to projected deep soil thaw through the current century. Such changes in deep subsurface soil temperatures are associated with a shift away from the conditions favorable for frost cracking processes at depths <50m. A deepening of the active layer would allow water to drain into the deep subsurface, reducing

soil water content and hydraulic conductivity in the shallow subsurface. As saprolite and fractured bedrock have lower permeabilities than shallow soils, vertical and lateral flow rates are expected to decrease, extending travel times to discharge locations. Such a result presents cause for optimism: the thermal lag between changes in climate and subsurface temperatures offers a window of opportunity to take actions mitigating the warming effects of climate change.

BIBLIOGRAPHY

Anderson, R. S. (2002). Modeling the tor-dotted crests, bedrock edges, and parabolic profiles of high alpine surfaces of the Wind River Range, Wyoming. Geomorphology, 46(1), 35–58. https://doi.org/10.1016/S0169-555X(02)00053-3

Anderson, R. S., Anderson, S. P., & Tucker, G. E. (2013). Rock damage and regolith transport by frost: An example of climate modulation of the geomorphology of the critical zone. Earth Surface Processes and Landforms, 38(3), 299–316. https://doi.org/10.1002/esp.3330

Anderson, S. P., Anderson, R. S., & Tucker, G. E. (2012). Landscape scale linkages in critical zone evolution. Comptes Rendus Geoscience, 344(11), 586–596. https://doi.org/10.1016/j.crte.2012.10.008

Anderson, S. P., Anderson, R. S., Hinckley, E.-L. S., Kelly, P., & Blum, A. (2011). Exploring weathering and regolith transport controls on Critical Zone development with models and natural experiments. Applied Geochemistry, 26, S3–S5. https://doi.org/10.1016/j.apgeochem.2011.03.014

Anderson, R. S., Anderson, S. P., Ragar, D. [2020]. CZO Dataset: Gordon Gulch: Lower - Electrical Conductivity, Soil Moisture, Soil Temperature (2012-2018) - North-Facing Middle Pit (GGL_NF_MP). Retrieved 2020, from HydroShare, http://www.hydroshare.org/resource/543c6572a58c434ea6507608eaf04924

Anderson, S. P., Ragar, D. [2018]. CZO Dataset: Gordon Gulch: Lower - Air Temperature, Meteorology (2012-2019) - North-Facing Meteorological Tower (GGL_NF_Met). Retrieved 2018, from http://criticalzone.org/boulder/data/dataset/2888/

Anderson, S. P., Ragar, D. [2018]. CZO Dataset: Gordon Gulch: Lower - Air Temperature, Meteorology (2012-2019) - South-Facing Meteorological Tower (GGL_SF_Met). Retrieved 2018, from http://criticalzone.org/boulder/data/dataset/2889/

Anderson, S. P., Ragar, D. [2018]. CZO Dataset: Gordon Gulch: Lower - Snow Depth, Air Temperature (2010-2018) - Judd Sensors (GGL_NF_SP3-4SF_SP10_SD_Array). Retrieved 2018, from http://criticalzone.org/boulder/data/dataset/2423/

Anderson, S. P., Ragar, D. [2020]. CZO Dataset: Gordon Gulch: Upper - Soil Temperature (2008-2017) (GGU_Hobo_Array). Retrieved 2020, from HydroShare, http://www.hydroshare.org/resource/95d124e2db0448e184c89e1859c67754

Anderson, S. P., Rock, N. [2017]. CZO Dataset: Gordon Gulch - Snow Pits (2008-2017) - Snow Pit Stratigraphy, Density - SWE (GG_SN_Array). Retrieved 2020, from http://criticalzone.org/boulder/data/dataset/2433/

Anderson, S. P., Rock, N., Ragar, D. [2019]. CZO Dataset: Betasso - Meteorology, Air Temperature (2009-2019) - (BT_Met). Retrieved 2018, from http://criticalzone.org/boulder/data/dataset/2435/

Andersson, J. G. (1906). Solifluction, a component of subaërial denudation. The Journal of Geology, 14(2), 91–112.

Andresen, C. G., Lawrence, D. M., Wilson, C. J., McGuire, A. D., Koven, C., Schaefer, K., … Zhang, W. (2020). Soil moisture and hydrology projections of the permafrost region – a

model intercomparison. The Cryosphere, 14(2), 445–459. https://doi.org/10.5194/tc-14-445-2020

Atchley, A. L., Painter, S. L., Harp, D. R., Coon, E. T., Wilson, C. J., Liljedahl, A. K., & Romanovsky, V. E. (2015). Using field observations to inform thermal hydrology models of permafrost dynamics with ATS (v0.83). Geoscientific Model Development; Katlenburg-Lindau, 8(9), 2701. http://dx.doi.org.colorado.idm.oclc.org/10.5194/gmd-8-2701-2015

Barnes, R. T., Williams, M. W., Parman, J. N., Hill, K., & Caine, N. (2014). Thawing glacial and permafrost features contribute to nitrogen export from Green Lakes Valley, Colorado Front Range, USA. Biogeochemistry; Dordrecht, 117(2–3), 413–430. http://dx.doi.org.colorado.idm.oclc.org/10.1007/s10533-013-9886-5

Baron, J. S., Schmidt, T. M., & Hartman, M. D. (2009). Climate-induced changes in high elevation stream nitrate dynamics. Global Change Biology, 15(7), 1777–1789. https://doi.org/10.1111/j.1365-2486.2009.01847.x

Bartlett, M. G., Chapman, D. S., & Harris, R. N. (2004). Snow and the ground temperature record of climate change. Journal of Geophysical Research: Earth Surface, 109(F4). https://doi.org/10.1029/2004JF000224

Bayard, D., Stähli, M., Parriaux, A., & Flühler, H. (2005). The influence of seasonally frozen soil on the snowmelt runoff at two alpine sites in southern Switzerland. Journal of Hydrology, 309(1), 66–84. https://doi.org/10.1016/j.jhydrol.2004.11.012

Benedict, J. B. (1970). Downslope soil movement in a Colorado alpine region: Rates, processes, and climatic significance. Arctic and Alpine Research, 2(3), 165–226. https://doi.org/10.2307/1550306

Benedict, J. B. (1992). Footprints in the snow: High-altitude cultural ecology of the Colorado Front Range, U.S.A. Arctic and Alpine Research, 24(1), 1–16. https://doi.org/10.1080/00040851.1992.12002922

Blanken, P. D., Williams, M. W., Burns, S. P., Monson, R. K., Knowles, J., Chowanski, K., & Ackerman, T. (2009). A comparison of water and carbon dioxide exchange at a windy alpine tundra and subalpine forest site near Niwot Ridge, Colorado. Biogeochemistry, 95(1), 61–76. Retrieved from JSTOR.

Boike, J., Roth, K., & Overduin, P. P. (1998). Thermal and hydrologic dynamics of the active layer at a continuous permafrost site (Taymyr Peninsula, Siberia). Water Resources Research, 34(3), 355–363. https://doi.org/10.1029/97WR03498

Bowman, W. D., & Seastedt, T. R. (2001). Structure and Function of an Alpine Ecosystem: Niwot Ridge, Colorado. Oxford University Press.

Brooks, P. D., Williams, M. W., Walker, D. A., & Schmidt, S. K. (1995). The Niwot Ridge snow fence experiment: Biogeochemical responses to changes in the seasonal snowpack. Unknown Journal, 293–302.

Brooks, Paul D., Schmidt, S. K., & Williams, M. W. (1997). Winter production of CO_2 and N_2O from alpine tundra: Environmental controls and relationship to inter-system C and N fluxes. Oecologia, 110(3), 403–413. https://doi.org/10.1007/PL00008814

Brooks, Paul D., & Williams, M. W. (1999). Snowpack controls on nitrogen cycling and export in seasonally snow-covered catchments. Hydrological Processes, 13(14–15), 2177–

2190. https://doi.org/10.1002/(SICI)1099-1085(199910)13:14/15<2177::AID-HYP850>3.0.CO;2-V

Brooks, Paul D., Williams, M. W., & Schmidt, S. K. (1998). Inorganic nitrogen and microbial biomass dynamics before and during spring snowmelt. Biogeochemistry, 43(1), 1–15. https://doi.org/10.1023/A:1005947511910

Burt, T. P., & Williams, P. J. (1976). Hydraulic conductivity in frozen soils. Earth Surface Processes, 1(4), 349–360. https://doi.org/10.1002/esp.3290010404

Caine, N. (2010). Recent hydrologic change in a Colorado alpine basin: An indicator of permafrost thaw? Annals of Glaciology, 51. https://doi.org/10.3189/172756411795932074

Campbell, J. L., Ollinger, S. V., Flerchinger, G. N., Wicklein, H., Hayhoe, K., & Bailey, A. S. (2010). Past and projected future changes in snowpack and soil frost at the Hubbard Brook Experimental Forest, New Hampshire, USA. Hydrological Processes, 24(17), 2465–2480. https://doi.org/10.1002/hyp.7666

Carslaw, H.S., Jaeger, J.C., 1959. Conduction of Heat in Solids. 2nd. Oxford University Press.

Cautenet, G., Coulibaly, Y., & Boutin, C. (1985). Calculation of ground temperature and fluxes by surface models: A comparison with experimental data in the African savannah. Tellus B: Chemical and Physical Meteorology, 37(2), 64–77. https://doi.org/10.3402/tellusb.v37i2.14998

Charbeneau, R. J. (2000). Groundwater Hydraulics and Pollutant Transport. Upper Saddle River, NJ: Prentice Hall.

Clow, D. W. (2010). Changes in the timing of snowmelt and streamflow in Colorado: A response to recent warming. Journal of Climate; Boston, 23(9), 2293–2306.

Comola, F., Schaefli, B., Ronco, P. D., Botter, G., Bavay, M., Rinaldo, A., & Lehning, M. (2015). Scale-dependent effects of solar radiation patterns on the snow-dominated hydrologic response. Geophysical Research Letters, 42(10), 2015GL064075. https://doi.org/10.1002/2015GL064075

Connon, R. F., Quinton, W. L., Craig, J. R., & Hayashi, M. (2014). Changing hydrologic connectivity due to permafrost thaw in the lower Liard River valley, NWT, Canada. Hydrological Processes, 28(14), 4163–4178. https://doi.org/10.1002/hyp.10206

Coxson, D. S., & Parkinson, D. (1987). Winter respiratory activity in aspen woodland forest floor litter and soils. Soil Biology and Biochemistry, 19(1), 49–59. https://doi.org/10.1016/0038-0717(87)90125-8

Croley, T. E. (1989). Verifiable evaporation modeling on the Laurentian Great Lakes. Water Resources Research, 25(5), 781–792. https://doi.org/10.1029/WR025i005p00781

Cuo, L., Zhang, Y., Bohn, T. J., Zhao, L., Li, J., Liu, Q., & Zhou, B. (2015). Frozen soil degradation and its effects on surface hydrology in the northern Tibetan Plateau. Journal of Geophysical Research: Atmospheres, 120(16), 8276–8298. https://doi.org/10.1002/2015JD023193

Davis, T. N. (2001). Permafrost: A Guide to Frozen Ground in Transition. Fairbanks: University of Alaska Press.

Dingman, S. L. (2015). Physical Hydrology (Third edition). Long Grove, Illinois: Waveland Press, Inc.

Donhauser, J., & Frey, B. (2018). Alpine soil microbial ecology in a changing world. FEMS Microbiology Ecology, 94(9). https://doi.org/10.1093/femsec/fiy099

Dunne, T., & Black, R. D. (1971). Runoff processes during snowmelt. Water Resources Research, 7(5), 1160–1172. https://doi.org/10.1029/WR007i005p01160

Dunne, T., & Leopold, L. B. (1978). Water in environmental planning. San Francisco: W. H. Freeman.

Edlefsen, N., & Anderson, A. (1943). Thermodynamics of soil moisture. Hilgardia, 15(2), 31–298.

Ehlers, T. A. (2005). Crustal thermal processes and the interpretation of thermochronometer data. Reviews in Mineralogy and Geochemistry, 58(1), 315–350. https://doi.org/10.2138/rmg.2005.58.12

Endrizzi, S., Gruber, S., Dall'Amico, M., & Rigon, R. (2014). GEOtop 2.0: Simulating the combined energy and water balance at and below the land surface accounting for soil freezing, snow cover and terrain effects. Geoscientific Model Development, 7(6), 2831–2857.

Erickson, T. A., Williams, M. W., & Winstral, A. (2005). Persistence of topographic controls on the spatial distribution of snow in rugged mountain terrain, Colorado, United States. Water Resources Research, 41(4). https://doi.org/10.1029/2003WR002973

Evans, S. G., & Ge, S. (2017). Contrasting hydrogeologic responses to warming in permafrost and seasonally frozen ground hillslopes. Geophysical Research Letters, 44(4), 2016GL072009. https://doi.org/10.1002/2016GL072009

Evans, S. G., Ge, S., Voss, C. I., & Molotch, N. P. (2018). The role of frozen soil in groundwater discharge predictions for warming alpine watersheds. Water Resources Research, 54(3), 1599–1615. https://doi.org/10.1002/2017WR022098

Fisk, M. C., Brooks, P. D., & Schmidt, S. K. 2001. Nitrogen Cycling. In: W. D. Bowman and T. R. Seastedt, editors, Structure and Function of an Alpine Ecosystem: Niwot Ridge, Colorado. Oxford University Press. p. 237-253.

Fitzhugh, R. D., Driscoll, C. T., Groffman, P. M., Tierney, G. L., Fahey, T. J., & Hardy, J. P. (2001). Effects of soil freezing disturbance on soil solution nitrogen, phosphorus, and carbon chemistry in a northern hardwood ecosystem. Biogeochemistry, 56(2), 215–238. https://doi.org/10.1023/A:1013076609950

Fitzhugh, R. D., Likens, G. E., Driscoll, C. T., Mitchell, M. J., Groffman, P. M., Fahey, T. J., & Hardy, J. P. (2003). Role of soil freezing events in interannual patterns of stream chemistry at the Hubbard Brook Experimental Forest, New Hampshire. Environmental Science & Technology, 37(8), 1575–1580. https://doi.org/10.1021/es026189r

Frampton, A., Painter, S., Lyon, S. W., & Destouni, G. (2011). Non-isothermal, three-phase simulations of near-surface flows in a model permafrost system under seasonal variability and climate change. Journal of Hydrology, 403(3), 352–359. https://doi.org/10.1016/j.jhydrol.2011.04.010

Frauenfeld, O. W., & Zhang, T. (2011). An observational 71-year history of seasonally frozen ground changes in the Eurasian high latitudes. Environmental Research Letters, 6(4), 044024. https://doi.org/10.1088/1748-9326/6/4/044024

Fuss, C. B., Driscoll, C. T., Green, M. B., & Groffman, P. M. (2016). Hydrologic flowpaths during snowmelt in forested headwater catchments under differing winter climatic and soil frost regimes. Hydrological Processes, 30(24), 4617–4632. https://doi.org/10.1002/hyp.10956

Gabarrón-Galeote, M. A., Ruiz-Sinoga, J. D., & Quesada, M. A. (2013). Influence of aspect in soil and vegetation water dynamics in dry Mediterranean conditions: Functional adjustment of evergreen and semi-deciduous growth forms. Ecohydrology, 6(2), 241–255. https://doi.org/10.1002/eco.1262

Greenland, D. & Losleben, M. 2001. Climate. In: W. D. Bowman and T. R. Seastedt, editors, Structure and Function of an Alpine Ecosystem: Niwot Ridge, Colorado. Oxford University Press. p. 1-15.

Groffman, P. M., Driscoll, C. T., Fahey, T. J., Hardy, J. P., Fitzhugh, R. D., & Tierney, G. L. (2001a). Colder soils in a warmer world: A snow manipulation study in a northern hardwood forest ecosystem. Biogeochemistry, 56(2), 135–150.

Groffman, P. M., Driscoll, C. T., Fahey, T. J., Hardy, J. P., Fitzhugh, R. D., & Tierney, G. L. (2001b). Effects of mild winter freezing on soil nitrogen and carbon dynamics in a northern hardwood forest. Biogeochemistry, 56(2), 191–213.

Groffman, P. M., Hardy, J. P., Fashu-kanu, S., Driscoll, C. T., Cleavitt, N. L., Fahey, T. J., & Fisk, M. C. (2011). Snow depth, soil freezing and nitrogen cycling in a northern hardwood forest landscape. Biogeochemistry; Dordrecht, 102(1–3), 223–238. http://dx.doi.org.colorado.idm.oclc.org/10.1007/s10533-010-9436-3

Groffman, P. M., Hardy, J. P., Nolan, S., Fitzhugh, R. D., Driscoll, C. T., & Fahey, T. J. (1999). Snow depth, soil frost and nutrient loss in a northern hardwood forest. Hydrological Processes, 13(14–15), 2275–2286. https://doi.org/10.1002/(SICI)1099-1085(199910)13:14/15<2275::AID-HYP858>3.0.CO;2-A

Gruber, S., & Haeberli, W. (2007). Permafrost in steep bedrock slopes and its temperature-related destabilization following climate change. Journal of Geophysical Research: Earth Surface, 112(F2), F02S18. https://doi.org/10.1029/2006JF000547

Guo, D., & Wang, H. (2013). Simulation of permafrost and seasonally frozen ground conditions on the Tibetan Plateau, 1981–2010. Journal of Geophysical Research: Atmospheres, 118(11), 5216–5230. https://doi.org/10.1002/jgrd.50457

Gutiérrez-Jurado, H. A., Vivoni, E. R., Cikoski, C., Harrison, J. B. J., Bras, R. L., & Istanbulluoglu, E. (2013). On the observed ecohydrologic dynamics of a semiarid basin with aspect-delimited ecosystems. Water Resources Research, 49(12), 8263–8284. https://doi.org/10.1002/2013WR014364

Guymon, G. L., Hromadka, T. V., & Berg, R. L. (1980). A one dimensional frost heave model based upon simulation of simultaneous heat and water flux. Cold Regions Science and Technology, 3(2), 253–262. https://doi.org/10.1016/0165-232X(80)90032-4

Guymon, Gary L., & Luthin, J. N. (1974). A coupled heat and moisture transport model for Arctic soils. Water Resources Research, 10(5), 995–1001. https://doi.org/10.1029/WR010i005p00995

Haeberli, W., & Patzelt, G. (1982). Permafrostkartierung im Gebiet der Hochebenkar-Blockgletscher, Obergurgl, Ötztaler Alpen. Zeitschrift Für Gletscherkunde Und Glazialgeologie, 18(2), 127–150.

Hardy, J. P., Groffman, P. M., Fitzhugh, R. D., Henry, K. S., Welman, A. T., Demers, J. D., … Nolan, S. (2001). Snow depth manipulation and its influence on soil frost and water dynamics in a northern hardwood forest. Biogeochemistry; Dordrecht, 56(2), 151–174. http://dx.doi.org.colorado.idm.oclc.org/10.1023/A:1013036803050

Harlan, R. L. (1973). Analysis of coupled heat-fluid transport in partially frozen soil. Water Resources Research, 9(5), 1314–1323. https://doi.org/10.1029/WR009i005p01314

Harris, C., Arenson, L. U., Christiansen, H. H., Etzelmüller, B., Frauenfelder, R., Gruber, S., … Vonder Mühll, D. (2009). Permafrost and climate in Europe: Monitoring and modelling thermal, geomorphological and geotechnical responses. Earth-Science Reviews, 92(3), 117–171. https://doi.org/10.1016/j.earscirev.2008.12.002

Harris, S. A., French, H. M., Heginbottom, J. A., Johnston, G. H., Ladanyi, B., Sego, D. C., & van Everdingen, R. O. (1988). Glossary of Permafrost and Related Ground-Ice Terms (No. 0-660-12540–4). https://doi.org/10.4224/20386561

Hayashi, M. (2013). The cold vadose zone: hydrological and ecological significance of frozen-soil processes. Vadose Zone Journal, 12(4). https://doi.org/10.2136/vzj2013.03.0064

Hill, A. (2015, December 15). Controls on snowmelt partitioning to surface and groundwater flow. Presented at the 2015 AGU Fall Meeting. Retrieved from https://agu.confex.com/agu/fm15/webprogram/Paper59175.html

Hill, A. (2019). Rapid assessment of hydrologic controls on mountain water resources. Geography Graduate Theses & Dissertations. Retrieved from https://scholar.colorado.edu/geog_gradetds/118

Hinckley, E.-L. S., Barnes, R. T., Anderson, S. P., Williams, M. W., & Bernasconi, S. M. (2014). Nitrogen retention and transport differ by hillslope aspect at the rain-snow transition of the Colorado Front Range. Journal of Geophysical Research: Biogeosciences, 119(7), 2013JG002588. https://doi.org/10.1002/2013JG002588

Hinckley, E.-L. S., Ebel, B. A., Barnes, R. T., Anderson, R. S., Williams, M. W., & Anderson, S. P. (2014). Aspect control of water movement on hillslopes near the rain–snow transition of the Colorado Front Range. Hydrological Processes, 28(1), 74–85. https://doi.org/10.1002/hyp.9549

Imhof, M., Pierrehumbert, G., Haeberli, W., & Kienholz, H. (2000). Permafrost investigation in the Schilthorn massif, Bernese Alps, Switzerland. Permafrost and Periglacial Processes, 11(3), 189–206. https://doi.org/10.1002/1099-1530(200007/09)11:3<189::AID-PPP348>3.0.CO;2-N

IPCC, 2013: Climate Change 2013: The Physical Science Basis. Contribution of Working Group I to the Fifth Assessment Report of the Intergovernmental Panel on Climate Change [Stocker, T.F., D. Qin, G.-K. Plattner, M. Tignor, S.K. Allen, J. Boschung, A. Nauels, Y. Xia, V. Bex and P.M. Midgley (eds.)]. Cambridge University Press, Cambridge, United Kingdom and New York, NY, USA, 1535 pp, doi:10.1017/CBO9781107415324.

Ishikawa, M. (2003). Thermal regime at the snow–ground interface and their implications for permafrost investigation. Geomorphology, 52, 105–120. https://doi.org/10.1016/S0169-555X(02)00251-9

Ives, J. D., & Fahey, B. D. (1971). Permafrost Occurrence in the Front Range, Colorado Rocky Mountains, U.S.A. Journal of Glaciology, 10(58), 105–111. https://doi.org/10.3189/S0022143000013034

Iwata, Y., Hayashi, M., & Hirota, T. (2008). Effects of snow cover on soil heat flux and freeze-thaw processes. Journal of Agricultural Meteorology, 64(4), 301–309. https://doi.org/10.2480/agrmet.64.4.12

Jame, Y.-W., & Norum, D. I. (1980). Heat and mass transfer in a freezing unsaturated porous medium. Water Resources Research, 16(4), 811–819. https://doi.org/10.1029/WR016i004p00811

Janke, J. R. (2005). Modeling past and future alpine permafrost distribution in the Colorado Front Range. Earth Surface Processes and Landforms, 30(12), 1495–1508. https://doi.org/10.1002/esp.1205

Janke, J. R., Williams, M. W., & Evans, A. (2012). A comparison of permafrost prediction models along a section of Trail Ridge Road, Rocky Mountain National Park, Colorado, USA. Geomorphology, 138(1), 111–120. https://doi.org/10.1016/j.geomorph.2011.08.029

Jennings, K. S., Kittel, T. G. F., & Molotch, N. P. (2018). Observations and simulations of the seasonal evolution of snowpack cold content and its relation to snowmelt and the snowpack energy budget. The Cryosphere, 12(5), 1595–1614. https://doi.org/10.5194/tc-12-1595-2018

Jepsen, S. M., Molotch, N. P., Williams, M. W., Rittger, K. E., & Sickman, J. O. (2012). Interannual variability of snowmelt in the Sierra Nevada and Rocky Mountains, United States: Examples from two alpine watersheds. Water Resources Research, 48(2). https://doi.org/10.1029/2011WR011006

Jones, M.-F., Castonguay, M., Nasr, M., Ogilvie, J., Arp, P. A., & Bhatti, J. S. (2014). Modeling hydrothermal regimes and potential impacts of climate change of permafrost within the South Mackenzie Plain, Northwest Territories, Canada. 21(1), 21–33. https://doi.org/10.2980/21-1-3663

Judd, K. E., Likens, G. E., & Groffman, P. M. (2007). High nitrate retention during winter in soils of the Hubbard Brook Experimental Forest. Ecosystems, 10(2), 217–225.

Kane, D. L., & Stein, J. (1983). Water movement into seasonally frozen soils. Water Resources Research, 19(6), 1547–1557. https://doi.org/10.1029/WR019i006p01547

Karra, S., Painter, S. L., & Lichtner, P. C. (2014). Three-phase numerical model for subsurface hydrology in permafrost-affected regions (PFLOTRAN-ICE v1.0). The Cryosphere, 8(5), 1935–1950. https://doi.org/10.5194/tc-8-1935-2014

Kaste, Ø., Austnes, K., Vestgarden, L. S., & Wright, R. F. (2008). Manipulation of snow in small headwater catchments at Storgama, Norway: Effects on leaching of inorganic nitrogen. Ambio, 37(1), 29–37.

Knowles, J. F., Burns, S. P., Blanken, P. D., & Monson, R. K. (2015). Fluxes of energy, water, and carbon dioxide from mountain ecosystems at Niwot Ridge, Colorado. Plant Ecology & Diversity, 8(5–6), 663–676. https://doi.org/10.1080/17550874.2014.904950

Koch, J. C., Kikuchi, C. P., Wickland, K. P., & Schuster, P. (2014). Runoff sources and flow paths in a partially burned, upland boreal catchment underlain by permafrost. Water Resources Research, 50(10), 8141–8158. https://doi.org/10.1002/2014WR015586

Kollet, S. J., & Maxwell, R. M. (2006). Integrated surface–groundwater flow modeling: A free-surface overland flow boundary condition in a parallel groundwater flow model. Advances in Water Resources, 29(7), 945–958. https://doi.org/10.1016/j.advwatres.2005.08.006

Koven, C. D., Riley, W. J., & Stern, A. (2013). Analysis of permafrost thermal dynamics and response to climate change in the CMIP5 Earth System Models. Journal of Climate; Boston, 26(6), 1877–1900.

Kumar, J., Collier, N., Bisht, G., Mills, R. T., Thornton, P. E., Iversen, C. M., & Romanovsky, V. (2016). Modeling the spatiotemporal variability in subsurface thermal regimes across a low-relief polygonal tundra landscape. The Cryosphere, 10(5), 2241–2274. https://doi.org/10.5194/tc-10-2241-2016

Lambiel, C., & Pieracci, K. (2008). Permafrost distribution in talus slopes located within the alpine periglacial belt, Swiss Alps. Permafrost and Periglacial Processes, 19(3), 293–304. https://doi.org/10.1002/ppp.624

Langston, A. L., Tucker, G. E., Anderson, R. S., & Anderson, S. P. (2015). Evidence for climatic and hillslope-aspect controls on vadose zone hydrology and implications for saprolite weathering. Earth Surface Processes and Landforms, 40(9), 1254–1269. https://doi.org/10.1002/esp.3718

Laudon, H., Seibert, J., Köhler, S., & Bishop, K. (2004). Hydrological flow paths during snowmelt: Congruence between hydrometric measurements and oxygen 18 in meltwater, soil water, and runoff. Water Resources Research, 40(3), W03102. https://doi.org/10.1029/2003WR002455

Lawrence, D. M., Slater, A. G., & Swenson, S. C. (2012). Simulation of present-day and future permafrost and seasonally frozen ground conditions in CCSM4. Journal of Climate; Boston, 25(7), 2207–2225.

Lee, R. (1962). Theory of the "equivalent slope." Monthly Weather Review, 90(4), 165–166. https://doi.org/10.1175/1520-0493(1962)090<0165:TOTES>2.0.CO;2

Leopold, M., Völkel, J., Dethier, D. P., & Williams, M. W. (2014). Changing mountain permafrost from the 1970s to today—Comparing two examples from Niwot Ridge, Colorado Front Range, USA. Zeitschrift Für Geomorphologie, Supplementary Issues, 137–157. https://doi.org/10.1127/0372-8854/2013/S-00129

Lestak, L. and University of Colorado, Institute of Arctic and Alpine Research (INSTAAR), Niwot Ridge LTER. 2013. Snow depth sensor measurement data for Alpine site, 2010 - ongoing. ver 1. Environmental Data Initiative. https://doi.org/10.6073/pasta/d64fa1dbf6e12609a8c4f5b93427f180. Accessed 2019-01.

Lestak, L. and University of Colorado, Institute of Arctic and Alpine Research (INSTAAR), Niwot Ridge LTER. 2013. Snow depth sensor measurement data for Lower Sub Alpine site, 2010 - ongoing. ver 1. Environmental Data Initiative. https://doi.org/10.6073/pasta/5bf5773eecdd0ad58dd38fbde4aa8c73. Accessed 2019-01.

Li, X., Jin, R., Pan, X., Zhang, T., & Guo, J. (2012). Changes in the near-surface soil freeze–thaw cycle on the Qinghai-Tibetan Plateau. International Journal of Applied Earth Observation and Geoinformation, 17, 33–42. https://doi.org/10.1016/j.jag.2011.12.002

Lindström, G., Bishop, K., & Löfvenius, M. O. (2002). Soil frost and runoff at Svartberget, northern Sweden—Measurements and model analysis. Hydrological Processes, 16(17), 3379–3392. https://doi.org/10.1002/hyp.1106

Litaor, M. I., Williams, M., & Seastedt, T. R. (2008). Topographic controls on snow distribution, soil moisture, and species diversity of herbaceous alpine vegetation, Niwot Ridge, Colorado. Journal of Geophysical Research: Biogeosciences, 113(G2). https://doi.org/10.1029/2007JG000419

Liu, C., Ikeda, K., Rasmussen, R., Barlage, M., Newman, A. J., Prein, A. F., … Yates, D. (2017). Continental-scale convection-permitting modeling of the current and future climate of North America. Climate Dynamics, 49(1–2), 71–95. https://doi.org/10.1007/s00382-016-3327-9

Luthin, J. N., Orhun, A., & Taylor, G. S. (1975). Coupled saturated-unsaturated transient flow in porous media: Experimental and numeric model. Water Resources Research, 11(6), 973–978. https://doi.org/10.1029/WR011i006p00973

Mastin, M., & Josberger, E. (2014). Monitoring recharge in areas of seasonally frozen ground in the Columbia Plateau and Snake River Plain, Idaho, Oregon, and Washington. In Monitoring recharge in areas of seasonally frozen ground in the Columbia Plateau and Snake River Plain, Idaho, Oregon, and Washington (USGS Numbered Series No. 2014–5083; p. 76). https://doi.org/10.3133/sir20145083

Matsuoka, N. (2001). Solifluction rates, processes and landforms: A global review. Earth-Science Reviews, 55(1), 107–134. https://doi.org/10.1016/S0012-8252(01)00057-5

McCabe, G. J., & Clark, M. P. (2005). Trends and variability in snowmelt runoff in the western United States. Journal of Hydrometeorology, 6(4), 476–482. https://doi.org/10.1175/JHM428.1

McCauley, C. A., White, D. M., Lilly, M. R., & Nyman, D. M. (2002). A comparison of hydraulic conductivities, permeabilities and infiltration rates in frozen and unfrozen soils. Cold Regions Science and Technology, 34(2), 117–125. https://doi.org/10.1016/S0165-232X(01)00064-7

McKenzie, J. M., Voss, C. I., & Siegel, D. I. (2007). Groundwater flow with energy transport and water–ice phase change: Numerical simulations, benchmarks, and application to freezing in peat bogs. Advances in Water Resources, 30(4), 966–983. https://doi.org/10.1016/j.advwatres.2006.08.008

Meybeck, M., Green, P., & Vörösmarty, C. (2001). A new typology for mountains and other relief classes. Mountain Research and Development, 21(1), 34–45. https://doi.org/10.1659/0276-4741(2001)021[0034:ANTFMA]2.0.CO;2

Mitchell, M. J., Driscoll, C. T., Kahl, J. S., Murdoch, P. S., & Pardo, L. H. (1996). Climatic control of nitrate loss from forested watersheds in the northeast United States. Environmental Science & Technology, 30(8), 2609–2612. https://doi.org/10.1021/es9600237

Morse, J. 2019. Climate data for C1 data loggers (CR23X and CR1000), 2000 - ongoing, daily. ver 3. Environmental Data Initiative. https://doi.org/10.6073/pasta/adac9d08d4c094a7e388a14e3885d6b7. Accessed 2020-05-02.

Morse, J. and M. Losleben. 2019. Climate data for saddle data loggers (CR23X and CR1000), 2000 - ongoing, daily. ver 3. Environmental Data Initiative. https://doi.org/10.6073/pasta/cf8ff4f209a889b4b20a4fb48be6f1d8. Accessed 2020-05-02.

Morse, J. and M. Losleben. 2019. Climate data for D1 data loggers (CR23X and CR1000), 2000 - ongoing, daily. ver 2. Environmental Data Initiative. https://doi.org/10.6073/pasta/05060472e8d1a6886fb50f1991a8344b. Accessed 2020-05-02.

Morse, J. and M. Losleben. 2019. Climate data for C1 chart recorder, 1952 - 1982. ver 3. Environmental Data Initiative. https://doi.org/10.6073/pasta/7f9c3681ef41e4b075a0f1535448d7e1. Accessed 2020-05-02.

Morse, J. 2018. Climate data for D1 chart recorder, 1952 - 1982. ver 1. Environmental Data Initiative. https://doi.org/10.6073/pasta/87a702445f76b74d8793c7b050aacf74. Accessed 2020-05-02.

Mote, P. W. (2006). Climate-driven variability and trends in mountain snowpack in western North America*. Journal of Climate; Boston, 19(23), 6209-6212,6214-6216,6218-6220.

Mualem, Y. (1976). A new model for predicting the hydraulic conductivity of unsaturated porous media. Water Resources Research, 12(3), 513–522. https://doi.org/10.1029/WR012i003p00513

Noetzli, J., Gruber, S., Kohl, T., Salzmann, N., & Haeberli, W. (2007). Three-dimensional distribution and evolution of permafrost temperatures in idealized high-mountain topography. Journal of Geophysical Research: Earth Surface, 112(F2). https://doi.org/10.1029/2006JF000545

Nyberg, L., Stähli, M., Mellander, P.-E., & Bishop, K. H. (2001). Soil frost effects on soil water and runoff dynamics along a boreal forest transect: 1. Field investigations. Hydrological Processes, 15(6), 909–926. https://doi.org/10.1002/hyp.256

Oldroyd, H. J., Higgins, C. W., Huwald, H., Selker, J. S., & Parlange, M. B. (2013). Thermal diffusivity of seasonal snow determined from temperature profiles. Advances in Water Resources, 55, 121–130. https://doi.org/10.1016/j.advwatres.2012.06.011

Oleson, W., Lawrence, M., Bonan, B., Flanner, G., Kluzek, E., Lawrence, J., … Zeng, X. (2010). Technical Description of version 4.0 of the Community Land Model (CLM). https://doi.org/10.5065/D6FB50WZ

Osterkamp, T. E. (2005). The recent warming of permafrost in Alaska. Global and Planetary Change, 49(3), 187–202. https://doi.org/10.1016/j.gloplacha.2005.09.001

Painter, S. L. (2011). Three-phase numerical model of water migration in partially frozen geological media: Model formulation, validation, and applications. Computational Geosciences, 15(1), 69–85. https://doi.org/10.1007/s10596-010-9197-z

Painter, S. L., Coon, E. T., Atchley, A. L., Berndt, M., Garimella, R., Moulton, J. D., … Wilson, C. J. (2016). Integrated surface/subsurface permafrost thermal hydrology: Model formulation and proof-of-concept simulations. Water Resources Research, 52(8), 6062–6077. https://doi.org/10.1002/2015WR018427

Painter, S. L., & Karra, S. (2014). Constitutive model for unfrozen water content in subfreezing unsaturated soils. Vadose Zone Journal, 13(4), vzj2013.04.0071. https://doi.org/10.2136/vzj2013.04.0071

Pastick, N. J., Jorgenson, M. T., Wylie, B. K., Nield, S. J., Johnson, K. D., & Finley, A. O. (2015). Distribution of near-surface permafrost in Alaska: Estimates of present and future conditions. Remote Sensing of Environment, 168, 301–315. https://doi.org/10.1016/j.rse.2015.07.019

Parrish, E., S. Anderson (2020). BCCZO -- LiDAR -- Derived DEM from LIDAR -- Boulder Creek -- (2010-2010), HydroShare, http://www.hydroshare.org/resource/a7b99c31adfe4f56899bef1a6700f9cf

Peppin, S. S. L., & Style, R. W. (2013). The physics of frost heave and ice-lens growth. Vadose Zone Journal, 12(1), vzj2012.0049. https://doi.org/10.2136/vzj2012.0049

Pribulick, C. E., Foster, L. M., Bearup, L. A., Navarre-Sitchler, A. K., Williams, K. H., Carroll, R. W. H., & Maxwell, R. M. (2016). Contrasting the hydrologic response due to land cover and climate change in a mountain headwaters system. Ecohydrology, 9(8), 1431–1438. https://doi.org/10.1002/eco.1779

Priestley, C. H. B., & Taylor, R. J. (1972). On the assessment of surface heat flux and evaporation using large-scale parameters. Monthly Weather Review, 100(2), 81–92. https://doi.org/10.1175/1520-0493(1972)100<0081:OTAOSH>2.3.CO;2

Qin, Y., Lei, H., Yang, D., Gao, B., Wang, Y., Cong, Z., & Fan, W. (2016). Long-term change in the depth of seasonally frozen ground and its ecohydrological impacts in the Qilian Mountains, northeastern Tibetan Plateau. Journal of Hydrology, 542(Supplement C), 204–221. https://doi.org/10.1016/j.jhydrol.2016.09.008

Riseborough, D., Shiklomanov, N., Etzelmüller, B., Gruber, S., & Marchenko, S. (2008). Recent advances in permafrost modelling. Permafrost and Periglacial Processes, 19(2), 137–156. https://doi.org/10.1002/ppp.615

Rogora, M. (2007). Synchronous trends in N-NO$_3$ export from N-saturated river catchments in relation to climate. Biogeochemistry, 86(3), 251–268.

Romanovsky, V. E., Smith, S. L., & Christiansen, H. H. (2010). Permafrost thermal state in the polar Northern Hemisphere during the international polar year 2007–2009: A synthesis. Permafrost and Periglacial Processes, 21(2), 106–116. https://doi.org/10.1002/ppp.689

Sarady, M., & Sahlin, E. A. U. (2016). The influence of snow cover on ground freeze-thaw frequency, intensity, and duration: An experimental study conducted in coastal northern Sweden. Norsk Geografisk Tidsskrift - Norwegian Journal of Geography, 70(2), 82–94. https://doi.org/10.1080/00291951.2016.1154102

Scapozza, C., Lambiel, C., Baron, L., Marescot, L., & Reynard, E. (2011). Internal structure and permafrost distribution in two alpine periglacial talus slopes, Valais, Swiss Alps. Geomorphology, 132(3), 208–221. https://doi.org/10.1016/j.geomorph.2011.05.010

Scherler, M., Hauck, C., Hoelzle, M., Stähli, M., & Völksch, I. (2010). Meltwater infiltration into the frozen active layer at an alpine permafrost site. Permafrost and Periglacial Processes, 21(4), 325–334. https://doi.org/10.1002/ppp.694

Schimel, J. P., Kielland, K., & Chapin, F. S. (1996). Nutrient availability and uptake by tundra plants. In J. F. Reynolds & J. D. Tenhunen (Eds.), Landscape Function and Disturbance in Arctic Tundra (pp. 203–221). https://doi.org/10.1007/978-3-662-01145-4_10

Seastedt, T. R. 2001. Soils. In: W. D. Bowman and T. R. Seastedt, editors, Structure and Function of an Alpine Ecosystem: Niwot Ridge, Colorado. Oxford University Press. p. 157-173.

Seastedt, T. R., Bowman, W. D., Caine, T. N., McKnight, D., Townsend, A., & Williams, M. W. (2004). The landscape continuum: A model for high-elevation ecosystems. BioScience, 54(2), 111–121. https://doi.org/10.1641/0006-3568(2004)054[0111:TLCAMF]2.0.CO;2

Shanley, J. B., & Chalmers, A. (1999). The effect of frozen soil on snowmelt runoff at Sleepers River, Vermont. Hydrological Processes, 13(12–13), 1843–1857. https://doi.org/10.1002/(SICI)1099-1085(199909)13:12/13<1843::AID-HYP879>3.0.CO;2-G

Slater, A. G., & Lawrence, D. M. (2013). Diagnosing present and future permafrost from climate models. Journal of Climate; Boston, 26(15), 5608–5623.

Smith, M. W. 1985. Models of soil freezing. In: M. Church and O. Slaymaker, editors, Field and theory: Lectures in geocryology. Univ. of British Columbia Press, Vancouver. p. 96–120.

Stähli, M., Jansson, P.-E., & Lundin, L.-C. (1996). Preferential water flow in a frozen soil—A two-domain model approach. Hydrological Processes, 10(10), 1305–1316. https://doi.org/10.1002/(SICI)1099-1085(199610)10:10<1305::AID-HYP462>3.0.CO;2-F

Staub, B., Marmy, A., Hauck, C., Hilbich, C., & Delaloye, R. (2015). Ground temperature variations in a talus slope influenced by permafrost: A comparison of field observations and model simulations. Geographica Helvetica, 70(1), 45–62. https://doi.org/10.5194/gh-70-45-2015

Stewart, I. T. (2009). Changes in snowpack and snowmelt runoff for key mountain regions. Hydrological Processes, 23(1), 78–94. https://doi.org/10.1002/hyp.7128

Suckling, P. W., & Hay, J. E. (1976). Modelling direct, diffuse, and total solar radiation for cloudless days. Atmosphere, 14(4), 298–308. https://doi.org/10.1080/00046973.1976.9648425

Taber, S. (1929). Frost heaving. The Journal of Geology, 37(5), 428–461.

Tarboton, D. G., & Luce, C. H. (1996). Utah Energy Balance Snow Accumulation and Melt Model (UEB). Retrieved from https://digitalcommons.usu.edu/cee_facpub/2977

Thies, H., Nickus, U., Mair, V., Tessadri, R., Tait, D., Thaler, B., & Psenner, R. (2007). Unexpected response of high alpine lake waters to climate warming. Environmental Science & Technology, 41(21), 7424–7429. https://doi.org/10.1021/es0708060

Thies, H., Nickus, U., Tolotti, M., Tessadri, R., & Krainer, K. (2013). Evidence of rock glacier melt impacts on water chemistry and diatoms in high mountain streams. Cold Regions Science and Technology, 96(Supplement C), 77–85. https://doi.org/10.1016/j.coldregions.2013.06.006

Thunholm, B., Lundin, L.-C., & Lindell, S. (1989). Infiltration into a frozen heavy clay soil. Nordic Hydrology; Copenhagen, 20(3), 153–166.

Tierney, G. L., Fahey, T. J., Groffman, P. M., Hardy, J. P., Fitzhugh, R. D., & Driscoll, C. T. (2001). Soil freezing alters fine root dynamics in a northern hardwood forest. Biogeochemistry, 56(2), 175–190.

van Genuchten, M. T. (1980). A closed-form equation for predicting the hydraulic conductivity of unsaturated soils 1. Soil Science Society of America Journal, 44(5), 892–898. https://doi.org/10.2136/sssaj1980.03615995004400050002x

Walder, J., & Hallet, B. (1985). A theoretical model of the fracture of rock during freezing. GSA Bulletin, 96(3), 336–346. https://doi.org/10.1130/0016-7606(1985)96<336:ATMOTF>2.0.CO;2

Walker, D. A., Halfpenny, J. C., Walker, M. D., & Wessman, C. A. (1993). Long-term studies of snow-vegetation interactions. BioScience, 43(5), 287–301. https://doi.org/10.2307/1312061

Walker, M. D., Walker, D. A., Theodose, T. A., & Webber, P. J. 2001. The Vegetation: Hierarchical Species-Environment Relationships. In: W. D. Bowman and T. R. Seastedt, editors, Structure and Function of an Alpine Ecosystem: Niwot Ridge, Colorado. Oxford University Press. p. 99-127.

Walvoord, M. A., & Kurylyk, B. L. (2016). Hydrologic impacts of thawing permafrost—A review. Vadose Zone Journal, 15(6), vzj2016.01.0010. https://doi.org/10.2136/vzj2016.01.0010

Williams, M. 2019. Groundwater well chemistry data for Niwot Saddle, C1 and Martinelli, 2005 - ongoing. ver 2. Environmental Data Initiative. https://doi.org/10.6073/pasta/00dddc061dd0b97d28f3c375b5f6ada2 (Accessed 2020).

Woo, M. (2012). Permafrost Hydrology. https://doi.org/10.1007/978-3-642-23462-0

Wright, N., Hayashi, M., & Quinton, W. L. (2009). Spatial and temporal variations in active layer thawing and their implication on runoff generation in peat-covered permafrost terrain. Water Resources Research, 45(5), W05414. https://doi.org/10.1029/2008WR006880

Yamazaki, Y., Kubota, J., Ohata, T., Vuglinsky, V., & Mizuyama, T. (2006). Seasonal changes in runoff characteristics on a permafrost watershed in the southern mountainous region of eastern Siberia. Hydrological Processes, 20(3), 453–467. https://doi.org/10.1002/hyp.5914

Yin, X. (1997). Optical air mass: daily integration and its applications. Meteorology and Atmospheric Physics, 63(3–4), 227–233. https://doi.org/10.1007/BF01027387

Zhang, N., & Wang, Z. (2017). Review of soil thermal conductivity and predictive models. International Journal of Thermal Sciences, 117, 172–183. https://doi.org/10.1016/j.ijthermalsci.2017.03.013

Zhang, T., Osterkamp, T. E., & Stamnes, K. (1996). Influence of the depth hoar layer of the seasonal snow cover on the ground thermal regime. Water Resources Research, 32(7), 2075–2086. https://doi.org/10.1029/96WR00996

Zhang, T., Osterkamp, T. E., & Stamnes, K. (1997). Effects of climate on the active layer and permafrost on the North Slope of Alaska, U.S.A. Permafrost and Periglacial Processes, 8(1), 45–67. https://doi.org/10.1002/(SICI)1099-1530(199701)8:1<45::AID-PPP240>3.0.CO;2-K

Zhang, Tingjun. (2005). Influence of the seasonal snow cover on the ground thermal regime: An overview. Reviews of Geophysics, 43(4), RG4002. https://doi.org/10.1029/2004RG000157

Zhang, Tingjun, Barry, R., Knowles, K., Ling, F., & Armstrong, R. L. (2003). Distribution of seasonally and perennially frozen ground in the Northern Hemisphere. Proc. 8th Int. Conf. Permafrost, 2, 1289–1294.

Zhao, L., Ping, C.-L., Yang, D., Cheng, G., Ding, Y., & Liu, S. (2004). Changes of climate and seasonally frozen ground over the past 30 years in Qinghai–Xizang (Tibetan) Plateau, China. Global and Planetary Change, 43(1), 19–31. https://doi.org/10.1016/j.gloplacha.2004.02.003

APPENDIX A

SENSITIVITY OF SHALLOW SOIL TEMPERATURE TO SNOW SURFACE HEAT CONDUCTANCE PARAMETER

During snowpack model development (Chapter II, section 2), it was found that in the original model framework based on the Utah Energy Balance [Tarboton and Luce, 1996], snowpack cold content, which exerts a primary control on winter shallow soil temperatures, was almost entirely determined by precipitation events, rather than heat loss at the snowpack surface. In order to properly represent the influence of snowpack depth on ground temperatures for frozen ground applications, a snow model must accurately simulate the relative influence of precipitation events (73-85%) and heat fluxes at the surface of the snowpack on the overall snowpack energy balance (16-27%) [Jennings et al., 2018].

The snow surface heat conductance K_s is the snowpack model parameter that determines the ability of heat fluxes at the snowpack surface to influence the overall snowpack energy balance. In an effort to better represent in the influence of heat fluxes at the snowpack surface, K_s was varied by a factor of ten. Physically, as the depth of the snowpack increases, heat fluxes at the snowpack surface should contribute less to the snowpack energy balance and resulting winter ground temperatures. To verify that the model accurately simulates the influence of snow depth on ground temperatures, snow depth was manipulated by scaling snowfall by a factor of two. The north-facing slope at the Gordon Gulch site (introduced in Chapters II and III) was used for this analysis.

With the K_s parameter of the original model ($K_s = 0.02\ m\ hr^{-1}$), manipulation of snowfall by a factor of two produces no overall change in winter ground temperatures (Figure 48, December-February). Spring (March-May) ground temperatures, however, do respond to

194

snowfall manipulation: a thicker snowpack requires more time to melt and preserves the cold state of the ground later into the spring.

Reducing K_s by a factor of ten ($K_s = 0.002 \ m \ hr^{-1}$) reduces winter soil temperatures compared to the original analyses, but changes in snow depth still do not exert any influence on shallow soil temperatures (Figure 49, December-February). Increasing K_s by a factor of ten ($K_s = 0.2 \ m \ hr^{-1}$, Figure 50) increases soil temperatures and increases the insulating effect of the snowpack, but again, changes in snow depth exert no influence on shallow soil temperatures. The fact that changing the snowfall rate by a factor of 2 does not induce changes in the intensity of frozen ground indicates that the modeled cold content of the snowpack (which is used to compute the soil temperature boundary condition) is mostly controlled by snow events, rather than heat loss at the snowpack surface. Consider a snowpack formed by a single snow event at a particular air temperature: since the model computes bulk snowpack temperature between energy and water contained in the snowpack (see Chapter II, section 2.1) multiplying snowfall by an integer factor scales both energy and water, producing little overall change in bulk snow temperature. When K_s is reduced, less heat escapes from the snowpack surface and the snowpack temperature is more controlled by the temperature of snow events and the ground heat flux. When K_s is increased, more heat is able to escape from the snowpack surface and the snowpack temperature decreases. However, in no K_s case was the influence of snow depth on ground temperatures represented. Thus, a modification of K_s from a constant parameter to a parameter that scales with snow depth was necessary (Chapter II, section 2.2).

Figure 48. Shallow soil temperatures produced from a snowpack model using the K_s parameter of the original modeling framework ($K_s = 0.02 \ m \ hr^{-1}$) Changes in snow depth produced by scaling snowfall by a factor of two (0.5X, 2X) do not change the intensity of winter (December-February) soil freezing significantly.

Figure 49. Shallow soil temperatures produced from a snowpack model in which the K_s parameter is reduced by a factor of ten ($K_s = 0.002\ m\ hr^{-1}$). Changes in snow depth produced by scaling snowfall by a factor of two (0.5X, 2X) do not change the intensity of winter (December-February) soil freezing significantly.

Figure 50. Shallow soil temperatures produced from a snowpack model in which the K_s parameter was multiplied by a factor of ten ($K_s = 0.2\ m\ hr^{-1}$) Changes in snow depth produced by scaling snowfall by a factor of two (0.5X, 2X) do not change the intensity of winter (December-February) soil freezing significantly.

APPENDIX B

EMERGENCE OF DEPTH DEPENDENCE IN BULK REPRESENTATION OF TRANSIENT HEAT FLOW

In Chapter II, section 3.2, the snow surface heat conductance K_s was modified from a constant value to a parameterization that scales inversely with snow depth. Sensitivity analyses presented in Appendix A suggested the need for such a modification, the utility of which was demonstrated in the snowpack sensitivity analysis presented in Figure 28, Chapter III, section 4.4.1. In this Appendix, a one-dimensional heat equation is applied to the case of a snowpack with constant depth and heat fluxes specified at both boundaries. When the equation is averaged with depth, an inverse relationship with snow depth naturally emerges. Recall Fourier's law of heat conduction in one spatial dimension (75), which was introduced in Chapter II, section 7.1.2 and is reproduced here:

$$\frac{\partial u}{\partial t} = \frac{\kappa}{C} \frac{\partial^2 u}{\partial z^2} \tag{75}$$

u is temperature, t is time, κ is thermal conductivity, C is soil volumetric heat capacity, and z is depth. For the case of a snowpack, the boundary condition at the base of the snowpack is the ground heat flux $G(t)$, which varies in time:

$$-\kappa_{z=0} \frac{\partial u_{z=0}}{\partial t} = G(t) \tag{86}$$

The boundary condition at the snowpack surface is a specified heat flux $S(t)$, which also varies in time:

$$-\kappa_{z=z_s(t)} \frac{\partial u_{z=z_s(t)}}{\partial t} = S(t) \tag{87}$$

$z_s(t)$ is the time-varying snowpack depth. Bulk representations of transient heat flow in snowpacks [e.g. Tarboton and Luce, 1996] seek to describe the stark temperature gradients present in a snowpack, while maintaining the computational efficiency of a single-layer model. To maintain fidelity to the underlying physics, the heat equation can be averaged with depth $z_s(t)$:

$$\frac{1}{z_s(t)} \int_{z=0}^{z=z_s(t)} \frac{\partial u}{\partial t} = \frac{1}{z_s(t)} \int_{z=0}^{z=z_s(t)} \frac{\kappa}{C} \frac{\partial^2 u}{\partial z^2} \tag{88}$$

Denoting the snowpack average temperature $\overline{u(t)}$, the equation becomes:

$$\frac{\partial \overline{u(t)}}{\partial t} = \frac{1}{z_s(t)} \left[\frac{\kappa_{z=z_s(t)} \frac{\partial u}{\partial z}|_{z=z_s(t)}}{C_{z=z_s(t)}} - \frac{\kappa_{z=0} \frac{\partial u}{\partial z}|_{z=0}}{C_{z=0}} \right] \tag{89}$$

Substituting the boundary conditions (84) and (85) for the terms in brackets:

$$\frac{\partial \overline{u(t)}}{\partial t} = \frac{1}{z_s(t)} \left[\frac{G(t)}{C_{z=0}} - \frac{S(t)}{C_{z=z_s(t)}} \right] \tag{90}$$

Although the time dependence of $S(t)$ and $G(t)$ limits any further analytical solution development, the $\frac{1}{z_s(t)}$ relationship evident in (90) holds for any $S(t)$ and $G(t)$.

APPENDIX C

EFFECTIVE LOCATION OF AVERAGE SNOWPACK TEMPERATURE DERIVED FROM ONE-DIMENSIONAL NUMERICAL HEAT CONDUCTION MODEL

In Chapter II, section 3.2, the snow surface heat conductance K_s was modified from a constant value to a parameterization that scales inversely with snow depth. Recall that net available energy at the snowpack surface is balanced by conduction into the snow, represented based on a gradient between the average temperature T_{snow} of the snowpack and the snow surface temperature T_{ss}:

$$Q_{sn} + Q_{li} + Q_p - Q_{le}(T_{ss}) + Q_h(T_{ss}) + Q_e(T_{ss}) = K_s \rho_s c_s (T_{ss} - T_{snow}) \qquad (34)$$

ρ_s is snow density (kg m³), c_s is the specific heat of snow, and K_s is a snow surface heat conductance (m hr⁻¹) related to the thermal diffusivity of the snow α_s and the depth over which the gradient acts Z_e:

$$K_s = \frac{\alpha_s}{Z_e} \qquad (35)$$

In the original model, the effective depth Z_e, over which the thermal gradient between the snowpack surface temperature T_{ss} and bulk snowpack temperature T_{snow} acts, is held constant at the depth of thermal penetration of diurnal temperature variations at the snowpack surface. The fixed Z_e of the original model was replaced with a quantity that scales with snow depth: Z_e was assumed to be equal to half of the snow depth.

In this Appendix, a one-dimensional numerical heat conduction model is applied to the case of a snowpack with constant depth to determine the effective location of the average snowpack temperature T_{snow}, and therefore justify the validity of assuming that T_{snow} occurs at approximately half the snow depth. The model is similar to that described in Chapter II, section 7.1.2, with the domain extended and assigned a combination of snowpack and soil properties. Again, a Crank-Nicholson scheme with a time step of 1hr and

vertical resolution of 1cm is used to simulate the propagation of heat according to Fourier's law:

$$\frac{\partial u}{\partial t} = \frac{\kappa}{C}\frac{\partial^2 u}{\partial z^2} \tag{75}$$

u is temperature, t is time (s), κ is thermal conductivity, C is soil volumetric heat capacity, and z is depth. The model includes a 5m soil layer (z_{soil}) and three snow depth (z_{snow}) cases: 10cm, 50cm, and 100cm snow depths are considered in this analysis. The soil layer is assigned the mean of thermal parameters for organic and clastic materials from Woo [2012] using equations (58), (59), and (60), assuming zero liquid and solid water content. The snowpack layer is assigned a thermal diffusivity from Oldroyd et al. [2013]:

$$\frac{\kappa}{C} = 2.5 \times 10^{-7} m^2 s^{-1} \tag{91}$$

The thermal boundary condition applied to the deep subsurface ($z = z_{soil} + z_{snow}$) is a geothermal heat flux condition [Ehlers, 2004]:

$$\frac{\partial u_{z=z_{soil}+z_{snow}}}{\partial z} = 0.04\ W\ m^{-2} \tag{92}$$

In this case, z is positive downward. The condition on the top boundary of the domain ($z = 0$) prescribed as the snowpack surface temperature, derived by solving (34):

$$u_{z=0} = T_{ss} \tag{93}$$

The model is run for the full duration of the snow season for water years 2013-2016 on the north-facing slope at Gordon Gulch (see Chapter II, sections 2 and 3). During each timestep, the average snowpack temperature is computed, and the location of the average snowpack temperature within the snowpack is retained. Next, the locations are averaged across water years 2013-2016; average values are presented in Table 9. The location of the average snowpack temperature as a fraction of snow depth is 0.42, 0.48, and 0.50 for snow depths 10cm, 50cm, and 100cm respectively, indicating that an effective depth Z_e of half the snow depth is an excellent approximation. Compared to the 100cm case, the snowpack

average temperature is closer to the snowpack surface in the 10cm case, suggesting that with increasing snow depth, the location approaches $\frac{z_{snow}}{2}$.

Snow Depth (cm)	Distance of Average Snowpack Temperature from Snowpack Surface (cm)	Location of Average Snowpack Temperature as a Fraction of Snow Depth
10	4.2	0.42
50	24.0	0.48
100	49.5	0.50

Table 9. Location of average snowpack temperature within the snowpack. Values are obtained using surface energy forcings from water years 2013-2016 on the north-facing slope at Gordon Gulch.

APPENDIX D

SENSITIVITY OF SHALLOW SOIL TEMPERATURE TO SUBSURFACE MODEL
VERTICAL DISCRETIZATION

In Chapter IV, 5cm soil temperatures are used to validate the soil temperature model at Niwot Ridge. As the subsurface model discretization is 10cm, 5cm modeled soil temperatures are taken from the cell nearest to the soil surface. To analyze the sensitivity of such 5cm modeled temperatures to subsurface model discretization, an additional set of simulations were performed with 1cm vertical discretization, instead of the 10cm vertical discretization used throughout this thesis. 5cm soil temperatures produced by the subsurface model with 1cm discretization are compared to the original 5cm soil temperatures produced with 10cm discretization (Figure 51). A Nash-Sutcliffe coefficient is computed between the two sets, indicating that the choice of vertical discretization has little effect on model results. As thermo-hydrologic model simulations require very high computational time and energy, it would not be feasible to conduct a thermo-hydrologic analysis of seasonally and perennially frozen ground with a 1cm discretization.
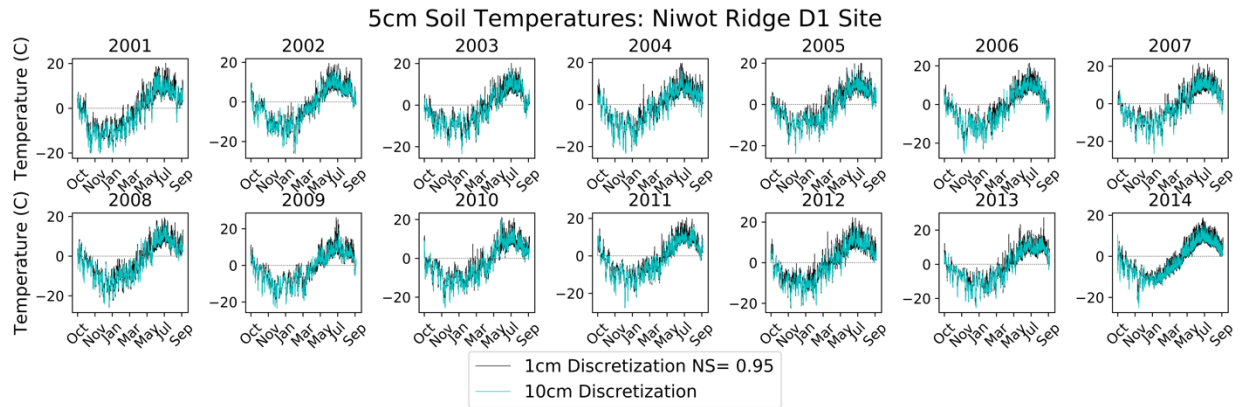
Figure 51. 5cm soil temperatures produced by subsurface model with 1cm discretization (black) and 10cm discretization (cyan). A Nash-Sutcliffe coefficient (NS=0.95) is computed between the two sets of modeled temperatures, indicating that the choice of vertical discretization has little effect on model results.

APPENDIX E

SENSITIVITY OF ACTIVE LAYER DEPTH TO POROSITY AND WATER TABLE
DEPTH

In Chapter IV, a set of shallow ground temperature profiles corresponding to three climate scenarios (past: 1952-1970, present: 2000-2013, and future: 2100) were presented and the active layer thickness was identified. In those simulations the active layer thicknesses for each simulation were 1.3m, 1.4m, and 6.4m. As those depths are relatively shallower than the observations of permafrost from the 1970's, a sensitivity analysis was performed in which the thermal parameters of the model were adjusted based on two mechanisms: (1) a reduction in porosity and (2) a deeper water table. For the porosity sensitivity analysis, porosities at depths 0-10m were reduced by a factor of two: base case porosities of 0.38, 0.29, and 0.2 for the soil, saprolite, and weathered bedrock layers, respectively, were set to 0.19, 0.15, and 0.1 for those layers. With lower porosity, bulk thermal parameters are influenced more strongly by the rock and soil matrix, resulting in a higher thermal diffusivity. For the water table sensitivity analysis, atmospheric pressure was specified at the base of the domain (1km beneath the soil surface) rather than at 10m below the surface. With a deeper water table, water content in the shallow subsurface decreases, and thermal diffusivity decreases, as a larger fraction of the pore space is occupied by air rather than water.

For the reduced porosity simulations, the active layer thicknesses are 2m, 3m and 23.9m in the past, present, and future scenarios, respectively. As expected, active layer thicknesses are significantly larger than those of the original simulations due to higher thermal diffusivity: changes in surface temperature are able to propagate more deeply into the subsurface. In addition, much greater thaw was simulated between the present and future scenarios in the reduced porosity case (20.9m) than in the original base case (5m). For the

deeper water table simulations, active layer thicknesses are 1.3m, 1.5m, and 8.2m. Although the active layer thickness for the past scenario is the same in the original simulation and the deeper water table simulation (1.3m), more thaw is simulated in the deeper water table simulation because there is less overall water occupying the pore space, resulting in a smaller latent heat buffer. Thus, the same energy flux results in different rates of thaw due to different water content. In general, the analysis is very sensitive to changes in porosity, due to consequent changes in thermal diffusivity, and insensitive to changes in the water table depth. However, the latter effect is also a consequence of soil properties: the clay soil water retention curve used in the model results in some soil water content at low capillary pressures. In contrast, for a sandy soil with an "abrupt" soil water retention curve instead of the "smooth" clay soil water retention curve, a change in water table depth would produce a much larger reduction in soil water content and bulk thermal diffusivity. In this case, the decrease in thermal diffusivity would reduce the ability of surface heat fluxes to propagate deep into the subsurface, resulting in a smaller active layer thickness and lower rates of thaw due to surface warming.
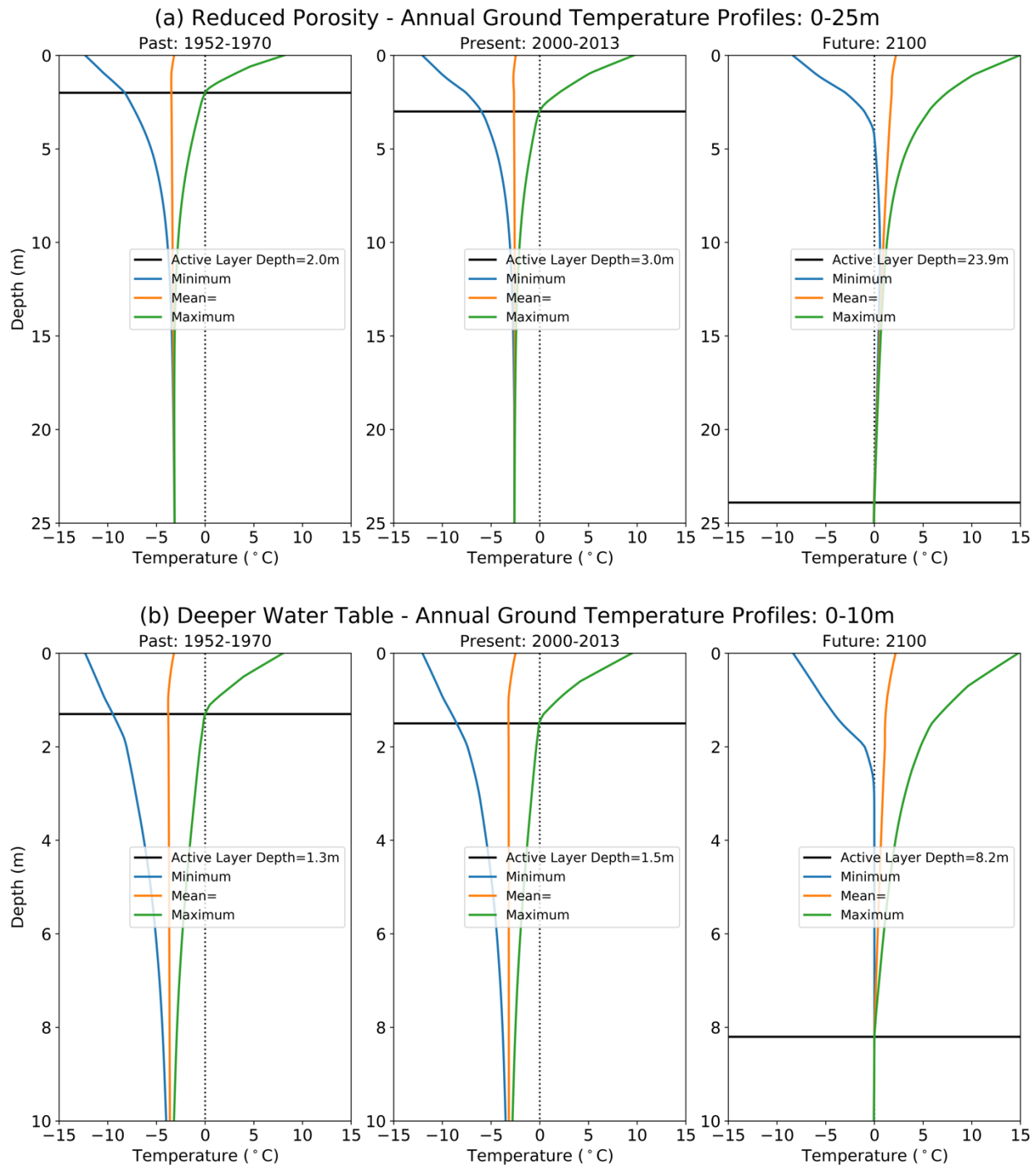
Figure 52. Annual ground temperature profiles (minimum, mean, maximum) for (a) reduced porosity simulations and (b) deeper water table simulations. Compared to 1952-1970, 2000-2013 simulations suggest little change in active layer thickness. The analysis is very sensitive to changes in porosity (which result in changes in thermal diffusivity) and mostly unsensitive to changes in water table depth.

APPENDIX F

COMPARISON OF PERMAFROST MODELS

A one-dimensional permafrost model comparison was performed. The simulation configuration from section 3.3.2 was compared to two simpler model configurations: heat conduction, and heat conduction with phase change. The heat conduction model is analogous to that described in Chapter II, section 7.1.2, with thermal properties allowed to vary as functions of temperature. One-dimensional heat conduction is modeled according to Fourier's law with an apparent heat capacity formulation:

$$\frac{\partial H(u)}{\partial t} = \frac{\partial}{\partial z}\left(\kappa \frac{\partial u}{\partial z}\right) \tag{94}$$

u is temperature, t is time, κ is thermal conductivity, C is bulk soil volumetric heat capacity, and z is depth. $H(u)$ is the volumetric enthalpy state function, given by:

$$H(u) = (1 - \phi)C_r u + \phi\left[C_i u\left(\frac{1}{2} - \frac{1}{2}tanh\,(Bu)\right) + \rho_w\left(h_f + \frac{C_w u}{\rho_w}\right)\left(\frac{1}{2} + \frac{1}{2}tanh\,(Bu)\right)\right] \tag{95}$$

ϕ is porosity, C_r is the soil volumetric heat capacity, C_i is ice volumetric heat capacity, ρ_w is the density of water, h_f is the latent heat of fusion, C_w is water volumetric heat capacity, and B is taken as 100. The hyperbolic tangent function is employed to smooth the discontinuity at $u = 0°C$. For the model without phase change, h_f is set to zero. The bulk thermal conductivity is given by:

$$\kappa = (1 - \phi)\kappa_r + \phi\left[\kappa_i\left(\frac{1}{2} - \frac{1}{2}tanh\,(Bu)\right) + \kappa_w\left(\frac{1}{2} + \frac{1}{2}tanh\,(Bu)\right)\right] \tag{96}$$

κ_r, κ_i, and κ_w are soil, ice, and water thermal conductivities. Both models are run with the same configuration and subsurface parameters as the thermo-hydrologic simulations described in section 3.3.2 (i.e. 1km domain, 10cm-1m discretization, monthly average air temperature surface boundary condition, geothermal heat flux bottom boundary condition). The heat conduction models were fully saturated with water in liquid and/or solid phase; to provide a meaningful comparison between the heat conduction and thermo-hydrologic

models, a water table was established at the soil surface in the thermo-hydrologic simulation in order to maintain full saturation throughout the domain. As no recharge was imposed in any simulation, the primary difference between the heat conduction with phase change model and the thermo-hydrologic model are the heat capacity and thermal conductivity formulations, as well as vapor diffusion: the thermo-hydrologic model simulates vapor flow resulting from gradients in pressure.

We begin by discussing the active layer thicknesses simulated in each model, rounded to the nearest meter for simplicity. Compared to thicknesses of 1m, 1m, and 7m in the thermo-hydrologic model, the heat conduction model produces thicknesses of 4m, 5m, and 28m, whereas the heat conduction model with phase change produces thicknesses of 3m, 3m, and 8m in the past, present, and future scenarios, respectively. Thus, the thermo-hydrologic model and heat conduction with phase change model are in general agreement regarding the change in active layer thickness in response to warming: 5m from present to future. In contrast, the heat conduction model without phase change simulates significantly greater thaw than the other models: 23m from present to future. Active layer thickness in the heat conduction model with phase change is larger in the past and present scenarios than that of the thermo-hydrologic model because of the treatment of phase change: within PFLOTRAN-ICE, phase change begins occurring at 0°C and continues at temperatures significantly below 0°C based on the soil characteristic curve (see Chapter II, section 4 equations (51) and (52)) whereas the heat conduction model with phase change considers phase change to occur symmetrically about 0°C, within a narrower temperature range than PFLOTRAN-ICE. The heat conduction model without phase change produces slightly larger active layer thicknesses than the model with phase change because of the lack of a latent heat buffer.

In comparison to the subsurface temperatures produced by the thermo-hydrologic model, the heat conduction model without phase change tends to overestimate soil freezing at

depths 200m-800m (Figure 53) due to its lack of a latent heat buffer. In the range 800m-1km, the heat conduction model without phase change generally agrees with the thermo-hydrologic model, since temperatures remain above 0°C and heat transfer occurs by conduction only. The heat conduction model with phase change deviates from the thermo-hydrologic model (overestimates temperatures at 0-400m depth; underestimates temperatures at 400m-1km depth) due to the difference in the treatment of phase change discussed in above: within PFLOTRAN-ICE, phase change begins occurring at 0°C and continues at temperatures significantly below 0°C based on the soil characteristic curve (see Chapter II, section 4 equations (51) and (52)) whereas the heat conduction model with phase change considers phase change to occur symmetrically about 0°C, within a narrower temperature range than PFLOTRAN-ICE. Thus, the heat conduction model without phase change matches PFLOTRAN-ICE more closely than the heat conduction model with phase change at depths 0-100m because soils in the PFLOTRAN-ICE simulation have not completely changed phase.
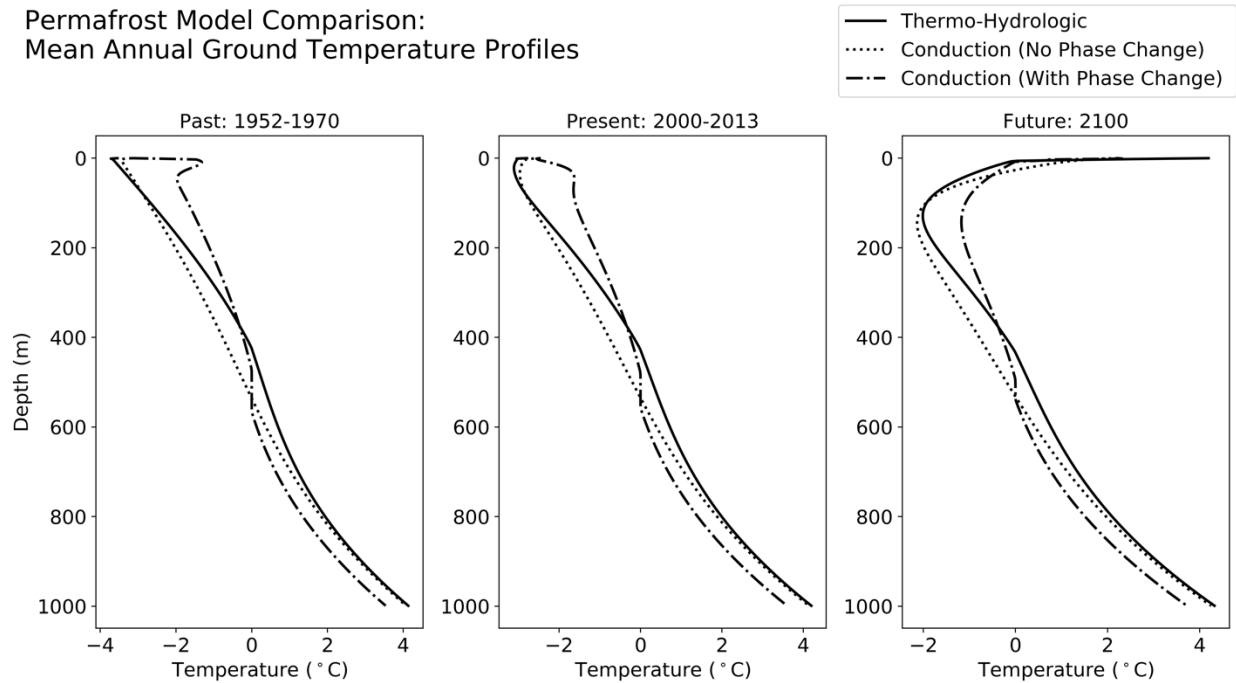
Figure 53. Comparison of mean annual ground temperature profiles simulated by thermo-hydrologic (solid line), conduction without phase change (dotted line), and conduction with phase change (dash-dotted line).